IN SITU SENSING OF MULTIPLE PARAMETERS FOR MULTI-FUNCTIONAL ADHESIVES

by

MAXIMILIAN HLATKY

A thesis submitted to the University of Birmingham for the degree of

DOCTOR OF PHILOSOPHY

School of Metallurgy and Materials
College of Engineering and Physical Sciences
University of Birmingham
February 2025

UNIVERSITY^{OF} BIRMINGHAM

University of Birmingham Research Archive

e-theses repository

Abstract

Optical fibre sensors (OFS) have been widely recognised for their effectiveness in monitoring processes associated with epoxy-based polymers. Building on this foundation, this research expands the application of OFS to adhesive joints, facilitating *in situ* monitoring during manufacturing. This approach provides a robust and comprehensive means of ensuring bond quality and performance.

The study centres on fabricating single-lap joints (SLJs) using aluminium-to-aluminium, composite-to-composite, and aluminium-to-composite configurations. These joints were produced under varying surface preparation conditions, including different grit-blasting durations and silane concentrations, to assess their effects on bond strength and joint performance. Additionally, the integration of advanced sensor technologies, such as Fourier-transform infrared spectroscopy (FTIR), fibre Bragg gratings (FBGs), Fresnel reflection sensors (FRS), and Fabry-Perot (FP) cavities, enabled the monitoring of critical parameters, including refractive index evolution, functional group changes, temperature, and shrinkage.

A comparative analysis of cure kinetics measured by FTIR and FRS demonstrated that FRS offers a cost-effective alternative to FTIR for monitoring the cure kinetics. The quantitative correlation of data between these methods reinforces the reliability of FRS for real-time monitoring applications. Furthermore, embedding multiple sensor types within SLJs provided valuable insights into the curing dynamics and performance of adhesive joints across diverse conditions. Additionally, a relation between FRS noise and viscosity could be established by comparing parallel rheology results with the noise thresholds of the FRS traces.

Key findings reveal that higher concentrations of silane treatments significantly reduce the ultimate tensile strength (UTS) of grit-blasted CFRP joints while not significantly improving

aluminium joints. Additionally, surface roughness was found to correlate with the formation of microvoids in adhesive layers; increased roughness led to a higher density of voids, potentially compromising bond integrity. These results emphasise the critical role of precise surface preparation in achieving durable adhesive bonds.

This research demonstrates the capability of OFS to enable *in situ* monitoring of key parameters, such as refractive index, temperature, shrinkage, and chemical changes in functional groups. Furthermore, the successful integration of these sensors highlights their potential for both real-time process monitoring and post-process evaluations, advancing the development of smarter adhesive joint technologies for a wide range of engineering applications.

Gewidmet meiner Uroma Resi Richter, die während meiner

Promotion von uns ging, sowie unserer Hündin Clara, die kurz vor

Abgabe dieser Arbeit von ihrem Leiden an Epilepsie erlöst wurde.

Acknowledgements

Table of Contents

List of Figures

List of Tables

List of Abbreviations

SLJ Single-lap joint

OFS Optical fibre sensor

FTIR Fourier-transform infrared spectroscopy

FP Fabry-Perot

FBG Fibre Bragg grating

FRS Fresnel reflection sensor

SOD Stand-off distance

TIR Total internal reflection

SEM Scanning electron microscopy

EDX/EDS Energy dispersive X-ray spectroscopy/ Energy dispersive spectroscopy

BLT Bond-line thickness

RI Refractive index

SFE Surface free energy

TGA Thermogravimetric analysis

OVD Outside vapour deposition

MCVD Modified Chemical Vapour Deposition

GFRP Glass Fibre-Reinforced Polymer

CFRP Carbon Fibre-Reinforced Polymer

^{1}H NMR Proton nuclear magnetic resonance

FVF Fibre Volume Fraction

FSP Fringe Spacing

FSR Free Spectral Range

MAE Mean Absolute Error

1. Introduction

1.1. Motivation

The demand for advanced adhesive joints in structural applications has grown significantly across aerospace, automotive, and renewable energy industries, driven by the need for lightweight materials and efficient load-bearing capabilities. Adhesive bonding offers numerous advantages over traditional joining methods, including reduced weight, improved stress distribution, and the ability to bond dissimilar materials. However, the performance and durability of adhesive joints remain influenced by factors such as the quality of surface preparation, adhesive properties, and environmental conditions during service. This complexity necessitates accurate characterisation methods to optimise joint design and predict long-term reliability.

Embedding optical fibre sensors (OFS) into adhesive joints has emerged as a promising approach to monitor their behaviour *in situ*. OFS technology offers unique advantages, including small size, immunity to electromagnetic interference, and the ability to provide distributed or localised measurements. These features make OFS highly suitable for characterising structural adhesives.

This thesis investigates the effects of abrasive blasting and silane treatments in metal-to-metal, composite-to-composite, and metal-to-composite SLJs. After assessing manufactured joints, the main aim was the integration of optical fibre sensors in SLJs to characterise (i) changes in functional groups during cross-linking, (ii) temperature changes, (iii) refractive index changes, and (iv) shrinkage. The study emphasises the usage of Fresnel reflection-based sensors, surface-mounted FTIR transmission sensors, FBGs and FP cavity sensors.

This work aims to bridge the gap between laboratory-scale characterisation and real-world application of adhesive joints. By addressing key challenges in embedding OFS within adhesive layers, including strain decoupling and sensor reliability, this research provides a foundation for developing bonded structures with integrated sensing capabilities, advancing the design and monitoring of adhesive joints in modern engineering applications.

1.1 Motivation

1.2. Project Aims and Objectives

The primary aim of this thesis is to evaluate the potential of embedding OFS into adhesive joints for *in situ* monitoring of (i) strain, (ii) chemical changes, (iii) temperature, and (iv) refractive index during curing at different isothermal temperatures. A secondary aim is to investigate the effect of surface treatments on the bond strength of metal, composite and hybrid SLJs.

To fulfil the aims mentioned above, the objectives were as follows:

i.   To assess the feasibility of embedding different types of OFS into adhesive joints.

ii.   To evaluate the capability of OFS to monitor strain, chemical changes, temperature, and refractive index in situ during adhesive curing and joint testing.

iii. To validate OFS measurements through cross-comparison with conventional characterisation techniques (e.g., FTIR, rheometry).

iv.   To develop and use an adhesive joint testbed to embed OFS and investigate sensor response under different curing temperatures.

v.   To determine the influence of grit-blasting and silane treatment on the surface morphology of CFRP and aluminium substrates and their corresponding effect on joint strength.

vi.   To investigate the formation of interfacial microvoids as a function of surface roughness induced by grit-blasting.

1.3. Thesis Outline

Chapter 2 presents a literature review on adhesive bonding, with a focus on surface treatments, including abrasive blasting and silane coupling agents. It discusses the principles of light guiding in optical fibre sensors, process monitoring using conventional techniques, and the role of optical fibre sensors in process monitoring.

Chapter 3 outlines the materials and methods used in this study. It describes the optical fibres and sensors, interrogation equipment, and the substrate materials and structural adhesive for SLJs. Key experimental setups, such as the FTIR-FRS configuration and the custom-built SLJ manufacturing rig, are detailed. Conventional analytical techniques, including DSC, parallel plate rheology, and FTIR, are described, along with surface treatments and their evaluation. The chapter concludes with tensile testing and glove box experiments for *in situ* sensor assessment during isothermal curing.

Chapter 4 presents experimental results and their implications. It covers FRS calibration using an Abbe refractometer and discusses FTIR-FRS experiments, including temperature non-uniformity, cure rate comparisons, and FRS noise correlations with gelation. The chapter validates focus variation microscopy, details SLJ manufacturing with surface treatments, and evaluates bond line thickness and tensile testing results. It also highlights the *in situ* assessment of SLJs using FRS, FBG, and FP sensors, including strain-temperature decoupling and peak tracking validation.

Chapter 5 summarises the thesis findings, highlighting the impact of grit-blasting and silane treatments on bond strength and the correlation between surface roughness, microvoid formation, and adhesion strength. It discusses advancements in FRS, including its noise correlation with gelation, and the effectiveness of FBG and FP sensors. Challenges with

embedded sensors and thermal lag in glove box experiments are also addressed, with recommendations for optimising joint performance and monitoring.

Chapter 6 outlines future research directions to advance SLJs and expand OFS applications. Key areas include investigating microvoid formation, optimising grit-blasting, addressing FRS noise and polymer diffusion, and exploring real-time adhesive mixing monitoring. Further studies are proposed on FP and FTIR sensors for detecting moisture ingress and shrinkage in SLJs, as well as multi-sensor approaches to analyse adhesive-substrate interactions and spatial variations in SLJs.

1.3 Thesis Outline

2. Literature Review

2.1. Adhesives in structural applications

An adhesive is a material designed to join two or more surfaces by creating a bond at their interface. It forms a strong attachment that holds the materials together. Adhesives can be derived from natural or synthetic sources and are widely utilised because they enable seamless and uniform connections without relying on mechanical fasteners such as nails or screws (Cognard, 2006). The unifying characteristic of adhesives is their ability to distribute stress across a bonded interface, enabling the assembly of dissimilar materials and complex geometries that might otherwise be unattainable (Monden, 2016, Ebnesajjad, 2010). On the contrary, quality assessments of adhesives are challenging, as bond strength is influenced by various factors, including surface preparation, control over the cross-linking process (such as stoichiometry, homogeneity, temperature, applied lateral forces, and humidity), wetting behaviour, and the thickness of the adhesive layer (Cognard, 2006, Ebnesajjad, 2010).

While adhesives are primarily associated with bonding in structural applications, their utility extends far beyond this domain. They are integral to coatings, paints, varnishes, and the manufacturing of composite materials. In these applications, adhesives contribute not only to the structural integrity of the components but also to functional and aesthetic properties, such as corrosion resistance, durability, and surface finish (Pearson et al., 2003). For the purposes of this study, however, the focus is limited to the structural applications of adhesives, specifically in the context of adhesive joints.

2.1.1. Theory of Adhesion

In the field of adhesive bonding, two crucial terminologies are adhesion and cohesion. Adhesion is defined by the American Society for Testing and Materials (ASTM) as: "the state in which two surfaces are held together by interphase forces" (ASTM, 2019). Cohesion is defined as: "the state in which the constituents of a mass of material are held together by chemical and physical forces" (ASTM, 2019). Both are essential for the effective performance of adhesive joints, as weak adhesion can cause interfacial failure, and poor cohesion may result in internal adhesive failure under applied stresses.

Mechanical Interlocking Theory

The mechanical interlocking theory of adhesion emphasises the contribution of two primary mechanisms: locking by friction and locking by dovetailing. This theory posits that surface roughness plays a critical role, as it creates pores and crevices into which the adhesive can penetrate and solidify, thereby enhancing the bond (Weiss, 1995). An increase in surface area, achieved through surface roughening, can further augment mechanical interlocking, provided the adhesive demonstrates sufficient absorption into these irregularities (Kim et al., 2010). Kinloch identifies mechanical interlocking as a significant adhesion mechanism, highlighting its significance in achieving robust and durable adhesive bonds (Kinloch, 2012).

Electrostatic Theory

The electrostatic theory of adhesion explains bonding as a result of electrostatic interactions between the adhesive and the substrate. This mechanism involves the generation of opposing charges at the interface, creating an attractive force that contributes to adhesion. However, its influence in non-metallic bonding is minimal, as the required charge separation is less pronounced in such materials (Ebnesajjad, 2010). The electrostatic theory is more commonly

applied to describe adhesion phenomena between powders and solid surfaces, where charge interactions play a more significant role in the bonding process (Horenstein, 2009).

Adsorption Theory (wetting theory)

Adhesion can be attributed to the molecular contact between two materials, driven by various interfacial forces such as van der Waals forces, hydrogen bonding, and acid-base interactions (Ebnesajjad, 2010, Gardner, 2017). These forces play a pivotal role in creating strong bonds by enhancing wettability, which is essential for achieving high bonding quality (Baldan, 2012). Among these, van der Waals forces and hydrogen bonds are the most commonly encountered mechanisms contributing to adhesion (Kinloch, 2012). Together, these interfacial forces facilitate intimate molecular contact and effective adhesion between the surfaces.

Diffusion Theory

The diffusion theory of adhesion describes the process in which two materials dissolve into one another, resulting in the formation of an interphase. This mechanism requires the materials to exhibit similar solubility parameters to enable effective interdiffusion (Temin, 1990). The strength of the bond formed is influenced by the intrinsic properties of the materials and the resulting diffusion potential. Since the materials are mutually dissolved at the interphase, the interface is stress-free, contributing to the stability of the bond. This mechanism is primarily applicable to polymer-to-polymer bonding, where the compatibility of the materials facilitates the interdiffusion process (Ebnesajjad, 2010).

Chemical Bonding Theory

Chemical bonding theory explains adhesion as a result of chemical forces, including hydrogen bonds, covalent bonds, and ionic bonds. These bonds form at the interface and contribute significantly to the strength and stability of the adhesive joint. The effectiveness of chemical bonding is highly dependent on the chemical composition of the substrate surface, as

2.1.1 Theory of Adhesion

compatibility between the adhesive and substrate dictates the potential for bond formation (Ebnesajjad, 2010). This theory underpins the use of silanes as coupling agents, where silane molecules react chemically with both the substrate and the adhesive to enhance interfacial adhesion (Gardner, 2017).

Weak Boundary Layer Theory

The weak boundary layer theory attributes adhesion failure to the presence of a layer with compromised strength at the interface. This layer can arise due to air bubbles, impurities, or adverse reactions between the adhesive and the substrate, all of which weaken the bond (Bikerman, 2013). Such a boundary layer may exist within the adhesive or the substrate itself, and failure within this layer often resembles interfacial failure (Ebnesajjad, 2010). Addressing these issues through surface preparation and careful selection of materials is critical to minimising the risk of weak boundary layer formation and ensuring robust adhesive performance.

The literature on adhesion describes these theories as complex, with each explaining specific mechanisms depending on the materials and conditions involved. While these theories provide valuable insights, no single theory comprehensively explains all adhesion phenomena, leading to ongoing discussions within the field. The choice of theory often depends on the specific application and material system, reflecting the complex and multifaceted nature of adhesion. As a result, the literature does not offer a clear consensus but highlights the importance of integrating multiple perspectives for a thorough understanding of adhesion (Kinloch, 2012, Ebnesajjad, 2010). The adsorption theory was stated to be the most universally applicable (Pearson et al., 2003, Kinloch, 2012).

2.1.1 Theory of Adhesion
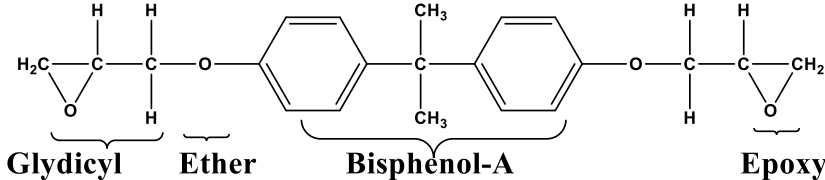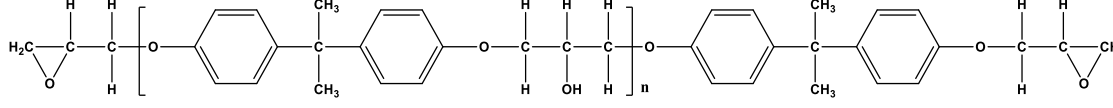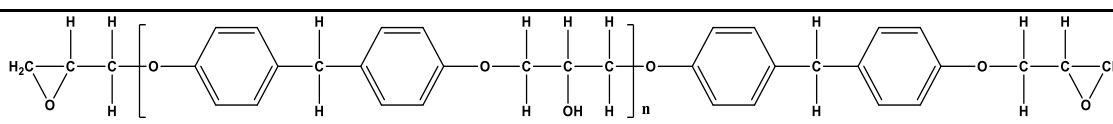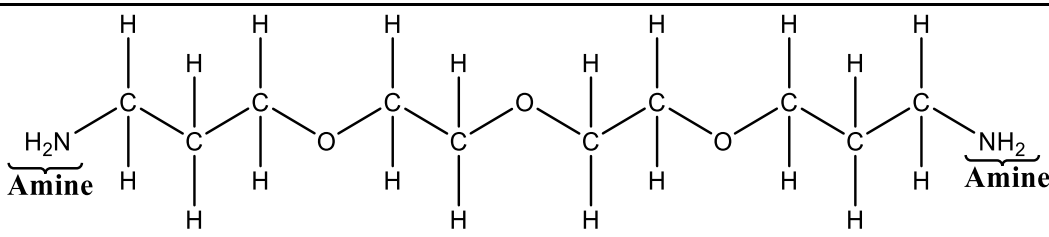
2.1.2. Epoxy-based adhesives for structural applications

As previously discussed, adhesives can be classified into several distinct categories based on their composition, curing mechanism, and application. This work focuses specifically on two-component structural epoxy adhesives, and therefore, only these are further explained.

Resin systems in polymer science are broadly categorised into two types: thermoplastics and thermosets. The primary distinction between these two classes lies in their behaviour during processing. Thermosets undergo an irreversible chemical reaction during curing, forming a rigid, crosslinked, three-dimensional network. This permanent structure provides thermal stability, mechanical strength, and chemical resistance, but it cannot be reshaped or reprocessed after curing. In contrast, thermoplastics do not form crosslinks but undergo reversible physical changes. Their linear or slightly branched molecular structure allows them to soften upon heating and solidify upon cooling, enabling repeated reshaping and recycling (Billmeyer, 1984). Epoxy resins are described as low-molecular-weight prepolymers that possess multiple epoxide groups in their structure (Tanaka, 2018). Epoxy resin systems have been extensively studied, particularly in terms of their reaction mechanisms, kinetics, and network formation (Karkanas and Partridge, 2000, Yamaguchi et al., 2022, Morsch et al., 2023). For this work, the focus is on epoxy-amine systems.

The cross-linking of a general epoxy-amine is initiated by its hardener, specifically the amine-based reagent. Table 1 presents typical examples of epoxy resins and amine hardeners used as structural adhesives.

Table 1 The chemical structures and naming conventions for a commercially available epoxy resin and amine hardener are as follows.

Structure

A

Glydicyl   Ether   Bisphenol-A   Epoxy

Bisphenol-A Diglycidyl Ether

B

Diglycidyl Ether of Bisphenol-A (DGEBA)

C

Diglycidyl Ether of Bisphenol-F (DGEBF)

D

Amine   Amine

3,3'-[Oxybis(Ethane-2,1-Diyloxy)]Dipropan-1-Amine

3,3'-Oxybis(Ethyleneoxy)Bis(Propylamine)

Referring to Table 1, structure (A) represents the fundamental unit of bisphenol-A diglycidyl ether (Morgan et al., 1984), along with the common names of the associated chemical functional groups. The chemical components involved in the cross-linking reactions are the epoxy and amine functional groups (structures B (Garcia et al., 2007), C (Tack and Ford, 2008), and D). Figure 1 shows a generalised reaction scheme illustrating this process, with the amine and epoxy groups depicted as short-form structures (A) and (B), respectively.

2.1.2 Epoxy-based adhesives for structural applications

For epoxy resins cured with amines, it is widely recognised that the reaction primarily involves two key addition mechanisms: the ring-opening of both primary and secondary amines (Su and Woo, 1995).

The reaction process outlined in Figure 1 proceeds as follows: The amine (A) and epoxy (B) are combined in the appropriate stoichiometric ratio, thoroughly mixed, and degassed. The mixture is then heated to the required temperature, initiating the first step of the reaction, where a hydrogen atom from the primary amine reacts with the oxygen atom in the strained epoxy ring. This forms a covalent bond between the nitrogen and carbon atoms, as shown in structure (C). The secondary amine in structure (C) contains a hydrogen atom that can react with another epoxy group, as represented in structure (D), leading to the formation of a cross-link between the two polymer chains, depicted in (E). As the reaction continues, the multi-functional nature of the amine results in the creation of a highly cross-linked, insoluble structure. Furthermore, physical entanglements increase the structural integrity of the network (Argon, 2013, Meijer and Govaert, 2005). Additional reactions, such as homo-polymerisation (Pustkova et al., 2009) and esterification (Hayes and Seferis, 2000), may also occur, depending on the reactivity of the starting materials and the processing conditions.

2.1.2 Epoxy-based adhesives for structural applications
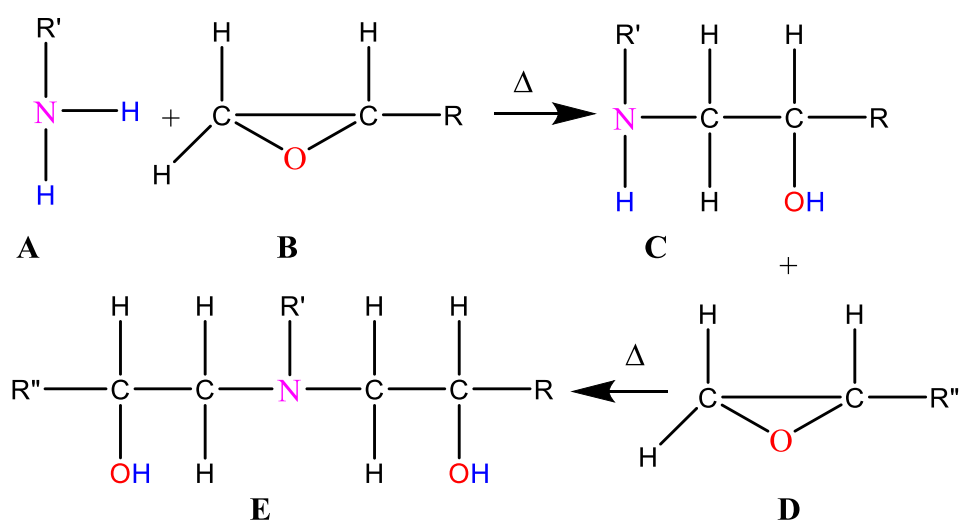
Figure 1 Generalised cross-linking reactions between epoxy and amine functional groups.

In terms of sample preparation, the individual components are weighed in the required stoichiometric ratio and mixed thoroughly until a uniform colour is observed (Katnam et al., 2011); this can be operator-dependent. Depending on the reactivity of the epoxy resin and the hardener, parameters that can influence the rate and extent of the cross-linking reactions include, the stoichiometry of the reagents (Palmese and McCullough, 1992), their shelf-life (Cuevas-Suárez et al., 2019), homogeneity of the mixed resin and hardener (Palmese and McCullough, 1992), the processing temperature (Banea et al., 2011), the rate of heating (Buch and Shanahan, 2000) and the relative humidity (Lettieri and Frigione, 2012). Furthermore, the curing reactions are of exothermic nature (Kim et al., 2002) and, precise thermal control during the processing is crucial (Machavaram et al., 2014).

2.1.3. Surface treatments

This chapter outlines surface treatment techniques aimed at improving adhesive bonding on aluminium and composite surfaces. Due to substantial differences in free surface energy and chemical composition, the treatment strategies for these materials vary significantly. The review specifically examines abrasive blasting methods and the use of silanes as coupling

agents, providing an in-depth analysis of their application and effectiveness. Crucial parameters are the surface chemistry, roughness, and wettability (Noeske et al., 2004).

For aluminium substrates, achieving higher surface roughness and surface free energy is generally a key objective following surface treatment. An oxide layer on aluminium significantly influences its surface chemistry, introducing hydroxyl groups that can interact with epoxy resins and other surface treatments such as silanes (Rider and Arnott, 2000, Rider et al., 2004). Surface contaminants are typically eliminated through processes such as degreasing, solvent wiping, or mechanical abrasion methods like grit-blasting (Borsellino et al., 2009, Boutar et al., 2016). In comparison, composites exhibit lower levels of surface free energies compared to aluminium. The highest recorded value concerning composites, at 43.1 mJm^{-2} (Baldan, 2012), and the lowest value for aluminium, which stands at 46.3 mJm^{-2}. This means that the CFRP substrates are generally failing earlier, if the surface is similar in roughness compared to a metal substrate. Unless fibres are exposed, only the polymeric matrix will contact the adhesive and a composite substrate can be treated as a polymer (Molitor et al., 2001). Composites may have peel ply or mould-release agents from manufacturing on their surface, hence, they need to be appropriately cleaned which is an important outcome of any treatment (Wingfield, 1993). Treatments that cause morphological alterations Treatments that result in morphological changes to the surface or solvent-cleaning can achieve this (Wingfield, 1993). Abrasive treatments are also known to decrease surface contaminants regarding metal adherends (Encinas et al., 2014).

2.1.4. Surface roughness

Surface roughness refers to irregularities present on a substrate, often quantified by the parameter average roughness (Ra). These surface features enhance bonding by increasing the contact area and enabling the adhesive to form a stronger connection through physical and

chemical mechanisms (Kinloch, 2012). However, excessively rough surfaces can create stress concentrations, which may weaken the bond (Bikerman, 2013).

One key contribution of surface roughness to adhesion is mechanical interlocking. Rough surfaces provide micro- and nano-scale peaks and valleys into which adhesives can flow, forming a physical anchorage after curing (Weiss, 1995). Studies have demonstrated that increasing surface roughness through methods like grit-blasting or sanding can significantly enhance bond strength (Fernando et al., 2013, Harris and Beevers, 1999, Rudawska et al., 2022, Spaggiari and Dragoni, 2013).

Surface roughness also indirectly influences adhesion by improving wettability. Rough surfaces often exhibit higher effective surface energy, which promotes better spreading of the adhesive and facilitates intimate molecular contact (Baldan, 2012). Improved wettability allows for stronger intermolecular interactions between the adhesive and substrate. However, if roughness levels are too high, trapped air pockets can reduce adhesive contact, potentially compromising bond quality (Pearson et al., 2003).

2.1.5.   Wettability

Surface free energy (SFE) is a critical parameter that significantly influences the wettability of a substrate. It represents the energy required to increase the surface area of a material, and it plays a pivotal role in determining the interaction between the substrate and a contacting liquid, such as an adhesive or coating. The relationship between FSE and wettability is governed by thermodynamic principles, particularly the balance of surface tensions at the solid-liquid interface. Contact angle measurements are a widely used method to calculate the surface free energy (SFE) of solid materials. This technique involves measuring the angles formed at the three-phase boundary (solid, liquid, and gas) of a droplet placed on the substrate. By combining

these measured angles with the known properties of the test liquids, the SFE of the solid can be determined (Baldan, 2012, Thomsen, 2008). When a liquid droplet is placed on a solid surface, it experiences adhesive interactions with the solid and cohesive forces within the liquid. These interactions influence the system's energy, leading to a reduction in surface areas at the solid-liquid and liquid-gas interfaces to achieve a more stable configuration (Kwok and Neumann, 1999). At equilibrium, the contact angle θ is related to the SFE of the solid σ_s and the liquid's surface tension σ_l through Young's equation:

$$\sigma_s = \gamma_{sl} + \sigma_l \cos \theta, \qquad\qquad [1]$$

where γ_{sl} represents the interfacial tension between the liquid and solid phases (Palencia, 2017, Kwok and Neumann, 1999). A contact angle less than 90° indicates the surface is wettable, while an angle of 0° signifies complete wetting. This equation assumes an ideal solid surface-one that is smooth, chemically homogeneous, and does not chemically interact with the test liquid (Bruel et al., 2019).

Building upon Young's equation, the Fowkes model divides the forces contributing to SFE into dispersive and polar components (Song and Fan, 2021). The SFE is calculated using:

$$\sigma_l(1 + \cos \theta) = 2\sqrt{\sigma_s^d \sigma_l^d} + 2\sqrt{\sigma_s^p \sigma_l^p}, \qquad\qquad [2]$$

where σ_s^d and σ_s^p represent the dispersive and polar components of the solid's SFE, respectively. Since these terms are unknown, at least two test liquids are required to solve for them; however, using more test liquids improves accuracy (Comyn, 1992). This approach is known as the geometric mean or extended Fowkes method.

The OWRK (Owens, Wendt, Rabel, and Kaelble) model similarly separates SFE into dispersive and polar contributions, with unknown components calculated through graphical evaluation of experimental data (Mazzola et al., 2012). Advanced models, such as the extended Fowkes

2.1.5 Wettability

model, further divide polar contributions into hydrogen bonding and dipole-dipole interactions, necessitating at least three test liquids for accurate calculations. An alternative method involves acid-base interactions, though this approach is limited by the scarcity of test liquids with well-characterised acidic and basic surface tension components (Baldan, 2012).

2.1.6. Effect of degreasing on the substrate surface

Degreasing is a critical surface preparation process employed to remove contaminants such as oils, grease, and other residues from substrates prior to bonding, coating, or other surface treatments. For materials like carbon fibre-reinforced polymer (CFRP) and aluminium, effective degreasing significantly influences adhesion performance by enhancing surface cleanliness and enabling stronger chemical or mechanical interactions. For metal substrates, solvent cleaning has been found to be able to increase bond strength, but is usually avoided as sole treatment (Fernando et al., 2013). Regarding CFRP substrates solvent cleaning may be employed to de-grease the surface and remove mould release agents from the adherend, which can significantly increase the bond strength (Wingfield, 1993).

2.1.7. Effect of grit-blasting on surface roughness

Mechanical pre-treatments include all treatments to mechanically clean and roughen the substrate surface. These methods are used to manipulate both surface topography and surface morphology in a defined manner. Common examples are manual/automatic grinding, shot-blasting or grit-blasting. The latter can be used with various abrasives such as aluminium oxide, glass beads or sand (Rasche, 2012). In general, shot and grit-blasting can be described as particles of different sizes and hardness being accelerated by compressed air and directed towards a surface. The terminologies grit and shot are used to describe the shape of the abrasive media, where shots have a round shape and grit can be described to have a coarse shape. The

2.1.6 Effect of degreasing on the substrate surface

main aim is to create a macroscopically rough surface to utilise the principle of mechanical interlocking. It should also be mentioned that blasting is accompanied by cleaning the surface (Molitor et al., 2001, Park et al., 2010). Grinding does also increase the surface roughness but literature indicates this technique to have a low repeatability (Monden, 2016, Spaggiari and Dragoni, 2013). Conducted research from several publications identified the following parameters as crucial for grit-blasting (i) grit-blast material, (ii) grit size, (iii) grit-blast angle, (iv) pressure, (v) flow rate, (vi) blast time, and (vii) stand-off distance (SOD) (Molitor et al., 2001, Park et al., 2010, Tamai and Aratani, 1972, Hitchcock et al., 1981, Harris and Beevers, 1999, Khan et al., 2019, Amada and Hirose, 1998, Amada and Satoh, 2000, Fernando et al., 2013, Ghara et al., 2021, Chander et al., 2009, Mellali et al., 1997, Baldan, 2004a, Baldan, 2004b, Asl and Sohi, 2010). It was observed that rougher surfaces display lower surface energy values compared to smoother surfaces (Tamai and Aratani, 1972, Hitchcock et al., 1981, Harris and Beevers, 1999, Khan et al., 2019). Surface roughness also does not correlate linearly to bonding strength. Comparative studies demonstrated fractal analysis to show a direct correlation between surface roughness and bond strength (Amada and Satoh, 2000, Amada and Hirose, 1998). Grit-blast material residues are heavily dependent on blasting angle and substrate material. The contamination amount of grit-blast material on the surface does increase with increasing grit-blast angle. The term grit-blasting angle can be understood as the angle between the plane of the blasting nozzle and the plane of the surface to be blasted. Also, an increase in hardness could be observed with higher angles (Ghara et al., 2021, Chander et al., 2009). It was suggested that two main phenomena occur, namely micro-cutting and indentation. Latter increases with increasing angle and produces rougher surfaces (Ghara et al., 2021).

Regarding the SOD and its influence on roughness, it was found that there usually occurs one ideal SOD which causes the highest roughness at the same pressure and blast time (Chander et al., 2009, Mellali et al., 1997, Baldan, 2004a, Baldan, 2004b). Below SOD particles lose

2.1.7 Effect of grit-blasting on surface roughness

efficiency due to collisions with ricocheting particles and above SOD efficiency is also reduced due to entrainment of air. Greater grit sizes do increase surface roughness (Harris and Beevers, 1999, Fernando et al., 2013) and finer grits cause higher surface energies and seem to cause faster adhesive degradation when submerged in water. Also, it was found that bigger grits decrease fractal dimension values. Blasting time seems to behave more randomly. When investigating short blasting times (> 15 seconds), a constant roughness increase was found (Asl and Sohi, 2010). For longer blasting durations (> 150 seconds) a peak value can usually be observed followed by a slow decrease or a constant roughness (Ghara et al., 2021, Chander et al., 2009). This is believed to be caused by the hardening work of the grit having a saturation point after which no roughening is achieved anymore but some of the folded over chip material was seen to be removed which was suspected to be the reason for the roughness decrease (Ghara et al., 2021).

Sanding can also be used as abrasive treatment. It was found to initially increases bond strength due to improved mechanical interlocking but decreases at high roughness because the adhesive cannot properly penetrate deep asperities, reducing effective bonding. In contrast, shot blasting and sand blasting continuously increase bond strength as roughness increases, as these processes create surface pits that enhance adhesive penetration and bonding area. Sand blasting results in higher roughness and superior strength compared to shot blasting. For sanding, the optimal roughness depends on adhesive viscosity, with high-viscosity adhesives performing better at lower roughness levels. The key reason shot and sand blasting do not show a plateau or decrease is that their roughened surfaces allow for sustained adhesive infiltration and interlocking (Safari et al., 2022).

Regarding composite materials, grit-blasting was found to be able to remove peel-ply contaminants after manufacturing (Monden, 2016). Fluorine contaminants on composite surfaces with a magnitude of 12 atomic per cent. Grit-blasting was effective in removing these

2.1.7 Effect of grit-blasting on surface roughness

contaminants as well as peel-ply contaminants from manufacturing (Monden, 2016, Boerio et al., 2006, Chin and Wightman, 1996).

2.1.8.   Silane coupling agents

Silane treatments are widely employed for surface modification of both metallic and composite substrates (Deflorian et al., 2006, Fiore et al., 2020, Lin et al., 2021, Wu et al., 2020). These treatments enhance the adhesion between the resin and substrate by serving as coupling agents, promoting chemical bonding or intermolecular interactions with both the adhesive and the substrate. The process involves hydrolysing silane in an aqueous solution, followed by immersing the substrate's bonding region (Del Real et al., 2008, Prakash and Jaisingh, 2018, Kim et al., 2012). Research employing FTIR and proton nuclear magnetic resonance (^{1}H NMR) spectroscopy has revealed that the rate at which silanes undergo hydrolysis is strongly dependent on the pH of the solution, with acidic environments being particularly beneficial to the process (Ciobotaru et al., 2016). As a result, silane solutions are commonly formulated to have a pH between 4 and 5.5 (Kim et al., 2011). Although an acidic pH accelerates hydrolysis, its influence on the strength of the adhesive bond is relatively limited when compared to other parameters, such as the concentration of the silane. These concentrations are typically prepared in the range of 0.1% to 5% (Rider and Arnott, 2000). Once hydrolysed, silane molecules can undergo self-condensation. In the absence of reactive functional groups on the substrate, these self-condensation reactions persist during the drying stage, ultimately forming a siloxane layer. This layer adheres to the substrate through intermolecular forces, where siloxane interacts with the substrate via hydrogen bonding. When the substrate possesses suitable functional groups, such as hydroxyl groups, condensation reactions occur directly between the hydrolysed silane and the substrate surface. Hydroxyl groups playing a pivotal role in adhesion to aluminium surfaces (Kiralfy, 2024).

2.2. Optical fibre sensors

Optical fibre sensors (OFS) leverage the fundamental properties of light propagation within optical fibres to enable the monitoring of physical, chemical, and mechanical changes in polymers. Due to their relatively small diameter of approximately 250 microns (Corning, 2002), they can be embedded into adhesive joints to enable *in situ* process monitoring. As they are joined with the polymer after curing, they can be used for post-process monitoring as well, which enables insights into post-process changes within adhesive joints. They are not affected by electromagnetic interference and, depending on the coating, are resistant to corrosion and, therefore, suitable for harsh environments. This chapter elaborates on the principles, types and applications of optical fibre sensors to characterise crucial parameters in the field of polymer cross-linking.

2.2.1. Principles of optical fibre technology

The following subchapters detail the fundamental concepts underlying optical fibre technology, starting with how light propagates through the fibre core. This process relies on the principle of total internal reflection (TIR), an idealised concept that assumes light is fully confined within the core under certain conditions. TIR occurs when light strikes the core-cladding interface at an angle greater than the critical angle, provided the refractive index contrast between the core and cladding is sufficient. However, in practice, perfect TIR is not always achieved due to factors such as imperfections, scattering, or light entering outside the acceptance angle. The differences between single-mode and multimode fibres, along with the effects of signal degradation mechanisms such as attenuation and dispersion, are also detailed. These concepts form the basis for understanding optical fibre performance and its use in sensor applications.

2.2.2.　Silica-based optical fibres

In general, optical fibres are cylindrical dielectric waveguides that guide light through a core surrounded by cladding. They typically consist of three primary components: the core, cladding, and a protective coating. Additionally, the coated fibre can be further protected by a buffer layer and a jacket for extra protection.

The core is the central region where light propagates, while the cladding ensures light confinement within the core through total internal reflection by having a lower refractive index. The refractive index can be described as the ratio of the speed of light in a vacuum and the speed of light in a material:

$$n = \frac{c}{v} \qquad\qquad [3]$$

where n is the refractive index [a.u.], c represents the speed of light in a vacuum, and v is the speed of light in a specific material.

This refractive index difference can be achieved by either increasing the refractive index of the core, e.g. by doping it with germanium, or decreasing the refractive index of the cladding, e.g. by doping it with fluorine or boron (Fleming and Wood, 1983). Silica-based optical fibres are usually created from a silica preform that is treated with germania (GeO_2) by modified chemical vapour deposition (MCVD) or outside vapour deposition (OVD).

The MCVD process begins with a hollow silica tube, which serves as the substrate for deposition and will ultimately form the cladding of the optical fibre. This tube also acts as a container for gaseous reactants, such as silicon tetrachloride ($SiCl_4$) and germanium tetrachloride ($GeCl_4$). During the process, the tube rotates while a moving torch heats it to temperatures typically exceeding 1600 °C, initiating chemical reactions that produce glass layers. These layers, composed of pure silica or doped silica (e.g., with germanium dioxide,

GeO₂), are deposited sequentially along the inner surface to create the desired refractive index profile. After deposition, the tube is heated further and collapsed into a solid glass rod, forming the preform. The preform is then transferred to a fibre-drawing tower, where it is heated and drawn vertically into a thin optical fibre. A protective polymer coating is applied immediately after fibre drawing to shield it from mechanical damage and environmental exposure (Buck, 2004, Crosby et al., 1996).

The OVD process differs significantly, as the glass soot is deposited on the outside of a rotating mandrel. This method eliminates the need for a silica tube and is particularly suitable for large-scale mass production of optical fibres, as it allows the creation of larger preforms. The deposited soot is later consolidated into dense glass in a high-temperature furnace (Wandel, 2006). Silica-based single-mode fibres experience intrinsic losses at approximately 0.2 dB/km at 1550 nm (Corning, 2002) and provide thermal stability up to approximately 1000 °C (Grobnic et al., 2005). The Young's modulus for an uncoated fibre is approximately 72 GPa (Li et al., 2022).

2.2.3.   Light propagation in optical fibres

Total internal reflection (TIR) is the fundamental mechanism that enables light propagation through optical fibres. This process confines light within the fibre core in silica-based fibres, allowing efficient transmission over long distances with minimal loss. The principle of TIR is governed by the refractive index difference between the fibre core and cladding, as well as the angle at which light rays are incident on the core-cladding interface. Light transmission within an optical fibre is primarily facilitated by total internal reflection at the core-cladding boundary. When light encounters the interface between two transparent materials with distinct refractive indices n_1 and n_2, it separates into two components: a reflected wave and a transmitted wave.

2.2.3 Light propagation in optical fibres

The relationship between the reflection angle, θ_r, and the angle of incidence, θ_i, is defined by the principles of the law of reflection:

$$\theta_i = \pi - \theta_r \tag{4}$$

Snell's law can be utilised to determine the refraction angle θ_t:

$$\frac{\sin(\theta_i)}{\sin(\theta_t)} = \frac{n_2}{n_1} \tag{5}$$

TIR occurs when a light ray travelling in a medium with a higher refractive index (n_1) reaches an interface with a medium of lower refractive index (n_2) at an angle greater than the critical angle (θ_c). The critical angle is given by:

$$\theta_c = arcsin\frac{n_2}{n_1} \tag{6}$$

In silica-based fibres, a germanium-doped core typically has a refractive index of around 1.4682 at 1550 nm (6), while the cladding has a slightly lower refractive index, as mentioned in (2.2.2). A commercial SMF-28e+ fibre has a refractive index difference of 0.36% between its core and cladding (Corning, 2010). This minute difference ensures that light entering the fibre at an angle within the acceptance cone is internally reflected at the core-cladding boundary, remaining confined within the core. Figure 2 illustrates a schematic of reflection and refraction under the non-TIR condition.

2.2.3 Light propagation in optical fibres
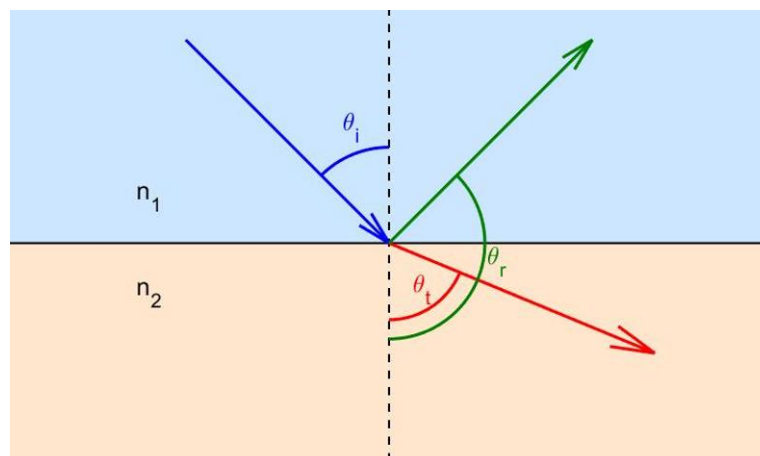
Figure 2 Schematic of Incident light (blue), reflected light (green) and refracted light (red) at the interface of two media with different refractive indices.

The ability of an optical fibre to capture and guide light is determined by its numerical aperture (NA), which quantifies the acceptance cone angle. The NA is expressed as:

$$NA = \sqrt{n_1^2 - n_2^2} \qquad [7]$$

where n_1 and n_2 are the refractive indices of the core and cladding, respectively.

For typical silica-based fibres, the NA is approximately 0.14 for single-mode fibres (Corning, 2010) and 0.2 to 0.3 for multimode fibres (Thorlabs, 2024, Venghaus and Grote, 2017). A higher NA allows for easier light coupling into the fibre and supports more modes, but it increases modal dispersion due to a wider range of propagation constants, which limits bandwidth and degrades signal quality over long distances (Marcatili, 1977). The NA also defines the angle of acceptance, θ_a. This angle defines the ability of the fibre to couple light inwards and further transmit it under the condition of total internal reflection. The angle of acceptance, θ_a, is defined as:

$$\theta_a = \arcsin\sqrt{n_1^2 - n_2^2} \qquad [8]$$

where n_1 and n_2 are the refractive indices of the core and the cladding, respectively. As can be seen, the angle of acceptance is directly proportional to the NA.

2.2.4.   Single-Mode and Multimode Fibres

Optical fibres can be broadly categorised into single-mode (SM) and multimode (MM) fibres, distinguished by their core dimensions, light propagation characteristics, and applications. These differences arise primarily from the interplay between the fibre geometry and the

2.2.4 Single-Mode and Multimode Fibres

wavelength of light used for transmission. A mode can be described as a specific path or pattern of light propagation within the optical fibre, determined by the fibre core size and refractive index profile. Each mode represents a stable distribution of the electromagnetic field that can travel through the fibre without significant distortion. Single-mode fibres are designed to propagate only the fundamental mode (LP01). This is achieved by maintaining the core diameter within a specific range, typically between 8 and 10 µm and a numerical aperture range of 0.1 to 0.3 (Agrawal, 2012). This ensures that the normalised frequency (V-number) of the fibre remains below the cut-off value of 2.405:

$$V = \frac{2\pi\alpha}{\lambda}\sqrt{n_1^2 - n_2^2} \qquad\qquad [9]$$

where α is the core radius, λ is the wavelength, and n_1 and n_2 are the refractive indices of the core and cladding, respectively. When looking at the V-number equation, it becomes clear that a larger transmitted spectral wavelength range requires an increase in core diameter.

Multimode fibres are designed with larger core diameters, generally ranging from 50 µm up to 300 µm (Senior and Jamro, 2009), but can reach up to 1500 µm. The larger core supports multiple propagation modes, each with its own unique path through the fibre. The V-number for multimode fibres is typically much greater than 2.405, allowing multiple modes to coexist. Multimode fibres are often categorised based on their refractive index profiles. Step-index fibres have a uniform core refractive index modulation, whereas graded-index fibres have a parabolic refractive index profile (Agrawal, 2012).

2.2.5.   Signal degradation in optical fibres

When light is transmitted through an optical fibre, it experiences attenuation due to various possible mechanisms. The attenuation can be expressed as:

2.2.5 Signal degradation in optical fibres

$$\alpha = \frac{10}{L} \times log_{10}\left(\frac{P_{in}}{P_{out}}\right) \qquad\qquad [10]$$

where α is the attenuation coefficient in dBkm^{-1}, L is the fibre length in km, and P_{in} and P_{out} represent the input and output optical powers.

Attenuation is dependent on several factors. There are two different bending losses affecting the attenuation of a fibre, namely micorbending and macrobending. Microbending is caused by small-scale deformations or irregularities within the optical fibre or in the cladding/core interface. The fibre coating also affects microbending. Polyimide coatings have been demonstrated to cause higher levels of microbending losses than acrylate coatings (Deparis et al., 1997). Macrobending losses are caused by light when the optical fibre is bent further than the critical angle within the core/cladding interface. Macrobending losses occur when the optical fibre is bent beyond a critical radius, causing some light rays to reach the core-cladding interface at angles smaller than the critical angle. This results in the light refracting into the cladding or escaping entirely, leading to power loss and, therefore, attenuation. Another mechanism is the intrinsic material absorption. Silica experiences material absorption in the ultraviolet and infrared regions. The presence of hydroxyl ions (OH$^-$) and Rayleigh scattering are attenuating factors as well (Bludau, 2013, Engelbrecht, 2015, Agrawal, 2012). Considering a spectral range ranging from 290 nm to 1700 nm, a silica-based waveguide will experience attenuation from (i) the Urbach absorption edge (ultraviolet region), (ii) vibrational absorption within the infrared region, (iii) Rayleigh scattering losses, and (iv) waveguide-dependent attenuation (Wandel, 2006).

Dispersion refers to the spreading of an optical signal as it propagates through a fibre. This broadening occurs due to differences in the propagation velocities of various components of the signal, which results in temporal overlap and distortion at the receiver. Dispersion limits

27

2.2.5 Signal degradation in optical fibres

the bandwidth and distance of optical communication systems, particularly in high-speed networks.

Modal dispersion occurs in multimode fibres, where multiple propagation modes follow different paths with varying lengths. This leads to differences in arrival times at the receiver, which can cause pulse broadening. Multimode step-index fibres exhibit the highest modal dispersion due to abrupt changes in the refractive index at the core-cladding interface, whereas graded-index fibres mitigate this effect by equalising mode velocities through a parabolic refractive index profile (Agrawal, 2012, Dubey and Shukla, 2014).

Chromatic dispersion affects both single-mode and multimode fibres. It arises from the wavelength dependence of the refractive index, causing different spectral components of a pulse to travel at different speeds. Chromatic dispersion has two components: material dispersion, due to the inherent properties of silica, and waveguide dispersion, influenced by fibre geometry (Dubey and Shukla, 2014).

Polarisation Mode Dispersion (PMD) occurs due to asymmetries in the fibre core, which cause polarised light components to travel at slightly different speeds. Although PMD is typically small in well-manufactured fibres, it becomes significant in ultra-high-speed systems, where even minor pulse broadening can degrade signal quality (Agrawal, 2012, Dubey and Shukla, 2014).

2.2.5.1.   Fibre Bragg gratings

Hill *et al*. (1978) demonstrated photosensitivity in Ge-doped silica fibres, leading to permanent refractive index changes under intense coherent light exposure. They fabricated the first FBGs using this effect but did not explicitly describe the GeO_2 defect mechanisms responsible for the

refractive index change. Higher Ge concentrations were observed to enhance photosensitivity (Hill et al., 1978).

An FBG is created within a germanium-doped core optical fibre by exposing it to a periodic pattern of ultraviolet (UV) light. This process induces refractive index modulations due to GeO_2 defects, forming a periodic structure along the fibre core, as illustrated in Figure 3. When broadband light propagates through the fibre, a specific wavelength—determined by the Bragg condition—is selectively reflected, while the remaining spectral components continue to transmit through the fibre. This interaction between the light and the periodic grating structure results in a characteristic reflection and transmission spectrum, as shown in Figure 3.
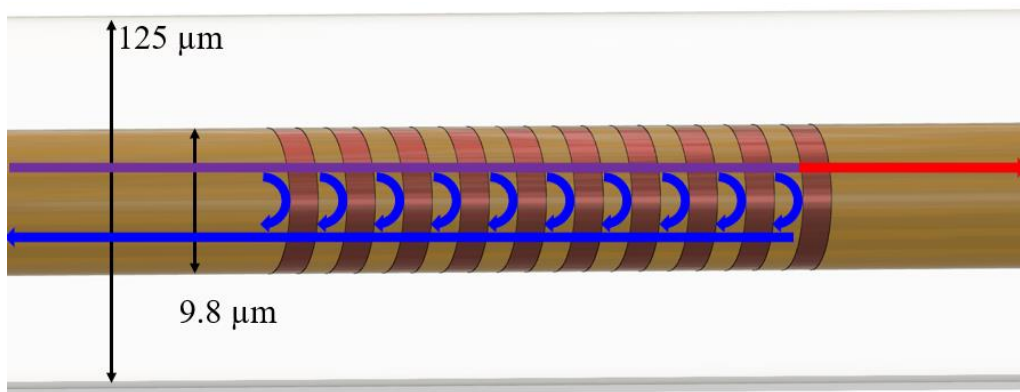
Figure 3 Schematic of a fibre Bragg grating.

When broadband light propagates through the fibre, a specific wavelength—determined by the Bragg condition—is selectively reflected, while the remaining spectral components continue to transmit through the fibre. This interaction between the light and the periodic grating structure results in a characteristic reflection and transmission spectrum, as shown in Figure 4.

2.2.5.1 Fibre Bragg gratings
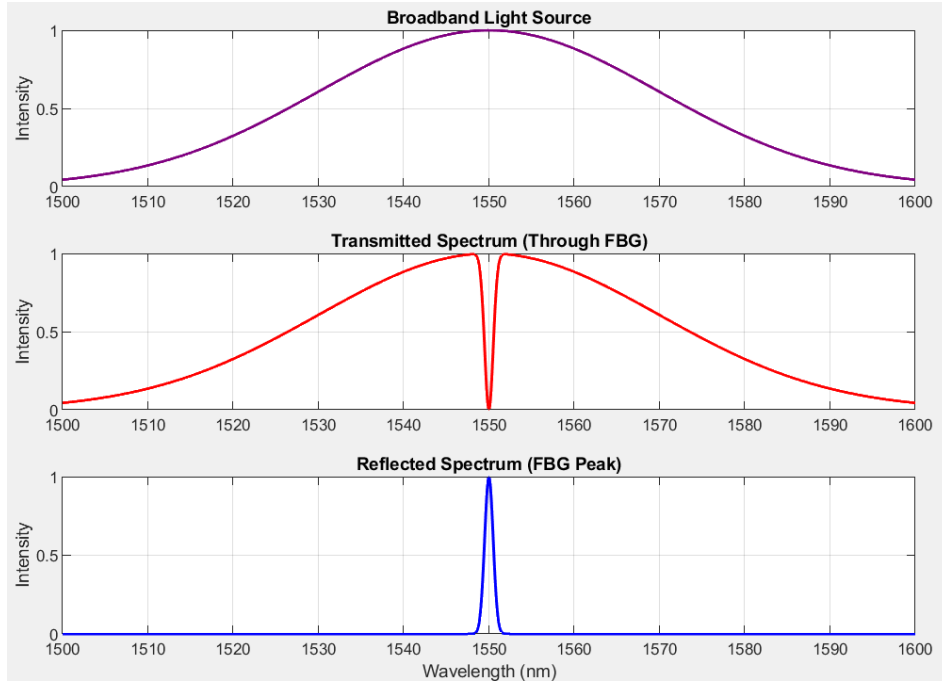
Figure 4 Simulated spectra of a light source, the transmitted FBG spectrum and the reflected FBG peak.

FBGs operate as optical sensors based on the periodic modulation of the refractive index along the fibre core. The fundamental Bragg wavelength (λB) is determined by the relationship (Hill and Meltz, 1997):

$$\lambda_B = 2n_{eff}\Lambda \qquad [12]$$

where n_{eff} is the effective refractive index of the fibre core, and Λ is the grating period. Changes in strain or temperature alter either n_{eff} or Λ, leading to a shift in the Bragg wavelength.

The Bragg wavelength shift under the influence of strain *(Δl)* and temperature *(ΔT)* is expressed as (Venghaus, 2006):

$$\Delta\lambda_B = 2\left(\Lambda\frac{\partial n_{eff}}{\partial l} + n_{eff}\frac{\partial\Lambda}{\partial l\Lambda}\right)\Delta l + 2\left(\Lambda\frac{\partial n_{eff}}{\partial T} + n_{eff}\frac{\partial\Lambda}{\partial T}\right)\Delta T \qquad [13]$$

This equation highlights that both mechanical strain and thermal effects contribute to the wavelength shift. The thermal response of an FBG is governed by both the thermo-optic effect and thermal expansion:

2.2.5.1 Fibre Bragg gratings

$$\Delta\lambda_B = \lambda_B(\alpha_\Lambda + \alpha_n)\Delta T \tag{14}$$

Where $\alpha_\Lambda = (1/\Lambda)(\partial\Lambda/\partial T)$ is the thermal expansion coefficient, and $\alpha_n = (1/n)(\partial n/\partial T)$ is the thermo-optic coefficient, representing the refractive index change due to temperature.

Equation 14 can be simplified to (Luyckx, 2009):

$$\Delta\lambda_B = \lambda_B k_T \Delta T \tag{15}$$

For GeO_2-doped silica fibres, these coefficients are $\alpha_\Lambda \approx 0.55 \times 10^{-6} K^{-1}$, and $\alpha_n \approx 8.7 \times 10^{-6} K^{-1}$. Since α_n is an order of magnitude larger than α_Λ, the refractive index change due to temperature dominates the thermal response of the FBG, while the effect of thermal expansion is relatively small. This means that temperature-induced wavelength shifts in FBG sensors are primarily dictated by the thermo-optic effect rather than the physical expansion of the fibre.

2.2.5.1 Fibre Bragg gratings

Implications for Optical Sensing

FBGs exhibit a dual sensitivity to strain and temperature, necessitating careful decoupling when both factors vary simultaneously. In structural health monitoring and composite material embedding, thermal effects must be accounted for to ensure accurate strain measurements. The high thermo-optic coefficient of GeO_2-doped silica fibres underscores the importance of temperature compensation in FBG-based sensing systems.

A dual FBG system was utilised to simultaneously measure temperature and strain during the cure process of glass fibre-reinforced plastic (GFRP) composites, allowing for the decoupling of thermally induced and mechanical strain without the need for auxiliary sensors. One FBG (FBG_T) was enclosed in a capillary to act as a strain-free temperature reference, while the second (FBG_ε) captured both temperature and strain variations.

The study demonstrated that internal laminate temperatures exceeded the oven set-point by up to 50°C due to the exothermic polymerisation of the epoxy resin, highlighting the limitations of external thermocouples. Additionally, residual strain accumulated during cooling, reaching -540 µm/m in thicker laminates. Comparison with DSC data confirmed that the FBG system accurately tracked cure progression, identifying key stages such as gelation, vitrification, and residual stress development. This technique provides a non-intrusive method for optimising cure cycles while enabling long-term structural health monitoring of bonded joints and composite materials (Montanini and d'Acquisto, 2007).

FBG tubings are used to protect and modify the response of FBGs, influencing their strain sensitivity and thermal isolation. Metal tubings (Montanini and d'Acquisto, 2007), such as stainless steel or titanium, provide mechanical robustness, shielding the FBG from external damage while maintaining strain transfer. However, they can introduce thermal expansion effects, which must be accounted for in temperature-sensitive applications. Glass tubings

2.2.5.1 Fibre Bragg gratings

(Haran et al., 1998), on the other hand, offer low thermal expansion and optical compatibility, making them ideal for strain-free temperature sensing. While more fragile than metals, glass encapsulation reduces mechanical loading effects, ensuring pure thermal response in embedded sensing applications.

The temperature sensitivity of FBGs depends on both the thermo-optic effect (refractive index change) and the thermal expansion of the fibre and its surrounding coating. Different coatings influence the FBGs response by altering heat transfer, strain isolation, and mechanical robustness.

Metal coatings (e.g., aluminium, gold, or nickel) enhance thermal conductivity, allowing rapid heat transfer and improved response time. However, metals introduce thermal expansion effects, potentially inducing unwanted strain in temperature measurements. Polymer coatings, such as acrylate or polyimide, provide flexibility and strain isolation but have lower thermal conductivity, resulting in slower temperature response. Silica or ceramic coatings exhibit low thermal expansion and are often used when a pure temperature measurement is required, particularly in high-precision sensing applications.

For high-temperature environments, metal-coated or sapphire-fibre-based FBGs offer superior stability and durability, while polymer-coated FBGs are preferred in applications requiring mechanical flexibility and low-temperature sensitivity. Selecting the appropriate coating is crucial for achieving accurate and application-specific temperature sensing.

To enhance the temperature sensitivity of FBGs, various coatings with higher thermal expansion coefficients can be applied. Since bare FBGs, made of silica, exhibit low thermal sensitivity due to the small thermal expansion coefficient of silica (0.55×10^{-6} K^{-1}) (Wang et al., 2022), coatings induce additional strain, leading to a greater Bragg wavelength shift and improved temperature response.

2.2.5.1 Fibre Bragg gratings

Among the tested coatings, Polymethyl methacrylate (PMMA) demonstrated the highest temperature sensitivity, reaching 94.0 pm/K, which represents a 114% improvement over bare FBGs. Indium-coated FBGs exhibited the highest sensitivity among the metallic coatings, with 50.8 pm/K, while Aluminium coatings showed the greatest improvement (70.1%) compared to uncoated fibres. Other metallic coatings also enhanced sensitivity, with Lead at 43.2 pm/K, Copper at 25.6 pm/K, and Aluminium at 35.6 pm/K (Mishra et al., 2016).

These results highlight the significant role of coating selection in tuning FBG sensitivity. PMMA coatings offer the best temperature response, making them ideal for high-precision thermal sensing applications, while indium and aluminium provide effective metallic alternatives for environments requiring durability and moderate sensitivity enhancement.

2.3. Process monitoring of epoxy-based polymers

The conventional analytical techniques that are used for monitoring the cross-linking of epoxy resins include differential scanning calorimetry (DSC) (Pandita et al., 2012), FTIR spectroscopy (Duemichen et al., 2015), rheology (Jojibabu et al., 2016, Lee et al., 1982, Garschke et al., 2013), dynamic mechanical thermal analysis (DMTA) (Saldanha et al., 2013, Mafi et al., 2005, Xian and Karbhari, 2007), and thermogravimetric analysis (TGA) (Wu et al., 2002, Liu et al., 2004).

However, these techniques are unsuitable for providing in situ and real-time data on the cross-linking reactions. Hence, a number of optical (Crosby et al., 1996, Pandita et al., 2012, Fernando and Degamber, 2006) and electrical-based techniques (Hübner et al., 2018, Yang et al., 2021) have been developed and demonstrated to enable the acquisition of real-time and in situ data during the processing of thermosetting resins. Electrical-based sensors for monitoring cross-linking reactions generally take the form of interdigitated electrodes (Hübner et al.,

2.3 Process monitoring of epoxy-based polymers

2018). Optical-based sensing techniques can provide quantitative (Pandita et al., 2012) and qualitative (Crosby et al., 1997) information on the progression of cross-linking reactions. For example, FTIR spectroscopy can provide quantitative information on the relative concentration of the functional groups (epoxy, amine, hydroxyl, etc) as a function of the processing time and conditions. This is achieved by monitoring the relative changes in the peak areas (Pandita et al., 2012) or peak heights (Crosby et al., 1997) of the absorption bands corresponding to specific functional groups. Qualitative information on the cross-linking reactions can be obtained by monitoring the relative position of the baseline (away from an absorbance band) on the abscissa (absorbance). As the optical density of the cross-linking resin increases during cross-linking, a corresponding proportional increase in the relative position of the baseline will be observed.

With reference to FTIR spectroscopy, optical fibres have been used to couple light in and out of analytical and processing equipment to study cross-linking reactions. The quantitative sensing principles are based on transmission (Duemichen et al., 2015, Pandita et al., 2012), transmission/reflection (Wang and Fernando, 2014) and evanescent wave spectroscopy (Powell et al., 1996, Doyle et al., 1998). Qualitative analyses of cross-linking reactions have been demonstrated using optical fibre-based reflectometry (Crosby et al., 1996). Fibre-optic-based sensing approaches have gained significant attention due to their inherent advantages. For example, immunity to electromagnetic interference, capable of multiplexed distributed and point-sensing, multiple sensing methods can be assembled on a single device and their relatively small dimensions. One such technique is optical fibre reflectometry, which offers a practical route for monitoring the cross-linking of thermosetting resins by tracking changes in the refractive index of the material. Hence, it offers a route to infer the rate and the extent of the cross-linking reactions.

2.3 Process monitoring of epoxy-based polymers

An optical fibre-optic reflectometer was employed to scrutinise the cross-linking process within an epoxy/amine resin system. The calibration of the reflected signal emanating from the cleaved end of the optical fibre was accomplished through the utilisation of reference refractive index liquids. Remarkably, the Fresnel reflection sensor exhibited a commendable correlation with the quantitative kinetic data related to cross-linking, as determined by a conventional Fourier transform near-infrared spectrometer (Crosby et al., 1997).

2.4. Identified research gaps

FRS are commonly employed for intensity-based RI sensing (Vacher et al., 2004, Oelhafen et al., 2017) as well as for monitoring cure and temperature (Chen and Huang, 2010). FBGs have been used to measure strain (Torres et al., 2011), shrinkage and temperature (Khadka et al., 2020), while Fabry–Perot cavity sensors have demonstrated sensitivity to multiple parameters, including refractive index (Qi et al., 2003), strain (Liu et al., 1998), and temperature (Mathew et al., 2015). Despite these advances, systematic calibration of these sensors under adhesive curing conditions and validation against established techniques such as FTIR or DSC (105) remain limited. Most studies focus on single-parameter sensing, such as temperature or strain, and integrated, multi-parameter approaches capable of simultaneously capturing cure progress and strain within adhesive joints are largely lacking. Existing multi-parameter studies generally limit their scope to the resin matrix only (Nair et al., 2015). Furthermore, much of the previous optical fibre sensor work has been conducted in simplified environments, such as cuvettes or bulk resin samples (Harris, 2011, Grangeat et al., 2020). Fewer studies have demonstrated the embedding or surface-mounting of sensors directly within adhesive joints (Murayama et al., 2012). To the best of our knowledge, no published study has investigated the isothermal curing of SLJs using multiple types of optical fibre sensors to monitor strain, cure kinetics, temperature, and refractive index simultaneously.

2.4 Identified research gaps

3. Materials and experimental procedures

3.1. Introduction

The subsequent chapter provides details of the constituent materials utilised in the study, the experimental methodologies employed, and comprehensive insights into the bespoke instrumentation explicitly developed for the research endeavours undertaken herein.

3.2. Experimental overview

To provide an overview of the experimental workflow, schematic flowcharts of the OFS and SLJ testing procedures are presented in xx. These diagrams illustrate the sequence from specimen preparation, optical sensor fabrication, calibration, and integration, through to the preparation and manufacture of SLJ specimens and their subsequent mechanical testing. Detailed descriptions are provided in the following sections.
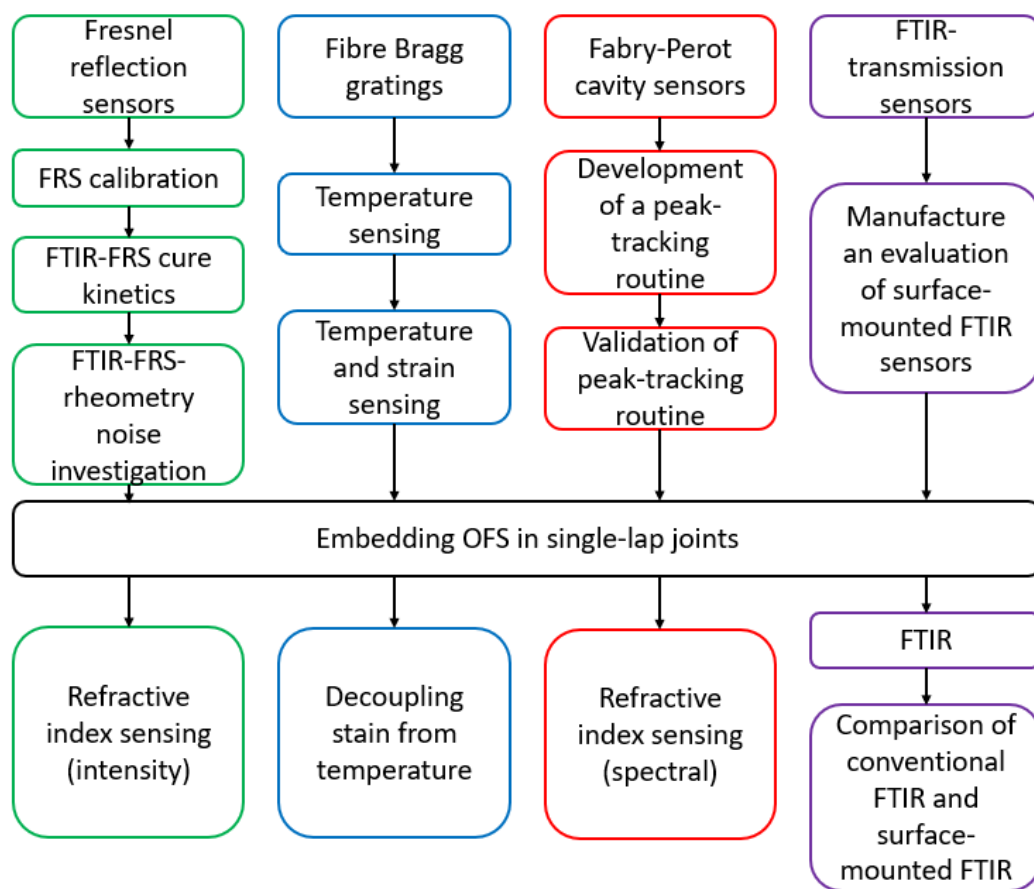
Figure 5 Flowchart of the experimental workflow for the OFS used, illustrating the sequence of experiments conducted.
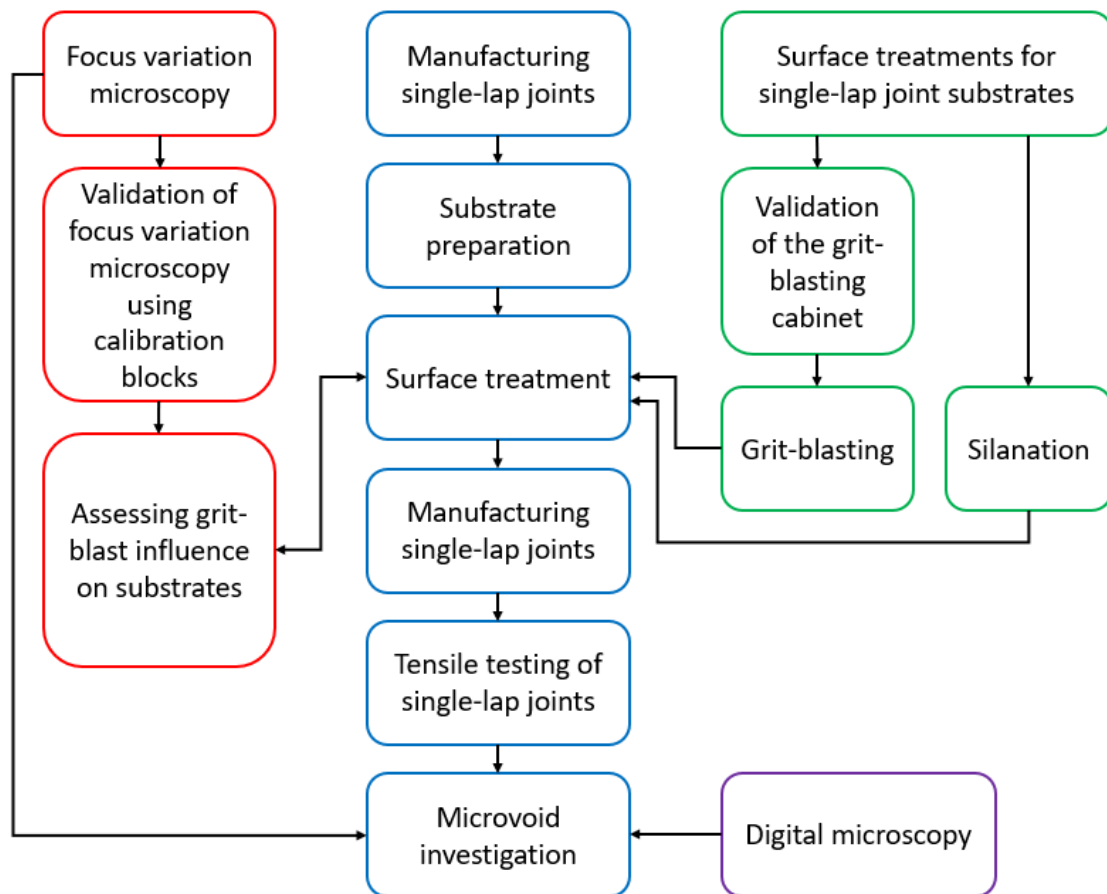
Figure 6 Flowchart of the experimental workflow for SLJ testing, showing the sequence from substrate preparation, surface treatments, surface assessment and tensile testing.

3.2 Experimental overview

3.3. Optical fibres and interrogation equipment

A variety of optical fibres were employed in the course of this study. The specific attributes of the acquired fibres are documented in Table 2.

(i) Corning SMF-28: This acrylic-coated single-mode fibre was utilised for all Fresnel reflection-based sensors and refractive index sensors, including intrinsic Fabry-Perot cavity sensors.

(ii) Fibercore SM1250BI: This polyimide-coated single-mode fibre, featuring Fiber Bragg gratings inscribed within, was procured from FemtoFibreTec (Germany, the new company name is engionic Femto Gratings GmbH). It was deployed for strain and temperature sensing purposes.

(iii) Thorlabs FG105LCA: This acrylic-coated multimode step-index fibre was utilised in the fabrication of large cavity extrinsic Fabry-Perot sensors for chemical sensing applications.

Table 2 Specifications of the optical fibres used in this study, where di is the outer fibre core diameter, do is the outer cladding diameter, and dc is the outer coating diameter.

Fibre Type	SMF-28™ (Corning, 2002)	SM1250BI-P (FiberCore, 2020)	FG105LCA (Thorlabs, 2024)
Supplier	Corning Inc, USA	Fibercore Ltd, UK	Thorlabs
Mode	Single-mode	Single-mode	Multi-mode
Core	Germanium-doped with d_i = 8.2 μm	Germanium-doped with d_i = 9.8 μm	Pure silica with d_i = 105± 3 μm
Cladding	Pure silica with d_o = 125± 0.7 μm	Pure silica with d_o = 125± 1 μm	Fluorine-doped with d_o = 125± 2 μm
Coating	Acrylate with d_c = 245± 5 μm	Polyimide with d_c = 155± 5 μm	Acrylate with d_c = 250± 10 μm
Numerical aperture	0.14	0.11 – 0.13	0.22
Fibre attenuation [dB/km]	≤0.05 at 1550 nm	≤0.4 at 1550 nm	8 at 808 nm

In order to provide sensor interrogation, appropriate fibre end-terminations were required. The Bruker Optics (Bruker Ltd, UK) FTIR system features SMA termination, while the SM130 (MicronOptics, now Luna, Inc.) interrogator uses FC/APC-terminated fibres, and the bespoke Fresnel stations (details given in Section 3.5.1) utilise FC/PC termination. Consequently, patch cables conforming to the specific fibre types were procured from Thorlabs (UK). Subsequently, to splice a fibre sensor to a patch cable, approximately 20 mm of the coating was stripped using a mechanical stripper (Miller FO 103-T-250-J series, Ripley tools LLC, USA) and meticulously cleaned with lint-free lens tissue (Tiffen, USA) soaked in isopropyl alcohol (IPA). The stripped

3.3 Optical fibres and interrogation equipment

fibre ends were then cleaved using a manual fibre cleaver (CT-08, Fujikura, Japan) and positioned within a core-aligning fusion splicer (FSM-45 F, Fujikura, Japan). The image processing system ensured precise core alignment of the cleaved fibre ends, splicing them if the cleave quality met the specified criterion (≤0.5°). The resulting splice exhibited an evaluated loss of ≤0.05 dB. Subsequently, the splice was safeguarded using a heat-shrinking protective sleeve (Spliceprotector 60, RS Components Ltd, UK).

3.3.1.　Substrate materials for single-lap joints

Single-lap joints were fabricated from an aluminium alloy (2024 T3) and carbon fibre-reinforced plastic substrates. The chemical composition of the metal is delineated in Table 3. The CFRP is described in detail after the metal.

Table 3 Chemical composition of 2024 T3 in [weight %] (Günther + Schramm, 2015).

	2024 T3
Al	90.7 to 94.7
Cu	3.8 to 4.9
Mg	1.2 to 1.8
Mn	0.3 to 0.9
Si	0 to 0.5
Fe	0 to 0.5
Zn	0 to 0.25
Ti	0 to 0.15
Cr	0 to 0.10
Residuals	0 to 0.15

The aluminium was procured as a large sheet with a thickness of approximately 2 mm. For the composite substrates, a CFRP sheet has been sourced from Refitech B.V. (Netherlands). The sheet had a thickness of approximately 2 mm. The technical datasheet is attached in Appendix A. To determine the fibre volume fraction (FVF), four 2 cm-wide strips were extracted from the remaining CFRP material after water jet cutting. From each strip, five samples were sectioned to ensure visibility of all four plies, including the twill layer. These samples were subsequently potted and polished to obtain clear cross-sections for analysis. The fibre volume fraction was then determined using ImageJ, which facilitated precise image-based measurements of the fibre and matrix regions. Five cut-outs were made from the panel to determine the fibre-volume fraction of the composite. Each sample was imaged five times in five sections, resulting in 100 images. The overall FVF was determined to be 49.18%. To create tensile testing coupons for the single lap joints, these sheets were water jet cut using a mach2 1313b (Shape Technologies Group UK Ltd. UK), to ASTM D1002 conform dimensions of l = 101.6 mm and w = 25.4 mm. The cut-out CFRP samples were immediately labelled and then measured in thickness using a digital external micrometre (293-832-30, Mitutoyo Corp., Japan) with a stated accuracy of ±0.002 mm. Further details are given in Section 3.8.

3.3.1 Substrate materials for single-lap joints

3.3.2. Adhesives and affiliated application equipment

A commercial high-performing structural epoxy-based adhesive was selected for this study, namely Henkel Loctite EA9466. The adhesive details are illustrated in Table 4.

Table 4 Details of commercially procured structural adhesive.

Specification	EA9466 (Loctite, 2006)
Supplier	Henkel/Loctite
Work-life in minutes	60
Fixture time in minutes	180
Shelf life in months	12
Mixing ratio by volume	2:1 (Resin:Hardener)
Thermal properties	$T_g = 62$ °C

The two-component adhesive was purchased in standard 50 ml cartridges. To ensure a uniform degree of mixing of the adhesive throughout the entire range of experiments, square element static mixers were used. Specifically, static mixers compatible with the cartridge locking mechanisms of the EA9466 adhesive (Type 984569, Loctite, UK) were procured. Additionally, an adhesive applicator (503-379, RS Components Ltd, UK), along with a plunger suitable for a 2:1 ratio cartridge, was procured from RS Components. A suitable plunger is necessary as the requisite mixing ratio is achieved through different bore diameters within the cartridge.

3.3.3. Chemicals

(i) Isopropanol (Fisher Scientific, UK): This served as the primary cleaning agent for optical fibres, utilised for both stripping and routine fibre hygiene applications.

(ii) Acetone (Fisher Scientific, UK): Acetone functioned as a cleaning agent during adhesive work, particularly in the production of single-lap joints and parallel-plate rheology experiments.

(iii) PAT-607/PCM (Würtz GmbH und Co. KG, GER): This external release agent was used in cure kinetics experiments with 1 mm path length cuvettes, allowing for the post-experimental removal of adhesive without damaging the quartz cuvette.

(iv) Hylomar (RS Components Ltd, UK): This instant gasket acted as a sealant in the assembly of release agent-coated 1 mm path length cuvettes prior to adhesive insertion.

(v) NOA68 (Norland, USA): This one-part ultraviolet curing photopolymer was utilised to fabricate fixtures accommodating both surface-mounted FTIR transmission sensors and Fabry-Perot cavity sensors simultaneously. Additionally, it was used to create the Fresnel reflection sensor "carrier" for the hyphenated FTIR-FRS experiments (described in Section 3.6.2.3).

(vi) Refractive index oils (Cargille, USA): Covering a refractive index range from 1.40 to 1.70, these oils were employed to "calibrate" Fresnel reflection sensors within the prism of an Abbe refractometer at constant temperature.

(vii) Methyl ethyl ketone (VWR, FR): MEK aided in the removal of cured adhesives from the 1 mm path cuvette as a pre-treatment. The cuvette was immersed in MEK for 48 hours to weaken the interface between the adhesive and release agent-coated cuvette, ensuring a "scratch-less" extraction of the adhesive.

3.4. Conventional analytical techniques for adhesive characterisation

The subsequent sections describe the conventional methodologies to assess adhesive properties, including chemical changes of the functional groups and viscosity, providing comprehensive insights into the equipment utilised, and experimental setups.

3.4.1. Parallel-plate rheology

An Ares parallel-plate rheometer sourced from TA Instruments (USA) was utilised to evaluate viscosity alterations throughout the curing process of the adhesive. This rheometer incorporates a constant air supply facilitated by a compressor unit, essential for the functioning of the air bearing, alongside an enclosable furnace module, thereby enabling viscosity assessments at varying temperatures. Custom-made 304 stainless steel plates, possessing a diameter of 25 mm, were employed. Prior to commencing each experiment, meticulous cleaning of the plates was carried out using acetone, followed by secure clamping into the upper and lower fixtures. After zeroing, the gap was set to 1 mm, with forces zeroed before adhesive application. Subsequently, the upper fixture was adjusted to a gap of approximately 20 mm to ensure uniform adhesive application. Application of the adhesive followed the methodology delineated in Section 2.3, with subsequent retraction of the upper fixture to a predefined 1 mm gap. Any surplus adhesive was removed using a PTFE spatula (Techmate, UK) to maintain a consistent testing diameter of 25 mm. The non-destructive oscillating test was executed at a strain of 5% and a frequency of 5 Hz. Following the parallel plate apparatus assembly, the furnace module was enveloped around the fixtures, and data logging commenced concurrently with the initiation of heating. Testing was conducted within a temperature range of 45 – 60 °C, progressing in increments of 5. Upon completion of testing, heating was discontinued, and the furnace was disengaged to

3.4 Conventional analytical techniques for adhesive characterisation

allow for the plates to cool down to room temperature (~ 30 minutes) before plate removal. Subsequently, the adhesive was oxidised off after each experiment within a furnace set at 600 °C for 10 hours, facilitating plate re-utilisation. Figure 7 illustrates the parallel plate rheometer system.

Figure 7 Parallel plate rheometer setup with 25 mm aluminium plates before adhesive application. The heat chamber, designed to wrap around the fixture columns, is not in position and is situated out of frame to the left.

3.4.2.   Fourier transform infrared spectroscopy

In the analysis of the resin system, a fibre-coupled Bruker Matrix-F duplex (Bruker Ltd, UK) was employed for transmission-based spectral acquisition. This apparatus captured Fourier-transform near-infrared spectra spanning from 11000 to 4000 cm^{-1}. Spectra were obtained through 64 scans at a resolution of 4 cm^{-1}, with a sampling rate of one spectrum every two minutes.

The absorbance peak areas of interest were integrated using a dynamic minima/maxima peak tracking routine within the OPUS software. This entailed the system automatically tracking the minima points to the left and right of the peak of interest throughout the experiment. The obtained integration values were then extracted and processed using MATLAB. Detailed information regarding the coupled light guides and their setup is contingent upon the specific experiments conducted and is thus detailed in the respective Sections 3.5.4 and 3.6.2.

3.5. Description of used optical fibre sensors

The ensuing sections delve into the distinct categories of optical fibre sensors and expound upon their fabrication and preparation methodologies.

3.5.1. Fresnel reflection sensors

The Fresnel reflection-based sensors were positioned within dedicated Fresnel sensor stations, each comprising standalone systems with designated computers as depicted in Figure 8.
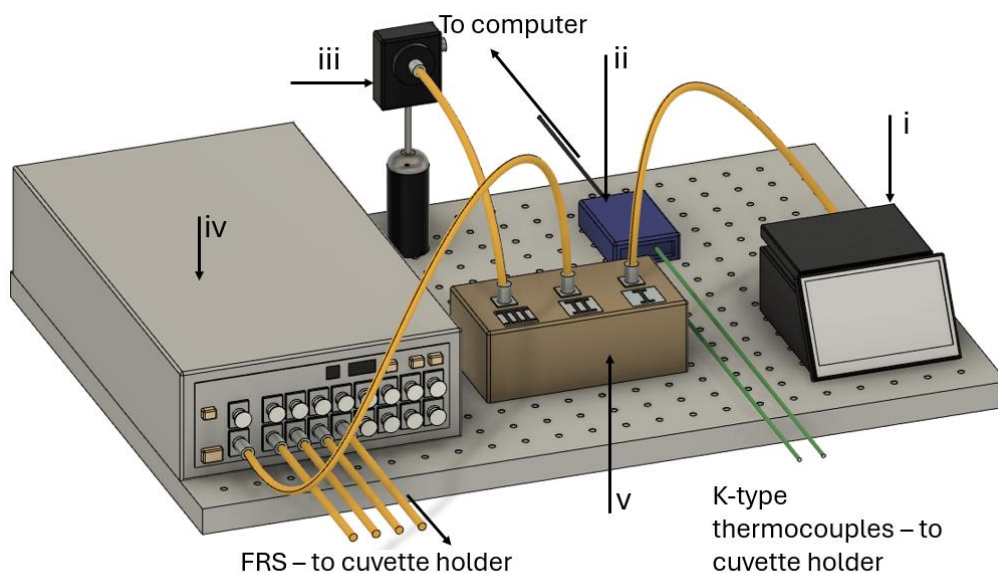
Figure 8 FRS station with (i) SLED light source, (ii)DAQ, (iii) photodetector, (iv) channel selector, and (v) circulator.

3.5 Description of used optical fibre sensors

A super-luminescent light source (SLD 761, Superlum, IRL) resided within a laser diode driver unit (CLD1015, Thorlabs Ltd, UK), transmitting near-infrared light with a central wavelength of 1550 nm into an optical fibre circulator (6015-3-FC, 1525 – 1610 nm, Thorlabs Ltd, UK). Within this circulator, the light was circulated to an SMF-28 fibre with a cleaved end-face. The resulting reflection passed through the circulator to an amplified photodetector (PDA10-CS-EC, 700-1800 nm, Thorlabs Ltd, UK), operating at a gain of 30 dB. Data logging was accomplished using an NI9171 analogue/digital converter (National Instruments, USA) from the manufacturer, along with custom-written software. Two distinct stations were utilised. Fresnel station one operated with a single sensor and achieved a maximum sampling rate of 10 samples per second. In contrast, Fresnel station two incorporated an additional channel selector (MN9674A, Anritsu, Japan) that distributed the light from the source into four different channels. Since the channel switching time was 2 seconds, the four-channel setup resulted in a sampling rate of 0.125 samples per second. To manufacture a Fresnel sensor, approximately 20 mm of the coating on an SMF-28 fibre was removed using a mechanical stripper (Miller FO 103-T-250-J series, Ripley tools LLC, USA) and meticulously cleaned with lint-free lens tissue soaked in isopropyl alcohol. Subsequently, the stripped fibre end was cleaved using a manual fibre cleaver (CT-08, Fujikura, JPN). Figure 9 illustrates a cleaved SMF-28 fibre.

3.5.1 Fresnel reflection sensors
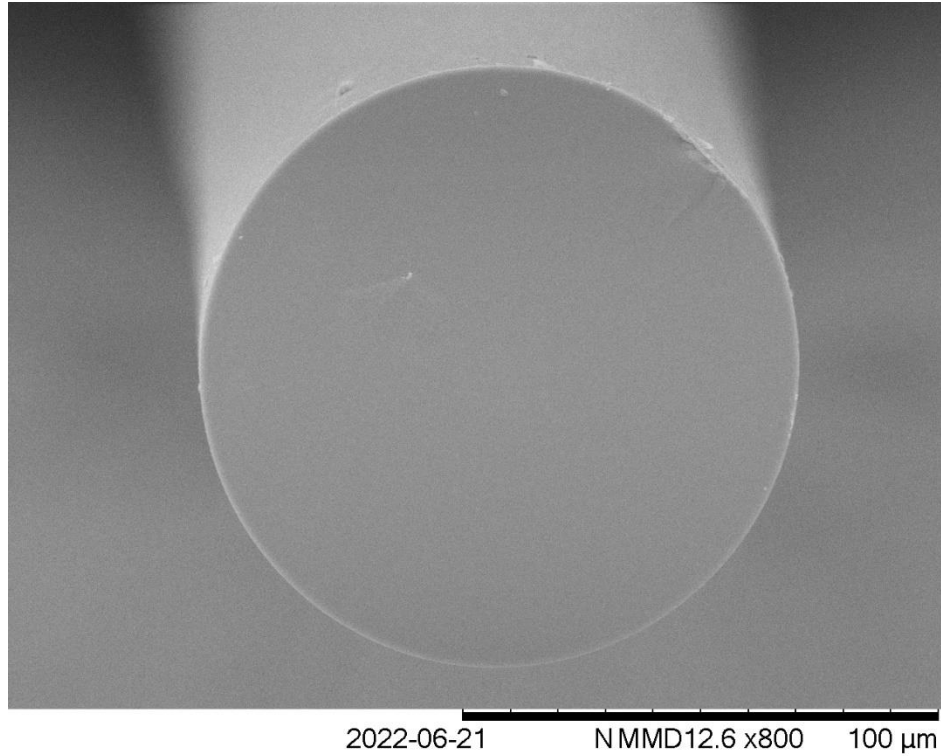
Figure 9 SEM image of an appropriately cleaved SMF 28 fibre end face.

Since the sensor operates based on intensity and relies on cleave quality, an appropriate band of reflection intensity was established for each FRS system and is presented in Section 4.1. This calibration process was repeated each time new SMF-28 fibre was spliced onto the system to create new sensors.

3.5.2.   Fibre Bragg gratings (FBGs)

The FBGs were obtained from FemtoFiberTec GmbH, Germany. They required APC termination to interface them with the SM130 interrogator, necessitating splicing to an APC-terminated optical fibre patch cable (Thorlabs Ltd, UK). The SM1250BI fibres used for the grating inscription were coated with polyimide, rendering conventional stripping impractical. Prior to mechanical stripping, they underwent a preparatory treatment. Subsequently, approximately 40 mm in length, their designated splice ends were submerged in a 1 mol NaOH solution at room temperature for 24 hours, followed by a 30-second rinse in deionised water

3.5.2 Fibre Bragg gratings (FBGs)

and subsequent stripping and cleaving. Approximately 10 ml of a 1 mol NaOH solution was contained in a 75 x 25 mm specimen tube (Scientific Glass Laboratories Ltd, UK). To secure the fibres during immersion, the polymer caps of the vials were drilled with a 1 mm hand drill to accommodate the SM1250BI fibre. The remaining fibre was held in a reel attached to a retort stand throughout the process. The splicing process is described in Section 3.3.

3.5.3.   Fabry-Perot cavity sensors

The following sections outline in-house manufacturing procedures for intrinsic and extrinsic Fabry-Perot reflection-based optical fibre sensors, along with the chemical transmission sensor, which shares similar manufacturing characteristics to an extrinsic Fabry-Perot cavity sensor and is consequently discussed in this context.

3.5.3.1.   Extrinsic Fabry-Perot cavity sensors

Extrinsic fibre optic sensors were produced through the following procedure: The acrylate coating of the fibres was removed using handheld strippers (Miller FO 103-T-250-J series, Ripley tools LLC, USA), and the fibres were then cleansed meticulously with lint-free lens tissue (Tiffen, USA) soaked in IPA. Subsequently, the fibres were cleaved utilising a CT-08 fibre cleaver (Fujikura, Japan). Silica capillaries (CMSL-CFQ, VitroCom Inc, USA) with an internal diameter of 128 and an external diameter of 300 μm, were processed using a capillary column cutter (ShortixTM SGT, Singapore), and they were further cleaned by immersion in ultrasonicated IPA for 3 minutes followed by drying in an air-circulating oven (ULE-500, Memmert, Germany) at 100 °C for 15 minutes. Finally, the fibres were introduced into the capillary and securely fused in place using a custom-modified fusion splicer (BFS-60CCD, UK). The fusion of the fibres to the capillary was achieved through electrical arcing.

3.5.3.2.   Intrinsic Fabry-Perot cavity sensors

The fibre FP sensor was fabricated using a focused ion beam (FIB) system (Helios G4 PFIB CXe, ThermoFisher Scientific). A length of optical fibre (SMF-28) approximately 20 cm long was coiled and secured, with around 5 cm of fibre extending from the coil. The acrylate coating was stripped using mechanical strippers (Miller FO 103-T-250-J series, Ripley tools LLC, USA), followed by cleaning the fibre with lint-free tissue soaked in isopropanol. The end face was deliberately fractured to prevent it from acting as a third reflective interface. Subsequently, the fibre was affixed to a standard 25 mm aluminium scanning electron microscope (SEM) stub (Agar Scientific Ltd, UK) using 25 mm double-sided conductive carbon tape (Agar Scientific Ltd, UK). The stub was then sputter-coated with an Au/Pd alloy for 3 minutes at 25 mA under 1 Torr pressure (SC 500, Emscope, UK).

After coating, the stub was positioned in the main chamber of the FIB system and ablated at an accelerating voltage of 30 kV and an accelerating current of 1 µA to create a cavity approximately 80 µm in length and 40 µm in width through the fibre's thickness (125 µm). A polishing milling process was conducted at 60 nA to reduce the tilt angle in the cavity walls. Finally, the stub was removed from the FIB system, and the FP sensor was detached from the stub using isopropanol to weaken the adhesive.

3.5.4.   Surface-mounted FTIR fibre sensor

A surface-mounted Fourier transform near-infrared (FTNIR) transmission fibre sensor was devised to enable the investigation of chemical changes during curing within an adhesive joint. Adopting a methodology akin to that employed in fabricating extrinsic FP sensors, a configuration involving two fibres aligned to form a substantial "cavity" for analyte containment was adopted. Initially, an SMF-28 single-mode fibre was positioned on the

targeted region and secured with polyimide tape under slight tension to maintain fibre alignment. Subsequently, approximately 1 g of NOA68 adhesive (Norland, USA) was dispensed onto the fibre at the designated sensor site. Given its low viscosity, the adhesive seeped beneath the fibre, enveloping it upon spreading. Following this, the adhesive was subjected to UV curing for 120 seconds using a UV light source (Ortholux Luminous Curing Light,3M United Kingdom PLC, UK). Upon completion of curing, the optical fibre was gently peeled out of the solidified adhesive, thus forming a "fixture" to accommodate the chemical sensor. A gap of approximately 1 mm was excised from the fixture to ensure free space for the sensor fibre ends using a ceramic and a PTFE spatula (RS Components Ltd, UK).

Subsequent steps involved the utilisation of two low-OH FG105LCA multimode fibres (Thorlabs Ltd, UK) to construct the chemical sensor. These fibres were spliced to multimode patch cables terminated with SMA connectors, facilitating their connection to the Matrix-F duplex (Bruker Ltd, USA), with one fibre serving as an inlet and the other as an outlet. Following the cleaving of two multimode fibres to suitable lengths, they were spliced onto the respective patch cables. The distal ends of the multimode fibres were then cleaved and aligned within the fixture using a manual 3D translation stage (Melles Griot Ltd, UK). Alignment precision was monitored using a USB microscope (Discovery VMS-004 Deluxe, Veho UK Ltd, UK) and by assessing the background quality of a conducted FTIR scan in air. The distance between cleaved ends was set to approximately 750 microns. Post-alignment, a drop of NOA68 adhesive was applied to both ends of the fixture and illuminated with the UV gun for 120 seconds to cure the adhesive, thus securing the fibres in place.

To evaluate the curing kinetics, the collected data underwent post-processing via MATLAB software. The autocatalytic (Kamal) model was employed to analyse the cure rates and determine the temperature-dependent nature of the rate constants, establishing the Arrhenius relationship.

3.5.4 Surface-mounted FTIR fibre sensor

3.6. Hyphenated conventional – optical fibre sensor techniques

The subsequent sections aim to explicate employed hyphenated methodologies, wherein optical fibre sensors were coupled with conventional instruments to assess and validate the output of the optical fibre sensors.

3.6.1. Refractometer-Fresnel reflection sensor measurements

Since the response of a Fresnel reflection-based optical fibre sensor is generated as a function of intensity of the photodetector, it is imperative to interpret the recorded voltage with respect to the refractive index at the cleaved end of the fibre. Consequently, the Fresnel reflection sensors (FRS) underwent a process of "calibration" utilising a 60/ED ABBE refractometer (Bellingham + Stanley, UK). The prism of the refractometer received external illumination from a sodium light source emitting at a central wavelength of 589.3 nm (Bellingham + Stanley, UK). To maintain a consistent temperature environment, the refractometer was affixed to a temperature-controlled water bath (TE-10D, Techne Ltd, UK). The calibration was conducted at 25 °C. K-type thermocouples (TC Ltd, UK) were mounted left and right of the prism using polyimide adhesive tape (RS Components Ltd, UK). The Fresnel reflection sensors, prepared as outlined in Section 3.5.1, were then secured onto the prism area using polyimide adhesive tape positioned outside the prism region as illustrated in Figure 10.
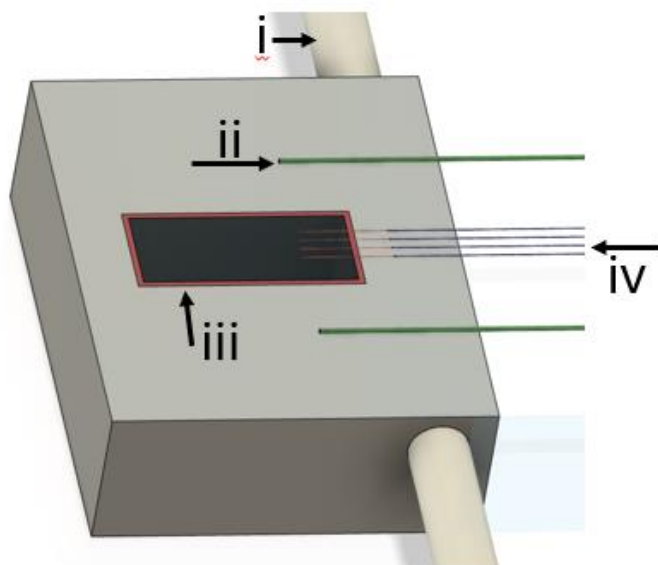
Figure 10 60/ED refractometer setup with (i) water connection for temperature control, (ii) thermocouples, (iii) measurement area, and (iv) Fresnel reflection sensors.

RF18005 refractive index oils (Cargille, USA), spanning refractive indices from 1.40 to 1.70, were applied onto the prism area in conjunction with the FRS. Subsequently, the top prism was clamped down, and the refractometer was calibrated accordingly. The Abbe value was recorded and, factoring in the temperature and the central wavelength of the sodium light source, converted into a refractive index value using the refractometer software from Bellingham + Stanley. The response of the FRS was logged concurrently for 120 seconds per oil. This procedure was repeated three times per oil. Following measurements, the prism area underwent thorough cleaning with acetone to eliminate any potential contamination.

3.6.2.   Fourier transform infrared spectroscopy – Fresnel reflection sensor setup

The subsequent sections describe the equipment employed along with its specifications. The configuration of the FTIR data acquisition setup is detailed in Section 3.4.2, while the Fresnel reflection-based sensor system is expounded upon in Section 3.5.1.

3.6.2.1. Cuvette holder assembly

To assess the adhesive cure kinetics related to refractive index change at isothermal conditions, the FRS was combined with a near-infrared spectrometer. This integration involved employing a temperature-controlled cuvette holder (CUV-TLC-50F, Ocean Optics Inc, USA) in tandem with a temperature controller (TLC 125, Quantum Optics, USA) and a submersible water pump (provided by the manufacturer) to ensure a recirculating water supply. The pump was submerged within a water bath (Techne TE-10D, UK), and the water temperature was regulated at 30 °C throughout the experiment. The cuvette holder is illustrated in Figure 11.
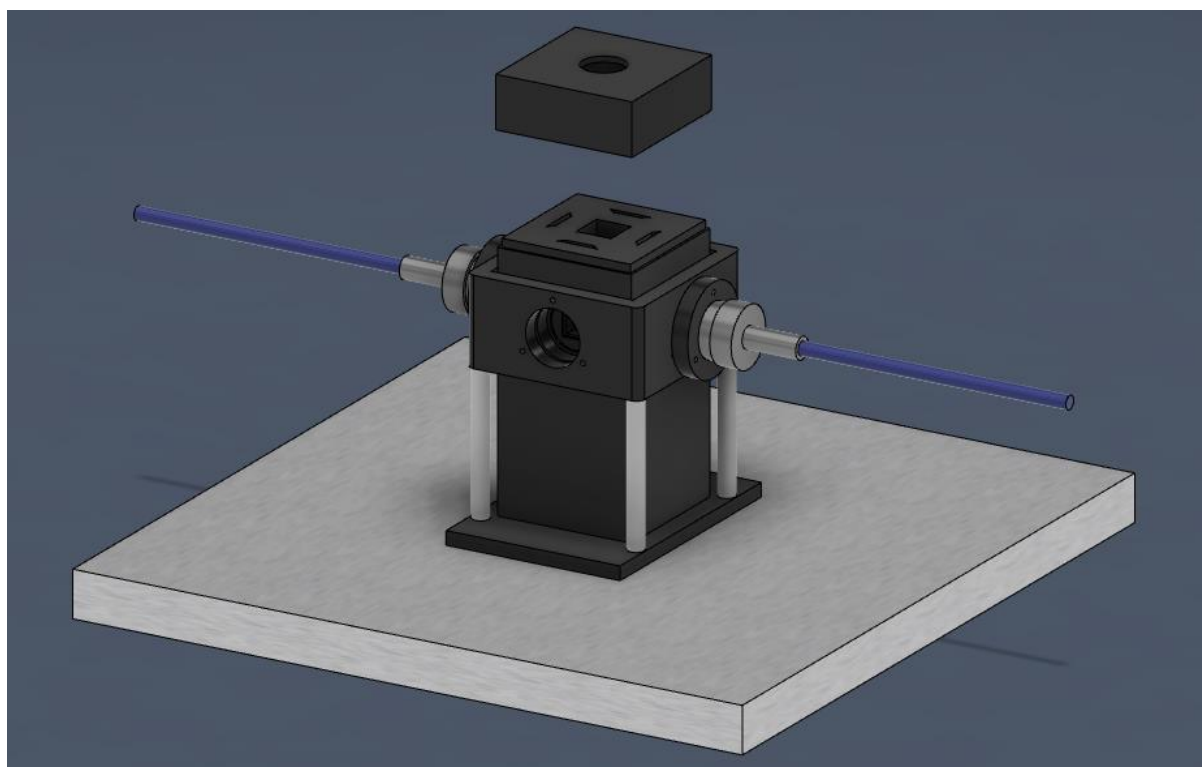
Figure 11 Temperature-controlled cuvette holder assembly.

Near-infrared light from the Bruker Matrix-F duplex FTIR (Bruker Ltd, USA) was transmitted to the cuvette holder and back via a pair of SMA-terminated low-OH fibre cables (QP1000-2-VIS-NIR, OceanOptics, USA) with a fibre bundle diameter of 1 mm. The cuvette holder comprises a lens assembly that collimates the incident light to approximately 8 mm, thereby enlarging the interrogation area. Subsequently, the light is collected and coupled back into the

3.6.2.1 Cuvette holder assembly

output fibre cable after traversing the analyte region within the mid-section of the cuvette holder.

3.6.2.2.   De-mountable cuvette

To confine the adhesive, a 1 mm path length de-mountable quartz cuvette sourced from Starna Scientific Ltd, UK, was employed. Prior to each experiment, the cuvette underwent preparatory steps involving the application of a release agent and a sealing procedure. The external release agent PAT-607/PCM (Würtz GmbH und Co. KG, GER) was delicately applied onto a flat surface using a cotton swab to ensure comprehensive coverage of the internal surfaces without contaminating the sealing area. Subsequently, it was left to dry at room temperature for 30 minutes. This process was repeated thrice to attain three layers of release agent. The two cuvette parts are illustrated in Figure 12.
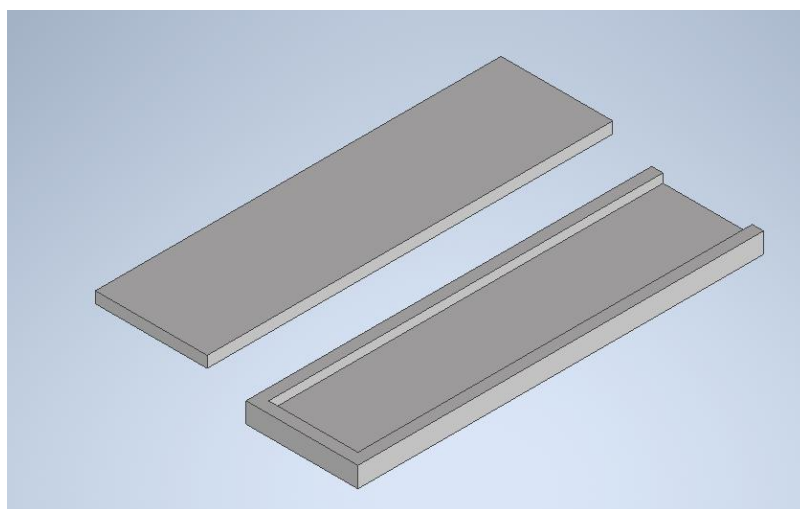
Figure 12 Schematic of de-mountable cuvette parts before the sealing process.

For cuvette sealing, a silicone-based sealant (Hylomar, RS Components Ltd, UK) was precisely applied onto the sealing area of the base part of the cuvette assembly, as depicted in the illustration and secured with miniature wooden clamps. The sealant was left to cure for 24 hours at room temperature.

3.6.2.2 De-mountable cuvette

3.6.2.3. Fresnel reflection sensor carrier assembly

Given that the cuvette holder is engineered to house for 10 mm path length cuvettes, a 9 mm spacer was acquired (Hellma GmbH & Co. KG, Germany) to securely position the cuvette without obstructing the FTIR beam. To facilitate immediate submersion of the FRS into the cuvette upon experiment initiation, ensuring the observation of intensity variation from air to analyte, a bespoke "sensor carrier" was devised. This entailed affixing four FRS units and a K-type thermocouple (TC Ltd, UK) onto a glass slide and designing a carrier to guide the sensors into the 1 mm path cuvette and maintain their stability post-insertion. A modular aluminium holder was consequently designed and manufactured, as illustrated (illustration). The cuvette holder incorporates two distinct light paths tilted at 90° from each other and was intended for fixation using the lens fixtures on the unused side.

A standard microscopy glass slide (Euroturbo, Deltalab, Spain) was deburred using a polishing machine in conjunction with 800-grit grinding paper (Hermes Schleifmittel GmbH, Germany). Subsequently, the K-type thermocouple was centrally affixed onto the glass slide using two 21-gauge needles (Micro Lance 3, BD, Spain) on either side to accommodate an FRS. The assembly was bonded onto the carrier using NOA68 adhesive. The distance from the cuvette to the topside of the cuvette holder was determined to be 15 mm, with the desired insertion depth being 25 mm. The ideal depth was investigated in an experiment illustrated in Section 4.2.1. Consequently, the thermocouple length from carrier to tip was set to 40 mm, and the needles extended over the carrier by 15 mm. A schematic illustration of the sensor assembly is illustrated in Figure 13.
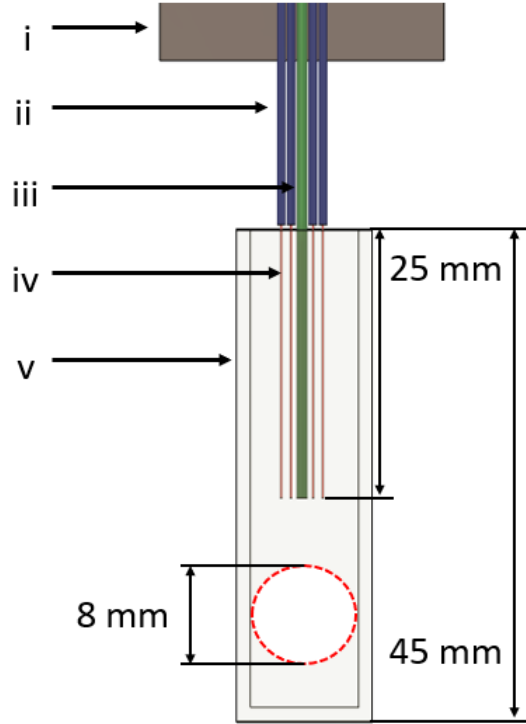
Figure 13 Carrier assembly consisting of (i) glass slide carrier, (ii) unstripped segments of the four FRS, (iii) thermocouple, (iv) stripped segments of the four FRS, and (v) demountable cuvette. The FTIR interrogation area is highlighted by the red circle.

In preparation for sensor deployment, the carrier assembly was vertically secured in a retort stand using a clamp. The thermocouple was coated three times with release agent (PAT-607/PCM, Würtz GmbH und Co. Germany) to facilitate thermocouple retrieval post-experimentation. Each of the four fibres was passed through a needle and prepared according to the methodology outlined in Section 3.5.1. Following preparation, the fibres were adjusted to match the thermocouple length and subsequently secured using NOA68 adhesive.

3.6.2.4. Experimental setup for FTIR-FRS isothermal cross-linking experiments

Prior to commencing each experiment, the setup for both the FTIR and the FRS was arranged according to the procedures outlined in Sections 3.4 and 4.1, respectively. An FTIR background scan was performed subsequent to inserting the prepared cuvette and spacer to mitigate the

3.6.2.4 Experimental setup for FTIR-FRS isothermal cross-linking experiments

effects of the quartz cuvette and applied release agent. The adhesive application followed the methodology detailed in Section 3.3.2, with the addition of a needle affixed to the static mixer due to the nozzle of the static mixer being incompatible with the 1 mm path cuvette. The 21-gauge needle (Micro Lance 3, BD, Spain), measuring 45 mm in length, was attached to the static mixer and positioned so that its tip rested at the bottom of the cuvette during adhesive application. After application, the needle was cautiously removed to ensure that the adhesive level remained approximately 2.5 mm below the upper edge of the cuvette.

Subsequently, the cuvette and spacer were inserted into the temperature-regulated cuvette holder set at 20 °C. Data logging for both the FTIR and FRS commenced, and approximately 10 seconds after initiation, the prepared carrier assembly was lowered until it was flush with the top side of the cuvette holder, positioning the fibres and thermocouple within the cuvette at a depth of 25 mm. Following the insertion of the carrier assembly, the target temperature was set using the temperature controller. Experiments were conducted within a temperature range of 20 to 50 °C, progressing in 5 °C increments, as outlined in 4.2.3. Figure 14 illustrates the cuvette holder with inserted cuvette sensor assembly.
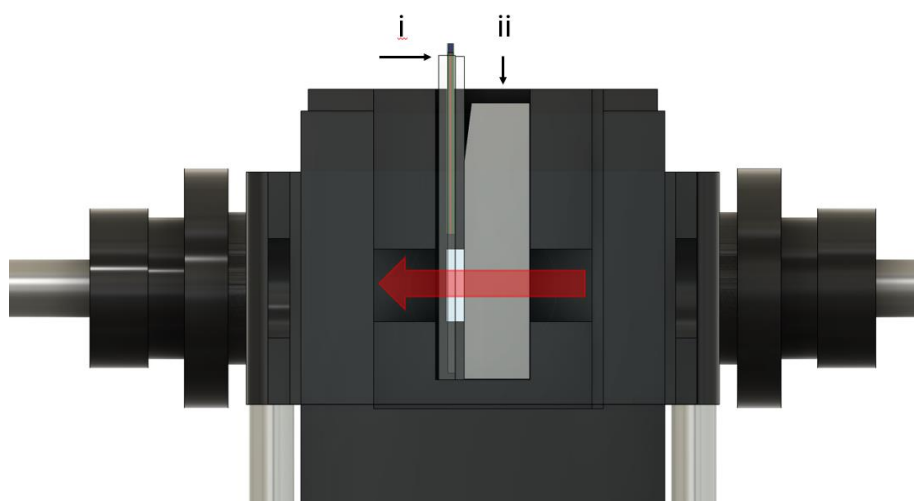
Figure 14 Section view of the cuvette holder with inserted cuvette sensor assembly (i) and hollow spacer (ii).

3.6.2.4 Experimental setup for FTIR-FRS isothermal cross-linking experiments

3.7. Single-lap joints

The study involved single lap joints comprising two distinct metal substrates. As detailed in Section 3.3.1, sheets of 2024 T3 aluminium and S235JR steel were acquired and subsequently subjected to water jet cutting to create coupons (substrates). Conforming to ASTM D1002 specifications, the required dimensions stipulated l = 101.6± 0.2 mm and w = 25.4± 0.2 mm. Accordingly, CNC machining aimed to achieve tolerances within a range of 101.7± 0.1 mm for length and w = 25.4± 0.1 mm for width. Subsequently, the edges of each coupon underwent individual grinding on a polishing machine operating at 300 rpm (GP-2B, Testlab, Poland), employing 800-grit silica carbide paper to attain dimensions of l = 101.6± 0.1 mm and w = 25.3± 0.05 mm. After attaining the desired dimensions, deburring was performed using the same setup. Surface areas were then ground for 5 seconds at 50 rpm to eliminate debris and irregularities, ensuring a level substrate surface. Each substrate was measured in length and width using a vernier calliper (CD-6"ASX, Mitutoyo Corp., Japan)) and in thickness using a digital micrometre. After determining the dimensions, each substrate was labelled with a scribe from 1 to 12. All measurements were logged.

3.7.1. Surface preparation techniques

The ensuing sections outline the methods employed for surface preparation and the equipment utilised to evaluate their impact on the substrates prior to the fabrication of single-lap joints. Following the grinding of substrates to meet specified dimensions, they were marked for grit-blasting and the subsequent manufacturing process, as depicted in Sections 3.7.2 and 3.8.

3.7.1.1. Degreasing

Methyl ethyl ketone (MEK) served as the degreasing agent for the metal substrates. An approximate volume of 100 ml of MEK was contained in a 250 ml glass beaker (Scientific Laboratory Supplies Ltd, UK) to ensure comprehensive coverage of the bonding areas. Twelve substrates were grouped into two sets, each sandwiched between end tabs to maintain a 2 mm spacing between substrates and ensure that bonding areas were immersed fully in the MEK. These packs were then secured with clamps and submerged into the MEK-filled beaker. The beaker was subsequently placed into an ultrasonic water bath (U100H, Scientific Laboratory Supplies Ltd, UK) and ultrasonicated for 5 minutes. Following this, the substrates were individually rinsed in deionised water for 10 seconds each.

3.7.1.2. Assessing the influence of degreasing on the surface chemical composition of metal substrates

To investigate the impact of the degreasing process on surface chemical composition, a Hitachi TM3030Plus scanning electron microscope (SEM) (Hitachi Analytical Science Ltd, UK) was employed in conjunction with an AZtecOne energy-dispersive X-ray spectroscopy (EDX/EDS) system (Oxford Instruments, UK). Due to the size of the substrates being unsuitable for the SEM holder, smaller representative samples were fabricated with dimensions of $l = w = 25.4$ mm. These samples were affixed to a 25 mm diameter SEM holder (Agar Scientific Ltd, UK) using 25 mm conductive carbon tape (Agar Scientific Ltd, UK). In order to ensure consistency in SEM micrographs before and after degreasing, a single indentation was made in the middle section of each specimen using a scriber, serving as an orientation point throughout the experiment. The punches can be seen in Section 5.2.6.2, Figure 115.

3.7.1.1 Degreasing

3.7.2.   Grit-blasting

Grit-blasting was selected as the method to enhance the surface roughness of the bonding area. The subsequent section outlines the equipment used in the grit-blasting experiments and describes the experimental setup.

3.7.2.1.   Grit-blast cabinet

A grit-blast cabinet manufactured by Guyson, UK, featuring an attached cyclone extractor, was utilised alongside a fixed-position wide-nozzle blasting gun (900 blast gun, Guyson, UK). The chosen abrasive media (Saftigrit 100, Guyson, UK) consisted of 99.73% alumina with an average grit diameter of 125 microns. A SEM micrograph of the abrasive media is illustrated in Figure 15.

Figure 15 SEM micrograph of Saftigrit 100.

Prior to commencing initial experiments, thorough cleaning of the grit-blast cabinet was undertaken to remove any remnants of previous abrasive media and prevent cross-contamination with other contaminants. Subsequently, approximately 25 kg of Saftigrit was inserted into the cabinet for use in the experiments.

3.7.2.2.   Substrate holder

In order to minimise variations in blasting between substrates, each substrate underwent individual blasting. For this purpose, a bespoke substrate holder was devised, consisting of a milling vice (RS Components Ltd, UK) securely attached to an adjustable lab jack (RS Components Ltd, UK), which in turn was affixed to a custom-made Trespa ground fixture, providing three-dimensional adjustability. An aluminium T-slot profile was clamped into the vice to hold the substrate. The substrate was then positioned onto the aluminium profile, sandwiched between a ground plate to shield the profile from abrasion and a sacrificial top substrate, exposing only the designated blasting area. This assembly was secured to the profile using two toolmaker clamps, as illustrated in Figure 16.

3.7.2.2 Substrate holder
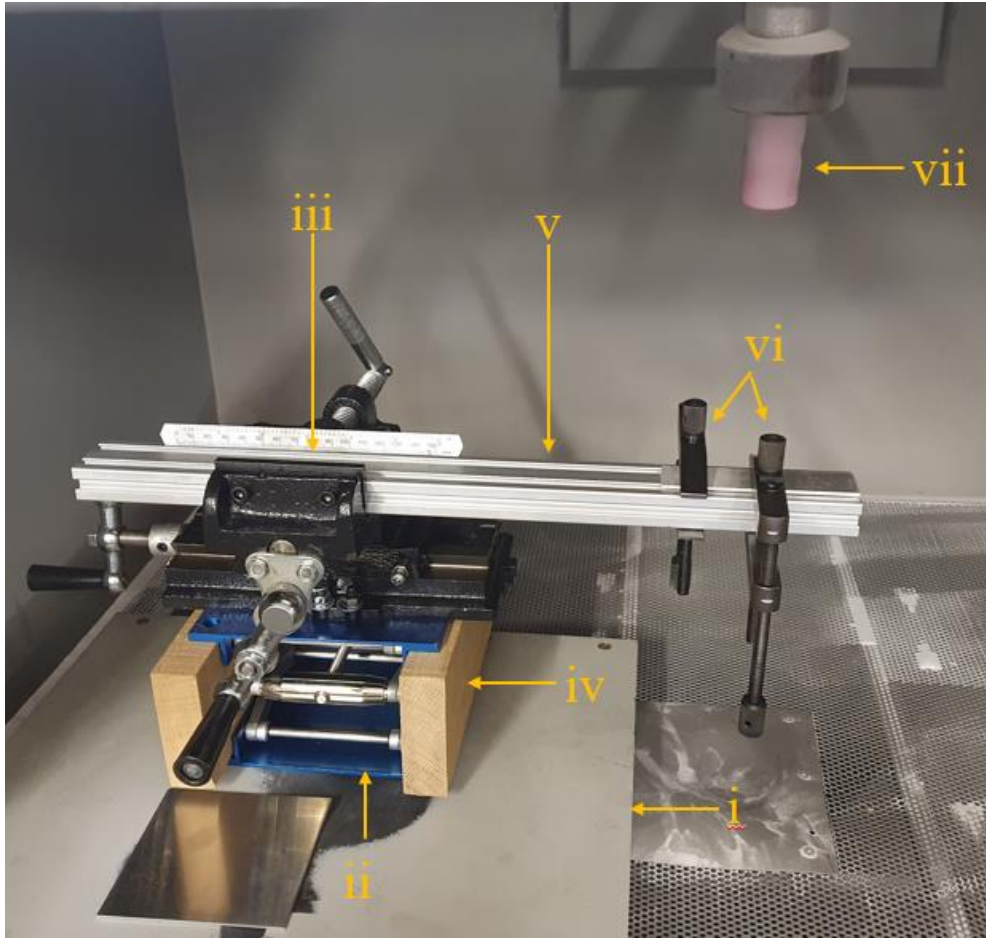
Figure 16 Substrate holder within the grit-blast cabinet with (i) Trespa ground plate, (ii) lab jack, (iii) milling vice, (iv) supports, (v) aluminium rail, (vi) tool maker camps fixing an aluminium substrate, and (vii) grit-blast nozzle.

To ensure the substrate area was centred under the grit-blast nozzle, a laser pointer (283-5378, RS Components Ltd, UK) was employed in conjunction with a sacrificial aluminium "target" plate prior to testing. This calibration allowed for the assessment of deviations and subsequent compensation for these deviations. The stand-off-distance was found to be 189 mm from the top side of a fixed substrate to the nozzle of the grit-blast gun.

3.7.2.3. Grit-blast procedure

The blasting region on the substrate was designated to have dimensions of w = l = 25.4 mm, which effectively doubled the grit-blasted area compared to the bonding area. This strategy aimed to prevent the occurrence of transition edges at the bonding area, which could introduce

3.7.2.3 Grit-blast procedure

non-uniformities and lead to stress concentrations during tensile testing, potentially resulting in premature specimen failure. Enlarging the blasted area further would have increased the degree of warping, consequently altering substrate flatness and potentially interfering with bond-line control. The boundary of the grit-blast area was scribed on the substrate using a height gauge (Mitutoyo, Japan) on a levelled ground plate. Air pressure for the blasting process was supplied by a compressor. Given the significant influence of blasting pressure on abrasion, pressure control was managed manually after each blasting cycle, ensuring a consistent starting pressure of 8.3±0.05 bar. The blasting pressure was logged both before and after each blasting process for every specimen treated.

3.7.2.4.   Assessing surface roughness

To evaluate alterations in substrate surface morphology resulting from the grit-blasting process, focus variation microscopy was employed. The following two subsections provide detailed explanations of the selected methodology for assessing these changes and verifying the obtained results.

3.7.2.5. Focus variation microscopy

The Alicona InfiniteFocus G5, (Alicona Imaging GmbH, Austria), featuring an integrated 2D translation stage, as illustrated in Figure 17.
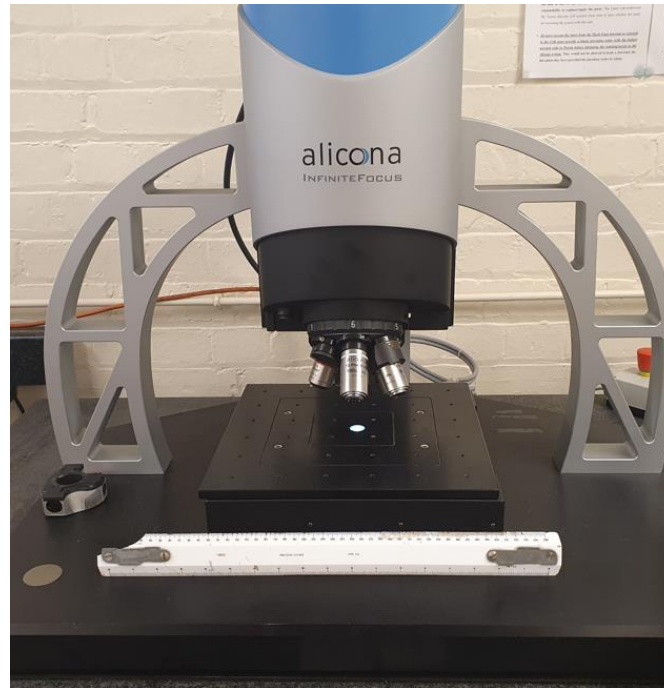
Figure 17 Alicona G5 with 2D translation stage.

Focus variation microscopy was employed to quantify the impact of grit-blasting on the substrates. Given the anticipated variation in the grit-blasting effect from the centre to the periphery, the entire grit-blasted areas were examined to assess surface texture. Subsequently, surface roughness measurements (line profiles) could be analysed as desired, as the entire areas were saved as datasets within the Alicona system. Prior to commencing a measurement, a substrate was positioned on the 2D translation stage to ensure that the grit-blasted area was roughly centred under the microscope, with the remainder of the substrate extending outward in the positive x direction. Alignment lines on the stage were used to parallel the edges, facilitating the designation of the top left corner of the grit-blasted area as the zero point and

3.7.2.5 Focus variation microscopy

ensuring no angular tilt of the substrate with respect to the instrument's coordinate system. To perform an automatic area scan, three coordinate points and the focal range ($\pm$ z-coordinates) needed to be defined. As previously mentioned, the first coordinate point was set at the top-left corner. From there, the next point determined the width of the substrate (- 25.4 mm in the y direction), while the last point defined the length of the overlap (+12.7 mm in the x direction). An appropriate focal range was determined to be +0.1 mm and -0.2 mm. Subsequently, the system automatically executed a rapid initial scan without varying the z-range to illustrate the area of interest. Following this, the actual scan, which typically lasted approximately 25 minutes, was conducted. Upon completion of the scan, a 3D profile was generated, which was then post-processed according to the ISO-conform Alicona methodology outlined in the manual. Due to the significant time consumption associated with this process, a set of three specimens was deemed sufficient to assess the resulting surface morphology of a grit-blasting setup.

3.7.2.6.   Data validation

A surface roughness calibration kit was acquired to validate the measurements obtained from the Alicona system (235-7544, RS Components Ltd, UK). This kit contained various metal blocks with predetermined surface roughness values resulting from different surface machining methods, as illustrated in Figure 18.
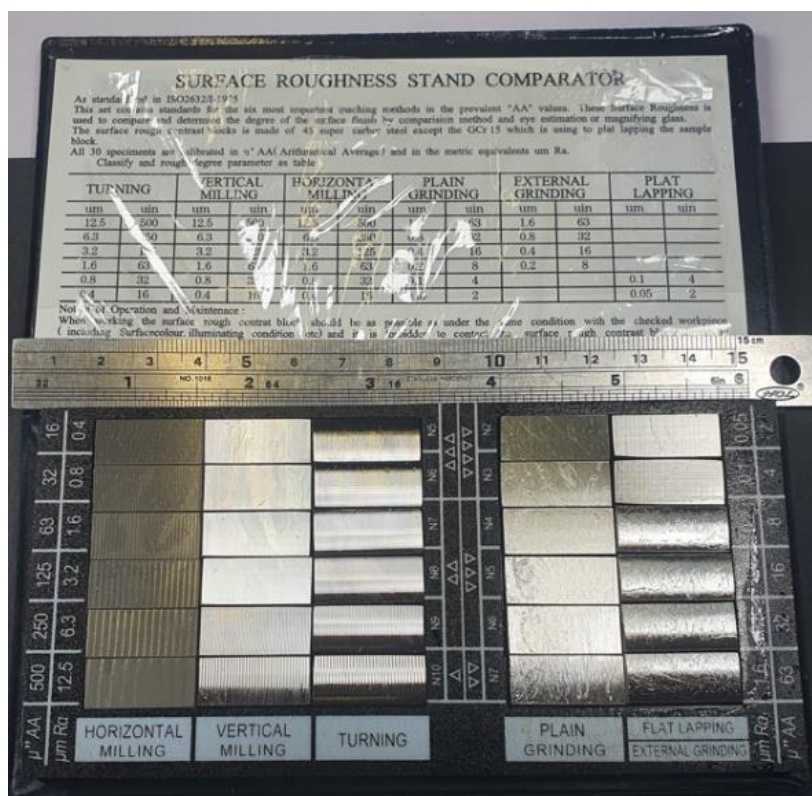
Figure 18 Surface roughness calibration kit.

The Alicona system was used to analyse these blocks, aiming to ascertain the system's accuracy and evaluate the impact of various parameters, including magnification and the differentiation between waviness and roughness.

3.7.3. Silanation procedure

Aqueous ethanoic acid was adjusted to pH 4.5 and utilised in the silane treatment process. (3-Aminopropyl)trimethoxysilane solutions were prepared by diluting this acid solution to final concentrations of 1, 2, and 3% (v/v) in 100 mL volumetric flasks. Once prepared, the solutions were transferred to beakers containing magnetic stir bars and allowed to hydrolyse for 1 hour. After hydrolysis, substrates were suspended using a retort stand, ensuring that an area twice the intended bonding surface was immersed in the silane solution. The treatment duration was set at 10 minutes for aluminium substrates and 5 minutes for composite substrates. Following immersion, the substrates were taken out, placed on a metal tray with their bonding regions

3.7.3 Silanation procedure

facing upward, and moved to a preheated air-circulating oven. Aluminium samples were subjected to drying at 115 °C for 1 hour, while composite samples were dried at 60 °C for 2 hours.

3.7.3.1. Assessment of free surface energy

A total of 15 substrates were designated for contact angle analysis to evaluate free surface energy, with measurements conducted in groups of three. The investigated surface conditions comprised untreated surfaces prior to MEK degreasing, post-MEK degreased surfaces, and samples subjected to silane treatments at concentrations of 1, 2, and 3%. To ensure consistency in contact angle measurements, the silane-treated specimens were not subjected to grit-blasting, as the technique requires smooth, uniform surfaces for accurate assessment.

3.8. Manufacturing single-lap joints

To ensure precise fabrication of single lap joints, a fixture was necessary to secure the substrates in position throughout the curing process. The following sections outline the development of this fixture and provide specifics regarding the standardised manufacturing procedure.

3.8.1. Single-lap joint rig

The apparatus was custom-fabricated from mild steel (F.H. Warden Ltd, UK) and consisted of a bottom plate and a top plate, as illustrated in Figure 19.
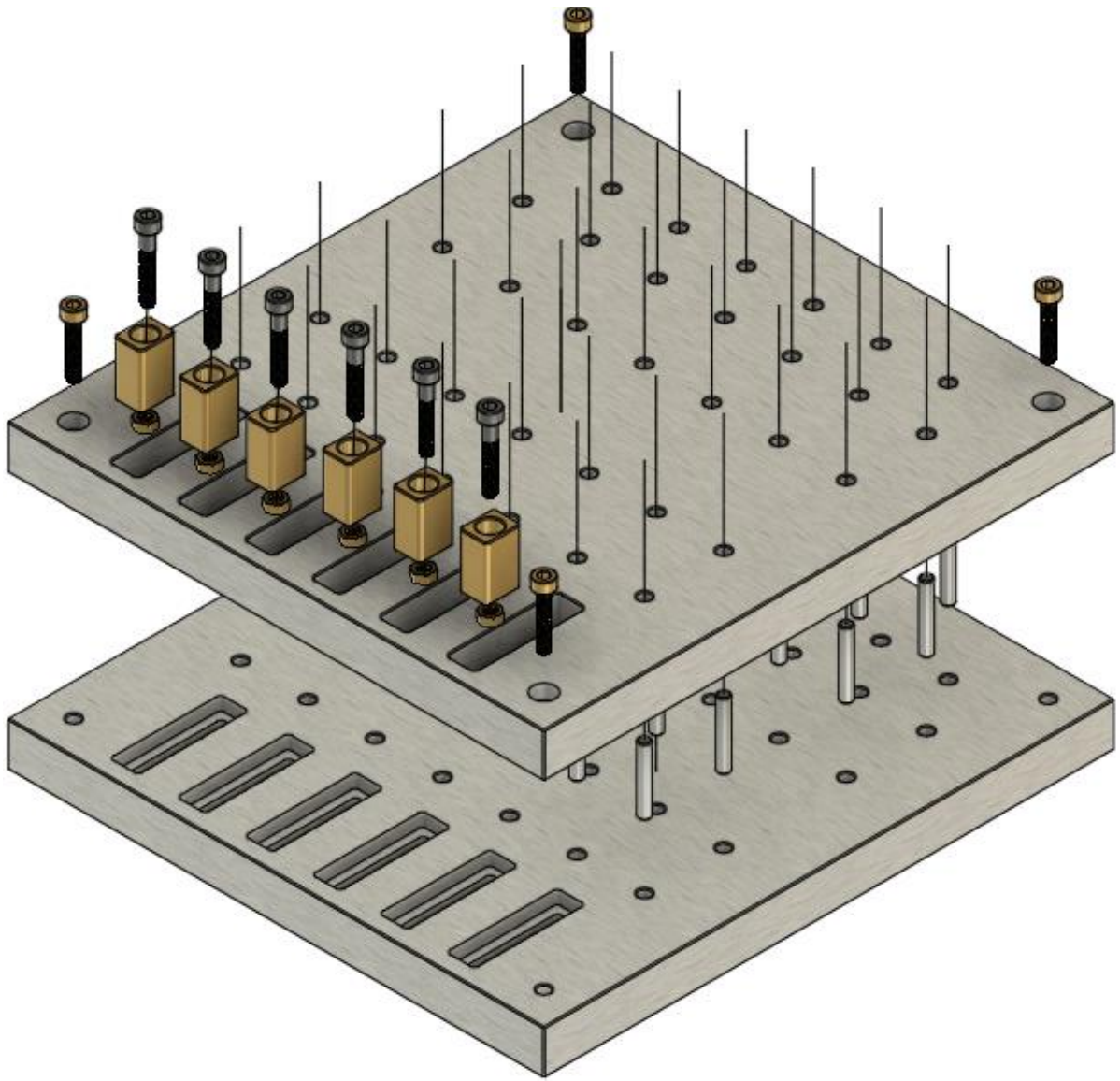
Figure 19 Exploded assembly view of the single lap-joint rig.

It was designed to accommodate 12 substrates simultaneously, enabling the production of 6 single lap joints in a single batch. The lower section was engineered to immobilise the substrates securely during curing, preventing any tilting or shifting. The spacing between the inner tangential points of the pins enclosing a substrate was set at 25.4 mm. The base plate was secured with dowel pins to ensure adequate positional tolerances. The fit was designed as a transition fit. The top row of dowel pins serves as a zero stop for half of the substrates. On the other side, there are recesses into which adjustment elements are inserted. These elements were used to fine-tune the overlap. They can be locked in place via a screw/nut connection after the

3.8.1 Single-lap joint rig

fine-tuning is completed. For this purpose, a centrally located ridge is present in the recesses, serving as a clamping surface. Centrally located on the base plate is a clear space where the substrates overlap. This clear space was designed to allow for smooth insertion and removal of the single lap joints. The top plate features a bore and recess arrangement symmetrically aligned with the base plate. However, the bores are slightly oversized to ensure frictionless guidance of the top plate during assembly. The recesses in the top plate are fully continuous to prevent the adjustment elements from jamming. Threaded holes are present in the corners of the base plate and through holes in the top plate, allowing both plates to be secured with screws after assembly.

3.8.2. Manufacturing process steps

The subsequent subsections describe the methodology to prepare the surface-treated substrates to fabricate single-lap joints. A schematic of the joints within the SLJ rig is illustrated in Figure 20.
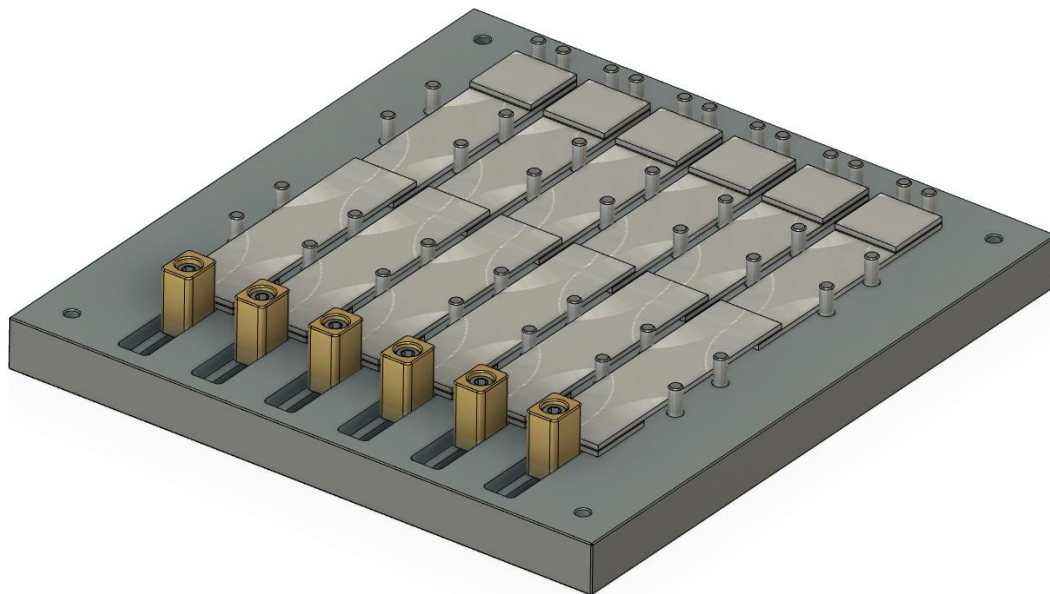
Figure 20 Schematic of SLJ placed on the bottom part of the manufacturing rig.

72

3.8.2 Manufacturing process steps

3.8.2.1.　Substrate preparation prior to manufacturing

Following the grinding process to achieve the desired dimensions, the bond area was designated using a height gauge, as detailed in Section 3.7.2.3. Furthermore, a 12.7 mm overlap was marked on the rear side of each substrate. Prior to masking the substrates for the fabrication of single lap joints, they underwent drying for one hour at 115 °C (2024 T3 aluminium) and two hours at 60 °C (CFRP) in the air-circulating oven. Subsequently, they were allowed to cool to room temperature, a process that took approximately 5 minutes. Upon cooling, polyimide tape of 0.572±0.032 mm thickness, measured using a digital external micrometre (293-832-30, Mitutoyo Corp., Japan), was used for masking. The front edge areas and the side up to the end of the overlap were masked.

Additionally, the overlap was marked on the upper surface using the scribed line on the rear side. Hence, the substrate was clamped with the scribed side facing upwards, and the tape was aligned accordingly. This method was crucial to prevent a scribed line at the overlap, which could lead to premature failure due to stress concentration, as discussed in Section 3.7.2.3. To precisely apply the masking tape, slightly larger pieces were pre-cut, applied, and then trimmed directly on the substrate, utilising the edges as guides at an approximate cutting angle of approximately 45°. A ceramic blade was employed for this purpose. Subsequent to masking the substrates, the overlap was adjusted using the rig adjustment elements. The substrates were inserted in a standardised manner, with substrates one and two forming the initial joint, wherein substrate one was positioned on the adjustment element side, serving as the substrate for adhesive application.

3.8.2.2.   Bond-line control

 Once the substrates were masked, adhesive was applied to the bond area of six out of the twelve substrates using the application setup detailed in Section 2.3. The adhesive was then carefully spread using a PTFE spatula to ensure complete area coverage. Feeler gauges (S0517, Sealey Group, UK) were employed to control the bond line thickness. Various feeler gauge sets were obtained, offering thicknesses ranging from 0.05 to 1 mm (provided by the manufacturer). Eight of the 0.5 mm feeler gauges were measured three times (left, centre, right) in thickness using the external micrometre. The average thickness was found to be 0.5072 ± 0.0072 mm. Achieving the desired bond line thickness of 0.5 mm involved a two-step process. Initially, the bond line thickness was pre-set to 0.9 mm using a substrate spacer assembly with a ceramic blade atop. The substrate with the applied adhesive was manoeuvred under this assembly to scrape off excess resin. Subsequently, a substrate with the predefined bond line thickness was promptly placed into the rig. Once all substrates with adhesive were inserted, the bond line needed to be further defined. Given that the resulting joint consisted of two substrate thicknesses plus a 0.5 mm bond line, each side required adjustment to this height. Consequently, four feeler gauges of 0.5 mm thickness were positioned atop each side, along with two additional substrates. On the opposite side, an equivalent number of gauges and substrates were pre-positioned, and the substrates were then placed on top. This setup is depicted in Figure 21 for clarity.

3.8.2.2 Bond-line control
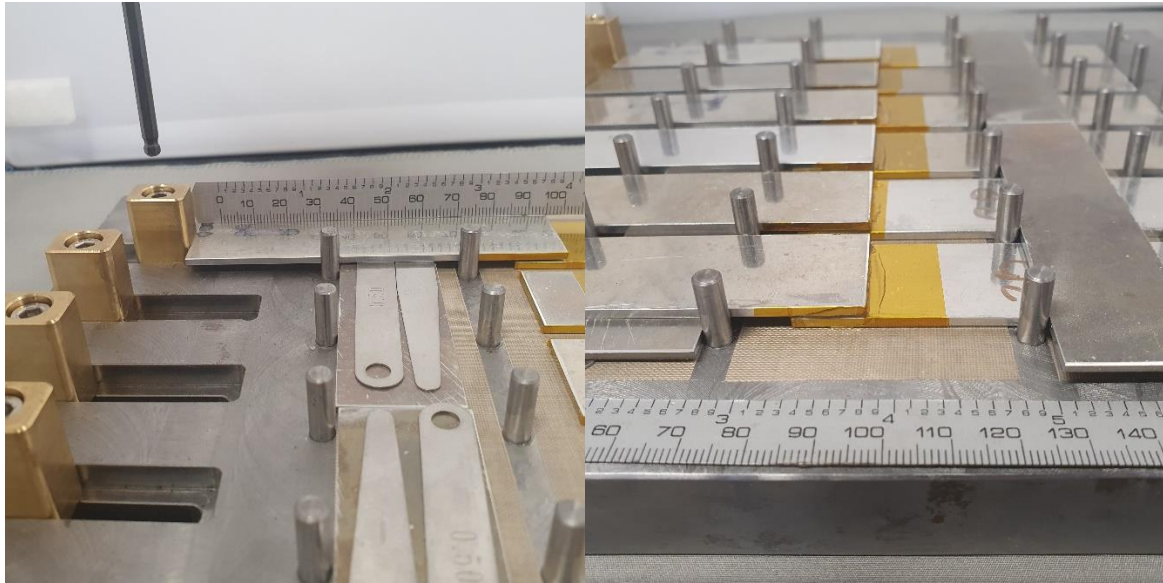
Figure 21 Left: SLJ rig prior to bonding with feeler gauges in place. Right: SLJ rig with freshly set-up joints with a BLT of 0.5 mm.

Following the setup of the joints, the top plate was positioned using a spirit level to prevent any misalignments. Once the curing process was complete, the top plate was removed, and each of the six SLJ was unmasked.

3.9. Tensile testing of single-lap joints

After the completion of manufacturing the SLJs, it was necessary to end-tab them using the same adhesive employed for creating the joints. For this purpose, some of the initial coupons were divided into four pieces. These segments were then ground to w = l = 25.4±0.1 mm dimensions and deburred to ensure smooth edges. The bond line for the end-tabs was maintained at 0.5 mm thickness and subjected to the designated curing schedule (detailed in Section 3.8). A 1484 tensile tester (ZwickRoell GmbH & Co. KG, Germany) with a 200 kN load cell and an external extensometer were utilised to evaluate the failure strength of each single lap joint. Fixing the single lap joints involved using two 100 kN manual wedge action grips (MWAG) featuring serrated jaw faces with one tooth per millimetre. The maximum specimen thickness for these jaw faces was 6.35 mm. The extensometer was adjusted to a gauge

3.9 Tensile testing of single-lap joints

length of 80 mm (40 mm from the centre of overlap outwards on both substrates). Each SLJ was fixed in a standardised procedure; the substrate with an odd number was inserted into the lower MWAG with the end tab facing to the left. Then, the force of the load cell was set to zero. The crosshead was then driven upwards until the upper SLJ was appropriately positioned in the upper MWAG. For the test parameters an initial pre-load to 150 N was conducted at 5 mm/min. After reaching the pre-load force, the extensometer arms were fixed to the SLJ and the the SLJ was tested to failure at 0.5 mm/minute. The force shutdown threshold was 80% of F_{max}. A schematic of the tensile testing setup is illustrated in Figure 22.
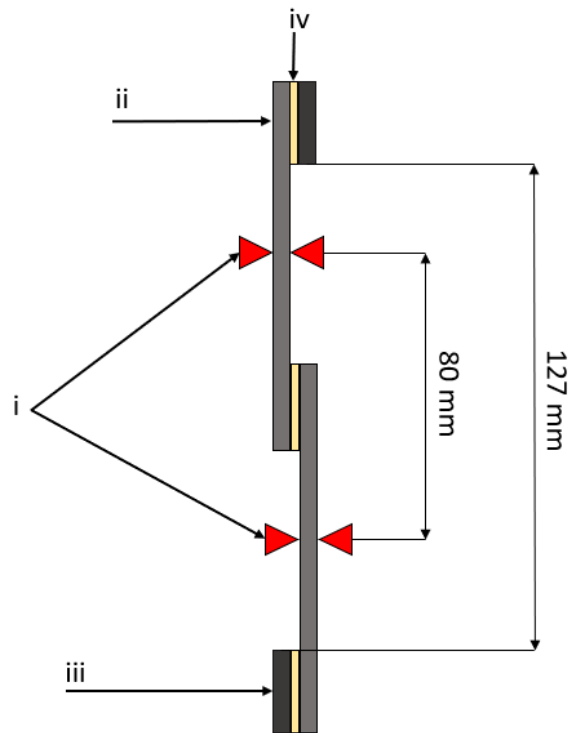
Figure 22 Tensile testing with external extensometer (i) adjusted to a gauge length of 80 mm, (ii) substrate, (iii) end-tab, and (iv) adhesive bond line. Grip-to-grip separation was 127 mm.

3.9 Tensile testing of single-lap joints

3.10. *In situ* measurements within adhesive joints

The subsequent section outlines the evaluation of various parameters within adhesive joints during the curing process under isothermal conditions, as well as the procedural intricacies involved in setting up the experiments.

3.10.1. Embedded optical fibre sensors

FRS, FBG, and FP sensors were embedded in the manufacture of single-lap joints to assess (i) chemical changes in the functional groups of the adhesive, (ii) temperature, (iii) refractive index, and (iv) shrinkage as a function of strain during the cross-linking of the adhesive joints under isothermal conditions. Areas of interest were strain, temperature, refractive index, and chemical changes. The sensor types used and their respective details are listed in Table 5.

Table 5 Overview of embedded sensor types embedded in the SLJ to enable the in situ measurement of (i) chemical changes, (ii) temperature, (iii) refractive index, and (iv) shrinkage / strain.

Parameter	Sensor-type	Details
Chemical changes	Transmission	Multimode cavity with l = 750 and d = 105 microns
Temperature	FBG	SM, Polyimide-coted, capillary-housed
Refractive index	Extrinsic FP	Cavity with l ~ 30 microns
	FRS	Cleaved SMF-28 single-mode fibre
Strain / shrinkage	FBG	Single-mode (SM), Polyimide-coated
	Intrinsic FP	Single-mode (SM), enclosed in a capillary, cavity with l ~ 50 and d ~ 40 microns

3.10 In situ measurements within adhesive joints

3.10.2. Glove box system for the temperature and humidity-controlled manufacture of adhesive joints

A temperature and humidity-regulated glove box system (Coy Laboratory Products Inc, USA) was utilised to accommodate the single-lap joint manufacturing setup, facilitating the evaluation of parameters illustrated in Section 3.10.1 during isothermal curing conditions. Figure 23 illustrates the glove box system used.
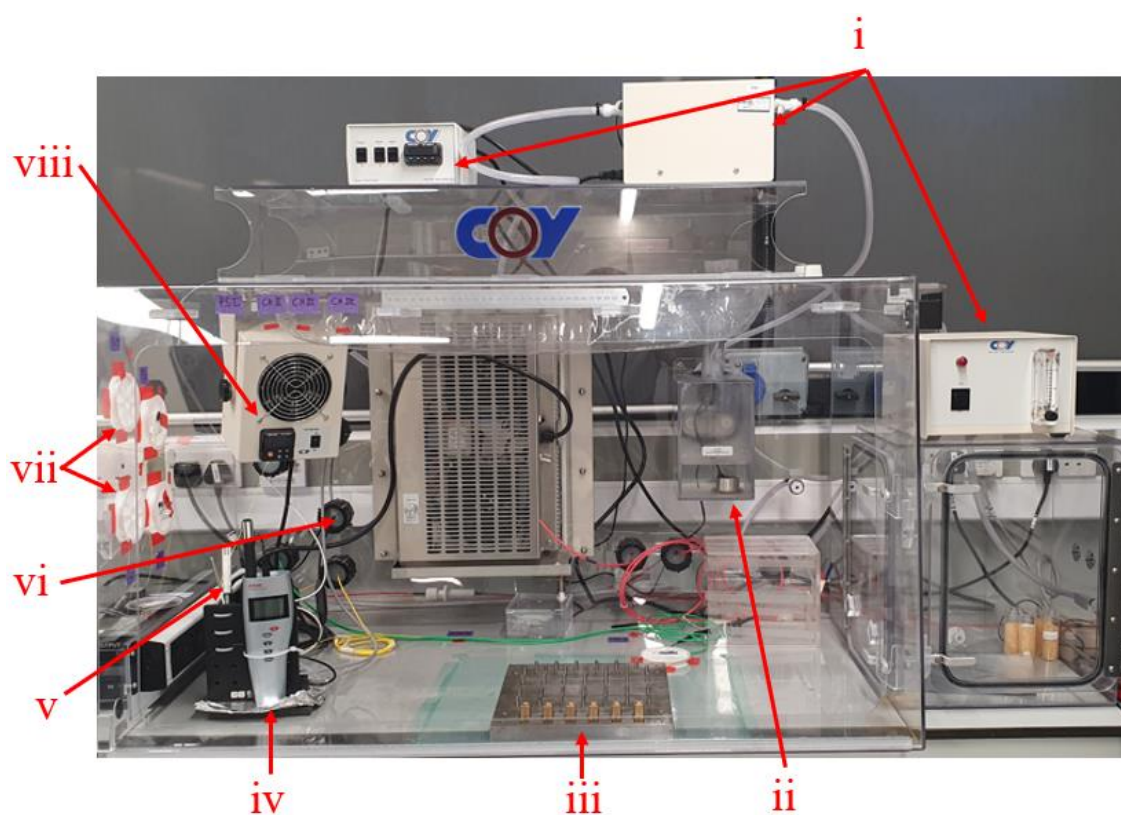
Figure 23 Glove box system including (i) humidity control array (Nitrogen), (ii) ultrasonic humidifier, (iii) SLJ rig, (iv) HP21, (v) glove box humidity and temperature sensors, (vi) ports, (vii) fibre holders, and (viii) temperature-controlled fan-heater.

Constructed from acrylic sheets, the glove box system features an external antechamber and a detachable front plate with a sealing lip. Temperature regulation is facilitated by a PID-controlled heating fan positioned inside the glove box, while humidity control consists of two components. Firstly, an ultrasonic humidifier within an enclosed water compartment is situated inside the glove box. Secondly, a nitrogen gas feeding system, including a flow regulator and

3.10.2 Glove box system for the temperature and humidity-controlled manufacture of adhesive joints

pump system, is located outside the glove box. Gas inlets and flushing valves for manual nitrogen gas flushing are positioned on the back side of the glove box. The nitrogen was fed from a compressed nitrogen gas bottle (200 bar). The regulator was adjusted to approximately 0.5 bar. The humidity control is managed by a PID controller located on the outside of the glove box. Internal temperature and humidity levels are monitored by sensors, and rubber membranes in the side sheets prevent internal overpressure. Although the temperature and humidity controllers lack data communication interfaces, an HP21 temperature/humidity sensor system is placed alongside the internal sensor assembly to facilitate data logging. Additionally, an automatic dehumidifier is installed inside (rear side) the glove box, but its lack of integration into the control circuit renders it inaccurate and unsuitable for use during experiments. Sealing ports on the rear side of the glove box system facilitate the integration of optical fibres. Cleaning of the glove box sheets is limited to isopropyl alcohol (IPA) due to their acrylic composition.

3.10.3. Glove box setup for curing experiment with embedded OFS

Prior to the experiments, the glove box was fitted with all the necessary fibres needed to assess the mentioned parameters. The intention was to lead the fibres into the box and store them there on reels attached to the inside sheets. The sensors were then spliced onto these fibres or directly manufactured inside the glove box. Table 6 illustrates the fibres/sensors and the interrogation equipment needed. Before commencing the experiments, the glove box was equipped with all the required fibres essential for the parameters specified in Section 3.10.1.

3.10.3 Glove box setup for curing experiment with embedded OFS

The objective was to introduce the fibres into the box and store them there on reels affixed to the inner sheets. Figure 24 illustrates a schematic of the sensors and interrogation equipment involved.
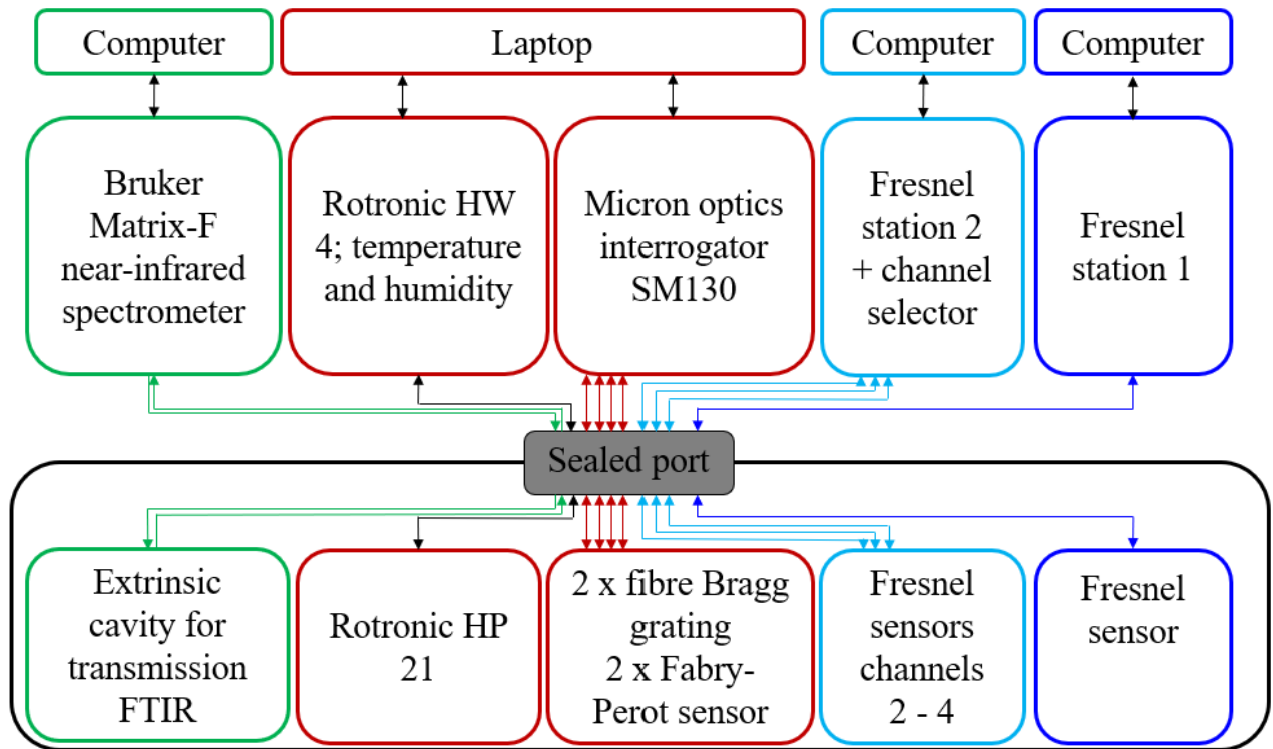
Figure 24 Glove box experiment with involved equipment. The glove box is indicated with the black frame at the bottom leading into the sealed port. The different colours indicate different measurement systems, meaning sensor(s) and interrogation equipment.

The sensors were subsequently spliced onto these fibres or fabricated directly within the glove box. Table 6 overviews the fibres/sensors and the interrogation equipment necessary for the experiments.

3.10.3 Glove box setup for curing experiment with embedded OFS

Table 6 Overview of fibres led into the glove box to enable splicing and manufacturing of listed optical fibre sensors.

Parameter	Sensor type	Interrogation equipment	Number of fibres
Chemical sensor	Transmission	FTIR	2
Refractive index	Intrinsic FP	SM130	1
	FRS	2 FRS stations	4
Temperature	FBG	SM130	1
Strain / shrinkage	Extrinsic FP	SM130	1
	FBG	SM130	1

The chemical sensor necessitated an inlet fibre to transmit light from the FTIR to the transmission sensor and another to lead back to the FTIR. Within the glove box, the chemical sensor, Fresnel reflection-based sensor, and extrinsic Fabry-Perot sensors were manufactured directly, while the FBGs and intrinsic FP sensors were merely spliced onto a single-mode fibre. Three experiments were conducted at isothermal temperatures of 30, 40, and 50 °C with 10% humidity, resulting in three batches of single-lap joints. Each batch comprised two lots of single-lap joints, with three joints in each manufacturing step, thus increasing the number of embedded sensors. Substrates were prepared according to Section 3.8, grit-blasted for 60 seconds over an area of l = w = 25.4 mm, with an overlap of l = 12.7 mm and a bond-line thickness set at 0.5 mm. As the sensors were affixed to the bottom substrates, adhesive was applied to the top substrates, pre-defined to a bond-line thickness of 0.9 mm. Data logging commenced approximately 2 minutes before joining the substrates and sealing the glove box. Temperature and humidity control were activated approximately 7.5 minutes after the start of

3.10.3 Glove box setup for curing experiment with embedded OFS

data logging to observe the equilibrating phase of the Fresnel reflection-based sensors. Upon completion of the curing experiments, the single-lap joints were retrieved, and the fibres were cleaved at a distance of around 10 cm from the bond area to facilitate resplicing.

3.10.3 Glove box setup for curing experiment with embedded OFS

4. Results and discussion – Optical fibre sensing

This chapter presents the application of several OFS techniques for monitoring adhesive curing and related processes. Fresnel reflection sensors were first calibrated and assessed, with investigations into normalisation, refractometer accuracy, and light source stability. Their performance was then compared with FTIR spectroscopy to evaluate cure kinetics.

Subsequently, *in situ* measurements were carried out within adhesive joints using a glove box system, enabling direct comparison between conventional FTIR, surface-mounted FTIR sensors, and Fresnel reflection sensors. Additional OFS approaches were also explored: FBGs for temperature and strain sensing, and FP-sensors for refractive index monitoring.

The results presented in this chapter, therefore, demonstrate the use of multiple OFS techniques, each applied to different aspects of adhesive characterisation, ranging from calibration studies to *in situ* multi-parameter monitoring.

4.1. Simultaneous calibration of multiple Fresnel reflection sensors

To calibrate a Fresnel reflection-based sensor, control over four key parameters was imperative: (i) the cleave angle, (ii) the ambient temperature, (iii) the refractive index of the analyte, and (iv) the spectral characteristics of the light source. The calibration process was bifurcated into two distinct phases. Initially, determining an optimal cleave angle was pursued through a series of experimental iterations, probing the response of the Fresnel reflection sensor (FRS) after cleavage under ambient conditions at room temperature. Subsequently, the response of the FRS

was observed under constant temperature conditions within the confines of the 60/ED refractometer. The ensuing subsection depicts the outcomes of these investigations in detail.

4.1.1. Normalisation of Fresnel reflection sensor output

In the context of this study, upon introducing the cleaved termination of the fibre into the medium, the alteration in refractive index can be detected through the intensity changes of light reflected from the interface formed between the cleaved-end of the fibre and its surrounding medium. The optical behaviour inherent in Fresnel reflection delineates itself through the variation in refractive indices between the core of the optical fibre and the medium encompassing the cleaved end-face. When light encounters the boundary of two dielectric media possessing refractive indices denoted as n_1 and n_2, at an angle of incidence θ_1, the coefficients governing the amplitudes of the reflected light intensities, both parallel (r_{ll}) and perpendicular ($r_\perp$) to the plane of incidence, can be mathematically articulated through the application of the Fresnel Equations.

$$r_\perp = \frac{n_1 cos\theta_1 - n_2 cos\theta_2}{n_1 cos\theta_1 + n_2 cos\theta_2} \qquad [16]$$

$$r_{ll} = \frac{n_2 cos\theta_1 - n_1 cos\theta_2}{n_2 cos\theta_1 + n_1 cos\theta_2} \qquad [17]$$

Where θ_1 represents the refraction angle upon entry into the second medium. Under the conditions of normal incidence ($\theta_1 = \theta_2 = 0$), the field amplitudes remain unaltered, and the reflectivity 'R' at the interface can be written as:

$$R = \left(\frac{n_1 - n_2}{n_1 + n_2}\right)^2 \qquad [18]$$

The cleaving angle assumes importance in facilitating FRS as it significantly impacts the intensity of reflection, as expounded by Equations (16 - 18). A computational simulation was

4.1.1 Normalisation of Fresnel reflection sensor output

executed to examine the variation of reflection intensity (R) concerning the cleaving angle (°) to elucidate the influence of the cleaving angle. n_1, representing the core refractive index of the SMF-28 fibre at 1550 nm, is set at 1.4682, whilst n_2, denoting the refractive index for air, is assumed to be 1. The resultant simulations are illustrated in Figure 25.
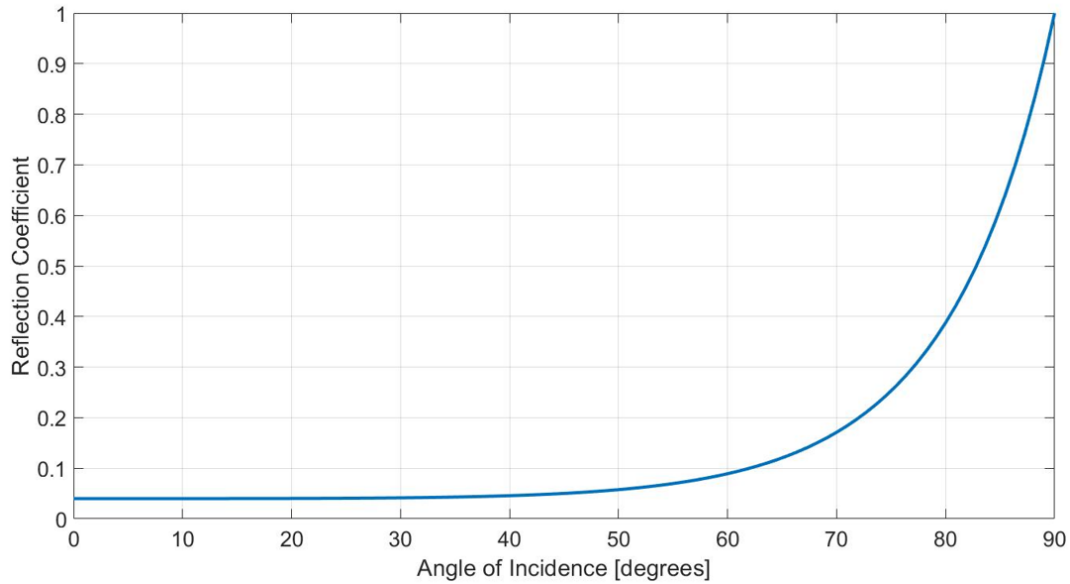
Figure 25 Simulation of the Fresnel reflection coefficient as a function of the cleave angle (angle of incidence).

A series of cleaving experiments was conducted to investigate the effect of the cleaving procedure on the resulting FRS response. The SMF-28 fibre under investigation was securely positioned within the cleaver, and data acquisition was initiated. Subsequently, the fibre underwent cleavage while changes in intensity were continuously monitored. In the context of the Fresnel station 2 being equipped with a channel selector, four distinct channels were subjected to investigation. Figure 26 represents the cleaving experiments conducted for each channel. A "band" of FRS responses was deemed appropriate for every channel. The tabulated data in Table 7 depicts the outcomes of these experiments alongside the determined band of suitable cleaves. Subsequent research was conducted with each sensor being facilitated within this predefined band to ensure consistency and comparability in the obtained results.

4.1.1 Normalisation of Fresnel reflection sensor output
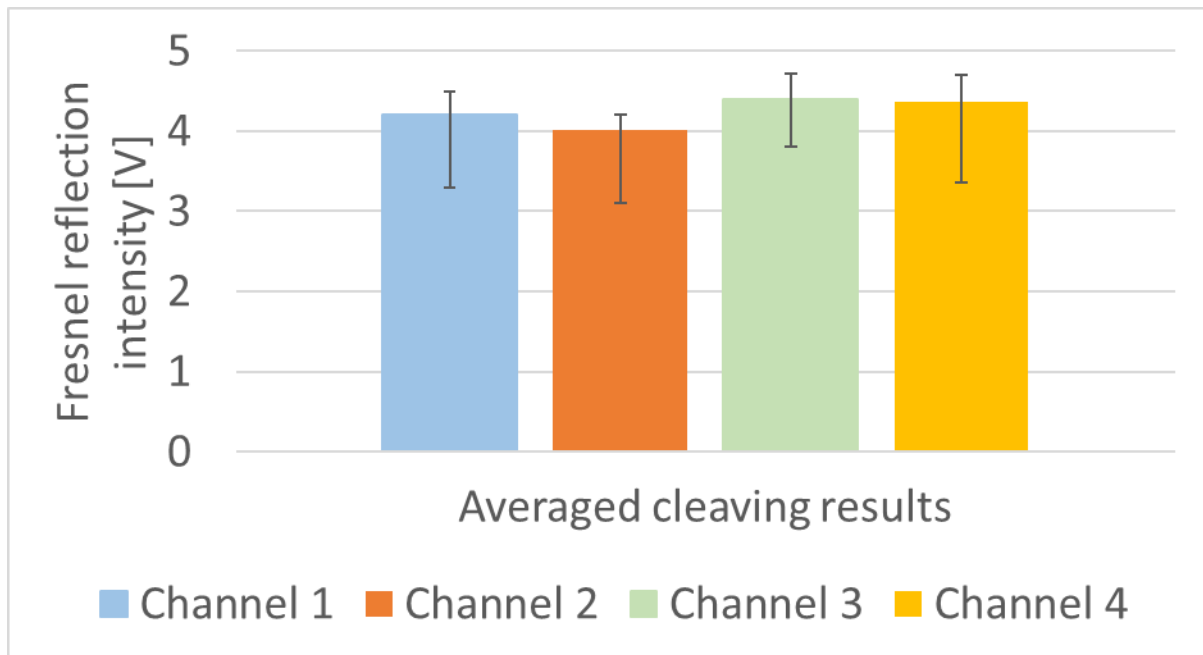
Figure 26 Results of the cleaving experiments for all four channels.

Channels one and two appear to have slightly lower averaged reflection intensities. The averaged intensity values for each channel indicate that the channels exhibit slightly different reflection intensities, which can be attributed to individual internal losses within each channel or their connectors.

Table 7 Cleaving values for all four channels in [V].

Cleave	Channel 1	Channel 2	Channel 3	Channel 4
1	4.5	4.2	4.7	3.4
2	4.4	4.0	4.6	4.6
3	4.2	4.0	4.7	4.0
4	4.5	4.2	4.3	4.4
5	3.3	4.0	4.6	4.6
6	4.4	3.9	3.8	4.6
7	3.6	4.2	4.7	4.0

4.1.1 Normalisation of Fresnel reflection sensor output

8	4.5	4.1	4.4	4.6
9	4.3	3.1	4.6	4.6
10	4.1	4.2	4.0	4.7
11	4.1	4.2	3.8	4.6
12	4.1	4.2	4.7	4.7
13	4.4	3.8	4.7	4.6
14	4.3	4.1	4.2	4.1
15	4.1	3.6	4.0	3.7
16	4.5	4.2	4.2	4.5
17	4.5	4.2	4.6	4.6
18	4.1	4.1	4.7	4.3
19	4.2	4.2	4.6	4.6
20	3.8	4.2	4.2	4.1
21	4.4	3.9	4.2	4.5
Average	4.2	4.0	4.4	4.4
Error max	0.3	0.2	0.3	0.3
Error min	0.9	0.9	0.6	1.0
Appropriate cleave band	4.5 – 4.3	4.2 – 4.1	4.7 – 4.5	4.7 – 4.5

4.1.1 Normalisation of Fresnel reflection sensor output

For determining appropriate cleaving quality, the maximum reflection intensities were considered as most interesting as they indicate what the best-reflected intensity, and therefore, the best-cleaved fibre interface, is. The overall deviation results from the cleaving process depend on parameters such as (i) the cleaving blade, (ii) the fibre stripping or de-coating and (iii) the fibre alignment within the cleaver. As the blade is assumed not to have changed significantly in quality throughout these tests, it may be concluded that the deviation is due to how the fibre was aligned. A good indicator for variation is the alignment groove of the cleaver, which is designed to hold the fibre (125 microns), including the cladding (250 microns). As the cladding has to be removed prior to cleaving, the fibre always has 125 microns of space to move, which could cause deviation. As inappropriate cleaves needed to be avoided, an appropriate band of reflection intensities needed to be established, as illustrated in Table 7. To enable cross-comparability of data, the data needed to be normalised as illustrated in Equation [19]:

$$R_{norm} = \frac{R_{fluid}}{R_{air}} \qquad [19]$$

Where R_{norm} represents the normalised reflectance intensity, R_{fluid} is the reflection intensity of the analyte, and R_{air} presents the reflection intensity of air. This normalisation is conducted to compensate for minor deviations regarding the cleaved end faces of the sensors and potential dark current falsifications due to the intensity-based photodetector system.

4.1.2. Assessment of the accuracy of the 60/ED refractometer

In order to establish the 60/ED measurement accuracy, refractive index oils in the refractive index range of 1.40 to 1.70 were applied. Two K-type thermocouples were positioned outside of the prims assembly to monitor the temperature. The temperature was adjusted to 25 °C with

a monitored deviation of ±0.2 °C. The prism was allowed to equilibrate to the temperature for 10 minutes before starting the oil application. Each measurement was executed three times to establish a measurement deviation. After the experiments were conducted, the measured refractive index values were plotted against the manufacturer-stated refractive index of the oils as illustrated in Figure 27.
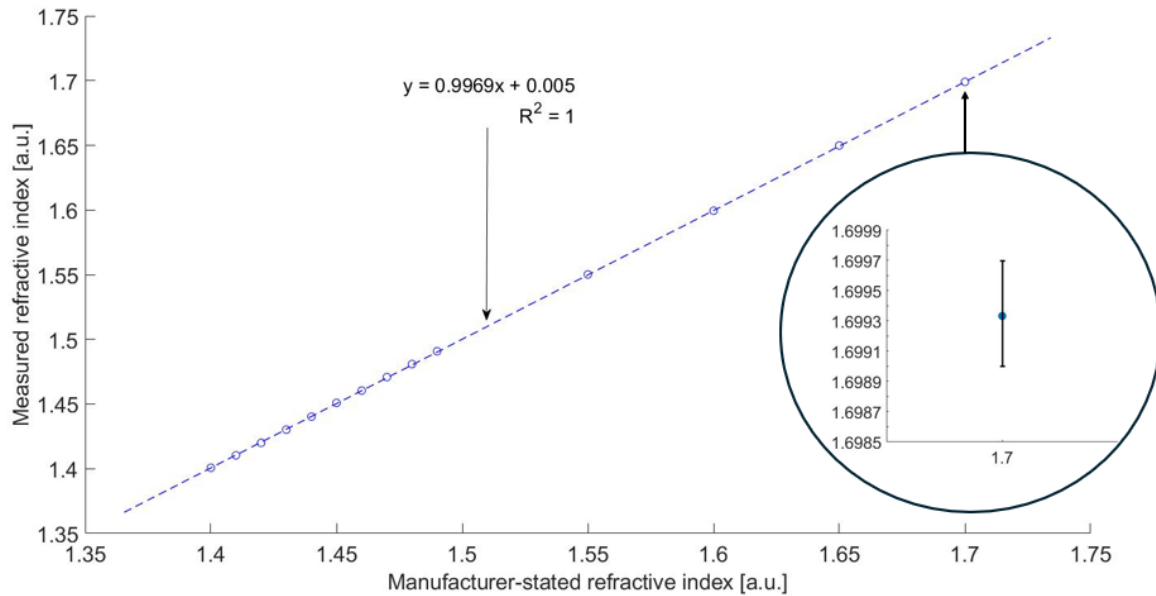
Figure 27 Linearity of refractive index measurements with magnified view on the error bar of the 1.7 RI measurement.

The linearity of the plotted results illustrates a high accuracy of the instrument. The error bars are included within the plot but the deviation was too insignificant to be seen on the plot. Therefore, the numerical values are stated in Table 8.

Table 8 Refractive index measurements include the calculated average and the calculated deviation.

Oil	Trial 1	Trial 2	Trial 3	Average	Deviation
1.4	1.40072	1.40072	1.40072	1.40072	0
1.41	1.41040	1.41040	1.41040	1.41040	0
1.42	1.42003	1.42003	1.42051	1.42019	±0.00032

4.1.2 Assessment of the accuracy of the 60/ED refractometer

1.43	1.43020	1.43008	1.43008	1.43012	±0.00004
1.44	1.44024	1.44052	1.44024	1.44033	±0.00019
1.45	1.45088	1.45041	1.45041	1.45057	±0.00031
1.46	1.46044	1.46021	1.46044	1.46036	±0.00015
1.47	1.47083	1.47060	1.47037	1.47060	±0.00023
1.48	1.48089	1.48066	1.48066	1.48074	±0.00015
1.49	1.49082	1.49082	1.49105	1.49090	±0.00015
1.55	1.55016	1.55037	1.55037	1.55030	±0.00014
1.6	1.59941	1.59905	1.59905	1.59917	±0.00024
1.65	1.64984	1.65076	1.65076	1.65045	±0.00061
1.7	1.69904	1.69926	1.69972	1.69934	±0.00038

The maximum deviation was seen to be in the range of ±0.00038 RI, which concludes an accurate system and, therefore, an appropriate validation technique for the FRS calibration.

4.1.3. Investigation of the Fresnel reflection sensor light source stability

In order to characterise the Fresnel reflection-based system, the light source stability needed to be investigated first to quantify possible light source-induced intensity changes on the Fresnel sensors. As the temperature-controlled laser driver housed a superluminescent diode with a central wavelength of 1550 nm, the output stability was monitored using a PM100D intensity meter (Thorlabs Ltd, UK) in conjunction a S122C external photodiode with a spectral range of

4.1.3 Investigation of the Fresnel reflection sensor light source stability

700 to 1800 nm (Thorlabs Ltd, UK). The intensity meter–laser assembly was positioned on an optical bench at room temperature, and the laser output was measured for 25 hours. This duration was chosen to replicate the estimated maximum cross-linking time for the FRS experiments. A FRS was, therefore, attached to a thermocouple. The FRS was positioned with an overlap of approximately 10 mm to avoid any FRS disturbance on the temperature reading. The data logging was initiated with the light source switched off to be able to investigate the behaviour of the light source after being switched on. After approximately 5 minutes the light source was switched on, the power meter and the FRS simultaneously increase in their readings.

Data logging commenced with the light source in the off position, enabling an examination of its behaviour upon activation. After a period of approximately five minutes, the light source was activated. As shown in Figure 28, there was a concurrent increase in the readings from the power meter and the FRS.
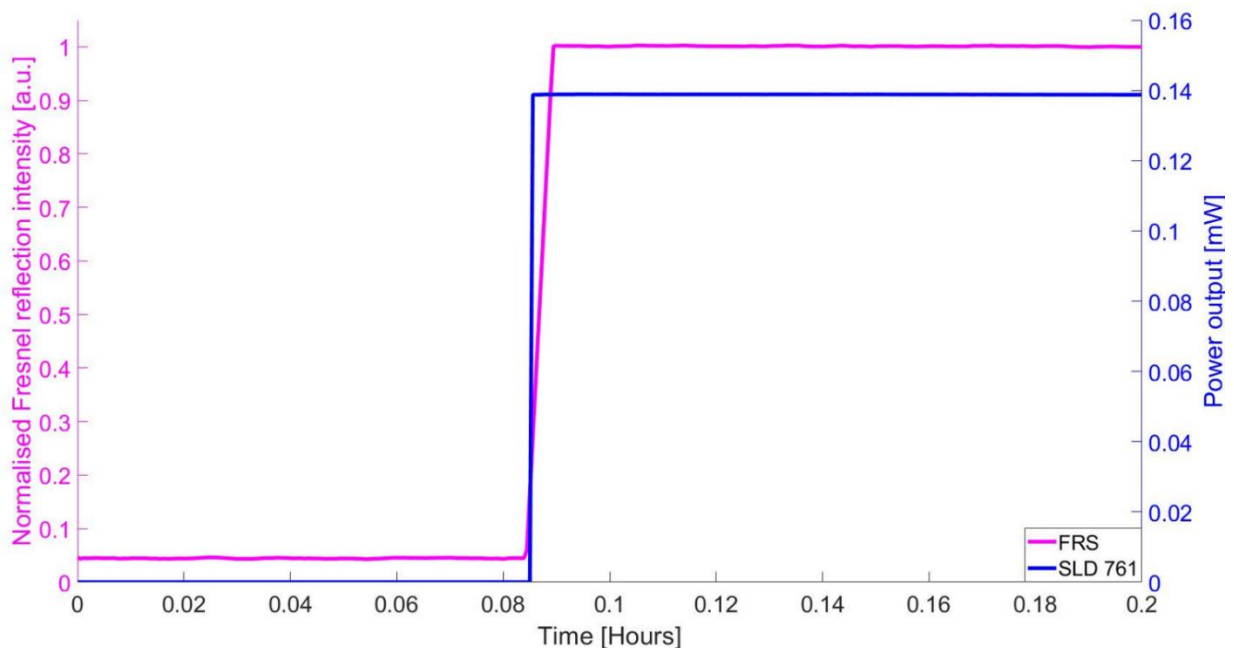
Figure 28 FRS and power meter during the "switch-on" of the laser.

4.1.3 Investigation of the Fresnel reflection sensor light source stability

As illustrated in Figure 29, upon activation, the light source exhibits a slight initial spike before stabilising after approximately one minute. Subsequently, the power output and temperature appear to follow a similar trend. Given that the power output of SLEDs is known to be sensitive to temperature changes (Holc et al., 2010, Park et al., 2006, Skalský et al., 2022), this behaviour may be attributed to a minor overcompensation by the laser diode driver.
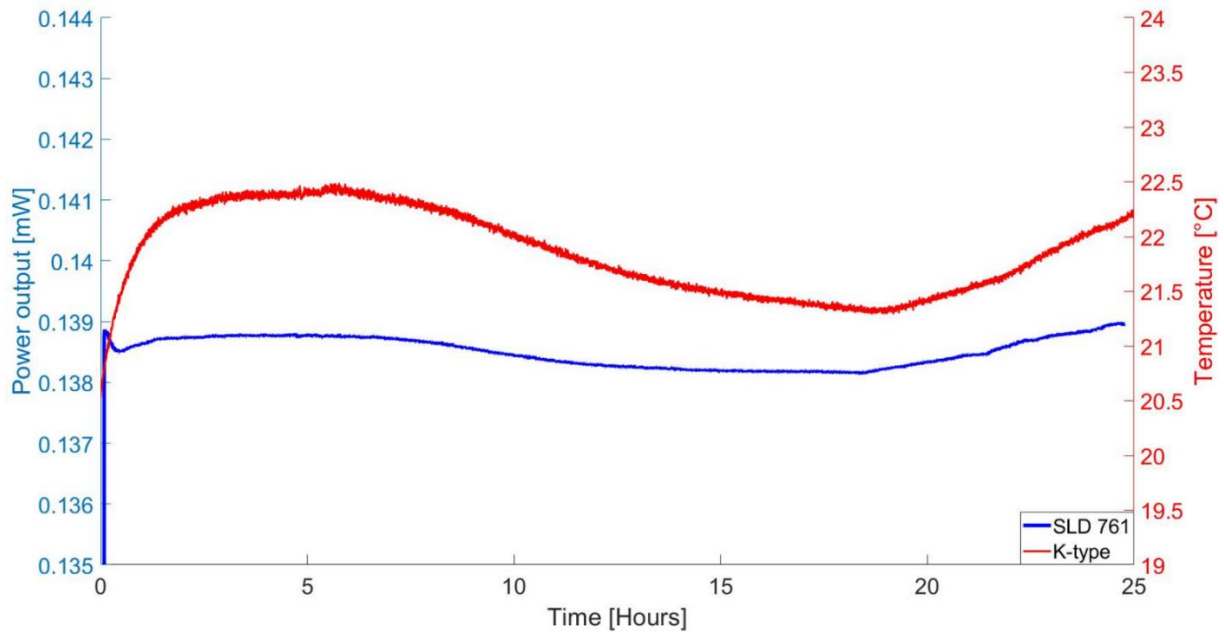
Figure 29 Power output vs measured temperature.

As illustrated in Figure 30, the Fresnel reflection intensity initially experiences a spike corresponding to the activation of the light source, subsequently stabilising within approximately five minutes. The FRS readings then remain quasi-constant until they begin to increase, correlating with a rise in room temperature after approximately 22 hours of the experiment. The evolution of the FRS signal and the temperature are illustrated in Figure 30.

4.1.3 Investigation of the Fresnel reflection sensor light source stability
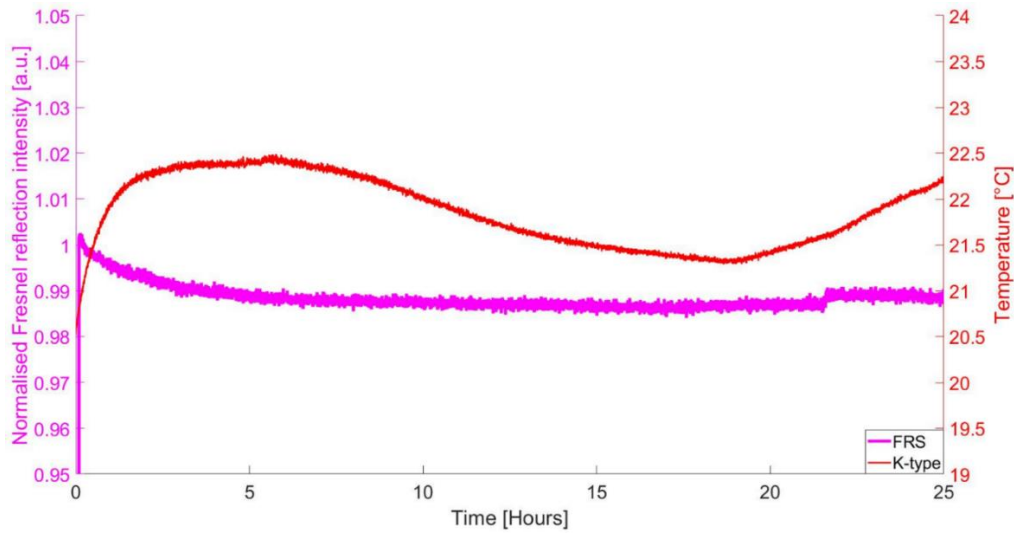
Figure 30 Fresnel reflection sensor plotted against the measured temperature.

Table 9 presents the average deviation of the sensor readings. The FRS exhibited a deviation of 1.186% throughout the experiment, accompanied by a temperature fluctuation of ±1.23 °C. This underscores the necessity for precise temperature control in subsequent experiments involving the FRS. The ambient temperature influences both the light source and the FRS by affecting the power supply and altering the refractive index at the sensor interface. Additionally, a light source equilibration time of 30 minutes was chosen for all following experiments to ensure a stable power output of the light source.

Table 9 Averaged data of the FRS, power meter and thermocouple readings during the experiment.

Parameter	Average	Deviation	Deviation in %
Power output in mW	0.1385	± 0.000489	0.353
Normalised FRI	0.98842	± 0.018443	1.186
Temperature in °C	20.39	± 1.23	6.038

4.1.3 Investigation of the Fresnel reflection sensor light source stability

4.1.4.   Fresnel reflection sensor calibration

To calibrate the FRS sensors, they were interrogated within the prism of the 60/ED refractometer. Therefore, the fibres were fixed onto the prism, and refractive index calibration oils were applied to the bottom prism. Two K-type thermocouples were positioned outside the prism assembly to monitor the temperature. The temperature was adjusted to 25 °C with a monitored deviation of ±0.2 °C. The prism was allowed to equilibrate to the temperature for 10 minutes prior to starting the oil application. The results are illustrated in Figure 31.

The graph contains the following fit equations:

$$\text{Channel 1} = -1.675x^3 + 10.24x^2 - 19.21x + 11.43; \quad R^2 = 0.9994$$
$$\text{Channel 2} = -2.378x^3 + 13.44x^2 - 24.07x + 13.88; \quad R^2 = 0.9997$$
$$\text{Channel 3} = -2.401x^3 + 13.54x^2 - 24.20x + 13.95; \quad R^2 = 0.9997$$
$$\text{Channel 4} = -2.247x^3 + 12.83x^2 - 23.11x + 13.39; \quad R^2 = 0.9997$$
$$\text{Simulation} = -0.06897x^3 + 0.4189x^2 - 0.7839x + 0.4663; \quad R^2 = 1$$
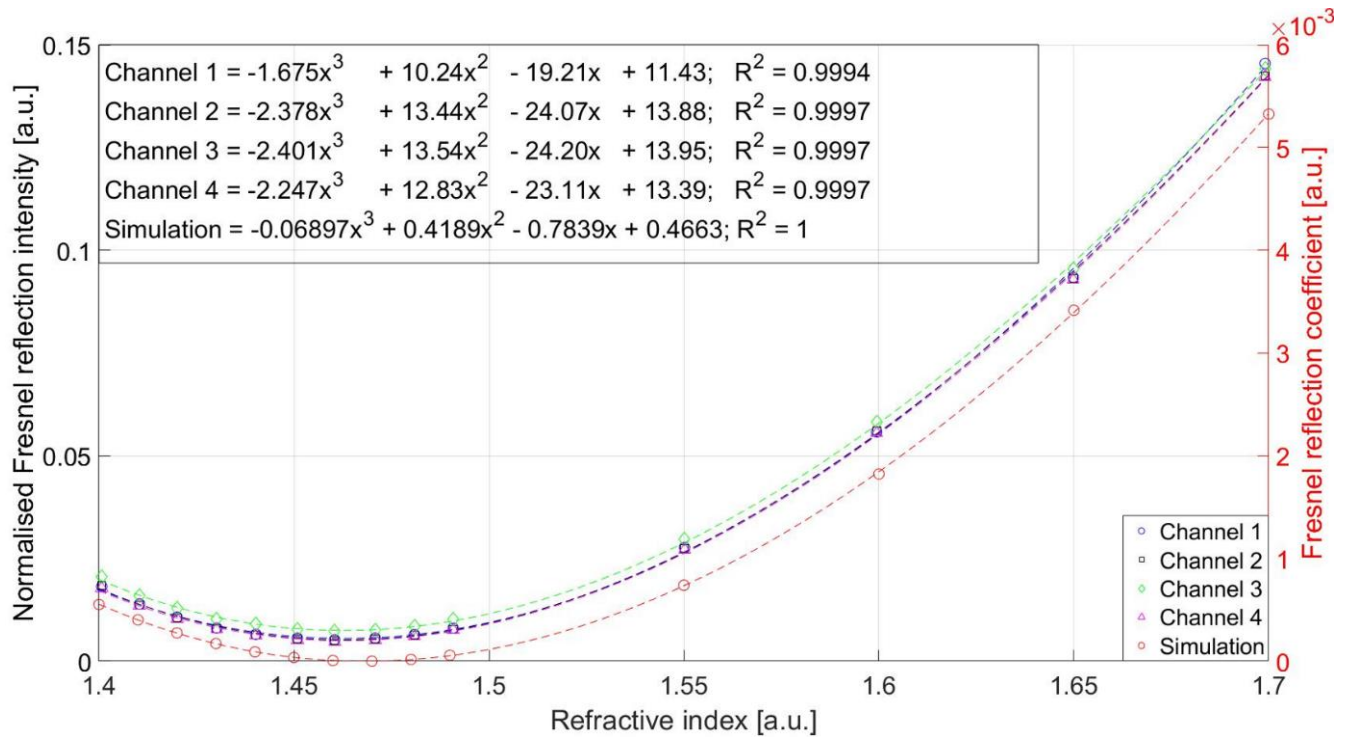
Figure 31 FRS calibration results, including curve fits and the simulated Fresnel reflection coefficient.

As described in Equation [18], the FRS response over the refractive index range of 1.40 to 1.70 is of a parabolic nature. The behaviour of the reflection coefficient with the vertex depicts the refractive index of the waveguide core. Hence, the vertex being an exception, each reflection coefficient value can be allocated as two refractive indices, which does correlate with literature (Oelhafen et al., 2017). Thus, a definite increase in the refractive index would lead to a coefficient decrease below the core index and vice versa. In conclusion, a sensor calibration

4.1.4 Fresnel reflection sensor calibration

needs to be conducted for a Fresnel reflection-based system to (i) account for specific system-induced attenuation losses and (ii) enable the designation of known refractive index values to the responding reflection coefficients. The normalised FRS responses show an excellent correlation between each other and the simulation. The offset may be attributed to a constant minor reflection within the Fresnel reflection system. Stray light coupled from the refractometer into the OFS can be excluded as the sodium light source emits 589.3 nm light and the wavelength range of the photodetector is 700 – 1800 nm.

As the calibration is done with reference oils measured at 589.3 nm the measured Fresnel sensor values are correlated to the calibration light source and not to the 1550 nm spectrum of the Fresnel sensor itself. It was, therefore, decided not to express the Fresnel sensor reading as a function of refractive index. For a correct conversion, the optical coefficients of the analyte need to be known.

4.2. Quantitative comparison of FTIR-FRS cross-linking kinetics

This chapter presents a comparative analysis of cross-linking kinetics using FTIR and FRS. FTIR enables direct chemical monitoring of functional group conversion, while FRS provides an optical response linked to refractive index changes during curing. Both methods were applied under identical isothermal conditions to assess their sensitivity and correlation in tracking the polymerisation process.

4.2.1. Evaluation of temperature nonuniformity within the cuvette holder

As the temperature-controlled cuvette holder was intended to house the 1 mm path length cuvette for the hyphenated FRS-FTIR experiments, the influence of room temperature on the cuvette needed to be investigated as well as the temperature discrepancy within the system as pointed out by King (King, 2018a). The cuvette holder has a closed-loop temperature control which consists of a thermoelectric heater/cooler in combination with a reference temperature sensor. The location of the sensor is not stated in the technical documentation but it was assumed that it does sit near to the actuator and therefore in the bottom region of the cuvette holder. This would result in a resulting spatial temperature gradient within the cuvette with the axis that coincides with the height of the cuvette being influenced the most as it linearly extends from the heat source if the bottom of the cuvette is defined as 0-point. Thus, a prepared 1 mm path-length cuvette was filled with only the Loctite EA9466 resin (part A) up to ~ 40 mm height. The cuvette was positioned in the cuvette holder in combination with the 9 mm spacer. Three K-type thermocouples were then positioned at three different heights within the cuvette as can be seen in Figure 32. A temperature scan was conducted ranging from 70 to 10 °C (set values on the temperature controller) in increments of 10 plus 25 °C as an additional point.

Each temperature was dwelled for at least 15 minutes to avoid thermal lag influencing the gradient calculation.
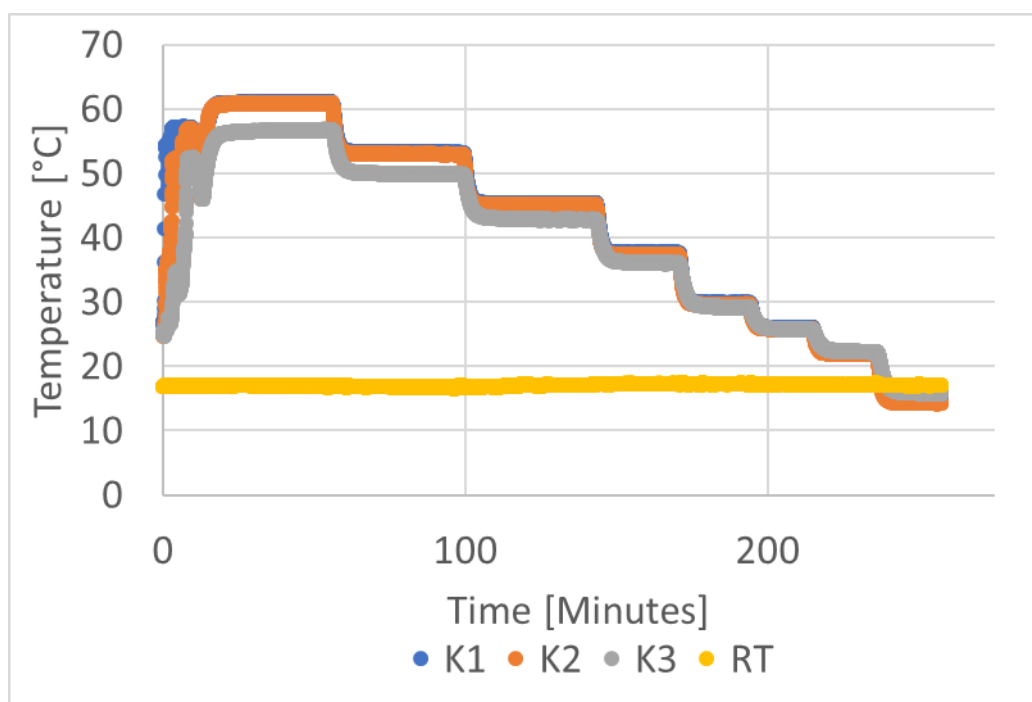
Figure 32 Temperature ramp experiment to establish the temperature gradient.

As seen in Figure 32, the cuvette was initially heated to (set temperature) 70 °C, which none of the sensors reached. The monitored room temperature during the experiment was 17.07 ±0.56 °C. The monitored temperatures were averaged during this duration to assess the temperatures during the ramp dwells. The measured temperature values of each sensor are presented in Table 10.

4.2.1 Evaluation of temperature nonuniformity within the cuvette holder

Table 10 Overview of measured temperatures of the three K-type thermocouples in [°C].

Set Temperature	K1	K2	K3
10	14.599	14.337	15.868
20	22.192	21.972	22.374
25	26.025	25.818	25.786
30	29.866	29.623	29.225
40	37.647	37.374	36.141
50	45.327	45.102	42.886
60	53.238	53.034	49.937
70	61.023	60.883	56.680

To better illustrate the gradient within the cuvette, three 2D maps were created using MATLAB

for three exemplary temperatures, namely 70 °C, 50 °C and 30 °C as illustrated in Figure 33.
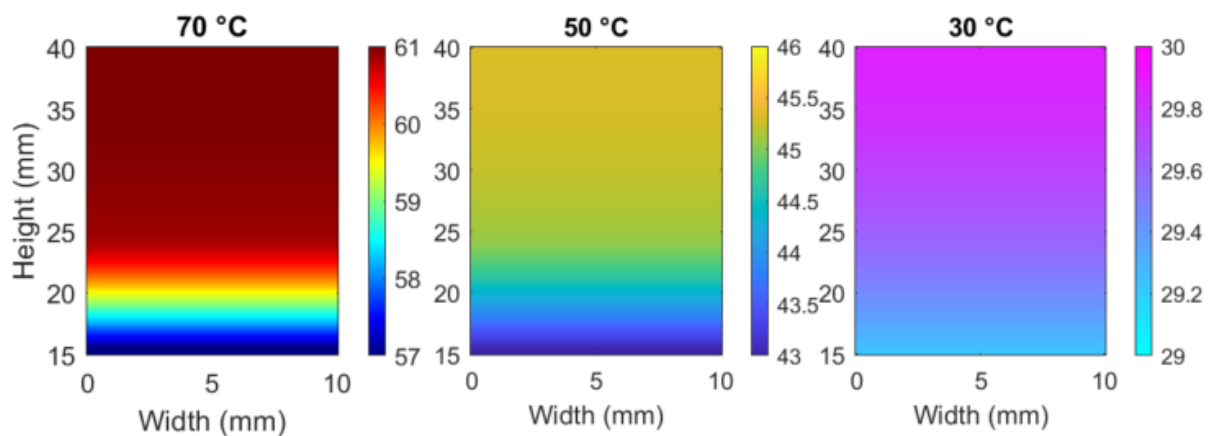
Figure 33 Spatial temperature gradients within the cuvette at 70, 50, and 30 °C.

The temperature maps show a clear vertical gradient, with lower temperatures at the top of the

cuvette due to heat loss to the surrounding environment. The gradient is steeper at higher

4.2.1 Evaluation of temperature nonuniformity within the cuvette holder

temperatures, indicating greater thermal dissipation at the top. At lower temperatures, the system is more thermally uniform, as heat loss is reduced, leading to better equilibrium. In order to illustrate the temperature discrepancy between the set and measured temperature for each sensor, a ratio was calculated using the following equation:

$$T_{ratio} = \frac{T_{measured}}{T_{set}} \qquad\qquad [20]$$

Where T_{ratio} represents the temperature ratio, $T_{measured}$ is the measured temperature of the analyte, and T_{set} presents the set temperature value of the temperature controller. The resulting ratios are presented in Figure 34. As can be seen, the measured temperatures between 70 and 40 °C are not reaching the set temperature ($T_{ratio} < 1$), hit a turning point at 30 °C ($T_{ratio} \sim 1$) and then overshoot the set temperature ($T_{ratio} > 1$). This behaviour indicates a room temperature influence on the system as an offset between the reference sensor of the cuvette and the thermocouples would have been expected to be of a more linear nature. As future experiments were planned to be conducted between 20 and 50 °C, this discrepancy could be compensated for on the temperature controller prior to each experiment taking the room temperature into consideration.
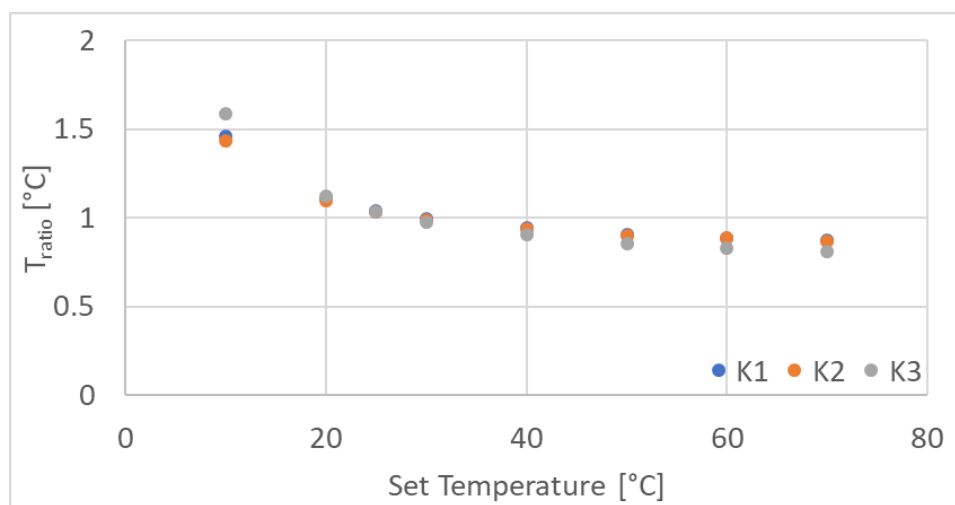
Figure 34 Determined temperature ratios during the non-uniformity investigation.

4.2.1 Evaluation of temperature nonuniformity within the cuvette holder

In order to visualise the spatial temperature gradient, the measured temperature was plotted against the set temperature as illustrated in Figure 35. From these temperature gradients maps it can be seen that the gradient between the sensors for a set temperature does become larger on both sides of the vertex point of approximately 25 °C.

K1 = 0.7746x + 6.707
R² = 1
K2 = 0.7759x + 6.435
R² = 1
K3 = 0.6835x + 8.8037
R² = 0.9999
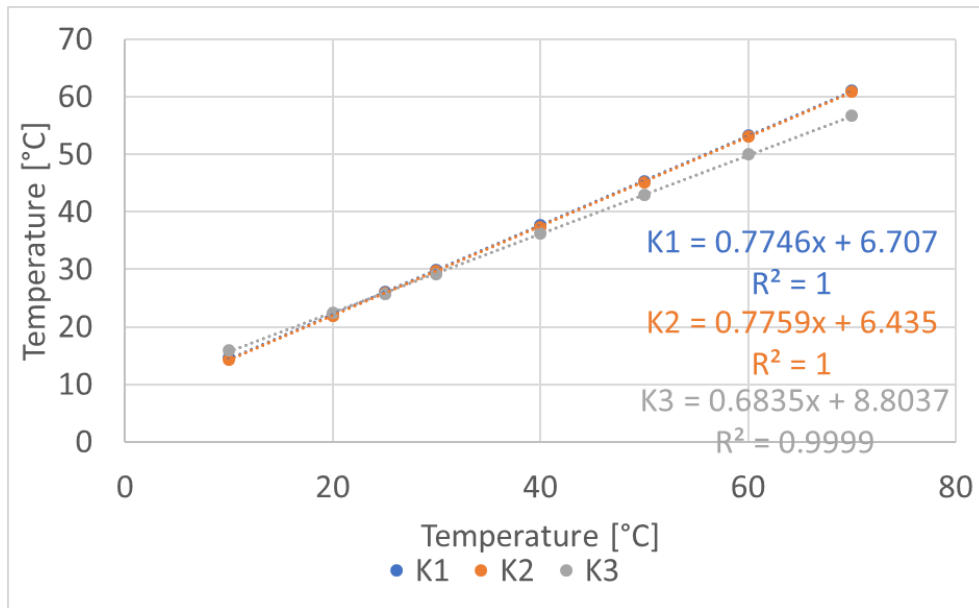
Figure 35 Determination of the temperature behaviour dependent on the thermocouple submersion depth within the cuvette.

The temperature response for K1 and K2 does have nearly the same slope (K1 = 0.7746; K2 = 0.7759) and y-offsets (K1 = 6.707; K2 = 6.435), indicating a similar temperature evolution. K3 (the most upward thermocouple) does behave slightly differently. Below and above 25 °C, K3 has a larger y-offset which is evidence for the room temperature having a larger effect on the temperature reading compared to the other two thermocouples. As a next step the, the temperature differences were put into relation by calculating the delta between two

4.2.1 Evaluation of temperature nonuniformity within the cuvette holder

thermocouples and then dividing it by the distance between the sensors. The results are plotted in Figure 36.
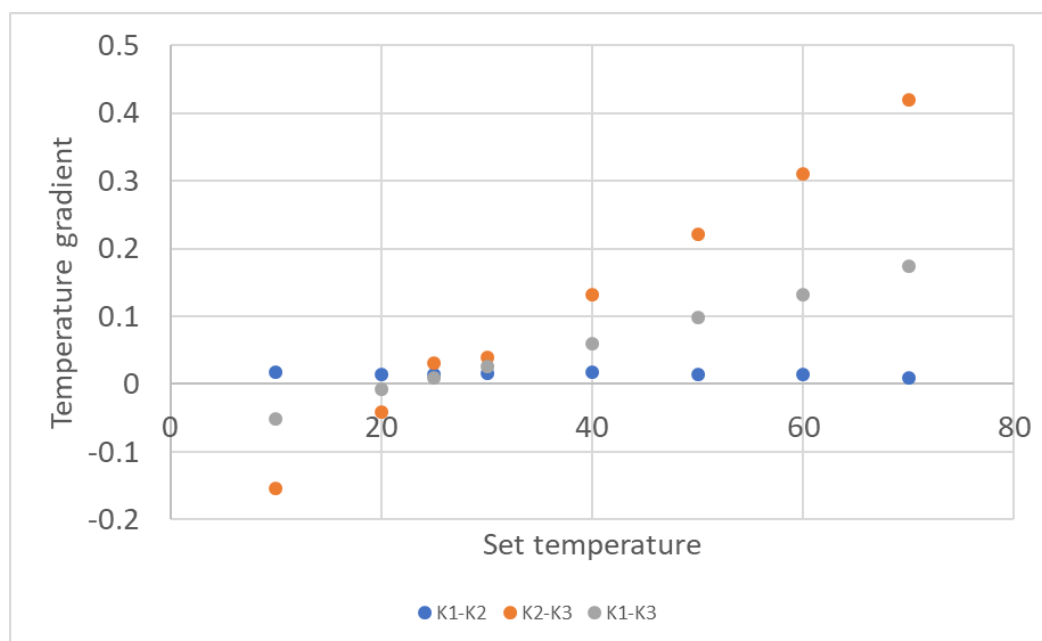
Figure 36 Temperature gradients within the cuvette at different submersion depths.

The gradient between K1 and K2 seems to be of a quasi-linear nature, indicating that the influence of room temperature within the distance of K1 and K2 is negligible. The most prominent gradient could be observed between K2 and K3, indicating that the room temperature influence above K2 is of significant nature. The overall gradient (K1 – K3) was found to behave as the average of both previous gradients. It was therefore decided, that OFS need to be submerged at least 25 mm within the cuvette to avoid significant falsification of temperature measurements due to the influence of the room temperature.

Another point of interest was the influence of the additional light coupled into the cuvette during the experiments. As the light source of the Fresnel station operates at a central wavelength of 1550 nm, it could further agitate the primary and secondary amine combination peak during the curing experiments and, therefore, falsify the FTIR results. To convert the

4.2.1 Evaluation of temperature nonuniformity within the cuvette holder

FRS central wavelength from the spectral to the wavenumber domain, the following equation was used:

$$\tilde{\nu} = \frac{1}{\lambda},$$ [21]

where $\tilde{\nu}$ is the wavenumber and λ is the wavelength.

When converting the FRS light source from the spectral (1550 nm) into the wavenumber domain (6452 cm^{-1}), it becomes evident that the FRS light source central wavelength lies within the wavenumber range of the primary and secondary amine peak of the Loctite EA 9466 system (peak assignment in Section 4.2.2). To investigate the effect of the Fresnel light source on the amine and the resin, two additional experiment were conducted. Two FRS were directly attached to a K-type thermocouple and submerged into a depth of 40 mm within a cuvette. The first experiment was using a cuvette filled with Loctite EA9466 resin (part A), and the second was filled with the hardener (part B). The temperature-controller was switched off and the water bath set to 25 °C to enable tracing temperature changes within the cuvette. The results of both experiments are illustrated in Figure 37 and Figure 38.

4.2.1 Evaluation of temperature nonuniformity within the cuvette holder
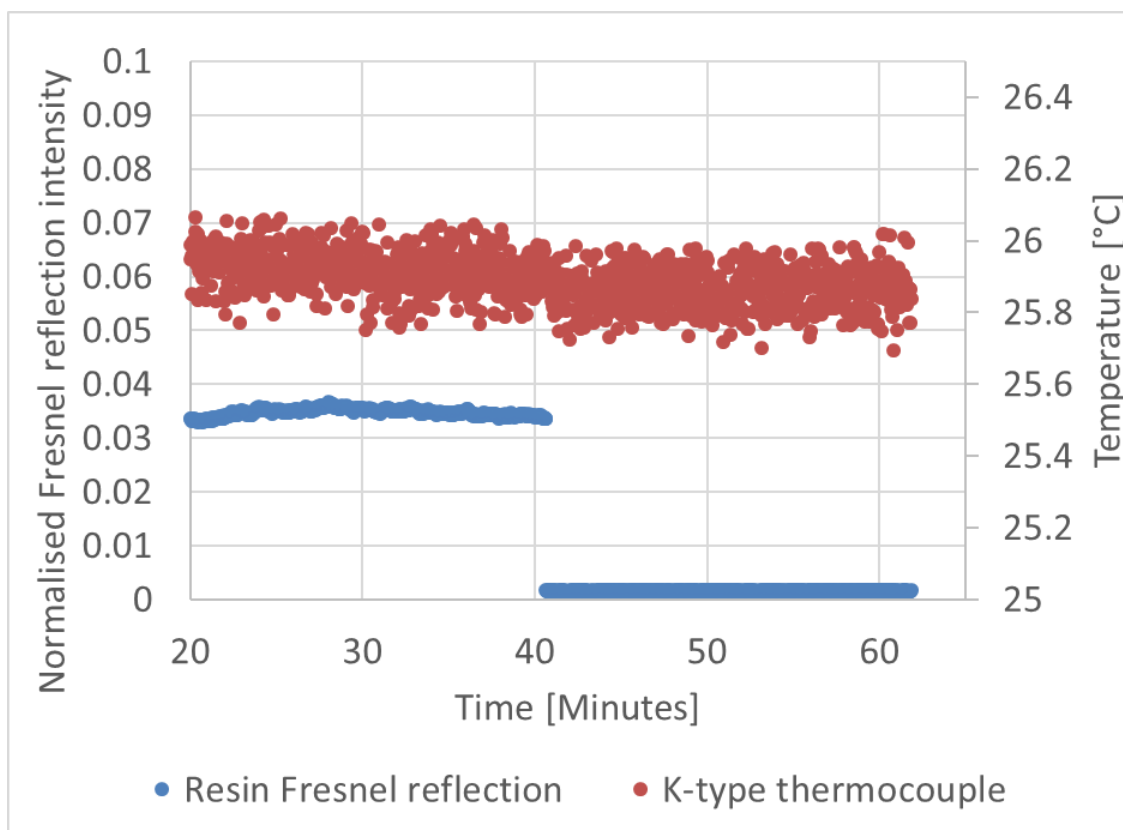
Figure 37 Determination of the effect of the FRS light source on the resin.

Initially, the FRS was switched on and then the data was logged for approximately 40 minutes. After that, the FRS light source was switched off, which can be seen on the FRS trace. As can be seen in the illustrations, the switching off of the FRS light source causes an immediate drop in temperature, but the drop is more prominent in the hardener compared to the resin. To be able to quantify the temperature drop, the average temperatures before and after switching off the FRS light source were determined in order to calculate the temperature delta (ΔT) for both analytes.

4.2.1 Evaluation of temperature nonuniformity within the cuvette holder
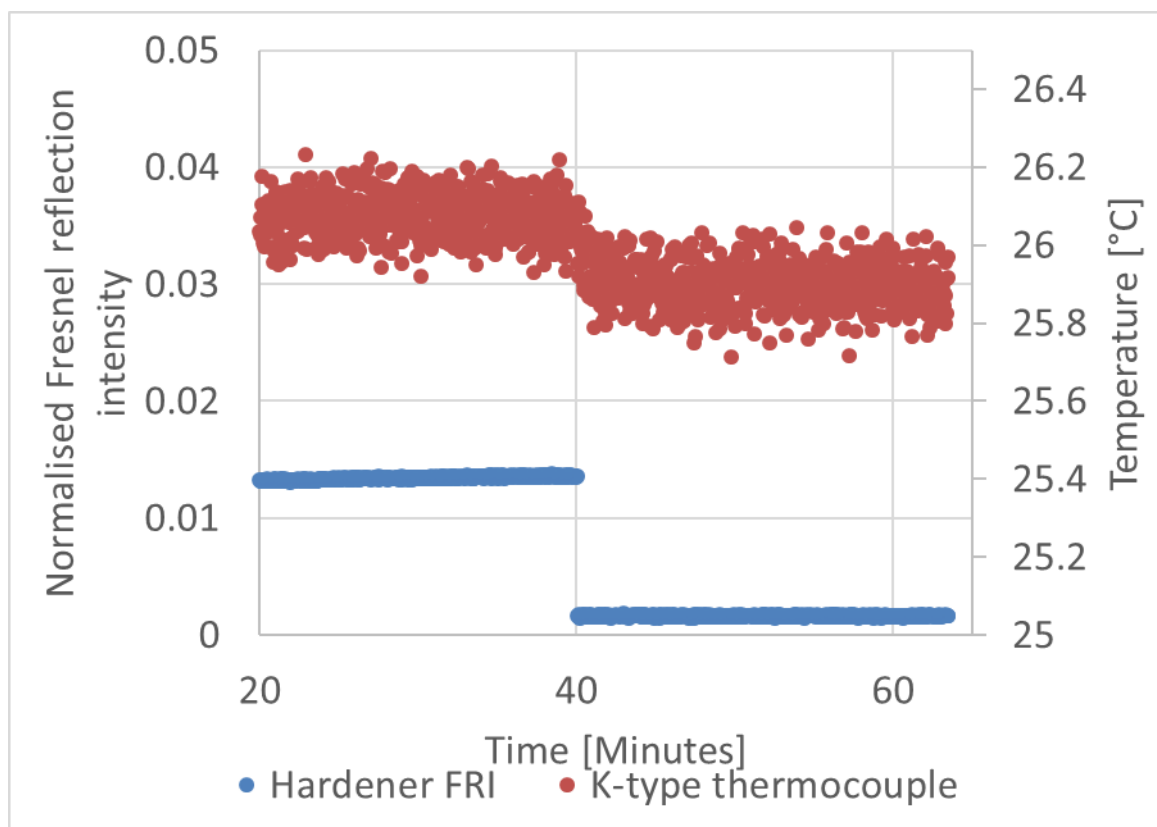
Figure 38 Determination of the effect of the FRS light source on the hardener.

The calculated averages and ΔT for the two experiments are illustrated in Table 11. The temperature drops for both systems are minimal, but the temperature drop of the hardener compared to the resin is threefold, indicating the functional groups of the hardener being sensitive to the 1550 nm light source.

Table 11 Results of the analysis of the influence of the FRS light source on the resin and the hardener.

Analyte	T pre [°C]	T post [°C]	ΔT [%]
Resin	25.923	25.863	0.23
Hardener	26.075	25.902	0.66

This can be explained by the relationship between the central wavelength of the light source and the combination bands of primary and secondary amines. These functional groups exhibit

4.2.1 Evaluation of temperature nonuniformity within the cuvette holder

characteristic absorption bands where vibrational modes occur. When the incident light matches these absorption bands, the molecules absorb energy, leading to an increase in absorption at those wavelengths (Osborne, 2006, Cholake et al., 2014).

The interaction between the central wavelength of the light source and the combination bands of primary and secondary amines results in the excitation of specific vibrational modes within these functional groups. As these modes absorb energy from the incident light, increased absorption occurs, particularly at wavelengths around 6580 cm^{-1}, as identified in the literature (Billaud et al., 2002). This absorption leads to a localised increase in energy, which may manifest as a rise in temperature within the material. Consequently, when the light source is turned off, a more pronounced temperature drop is expected due to the dissipation of the absorbed energy.

So, when the light source is switched off, a more significant drop in temperature is expected for the hardener, which is confirmed by the obtained data. In conclusion, for these experiments, it was decided to submerge the FRS sensors for a hyphenated FRS - FTIR run at 25 mm depth as the temperature gradient between the FTIR interrogation area (~ 40 mm depth) and FRS interrogation area (~ 25 mm depth) was found to be minimal (maximum deviation between 20 and 50 °C was found to be ±0.273 °C).

4.2.2. Fourier transform infrared spectroscopy

To characterise the curing kinetics of the Loctite EA 9466 adhesive, the decrease in absorbance of the epoxy functional groups at 4530 cm^{-1} and 6080 cm^{-1} was tracked over time and at varying temperatures (Duemichen et al., 2015). The consumption of the amine hardener was monitored through the primary absorbance band at 4925 cm^{-1} (Huang et al., 2020) and the combined primary and secondary amine vibrations at 6570 cm^{-1} and 6670 cm^{-1} (Yamasaki and Morita,

4.2.2 Fourier transform infrared spectroscopy

2014). Typical spectra for both the as-mixed resin and the cross-linked system after 160 minutes at 50 °C are shown in Figure 39. The spectral peak assignments for Loctite EA 9466 are provided in Table 12.
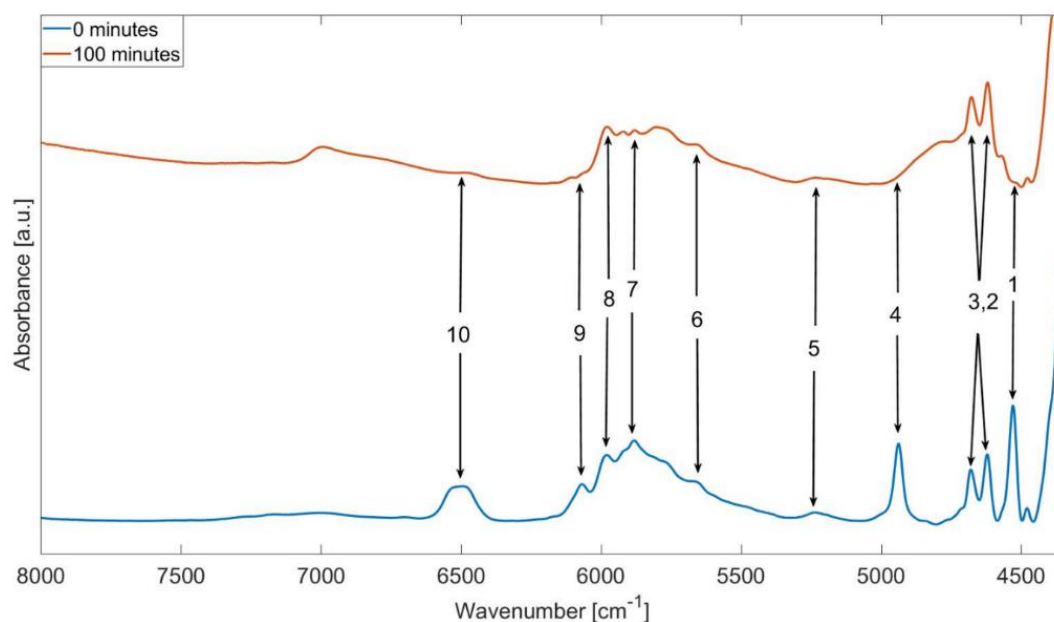
Figure 39 Loctite EA 9466 absorbance spectra pre- and post-cure at 50 °C.

Table 12 Peak assignment for the Loctite EA 9466 adhesive(Powell et al., 1996, Stjohn and George, 1992, Mijovic and Andjelic, 1995).

Peak label	Wavennumber in cm^{-1}	Peak assignment
1	4530	Epoxy combination band (C-H stretching and epoxy ring breathing.
2,3	4620, 4677	Aromatic combination band (C-H stretching).
4	4935	Primary amine combination band (N-H stretching and bending).
5	5249	OH asymmetric stretching and bending.
6	5668	Aliphatic, terminal R-CH$_3$ overtone (stretching).
7	5765	Methyl 1st overtone.

4.2.2 Fourier transform infrared spectroscopy

8	5889	Combination band of epoxy and primary amine overtones.
9	6067	Terminal epoxy 1st overtone (C-H stretching).
10	6635	Primary and secondary amine combination band (overtones of N-H stretching).

For the quantification of the cure kinetics, four peaks were selected for analysis: (i) the epoxy combination band at 4530 cm^{-1}, (ii) the unreactive C-H absorbance peak at 4620 cm^{-1}, (iii) the primary amine combination band at 4935 cm^{-1}, and (iv) the combined primary and secondary amine band at 6635 cm^{-1}, as shown in Figure 40.
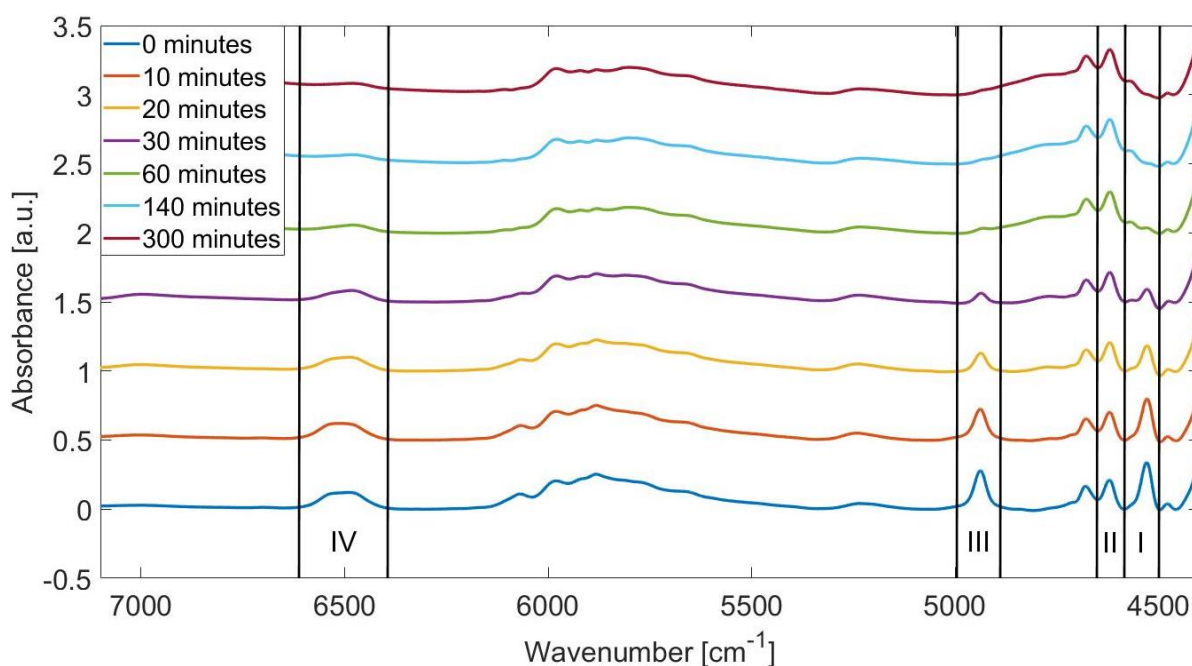
Figure 40 Stacked spectra of the cross-linking of Loctite EA9466 at 50 °C with highlighted peaks of interest.

The epoxy conversion was calculated as a function of the depletion of the 4530 cm^{-1} epoxy absorbance band, as shown in Figure 41:

$$\alpha_{epoxy,t} = 1 - \frac{(A_{epoxy,4530}/A_{reference,4620})_t}{(A_{epoxy,4530}/A_{reference,4620})_{t_0}}$$ [22]

4.2.2 Fourier transform infrared spectroscopy

where A_{epoxy} and $A_{reference}$ are the absorbance peak areas of the epoxy functional group at 4530 cm^{-1} and the unreactive C-H absorbance at 4620 cm^{-1} (Pandita et al., 2012). The start of the reaction is depicted as (t_0), and the absorbances at a particular time during processing are (t).
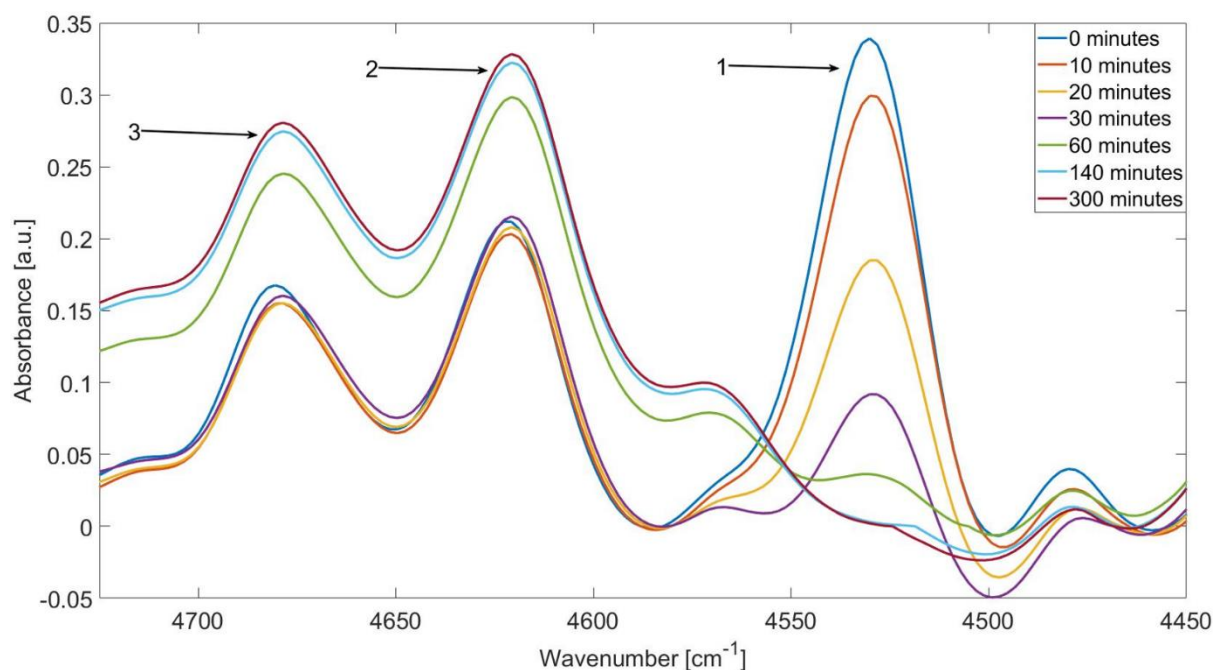
Figure 41 The epoxy absorbance peak at 4530 cm-1 and the reference C-H peak at 4620 cm-1 during cross-linking at 50 °C. The arrows and numbers correspond to the peak assignments listed in Table 12.

The cross-linking was carried out at 50 °C and normalised against the C-H absorbance at 4620 cm^{-1}, as indicated in Equation 22. A sub-peak at 4560 cm^{-1} gradually appears within the epoxy absorption band during the reaction. On closer inspection, this shoulder can be seen from the outset as a minor shift in the slope of the 4530 cm^{-1} epoxy peak. Previous studies (Mijovic et al., 1996, Duemichen et al., 2015) have reported this feature, commonly observed with various epoxy-hardener combinations, although its exact cause has not been identified. It was suggested, that this effect may be related to the C=C and C-H stretching of the aromatic ring (Maxwell and Pethrick, 1983). A deconvolution algorithm found the shoulder to have a relatively small impact of approximately 5% (Pandita et al., 2012). In this investigation, the dynamic integration approach, coupled with a suitable threshold, was found to manage this issue effectively.

4.2.2 Fourier transform infrared spectroscopy

The absorbance peak at 4935 cm^{-1} was used to calculate the depletion of the primary amine similarly to that for the epoxy functional group:

$$ß_{PA,t} = \frac{(A_{PA,4935}/A_{reference,4620})_t}{(A_{PA,4935}/A_{reference,4620})_{t_0}} \qquad [23]$$

, where $ß_{PA}$ represents the normalised depletion of the primary amine (PA) absorbance peak at 4935 cm^{-1} and the reference peak at 4620 cm^{-1}. Figure 42 illustrates the primary amine depletion during a 50 °C experiment.
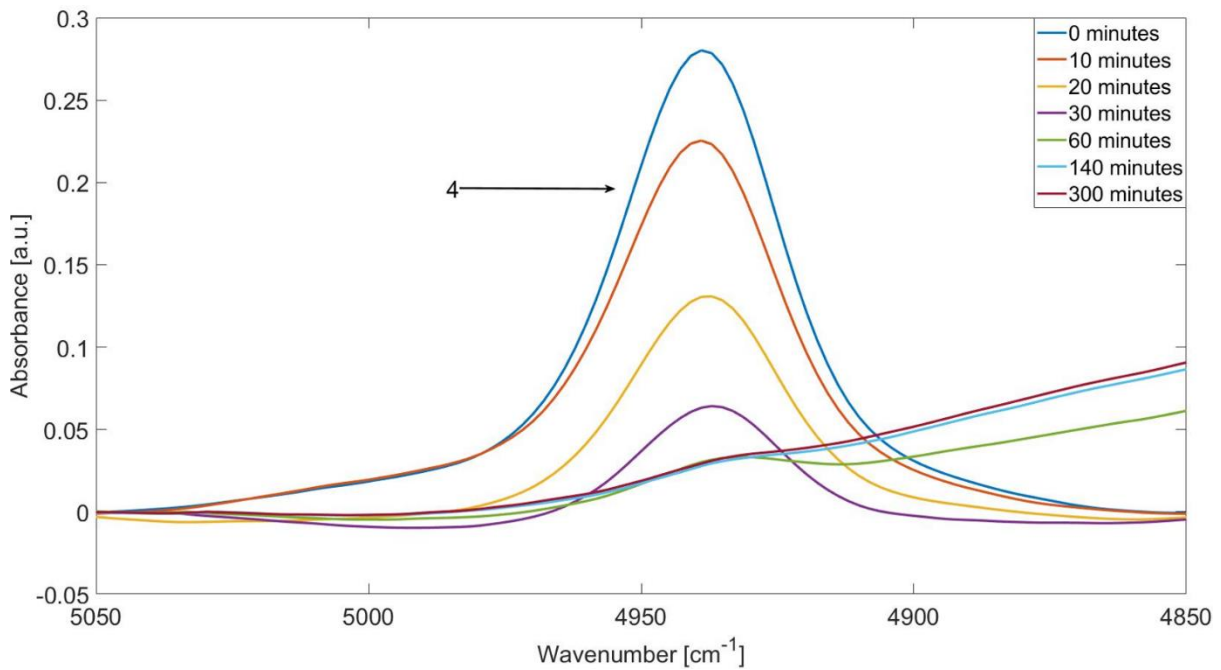
Figure 42 The primary amine absorption peak at 4935 cm-1 during cross-linking at 50 °C.
The overtones of the primary and secondary absorbance peaks merge into a combination absorption band between 6600 and 6400 cm^{-1}. As a result, the conversion rate of the secondary amine can be determined by calculating the difference between the absorbance peak of the primary amine at 4935 cm^{-1} and the combination band within the 6600 to 6400 cm^{−1} range, as shown in Equation 24:

4.2.2 Fourier transform infrared spectroscopy

$$SA_t = \frac{(\Delta_{6600-6400,t} - E_1 \times (PA)_t)}{E_2 \times l} \qquad [24]$$

where $\Delta_{A6600-A6400,t}$ represents the combination band of the primary and secondary amine at a given time, t. E1 and E2 are the molar absorptivities of the primary and secondary amines, respectively. SA_t denotes the calculated concentration of secondary amines at time t. The changes in absorbance, $\Delta_{A6600-A6400}$, of the combination peak during the cross-linking process at 50 °C are shown in Figure 43.
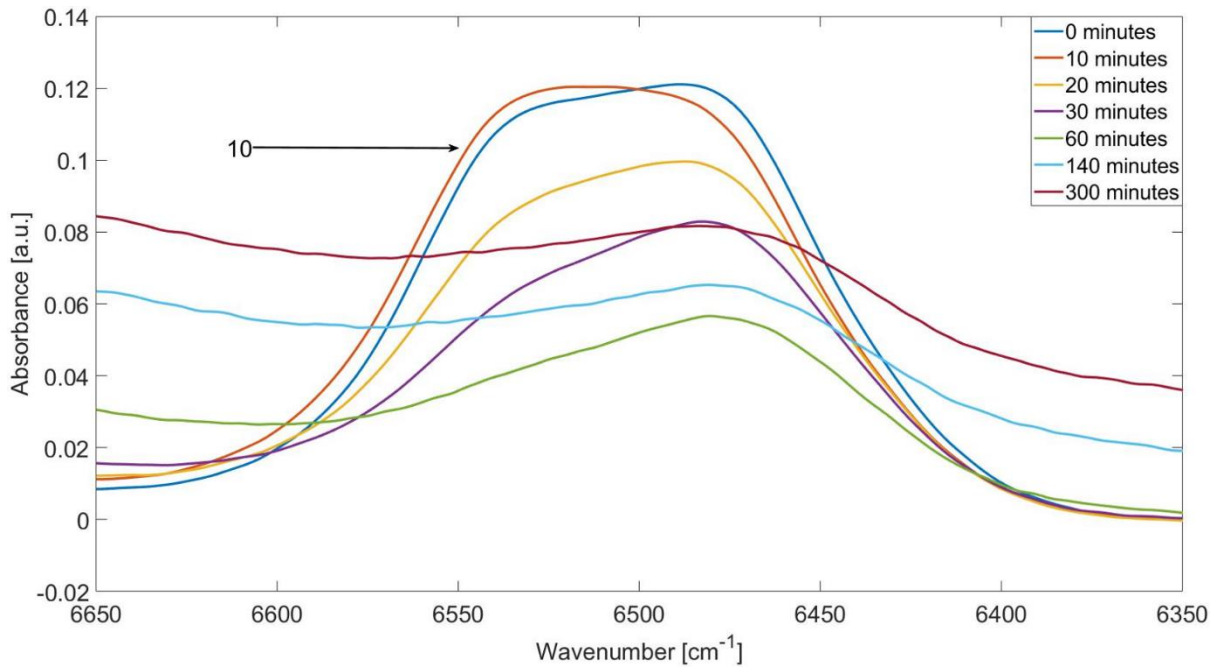
Figure 43 The combination peak of primary and secondary amines at 6635 cm-1 during cross-linking at 50 °C

To determine the concentrations of the secondary and tertiary amine groups (A2 and A3, respectively), a mass balance method was used in a stoichiometric bifunctional epoxy and amine system (PazAbuin et al., 1997):

$$A_2 = E_0 \times \left((1 - \beta_{PA,t}) B - \alpha_t \right) \qquad [25]$$

$$A_2 = E_0 \times \left(\alpha_t - \frac{B}{2}(1 - \beta_{PA,t}) \right) \qquad [26]$$

4.2.2 Fourier transform infrared spectroscopy

$$B = \frac{2A_{1,0}}{E_0} \tag{27}$$

Rearranging Equations 25 and 26:

$$\frac{A_2}{A_{1,0}} = \beta_{SA,t} = 2\left(1 - \beta_{PA,t} - \frac{\alpha_t}{B}\right) \tag{28}$$

$$\frac{A_2}{A_{1,0}} = \beta_{TA,t} = \frac{2}{B}\alpha_t + \beta_{PA,t} - 1 \tag{29}$$

where $\beta_{SA,t}$ and $\beta_{TA,t}$ represent the normalised secondary and tertiary amine groups at time t, respectively. E_0 indicates the initial epoxy absorbance, and $\beta_{PA,t}$ denotes the depletion rate of the primary amine at time t. At the beginning of the reaction, the ratio of epoxy to primary amine concentration is denoted as B, which equals 1 for stoichiometric mixtures (Pandita et al., 2012). α_t describes the degree of epoxy conversion at time t. The conversion rates mentioned above for cross-linking experiments conducted at 20 °C and 50 °C are shown in Figure 44 and Figure 45, respectively. The primary amine is continuously consumed. The secondary amine undergoes two opposing reactions: (i) it increases due to the consumption of primary amines, and (ii) it is consumed in the conversion to tertiary amines. In Figure 44, the secondary amine reaches a plateau at approximately 30% degree of conversion (DoC), indicating that the rates of the opposing reactions are nearly balanced. In Figure 45, the secondary amine concentration increases until a substantial amount of primary amine is consumed, after which it rapidly depletes.

4.2.2 Fourier transform infrared spectroscopy
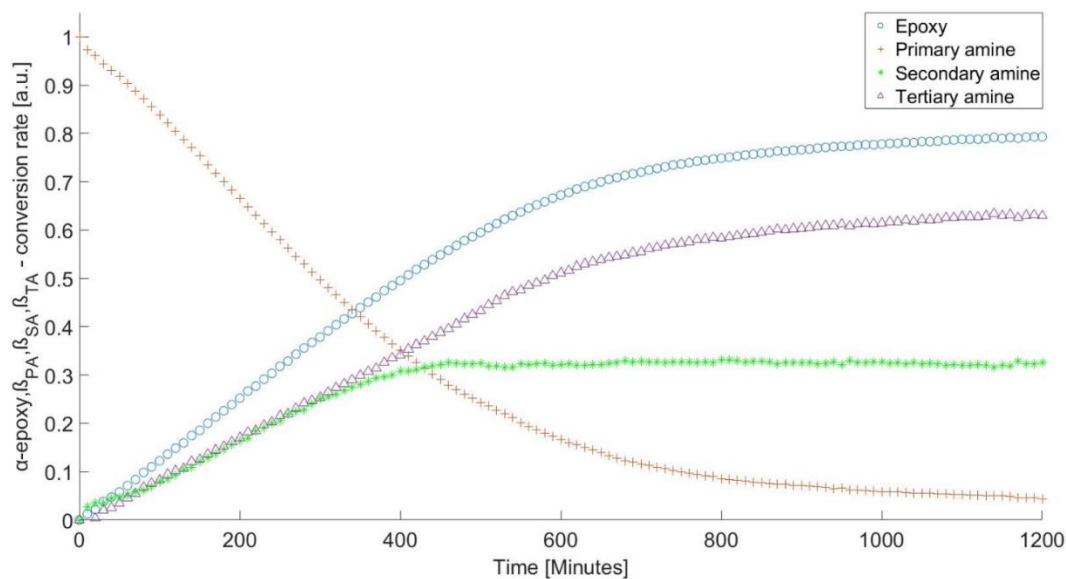
Figure 44 The dataset for the conversion of the following during cross-linking at 20 °C includes: (i) epoxy (α); (ii) primary amine (ßPA); (iii) secondary amine (ßSA); and (iv) tertiary amine (ßTA).
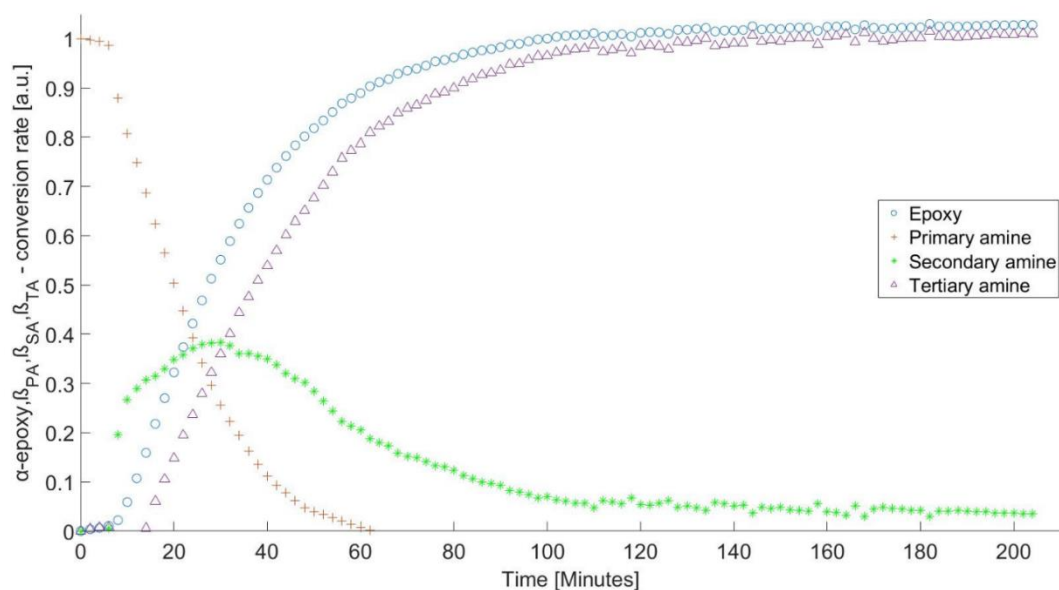
Figure 45 The dataset for the conversion of the following during cross-linking at 50 °C includes: (i) epoxy (α); (ii) primary amine (ßPA); (iii) secondary amine (ßSA); and (iv) tertiary amine (ßTA).

Temperature represents a significant influence on the curing rate and curing time. Higher curing temperatures generally correlate to a higher degree of cross-linking, therefore, a higher Tg and a decreased free volume. As a polymer cures, covalent bonds, known as cross-links, are formed between the polymer chains. As cross-linking occurs, the polymer chains become more tightly packed, and their movement becomes more restricted, resulting in increased Tg (Stutz et al.,

4.2.2 Fourier transform infrared spectroscopy

112

1993, Simon and Gillham, 1992, Lachenal et al., 1996, Patil et al., 2013) and decreased free volume (Patil et al., 2013, Simon and Gillham, 1992). As the curing temperature increases, the energy provided increases, and more cross-links are formed. The degree of cross-linking affects both Tg and free volume within the cured polymer, and therefore higher curing temperatures will result in greater Tg and lower free volume. As can be observed for the epoxy (α) conversion rate regarding the 4530 cm^{-1} peak depletion in Figure 45, solely the 50 °C and 45 °C curing temperatures reach the complete conversion. Therefore, it can be assumed that the Tg for these two temperatures might be of equal magnitude and will eventually decrease gradually with decreasing isothermal cure temperatures. The end of conversion, which can be described as the slope of the conversion rate reaching 0, behaves similarly to the slope angle. The higher the isothermal cure temperature, the steeper the angle and the earlier the slope reaches 0. This temperature- and time-dependence highly correlates with the literature (Achilias et al., 2012).

Table 13 Resulting degrees of cure for the different isothermal FTIR cuvette experiments.

Temperature [°C]	Maximum degree of cure [(α) conversion]
50	100
45	100
40	97
30	88
25	85
20	79

4.2.2 Fourier transform infrared spectroscopy

4.2.3.   Fresnel reflection sensor

For the cuvette-based cross-linking experiments, the FRS signals were recorded concurrently with the FTIR data. Figure 46 and Figure 47 depict the various stages of a typical cross-linking experiment.
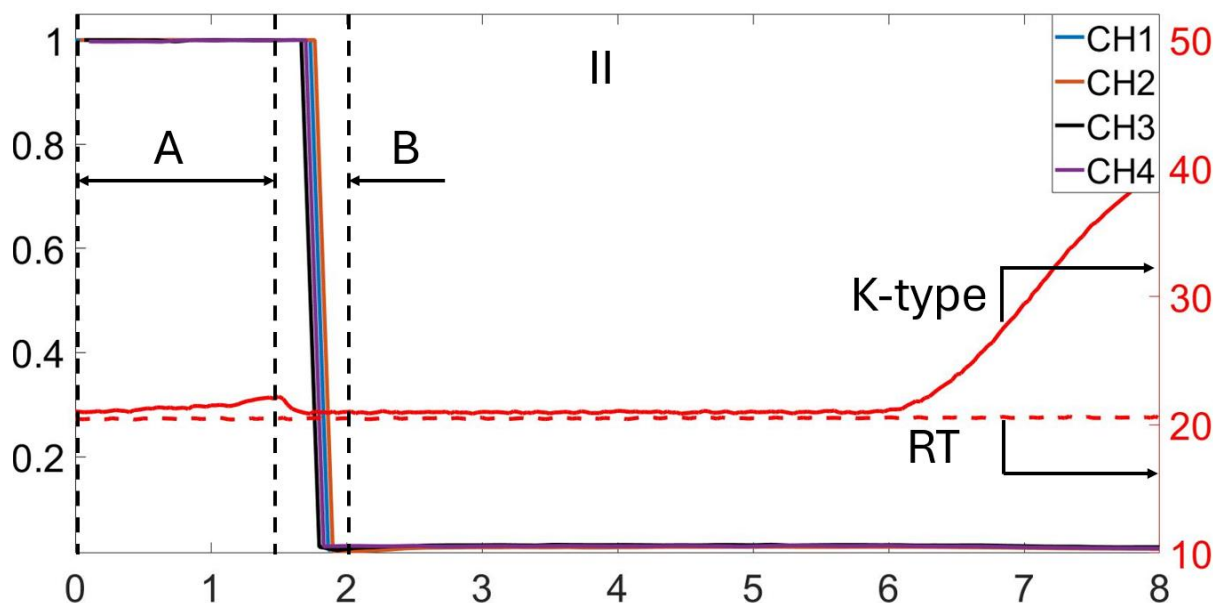
Figure 46 Adhesive submersion phase during 50 °C cross-linking with four FRS and thermocouple traces.

The normalised value in air is 1 for all sensors, as the reference value in air serves as the divisor for FRS normalisation (Phase A). Upon submerging the fibres into the cuvette, a marked decrease in reflection intensity was observed (Phase B). This drop signifies the sensor's immersion in the analyte. The intensity decreases because the analyte has a much higher refractive index than air. The magnitude of the signal drop is not linear, as it depends on the relationship between the refractive index of the analyte and that of the fibre core.
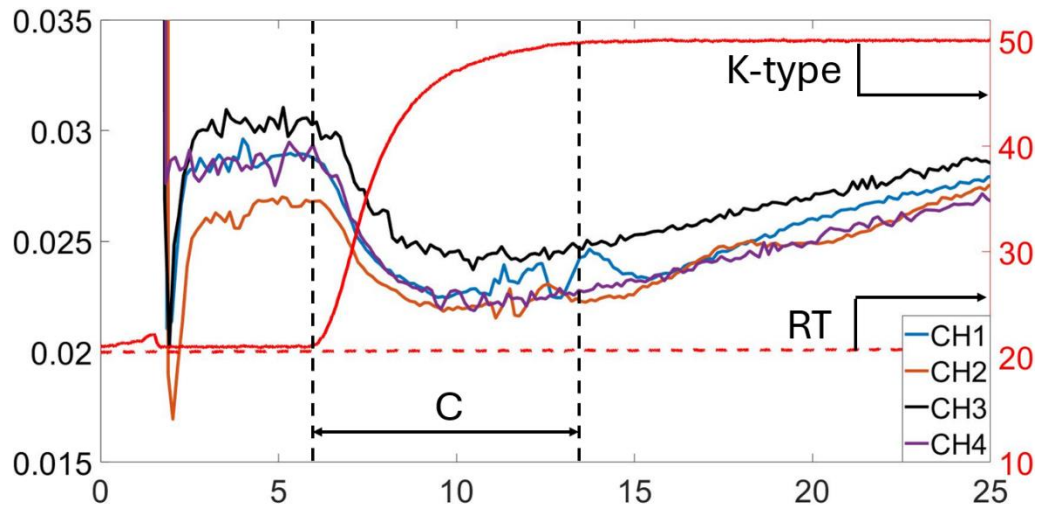
Figure 47 Detailed view of the heat ramp phase at 50 °C cross-linking with four FRS and thermocouple traces.

When scaling the y-axis to visualise the changes in the FRS traces, signal intensity decreases can be observed during the temperature ramp (Phase C). Once the target temperature is reached, the signal intensity begins to rise. The Fresnel equation [18] describes the parabolic behaviour of the reflection coefficient, with the minimum point representing the refractive index of the fibre core. For the optical fibre used in this study (SMF 28), the refractive index of the core is 1.4682 at 1550 nm. For the adhesive, a freshly mixed resin and hardener have a refractive index of 1.54915 at 589.3 nm and 25 °C. Given that the initial refractive index of the resin system is 1.54915 during cross-linking—and assuming other factors like temperature and shrinkage stresses are ignored—the Fresnel reflection coefficient will increase in response to the evolving cross-link density. The normalised data sets for curing at 30 °C and 50 °C are shown in Figure 48 and Figure 49.

4.2.3 Fresnel reflection sensor
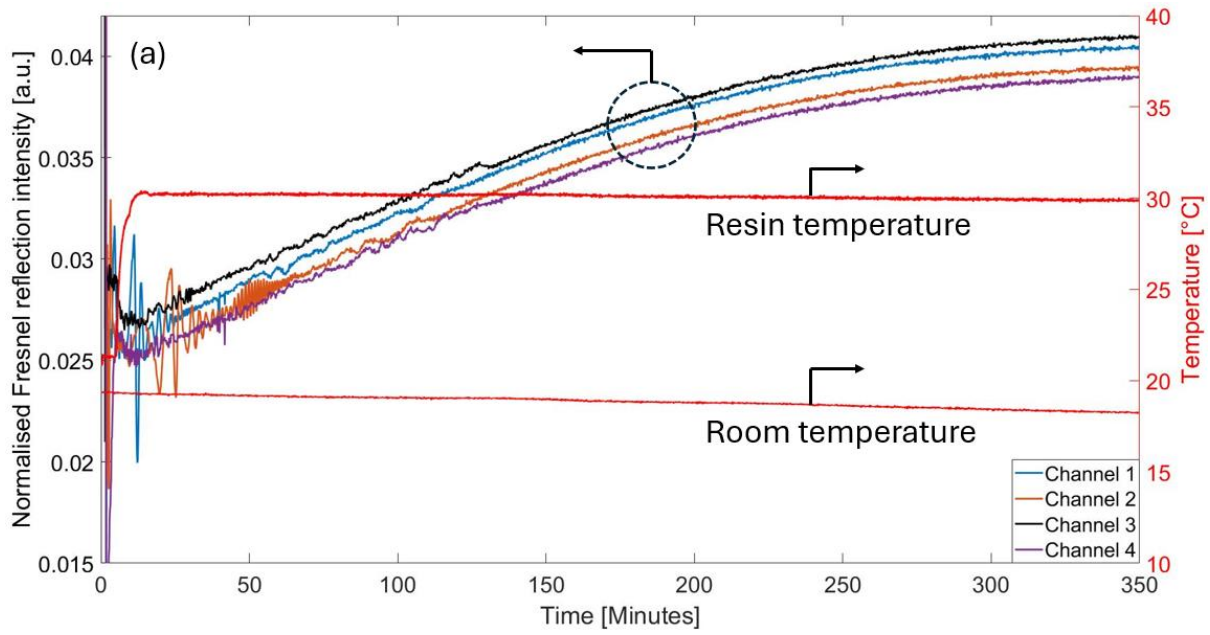
Figure 48 The output from the four FRSs when the cross-linking was performed at 30 °C, along with the output from the thermocouple immersed in the resin and another thermocouple monitoring the room temperature, are also shown.
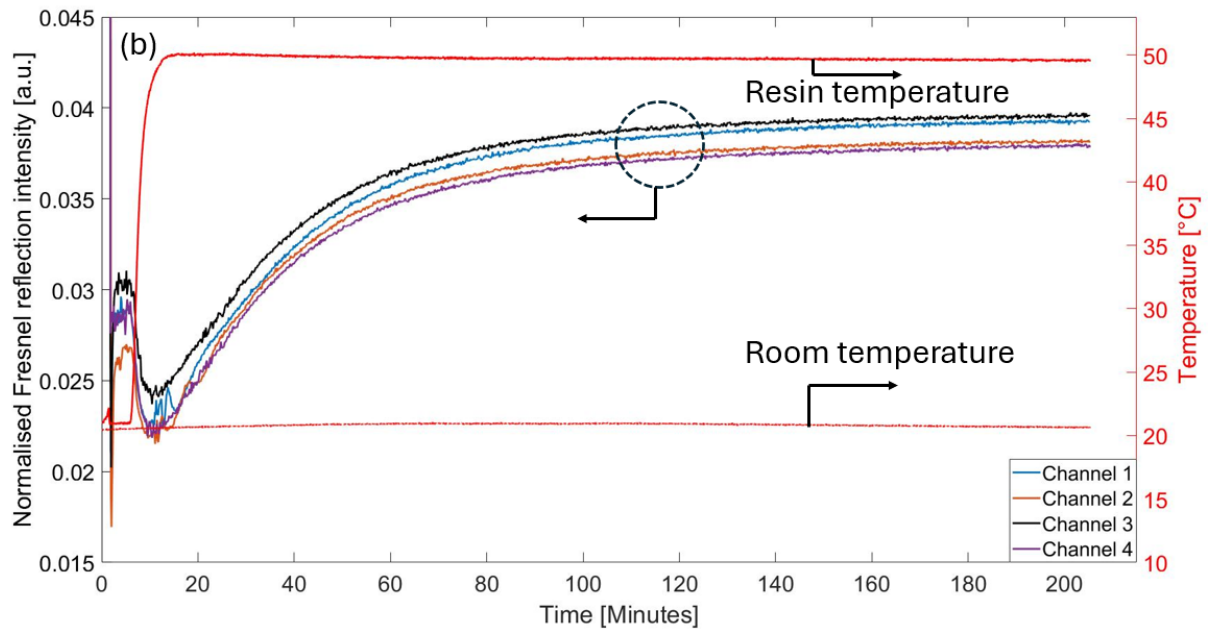
Figure 49 The output from the four FRSs when the cross-linking was performed at 50 °C, along with the output from the thermocouple immersed in the resin and another thermocouple monitoring the room temperature, are also shown.

The initial noisy signals observed in the FRSs were also reported by King (King, 2018b), who noted that the "noise" vanished when the resin system, prior to cross-linking, was frozen in liquid nitrogen. The apparent noise returned once the sample reached ambient room

4.2.3 Fresnel reflection sensor

temperature. A possible explanation for the observed noisy signal at the outset may be fluctuations in the localised concentrations of the amine and epoxy components within the resin system. The diameter of the sensing area, or the core of the SMF 28 optical fibres, is 8.4 micrometres. At the same time, the material volume interrogated in the transmission FTIR spectra is the product of beam diameter and path length (8 mm * 1 mm). Therefore, it is suggested that the smaller interrogation zone in the FRSs increases sensitivity to fluctuations in the concentrations of the resin components. The magnitude of the noise in the FRSs significantly decreased after approximately 60 and 20 minutes at 30 and 50 °C, respectively, during resin cross-linking. This reduction in signal noise may be attributed to the onset of gelation in the resin.

Another notable feature in Figure 48 and Figure 49 is the initial decrease in the FRS signals, followed by a gradual increase. The initial drop can be attributed to the reduction in density of the resin as it is heated from ambient temperature to the isothermal processing temperature (Degamber and Fernando, 2006, Chang et al., 1982). During the heating phase, the reduction in density and the corresponding decrease in refractive index compete with the increase caused by cross-linking (Holst et al., 2005). As heating progresses, the rise in refractive index due to cross-linking becomes the dominant factor, and the FRS signal intensity increases.

The positioning of the FRS and thermocouple at similar depths within the cuvette resulted in consistent signal outputs from both sensors, indicating their reliability. However, as seen in Figure 49, the onset of isothermal conditions within the resin does not coincide with the minimum FRS signals, as detailed in Table 14.

4.2.3 Fresnel reflection sensor

Table 14 Time difference between the cuvette reaching isothermal conditions and the FRSs showing the lowest signal intensity.

Temperature	FRS	Thermocouple	Δ time
20	9.4	11.4	2
25	9.5	11.9	2.4
30	9.7	11.9	2.2
40	8.89	11.8	2.91
45	11.09	12.9	1.81
50	11.5	14.5	3

Possible explanations for the observed discrepancy include: (i) Just before the target isothermal temperature is reached, the ramp rate of the temperature controller may decrease or increase stepwise, which could affect the FRS output. This observation is consistent with the literature (Machavaram et al., 2014). The time taken to achieve isothermal conditions appears relatively consistent, suggesting that the temperature controller uses variable ramp rates rather than a fixed one.

A maximum scatter of 2.63% is observed in the FRS datasets at the two temperatures. Several factors may have contributed to this observed scatter. Firstly, the cuvette holder used in this study included a Peltier heater and a recirculating water system to maintain near-isothermal conditions. However, the fused silica cuvette is an insulator, and it is reasonable to assume that the heat dissipation from the exothermic cross-linking reactions may not be as efficient as it would be in, for example, a differential scanning calorimeter. Secondly, slight variations in the total mass of resin injected into the cuvette could have influenced the results. Thirdly, the

4.2.3 Fresnel reflection sensor

maximum ambient temperature deviation across all experiments was ±1.461 °C. Finally, since the cross-linking reactions are inherently random and the reagents used are not model compounds, a variation of 5% in the datasets can be considered acceptable.

4.2.4.   Cure rate comparison

Figure 50 presents a comparison of the cross-linking rates using the datasets obtained from FTIRS and FRS. The results show a strong correlation in the cross-linking trends, indicating a proportional relationship between the change in refractive index and the epoxy conversion rate. The epoxy conversion rate for the FTIR data was calculated by normalising the epoxy absorbance peak at 4530 cm^{-1} to the corresponding aromatic reference peak at 4620 cm^{-1}. This normalisation accounts for the effects of temperature variations on both absorbance bands, thereby eliminating the impact of temperature fluctuations, such as those occurring during the heating phase until isothermal conditions are reached. The FRS data were normalised relative to the initial value in air, considering only the properties of the cleaved end-face of the fibre. As a result, the observed x-axis offset can be attributed to the decrease in refractive index as the resin is heated from ambient to the target isothermal temperature. A method for comparing the FTIR and FRS cross-linking kinetics has been developed and is detailed in the following section.
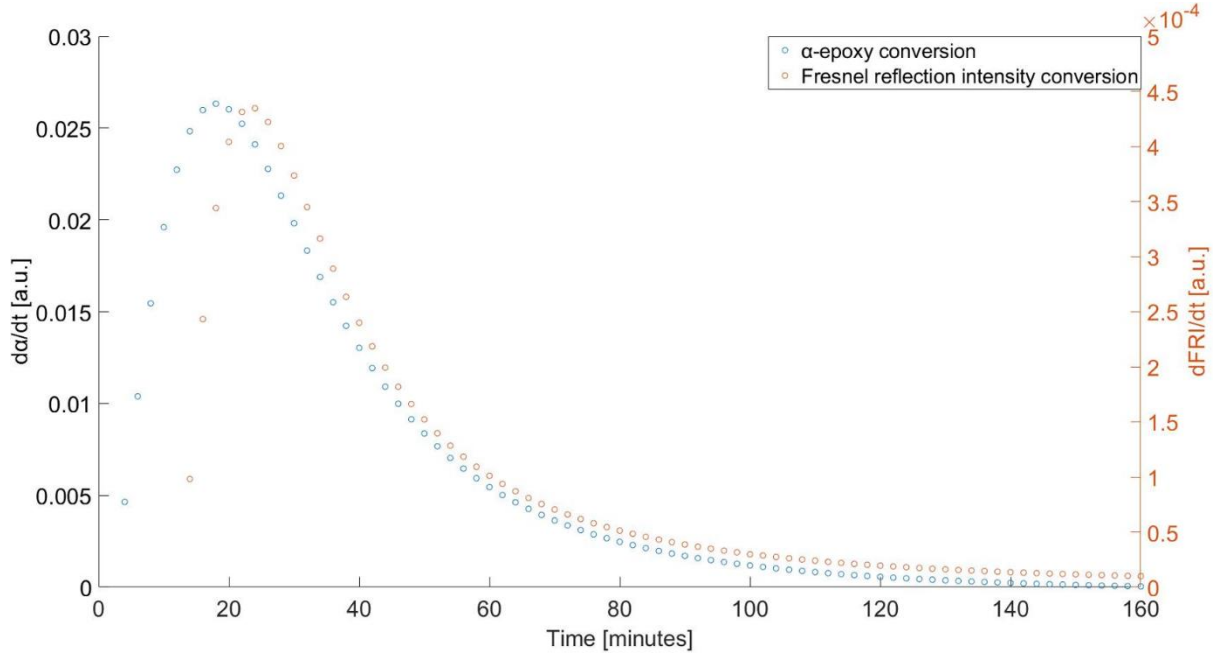
Figure 50 Obtained cross-linking rates from FTIR and FRS of the 50 °C experiment.

To illustrate the comparability of the FRS and FTIR, both data sets were characterised by the autocatalytic or Kamal model:

$$\frac{d\alpha}{dt} = k\alpha^m(1-\alpha)^n \qquad [30]$$

where k represents the reaction rate constant, α is the conversion rate for the epoxy functional group, and m and n are the reaction orders. The first derivative of the original FTIR data was calculated using MATLAB to fit the autocatalytic model to the data and determine appropriate values for the reaction exponents m and n, subject to the condition m+n = 2. The optimal values for m and n are presented in Table 15. These exponents were applied to both the FTIR and FRS datasets.

4.2.4 Cure rate comparison

Table 15 M and n reaction orders generated from the MATLAB curve fitting, including R^2 values.

Temperature	m	n	R^2
20	0.40	1.60	0.8487
25	0.42	1.58	0.9148
30	0.44	1.56	0.9090
40	0.48	1.52	0.9578
45	0.53	1.47	0.9048
50	0.54	1.46	0.9555

Neglecting contributions from defects, shrinkage, and residual stresses, it can be assumed that the FRS output reflects changes in the refractive index, with the primary influencing factors being temperature and cross-linking density. Since the temperature effect is most pronounced at the start (with the refractive index decreasing), the FRS traces were analysed with the point at which isothermal conditions are reached set as the zero point. Beyond this point, the temperature component is considered constant, and the change in the FRS signal from minimum to maximum can thus be attributed to the increase in density during polymerisation. The time at which the minimum signal occurs was cross-correlated with the FTIR data to determine the degree of cross-linking or "cure" (DOC). Due to the high variability of the FRS signals at the beginning of the reaction, the data were curve-fitted using MATLAB, as shown in Figure 51, to accurately identify the minimum point of the FRS (when isothermal conditions were reached).

4.2.4 Cure rate comparison
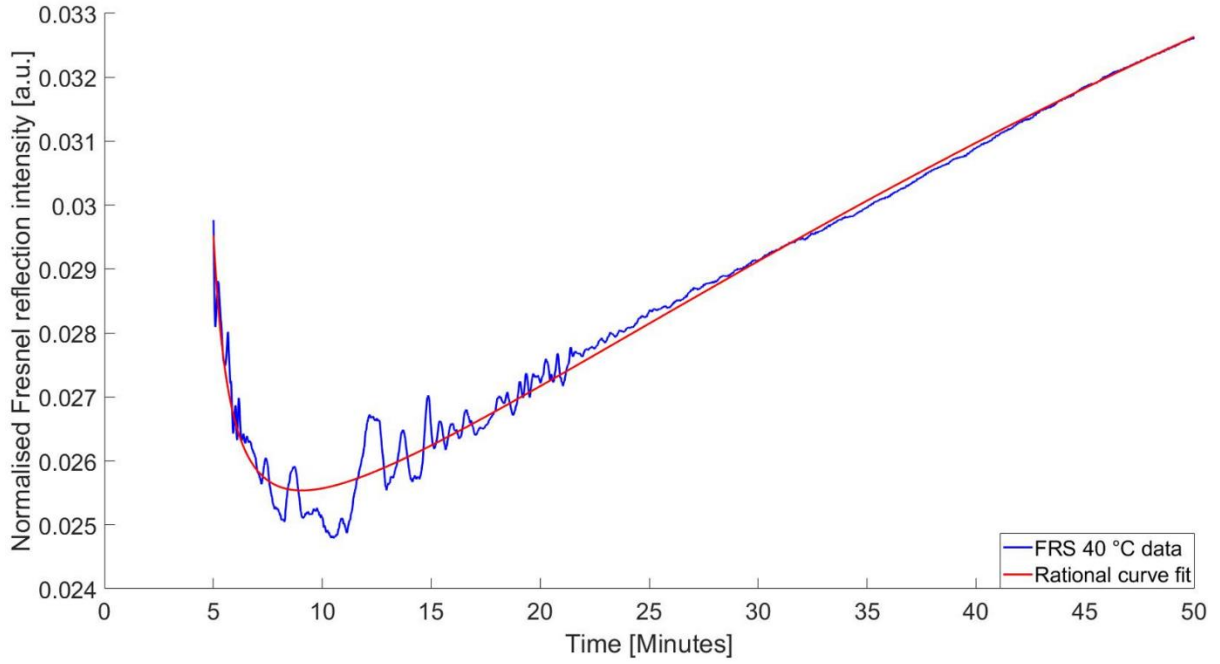
Figure 51 FRS data for the start of the isothermal curing phase at 40 °C (blue) overlaid with the rational curve fit (red), with an R² value of 0.9981.

After curve fitting, the point of interest was the rate constant, which describes the slope of the output from the sensors. Integrating the autocatalytic model results in Equation [31]:

$$t = \frac{1}{k}\frac{1}{n-1}\left(\frac{\alpha}{1-\alpha}\right)^{n-1} \tag{[31]}$$

The autocatalytic model and its fit to the isothermal cross-linking experiments are illustrated in Figure 52. A reasonable correlation is observed between the predicted and the experimentally derived values.

4.2.4 Cure rate comparison
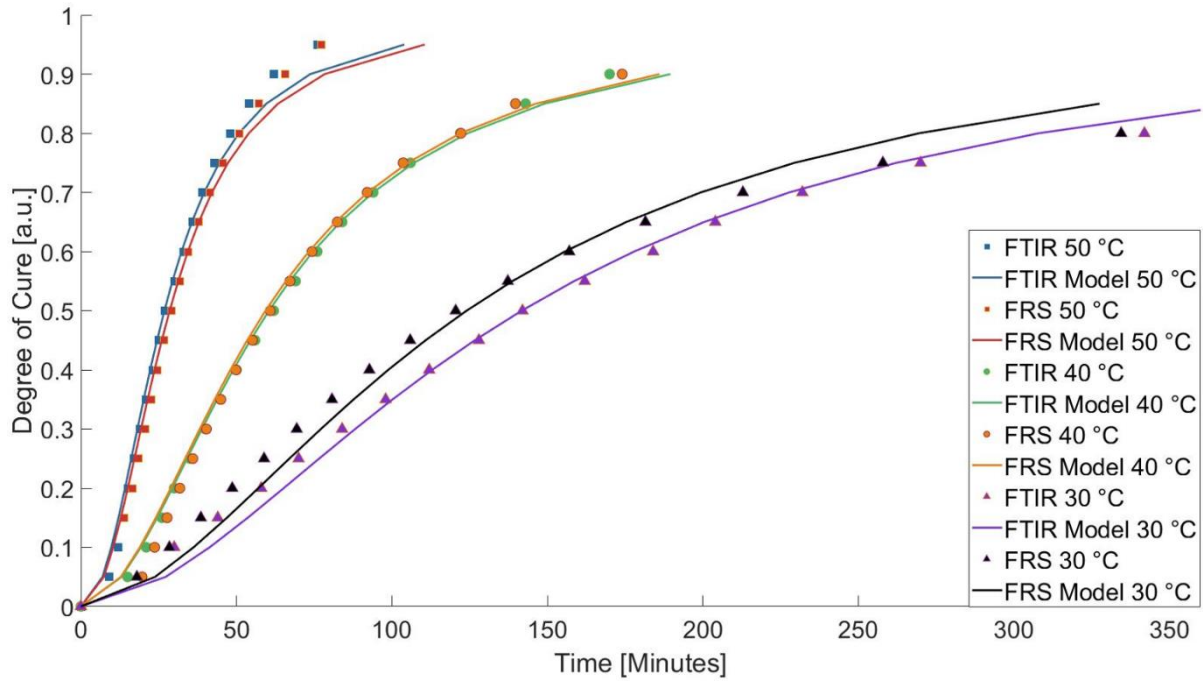
Figure 52 Degree of cure for the FTIR and FRS datasets at 30, 40, and 50 °C, including plots of the autocatalytic model.

The FRS data were subsequently fitted using the identical Kamal reaction order parameters. Following this fitting process, the rate constants were obtained. The reaction order parameters and rate constants are presented in Table 16.

The temperature dependency of the isothermal cross-linking reactions was determined using the Arrhenius relationship:

$$k = A \times exp\left(\frac{-E}{RT}\right)$$

[32]

where A denotes the pre-exponential factor, E signifies activation energy, R represents the universal gas constant, and T is the temperature.

4.2.4 Cure rate comparison

Temperature	1/T	k-FTIR	k-FRS	ln(k-FTIR)	ln(k-FRS)
20	0.003411	0.000072	0.000068	-9.53884	-9.59600
25	0.003354	0.000125	0.000120	-8.98719	-9.02801
30	0.003299	0.000210	0.000240	-8.46840	-8.33487
40	0.003193	0.000530	0.000540	-7.54263	-7.52394
45	0.003143	0.001010	0.000920	-6.89780	-6.99113
50	0.003095	0.001350	0.001270	-6.60765	-6.66874
Activation Energy [kjmol⁻¹]				75.29	74.12

The Arrhenius relationship for the FTIR and FRS results is presented in Figure 53. The strong correlation between the FTIR and FRS data indicates a high degree of comparability in the cross-linking rates obtained from both datasets.
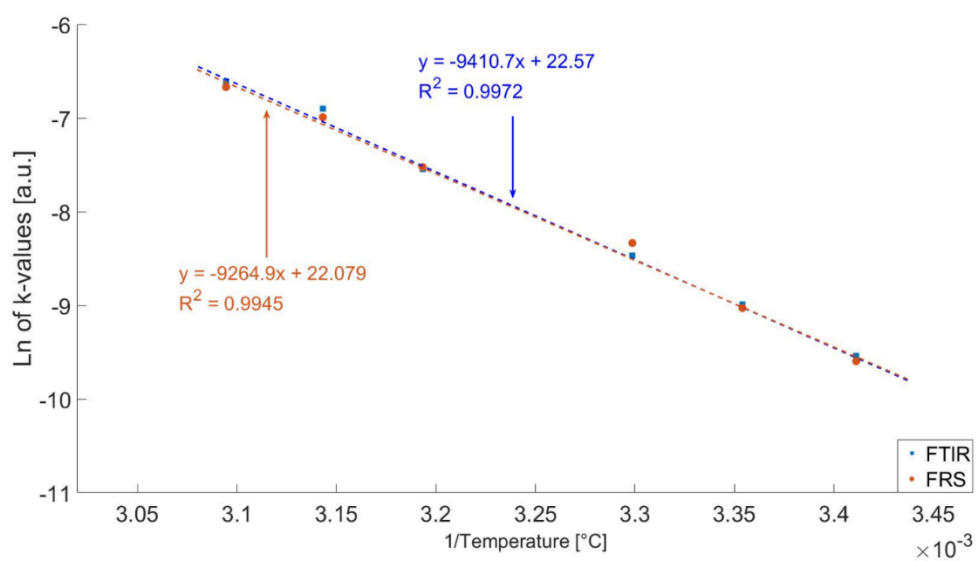
Figure 53 Arrhenius relationship determined for the FTIR (blue) and FRS (orange) datasets.

4.2.4 Cure rate comparison

The activation energy for the FTIR and FRS measurements was determined to be 75.29 kJ mol^{-1} and 74.12 kJ mol^{-1}, respectively; this slight difference may stem from the temperature distribution within the cuvette, which could vary across different regions. While the K-type thermocouple was positioned at the same depth as the FRS, it is important to note that the centre of the FTIR interrogation area is located approximately 11.5 mm below the FRS-TC assembly, and this slight positional discrepancy might lead to minor temperature differences that could influence the measurements. Additionally, the interrogated volumes for the FTIR and FRS methods differ significantly; by probing a larger volume, the FTIR method may experience different heat transfer characteristics compared to the more localised interrogation by the FRS, which further complicates the comparison. Despite these potential sources of variation, the correlation observed between the two methods in Figure 53 remains exceptionally strong, suggesting that the differences in activation energy are likely due to these minor variations rather than any fundamental discrepancy between the two techniques.

4.3. Investigation of Fresnel reflection sensor noise during cross-linking using parallel plate rheometry and FTIR

As the FRS noise levels seemed to end abruptly for all sensors within the experiment, the hypothesis was developed that the observed noise might be the two mixed adhesive components moving and therefore, causing "noise" as initially described in 4.2.3. To obtain evidence to prove this hypothesis, viscosity experiments were conducted using a parallel plate rheometer as described in Section 3.4.1. The aim of these experiments was to obtain the gelation point, as the adhesive cross-linking is supposed to start forming networks, and this point might be correlated to the noise threshold observed in the FRS traces.

During the initial phase of cross-linking, the analyte exhibits liquid-like behaviour, with the loss modulus (G'') exceeding the storage modulus (G'). This indicates that most of the deformation energy is dissipated as viscous losses within the adhesive, rather than being stored elastically. In this stage, polymerisation progresses without the formation of any significant crosslinked networks. The initially observed viscosity drop can be attributed to the heat ramp of the system.

The second phase, gelation, marks the transition of the system from a liquid to a viscoelastic solid as a continuous crosslinked network begins to form. During this stage, G' and G'' become comparable, and at the gel point, they intersect. This crossover signifies the onset of infinite molecular connectivity. The material transitions to a viscoelastic state, exhibiting a combination of viscous flow and elastic deformation. Gelation is a critical point in the curing process, as it denotes the loss of macroscopic flowability, although the material remains deformable.

In the third and final phase, which occurs after gelation, the material increasingly behaves like a solid, with G' becoming dominant over G''. The ongoing cross-linking leads to a progressive increase in the stiffness of the network structure. For the experiments conducted at temperatures between 45 and 65°C, the rheological measurements were terminated shortly after gelation to avoid potential damage to the force sensor caused by high shear forces. These results are presented in Figure 54.

4.3 Investigation of Fresnel reflection sensor noise during cross-linking using parallel plate rheometry and FTIR
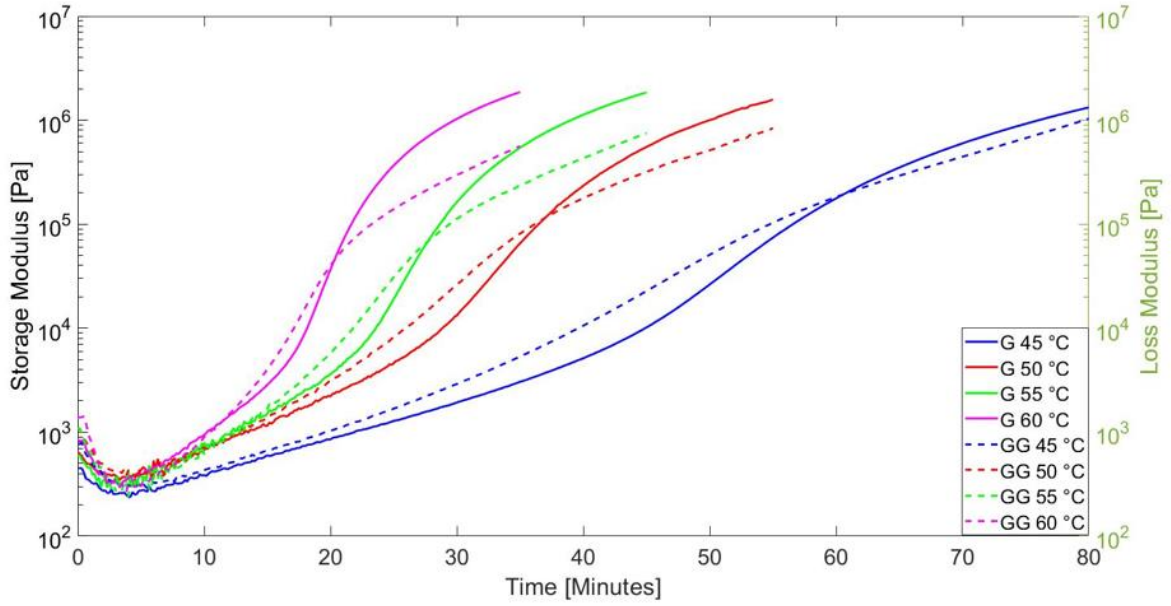
Figure 54 Determination of G'/G'' crossover points for temperatures 45, 50, 55, and 60 °C.

The gel points were experimentally determined between 45°C and 60°C. To enable a comparison with all the obtained FRS traces, it was necessary to extend this range down to 20°C. This extension was achieved by determining the Arrhenius relationship, which describes the behaviour of epoxy resins in parallel plate rheometry (Gazo Hanna et al., 2023). The Arrhenius relation can be expressed as:

$$t_{gel} = Ae^{\frac{E_a}{RT}} \qquad [33]$$

Where t_{gel} is the gelation time, A is a pre-exponential factor, E_a represents the activation energy, R stands for the universal gas constant, and T states the absolute temperature in Kelvin.

By establishing this relationship, the gel points at lower temperatures could be extrapolated from the linear trend, allowing for analysis across the extended temperature range. Figure 55 illustrates the Arrhenius relationship of obtained viscosity data.

4.3 Investigation of Fresnel reflection sensor noise during cross-linking using parallel plate rheometry and FTIR
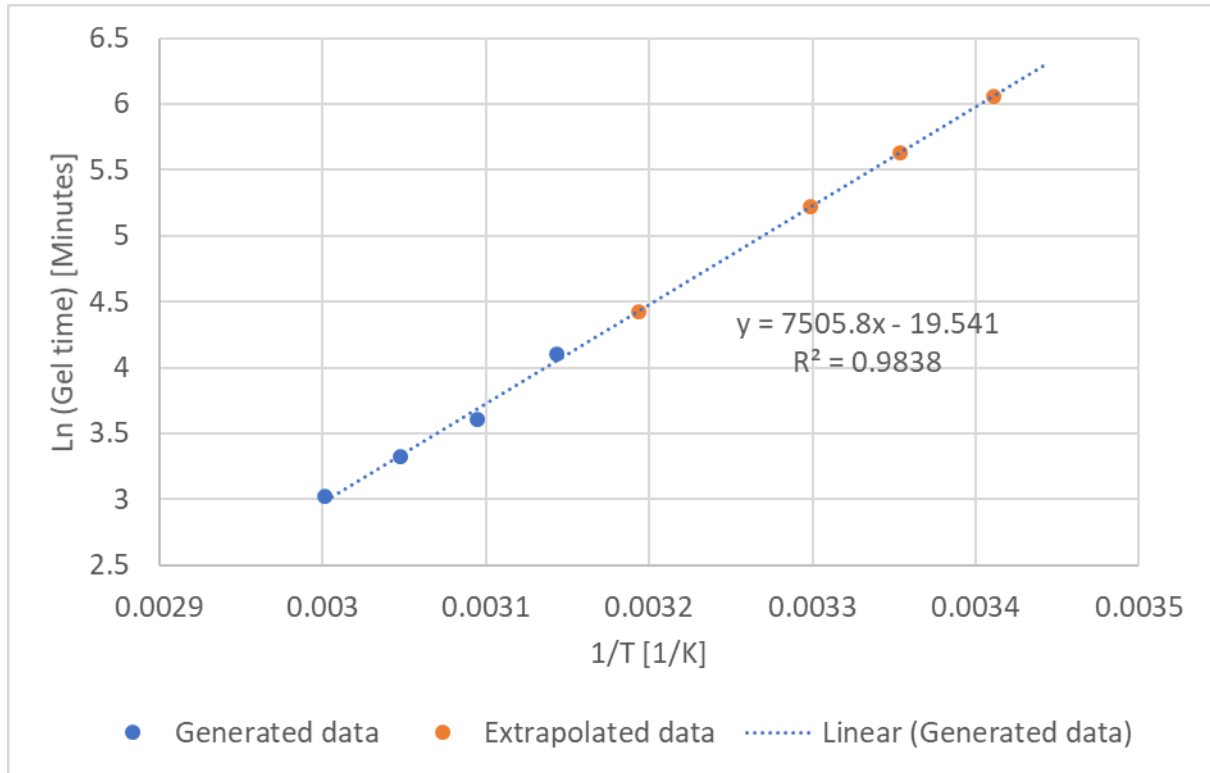
Figure 55 Arrhenius relation of parallel plate results with blue markers representing experimental data and orange markers representing extrapolated data.

A cross-correlation of the generated and extrapolated gel points was performed with the degree of cure obtained from FTIR-FRS experiments, as summarised in Table 17.

Table 17 Cross-correlation of gelation points (crossover) and DoC of FTIR and FRS experiments, including the determined activation energies.

T-Isothermal	Crossover [minutes]	FTIR DoC [%]	FRS DoC [%]
60	20.50	-	-
55	27.83	-	-
50	36.83	66	65
45	60.67	76	71
40	83.75 (extrapolated)	66	65
30	184.65 (extrapolated)	60	65
25	279.69 (extrapolated)	58	60
20	429.69 (extrapolated)	52	54

4.3 Investigation of Fresnel reflection sensor noise during cross-linking using parallel plate rheometry and FTIR

Gelation was observed to occur at degrees of cure ranging from 52% to 76%, including data obtained through extrapolation. A form correction procedure was applied to the FRS traces to compare the parallel plate rheometry gel points with the FRS noise thresholds to eliminate the polymerisation influence in the traces. This was achieved by fitting a curve to the raw FRS traces and subtracting the fitted data from the experimental measurements using MATLAB, yielding flat signals that included only the noise. The noise thresholds were determined manually and illustrated in Figure 56 to visualise the noise limits. The minute curvature of the traces after the noise threshold stems from the subtraction of the curve fits from the original data set, as illustrated in Figure 56.
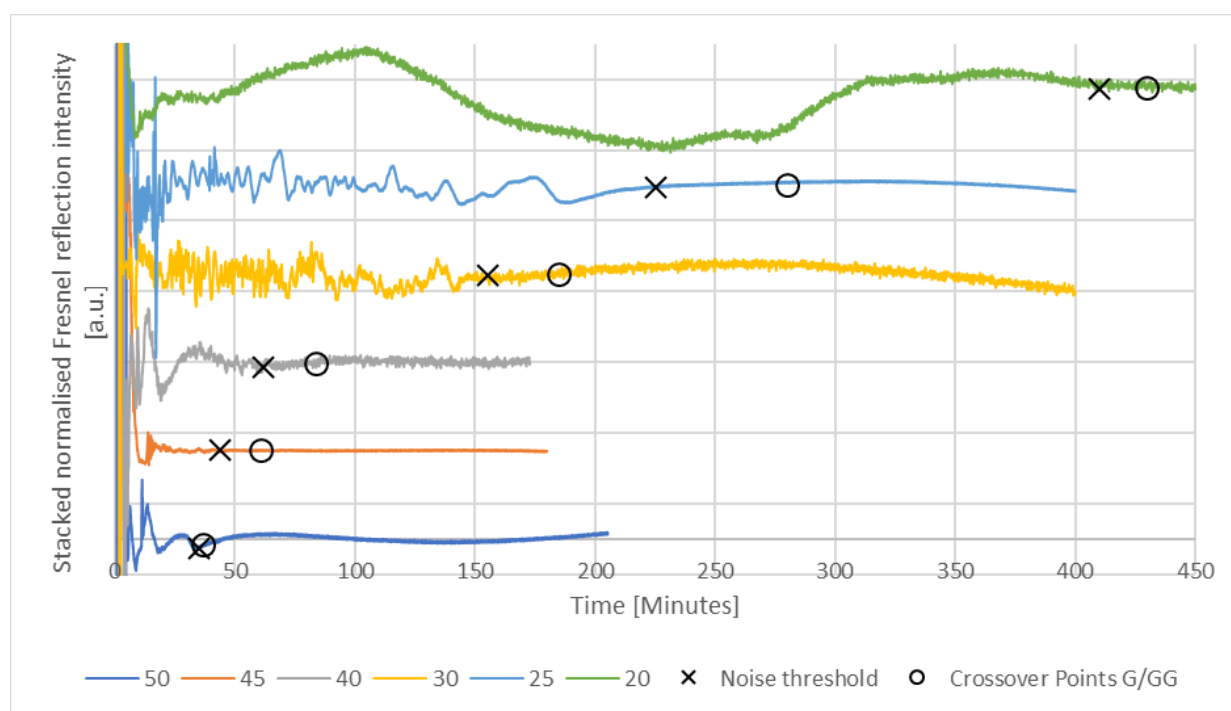
Figure 56 Form corrected FRS traces with overlaid crossover points and manually determined noise thresholds.

An offset was observed between the crossover points determined from rheology and the noise thresholds from FRS data. The magnitude of this offset was quantified, and its potential cause was investigated.

4.3 Investigation of Fresnel reflection sensor noise during cross-linking using parallel plate rheometry and FTIR

As the measurements were conducted using two different systems, variations in thermal management were identified as a likely explanation for the observed discrepancy. The FTIR-FRS experiments utilised a closed-loop temperature control system with a thermocouple placed directly within the analyte, providing moderate temperature regulation, as the thermocouple within the analyte was not the reference sensor for the temperature control. In contrast, the parallel plate rheometer relied on a heating chamber, where the temperature sensor is located in the chamber itself, rather than directly within the sample. This difference in thermal management could have resulted in temperature gradients or delays in thermal equilibration, contributing to the offset. The obtained Arrhenius relation was applied to determine the gelation temperature corresponding to the noise threshold times. This approach allowed the gelation temperature offset for the FRS traces to be simulated, providing a basis for comparing the two datasets. A numerical analysis of gel points and noise thresholds was performed, with the results summarised in Table 18.

4.3 Investigation of Fresnel reflection sensor noise during cross-linking using parallel plate rheometry and FTIR

Table 18 Determined rheometer crossover points, FRS noise thresholds, resulting time delta and calculated temperature offsets between both experiments.

Temperature [°C]	Gelation point [Minutes]	FRS noise threshold [Minutes]	Δ-t [Minutes]	T-offset [°C]
50	036.83	035	01.83	1.83
45	060.67	052	08.67	1.35
40	083.75	070	13.75	2.36
30	184.65	155	29.65	2.16
25	279.69	230	49.69	2.33
20	429.69	410	19.69	0.54

The calculated average temperature offset between the two experimental systems was determined to be 1.76 °C, with a maximum deviation of ±0.60 °C. This discrepancy is reasonable given the differing thermal management strategies employed in each setup. The FTIR-FRS system had a thermocouple directly immersed in the analyte, ensuring precise temperature monitoring. In contrast, the parallel plate rheometer relies on a heating chamber with an external temperature sensor, leading to potential delays or gradients in thermal equilibration within the sample. Additionally, parallel plate rheology for epoxy resins were found to deviate by between 5 to 10% when conducting repeat runs (Yu et al., 2005, King, 2018b).

Comparison of FTIR data and FRS

To further validate the results, the FTIR spectroscopy data were analysed to determine the gelation point, defined as the time corresponding to the maximum concentration of secondary amines in the FTIR-FRS dataset. Given the similarity in the experimental setup, a higher degree of congruency was anticipated in comparison to the parallel plate–FRS correlation. According

4.3 Investigation of Fresnel reflection sensor noise during cross-linking using parallel plate rheometry and FTIR

to the literature, the gelation point coincides with the maximum concentration of secondary amines at a given time during the cross-linking process (Tanaka et al., 2012). The peak secondary amine concentrations were directly extracted from the FTIR-FRS data and subsequently compared with the results obtained from the parallel plate rheometry and FRS, as summarised in Table 19.

Table 19 Comparison of times when reaching (i) the maximum amine concentration, (ii) the gelation point, and (iii) the FRS noise threshold.

T-Isothermal	Maximum secondary amine concentration [Minutes]	Gelation point [Minutes]	FRS noise threshold [Minutes]
50	032	036.83	035
45	042	060.67	044
40	060	083.75	062
30	146	184.65	155
25	256	279.69	240
20	446	429.69	410
Activation Energy [kJmol⁻¹]	69.98	63.10	65.92

The activation energy determined using the parallel plate rheometer was 63.10 kJmol⁻¹, which is slightly lower than the values obtained from FTIR (69.98 kJmol⁻¹) and FRS (65.98 kJmol⁻¹). Differences in the experimental setups and methodologies used in these systems will influence

4.3 Investigation of Fresnel reflection sensor noise during cross-linking using parallel plate rheometry and FTIR

the Arrhenius relation as well. For instance, the rheological measurements were initiated immediately, while the FTIR and FRS experiments began after approximately 5 minutes. This delay was necessary to monitor the equilibration phase of the FRS, which may have influenced the activation energy values. Variations in thermal management between the systems could contribute to the observed offset (Pandita et al., 2012). These differences underline the importance of accounting for experimental conditions when comparing results across different analytical techniques. As can be seen, the activation energies for FTIR and FRS are lower compared to the cure rate comparison (Section 4.2.4.) As the determined Arrhenius relation for this section only concerns the time until gel point, the reactions were not fully completed, and therefore a different activation energy is plausible.

4.3 Investigation of Fresnel reflection sensor noise during cross-linking using parallel plate rheometry and FTIR
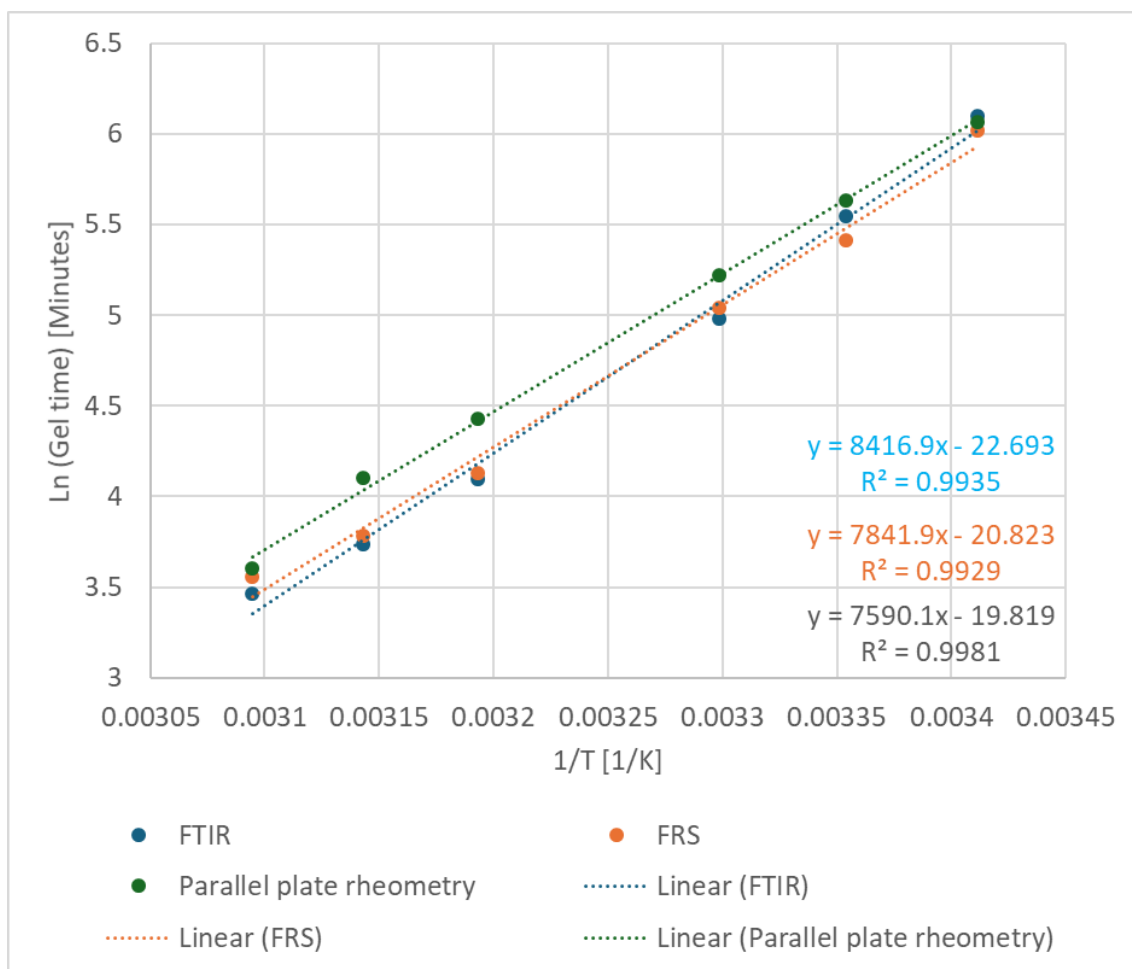
Figure 57 Comparison of determined gelation points for FTIR (blue), FRS (orange), and parallel plate rheometry (grey).

The Arrhenius relationships observed across the different experimental techniques exhibit a similar nature, highlighting the consistency in activation energy trends, as illustrated in Figure 57. In particular, the FTIR and FRS-derived kinetic parameters demonstrate strong congruence, suggesting that both methods capture comparable aspects of the curing process. However, a distinct temperature offset between the parallel plate rheometry and the FTIR-FRS setup becomes evident in the data. While the viscosity-based Arrhenius relationship follows a comparable slope, it shows a y-axis shift in the Arrhenius plot. This deviation may be directly attributed to the previously determined temperature offset between the two setups, reinforcing the influence of measurement conditions on the apparent kinetic parameters. Consequently, the

4.3 Investigation of Fresnel reflection sensor noise during cross-linking using parallel plate rheometry and FTIR

observed offset emphasises the necessity of accounting for system-specific thermal variations when comparing kinetic analyses from different methodologies.

As the FRS measures changes in the refractive index of the analyte, it can be influenced by the physical and chemical dynamics of the adhesive during curing. In the viscous phase, the two components of the adhesive are diffusing into each other, potentially causing fluctuations in the refractive index that manifest as noise. Additionally, the formation of microvoids within the adhesive could influence the FRS signal. However, given that air has a refractive index of approximately 1, any void large enough to cover the cross-sectional area of the sensor would theoretically result in a significant noise amplitude and an FRS signal approaching a refractive index of 1. Such extreme fluctuations have never been observed, suggesting that microvoids, while possible contributors are unlikely to fully explain the noise characteristics.

In summary, the noise observed in the FRS measurements appears to correlate with the gelation point of the structural adhesive. To eliminate potential influences from differences in thermal management, future work should explore a hyphenated rheology-FRS experiment. This combined approach would synchronise rheological and FRS measurements within a single system, providing a more comprehensive understanding of the curing dynamics and minimising temperature-related discrepancies. The secondary amine concentration peak and the FRS noise threshold show good correlation, as can be seen in the Arrhenius relationship.

4.4. *In situ* assessment of multiple parameters in adhesive joints

In the following sub-chapters, the results of the glove box experiments are presented. In this series of experiments, various optical fibre sensors were embedded in SJLs during the cross-linking to monitor (i) chemical changes, (ii) refractive index changes, (iii) strain changes due

to polymer shrinkage, and (iv) temperature changes. A schematic of the experimental setup is illustrated in Figure 58.
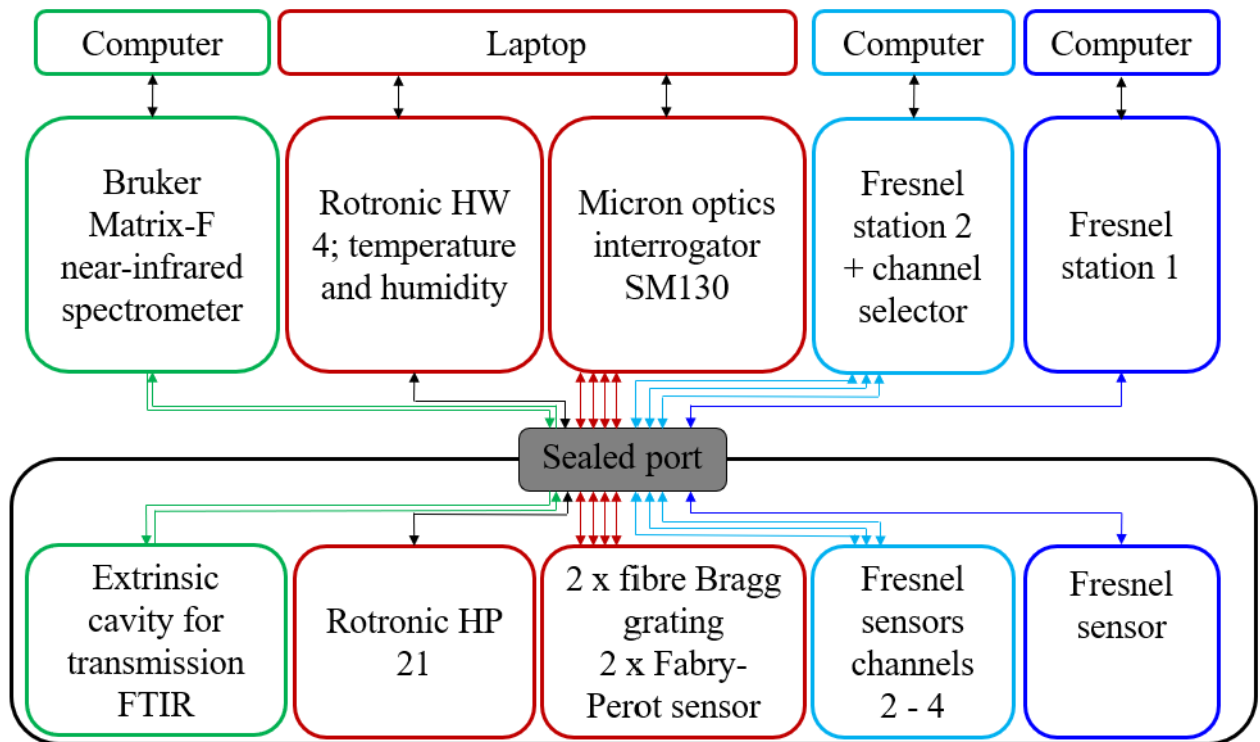
Figure 58 Schematic of the glove box and involved interrogation equipment.

The sealed port represents the sealable plugs located at the backside of the glove box. The black frame connected to the port is the glove box system itself, enclosing all of the sensing equipment that was located within the glove box. The upside of the sealed port is all of the utilised interrogation equipment necessary to interrogate the embedded optical fibre sensors.

4.4.1.   Glove box controls

The glove box consisted of a closed-loop control for temperature and relative humidity, but did not have an interface to log the data. Therefore, the Rotronic HP21 temperature and humidity sensor was used during the experiments to enable data logging of named parameters. The glove box data for two experiments at 40 °C are illustrated in Figure 59, and the data analysis is presented in Table 20.
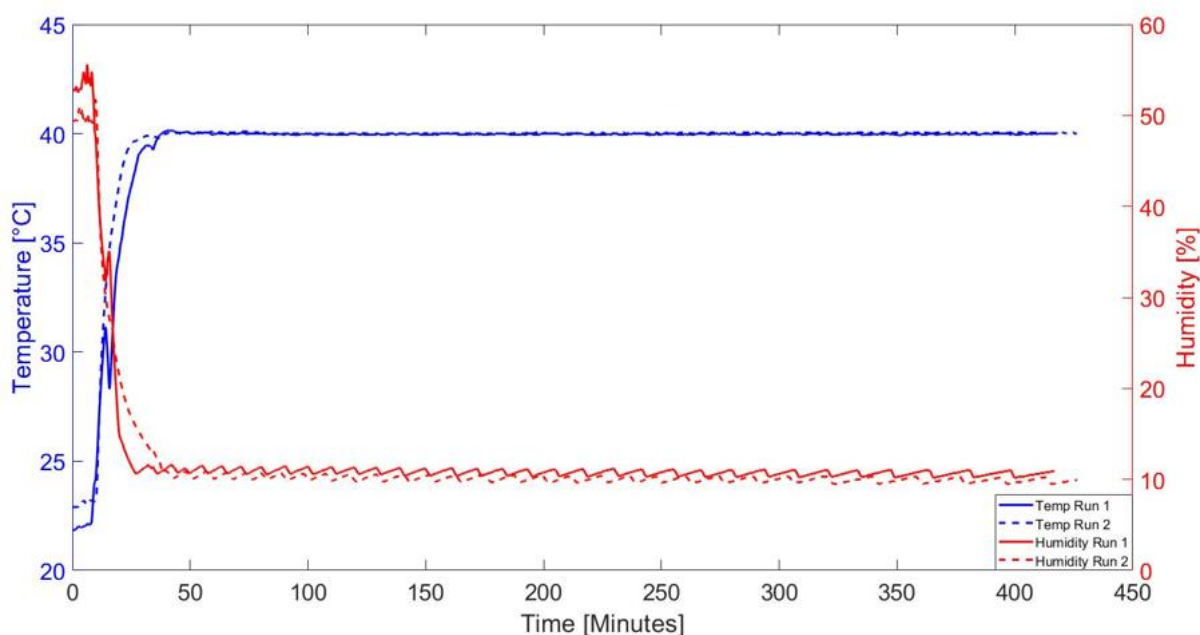
Figure 59 HP21 data on temperature and humidity during the 40 °C glove box experiment.
The HP21 was positioned directly next to the glove box sensor array to ensure similar readings, as the PID-controlled fan increases the glove box temperature asymmetrically. The temperature ramp rates show the same slope, indicating appropriate repeatability. The same can be said for the relative humidity data. Regarding experiment 1, The sharp temperature drop and relative humidity increase in the middle of the ramping phase are due to the glove box being opened and closed. After reaching isothermal conditions, the temperatures for both experiments are congruent. The sawtooth-like signal results from the humidity controller setup, which operates with upper and lower limits for the control. The observed elongation of the mentioned saw teeth may be due to a dynamic change in moisture. During the temperature ramp, the vapour saturation pressure of air increases, meaning the air can hold more water. Therefore, the relative humidity decreases. The reduced absolute moisture will take longer, as seen in the sawtooth signal periodicity change.

4.4.1 Glove box controls

Table 20 Temperature, humidity and their deviation during the glove box experiments.

Experiment	Average T [°C]	Max deviation [°C]	Average RH [%]	Max deviation [%]
30-1	30.008	±00.242	09.631	±00.869
30-2	30.068	±00.118	09.570	±01.030
40-1	39.970	±00.720	10.785	±00.815
40-2	40.024	±00.076	10.050	±00.850
50-1	49.426	±00.376	10.788	±00.612
50-2	50.013	±00.387	11.099	±00.701

The maximum temperature deviation from the target isothermal temperature was ± 0.72 °C for all temperature experiments. The maximum deviation in relative humidity was ± 1.03%. The deviation in temperature and relative humidity was considered to be appropriate. The PID heater was kept in the same position for all experiments to avoid deviation in the temperature readings. A minor offset was found between the glove box sensor array and the HP 21. The offset was found to be approximately 0.2 °C concerning temperature and 4% regarding relative humidity. This offset is room temperature dependent and needs to be compensated for by the operator.

4.4.1 Glove box controls

4.4.2. Fourier transform infrared spectroscopy

The following sub-chapters detail the manufacture of a surface-mounted FTIR sensor and the results during the isothermal cross-linking experiments. A schematic of a surface-mounted FTIR sensor is illustrated in Figure 60.
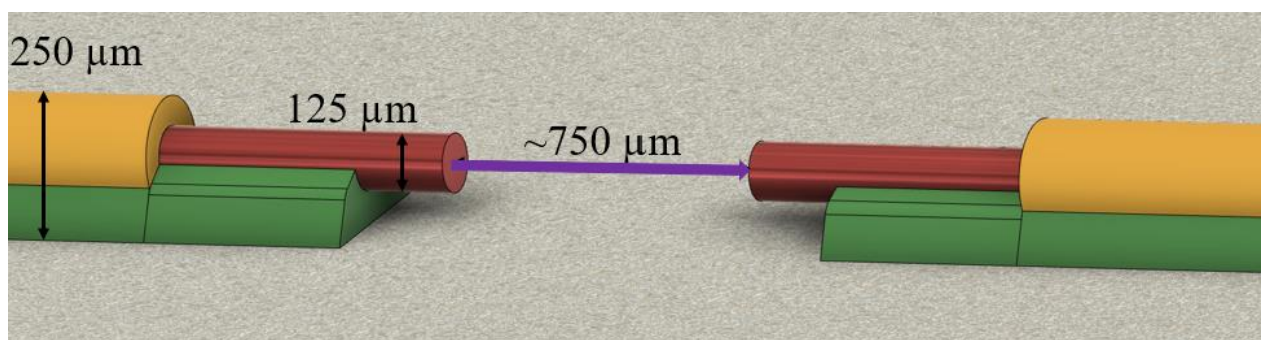
Figure 60 CAD-drawing of the surface-mounted FTIR sensor.

4.4.2.1. Manufacturing surface-mounted FTIR sensors

To enable FTIR interrogation within the adhesive bond line, a larger cavity sensor was needed. Attempts were made to manufacture an intrinsic FP with the PFIB system, but these sensors were found to be too delicate to handle. A surface-mounted extrinsic FP was, therefore, developed, as illustrated in Figure 61.
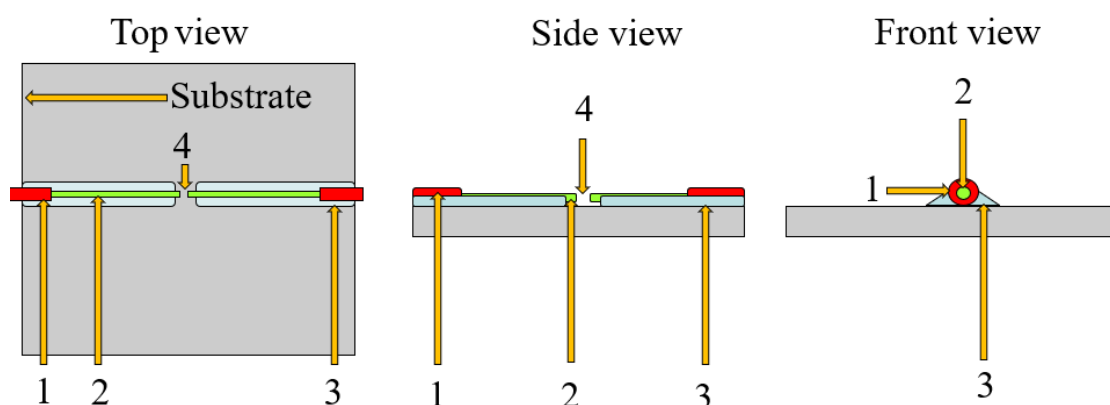
Figure 61 Schematic of the surface-mounted FTIR sensor.

4.4.2 Fourier transform infrared spectroscopy

One of the two substrates of an SLJ served as a fixture for the sensor. To manufacture the sensor, an SMF-28 fibre was fixed on the substrate with slight tension to ensure the fibre was straight. The sensor section of the fibre (~ 10 mm) was stripped before placing the fibre onto the substrate. Polyimide tape was used to hold the fibre in place. As the next step, a small amount of UV-curing adhesive was syringed into the designated area of the "cradle". Due to its low viscosity, the adhesive crept under the fibre and along the fibre. After curing, the SMF-28 fibre was removed, and a cut-out was made in the sensing region. The cleaved multimode fibres were carefully inserted into both sides of the cradle using a top-mounted CCD camera system. After positioning the multimode fibres, they were fixed into place using a drop of UV-curing adhesive at the outer sides of the cradle and cured. Figure 62 illustrates the resulting cradle and its dimensions from a top view, and Figure 63 shows the cradle from the front view.

Figure 62 Top view of the surface-mounted cradle.

The cradle consumes approximately 0.5 mm in width on the surface of the substrate. The tapering is due to the stripped middle section of the fibre. The stripping reduces the outer diameter of the fibre from 0.25 mm to 0.125 mm. The adhesive is a liquid form adapted to this geometrical change during its spreading out along the fibre. The mark in the cradle gap is caused by a scriber that was used to remove the middle section after cutting with a ceramic blade.

4.4.2.1 Manufacturing surface-mounted FTIR sensors
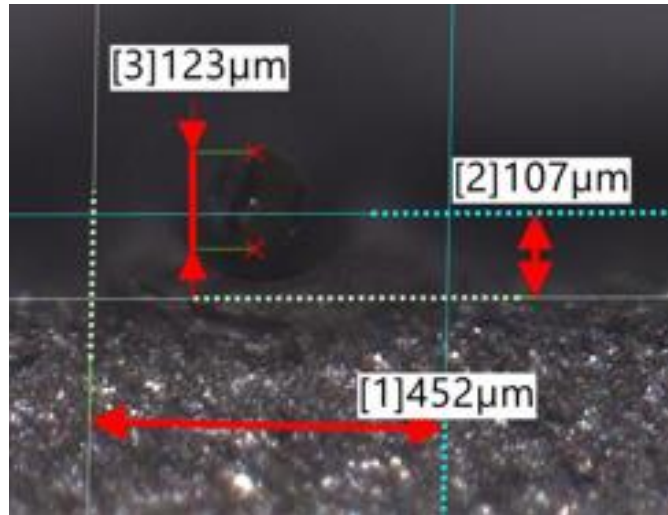
Figure 63 Front view on the surface-mounted cradle.

The front view illustrated the height of the cradle. The stripped fibre has a diameter of 0.125 mm. The cradle has a height of approximately 0.1 mm, but this height can vary depending on the adhesive used. The cavity gap length was adjusted to approximately 0.75 mm using the CCD camera system.

4.4.2.2. Evaluation of surface-mounted FTIR sensors

The FTIR analysis was conducted for the 30 and 40 °C cross-linking experiments. The results for the 50 °C experiments were found to be substandard due to low signal-to-noise ratios observed. Figure 64 and Figure 65 illustrate the chemical changes for the 30 and 40 °C experiments.
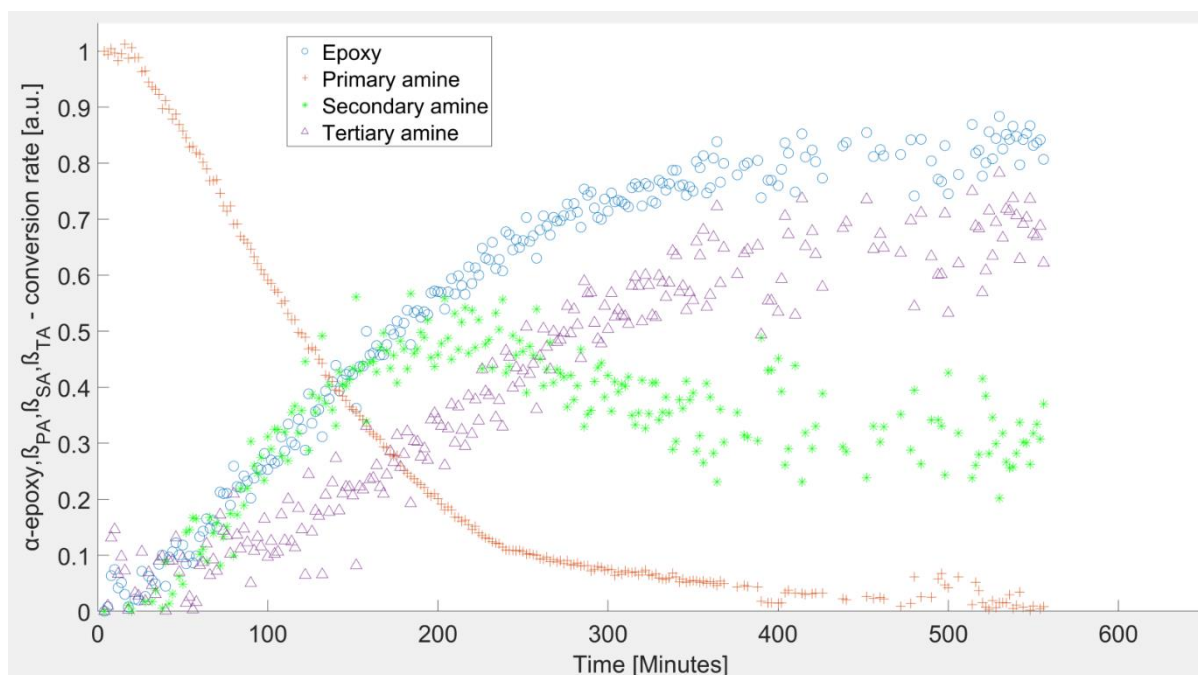
Figure 64 The surface-mounted FTIR dataset for the conversion of the following during cross-linking at 30 °C includes: (i) epoxy (α); (ii) primary amine (ßPA); (iii) secondary amine (ßSA); and (iv) tertiary amine (ßTA).

As can be seen, the functional groups behave in a similar manner as in the cuvette experiments, but with a significantly higher signal variance. A possible factor for this is believed to be the different interrogation cross-area and light-guiding setup. Where the cuvette holder operates with a 1000-micron optical fibre cable, the surface-mounted sensor operates with a multimode core diameter of 105 microns. Additionally, the cuvette holder has a lens assembly that collimates the light to 10 mm, guides it through the cuvette and then collects it back into the outgoing fibre cable. The surface-mounted FTIR sensor does not comprise any collimating or collecting capabilities; therefore, the light leaves the multimode fibres at an NA of 0.22. These two factors reduce the transmitted light significantly for the surface-mounted FTIR sensor. The significant increase in signal variance for the 30 °C experiment, from approximately 380 minutes to 520 minutes, cannot be readily explained, as the adhesive was already solidified at this point. Generally, the integration routine resulted in the epoxy peak at 4530 cm^{-1} having a higher signal variance than the primary amine peak at 4935 cm^{-1} or the 6635 cm^{-1} combination band.

4.4.2.2 Evaluation of surface-mounted FTIR sensors
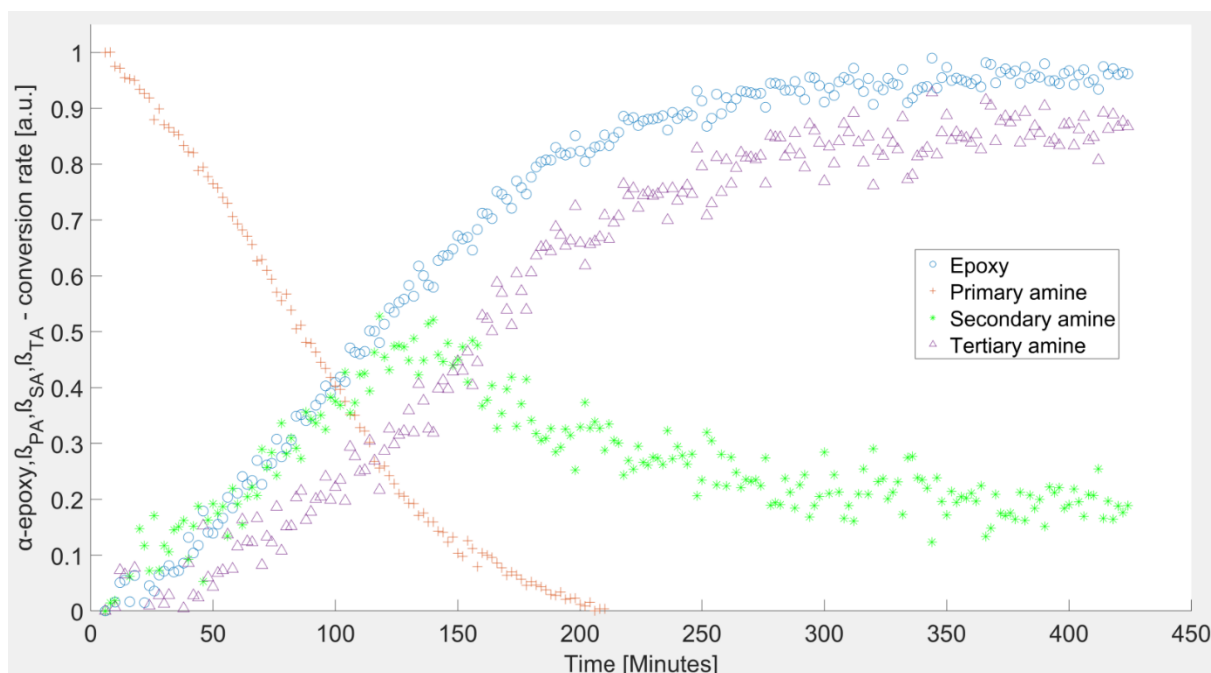
Figure 65 The surface-mounted FTIR dataset for the conversion of the following during cross-linking at 40 °C includes: (i) epoxy (α); (ii) primary amine (ßPA); (iii) secondary amine (ßSA); and (iv) tertiary amine (ßTA).

The 40 °C experiment does not show a signal variance increase within the late phase of cross-linking. The higher signal variance must result from the 4530 cm^{-1} epoxy peak, as the primary amine overtone seems unaffected. In order to investigate eventual differences in signal variance, the raw integration data were assessed. Figure 66 illustrates the integrated absorbance values for all peaks of interest during the 40 °C glove box experiment.

4.4.2.2 Evaluation of surface-mounted FTIR sensors
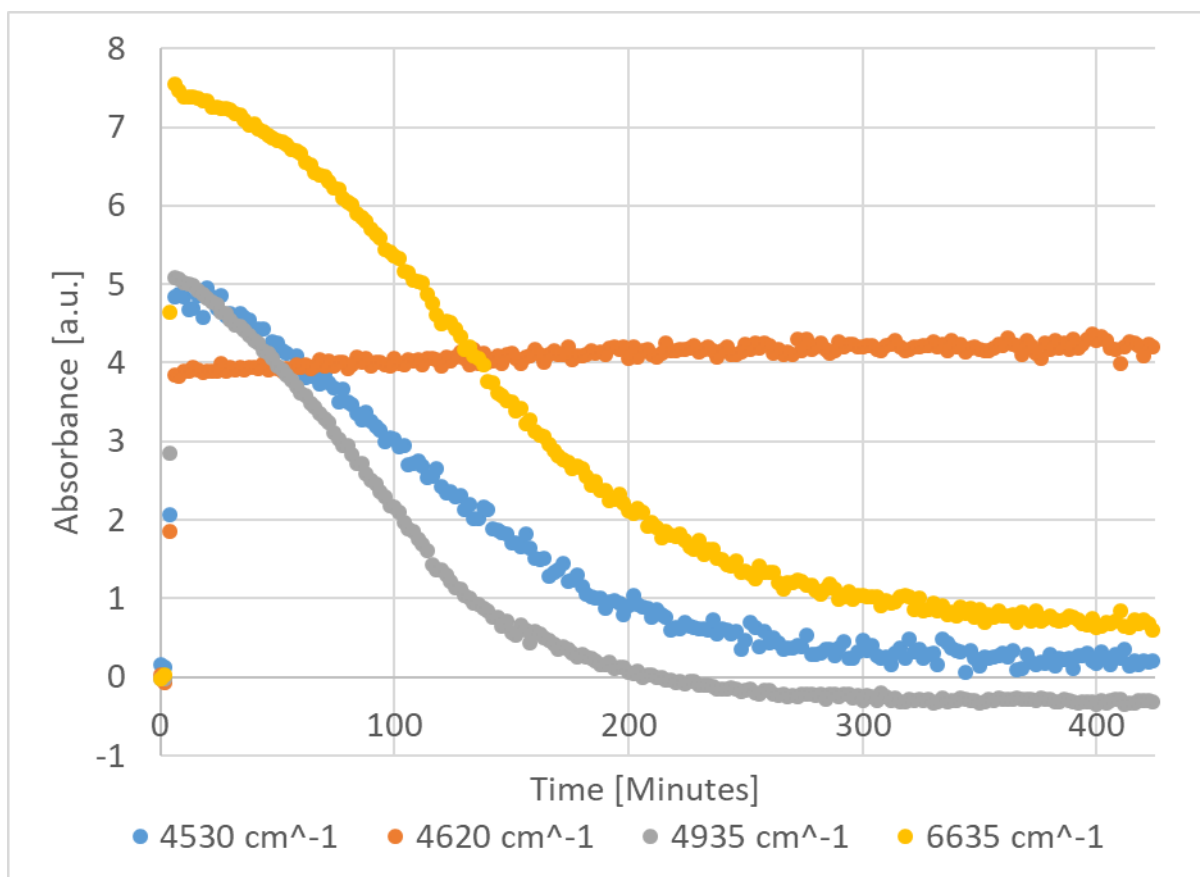
Figure 66 Raw data evolution of a surface-mounted FTIR sensor during cross-linking at 40 °C.

From visual inspection, the epoxy peak at 4530 cm^{-1} has the highest signal variance throughout the reaction. As the alpha-epoxy is used to calculate the primary and secondary amines, the high signal variance does affect the results for SA and TA. During the assessment of the 50 °C spectra, it was found that the baseline, in general, had a tilt, and the epoxy peak had a noisy form, as can be seen in Figure 67. The baseline tilt is clearly observable and the noisy shape of some 4530 cm^{-1} peaks. The 4935 cm^{-1} peaks are also included in the plot and do not show these issues. A possible reason for this may be a slight misalignment of the OFS. A misaligned cavity could cause a baseline drift, and therefore, the accuracy in the epoxy region might decrease. This is believed to be the main factor for the higher signal variability for the other experiments as well. The reason for the 50 °C run not being included in this subchapter is that the interference was significant enough to let the DoC plateau at 0.9, which is implausible.

4.4.2.2 Evaluation of surface-mounted FTIR sensors
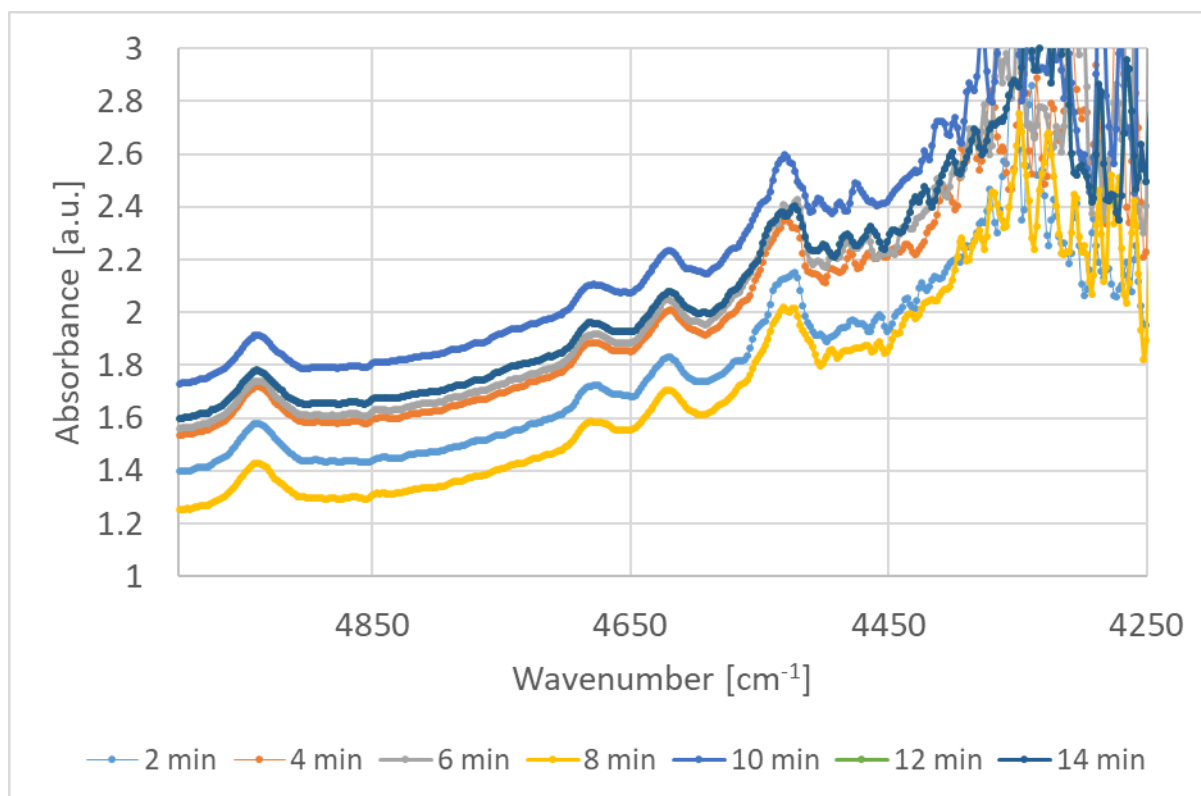
Figure 67 Illustration of noise influences on the surface-mounted FTIR sensor.

4.4.2.3. Comparison of conventional FTIR and surface-mounted FTIR sensors

As the cure kinetics are only calculated from the epoxy depletion and the data points are curve-fitted, the higher signal variance is believed not to significantly influence the data validity compared to the cuvette experiments. To enable comparison of the data sets, the standard deviation (σ) was determined. In order to obtain the σ, the changes caused by temperature and the polymerisation needed to be subtracted from the signal. Therefore, the data sets for 30 and 40 °C were curve-fitted with a rational curve fit (rat32) in MATLAB. The next step was to subtract the curve fit data points from the original data points. This "shape-removal" procedure enabled the illustration of the signals without the influence of temperature and polymerisation. The results are illustrated in Figure 68 and Table 21.
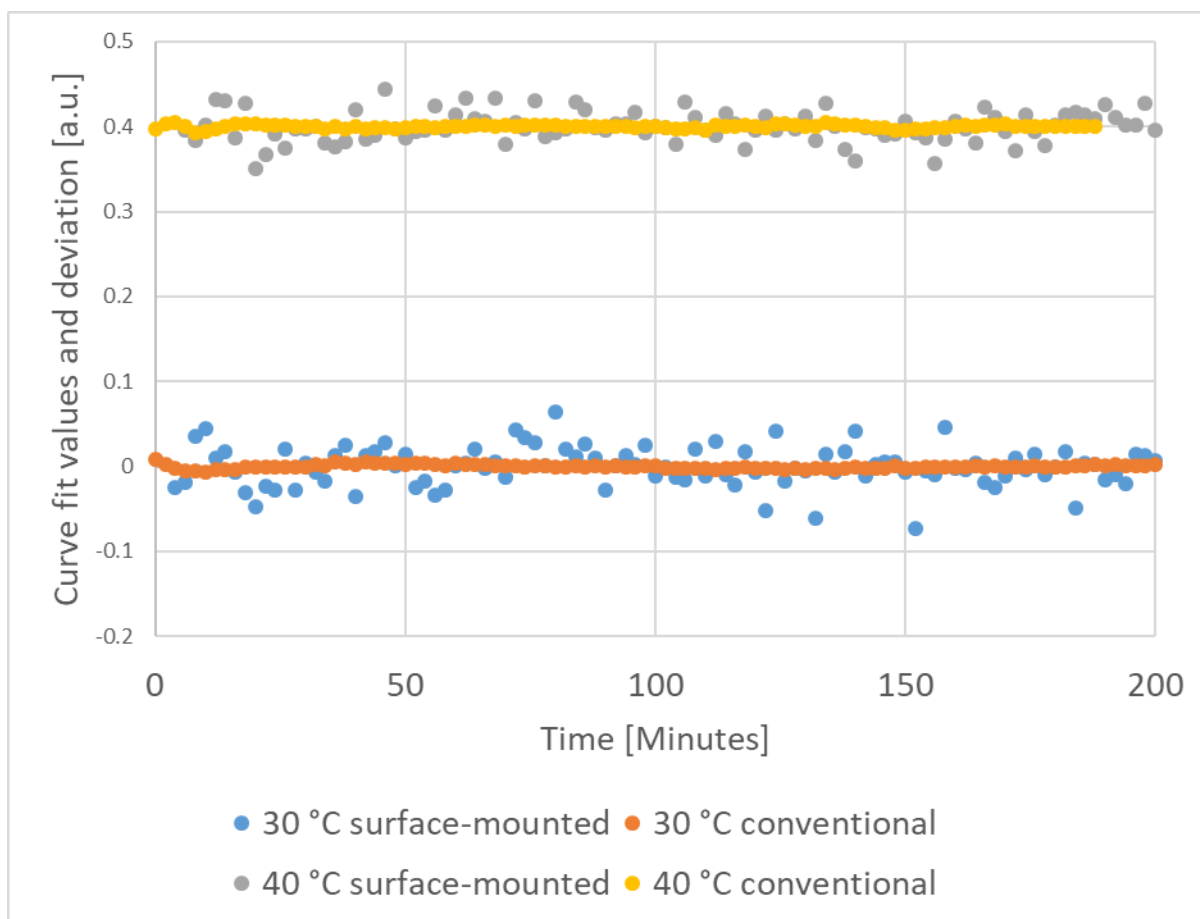
Figure 68 Comparison of signal variability of conventional and surface-mounted FTIR results.

To quantify the differences in signal variability, the conventional FTIR data for 40 °C and the surface-mounted sensor data were compared. To compare the conventional FTIR and the surface-mounted FTIR, the standard deviation was obtained from the inert 4620 cm^{-1} reference peak. The root mean square error in Table 21 was directly obtained from the MATLAB curve fitting routine and represents the signal deviation, as it expresses the magnitude of error between the data points and the curve fit. The standard deviation indicates how much the data points deviate from the mean (or curve-fit).

4.4.2.3 Comparison of conventional FTIR and surface-mounted FTIR sensors

Table 21 Numerical determination of goodness of fit.

Experiment	Curve fit R^2	RMSE	σ
30 °C conventional	0.99994	0.00217	0.00214
30 °C surface-mounted	0.99118	0.02513	0.02478
40 °C conventional	0.99996	0.00212	0.00206
40 °C surface-mounted	0.99724	0.01666	0.01646

As can be seen, the goodness of fit for the rational curve fits, expressed as R², all indicate highly congruent curve fits. The conventional curve fits show a higher R^2 value, which is an indicator of lower signal variability. The same can be said about the RMSE, which is a magnitude lower than the conventional FTIR data. A lower RMSE value indicates a smaller margin of error between the model and the data points, meaning the absolute distance between the curve fit and the data points is generally smaller. A highly similar behaviour can be observed with the standard deviation, where a lower number indicates a lower dispersion of data points around the curve fit models. When comparing the 30 and 40 °C data for both conventional and surface-mounted techniques, the most obvious difference is the slope between the aforementioned techniques, as illustrated in Figure 69.

4.4.2.3 Comparison of conventional FTIR and surface-mounted FTIR sensors
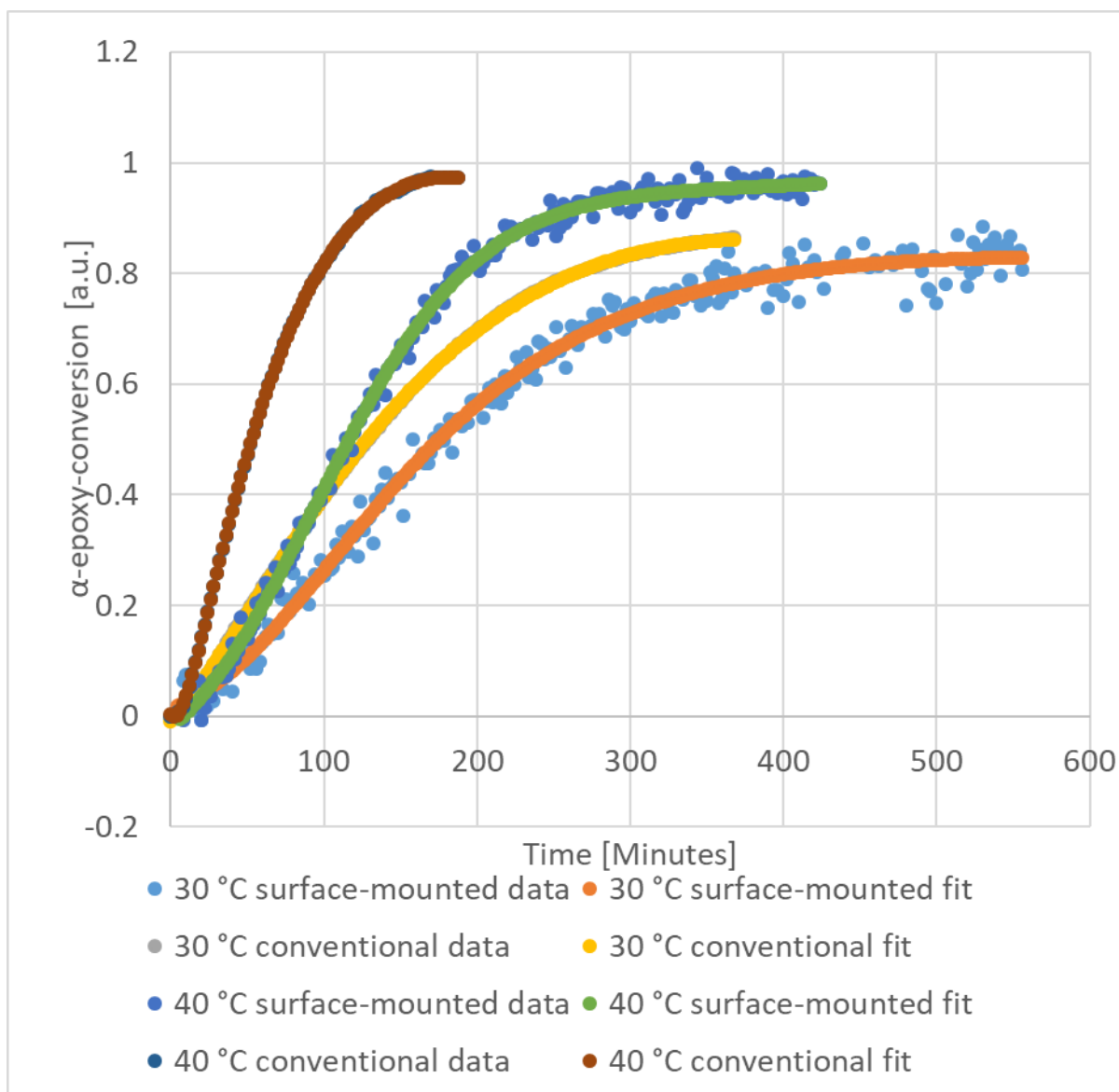
Figure 69 Comparison of cuvette-based and glove box FTIR results.

The slope difference can be explained by the different temperature-control setups. The cuvette setup had a significantly smaller volume of heat and a Peltier heater-cooler assembly at the bottom. The glove box system, on the other hand, had only a fan heater and a significantly larger volume of air to heat. The probably more influential factor is the SLJ rig. As the rig consists of two 20 mm mild-steel plates, the time to heat these up to target isothermal conditions will take considerably longer than the 1 mm path length quartz cuvette within the cuvette holder. This hypothesis is further enhanced in the Fresnel reflection sensor and the FBG sub-chapters later on. The maximum degree of conversion is assessed in Table 22.

4.4.2.3 Comparison of conventional FTIR and surface-mounted FTIR sensors

Table 22 DoC comparison of the cuvette and glove box experiments.

Experiment	DoC [%]	t [min] at DoC
30 °C conventional	86.0	350
30 °C surface-mounted	82.6	550
40 °C conventional	97.2	172
40 °C surface-mounted	96.2	420

A 4.03% difference could be observed for the 30 °C experiments and a 1.03% difference for the 40 °C experiments. This could indicate that the overall conversion is comparable, even if the temperature management until reaching isothermal conditions is variable. The percentual differences might be explained by minute differences in isothermal temperature within both experimental setups. The difference in time until reaching is believed to be, as written before, the different temperature ramp characteristics of both setups.

4.4.3. Fresnel reflection-based sensors

The FRS was embedded in the manufactured joints according to the methodology, ensuring each joint had at least one FRS to monitor the refractive index changes during the reaction. The results for the 30, 40 and 50 °C experiments are illustrated in Figure 70, Figure 71, Figure 72, and Table 23.
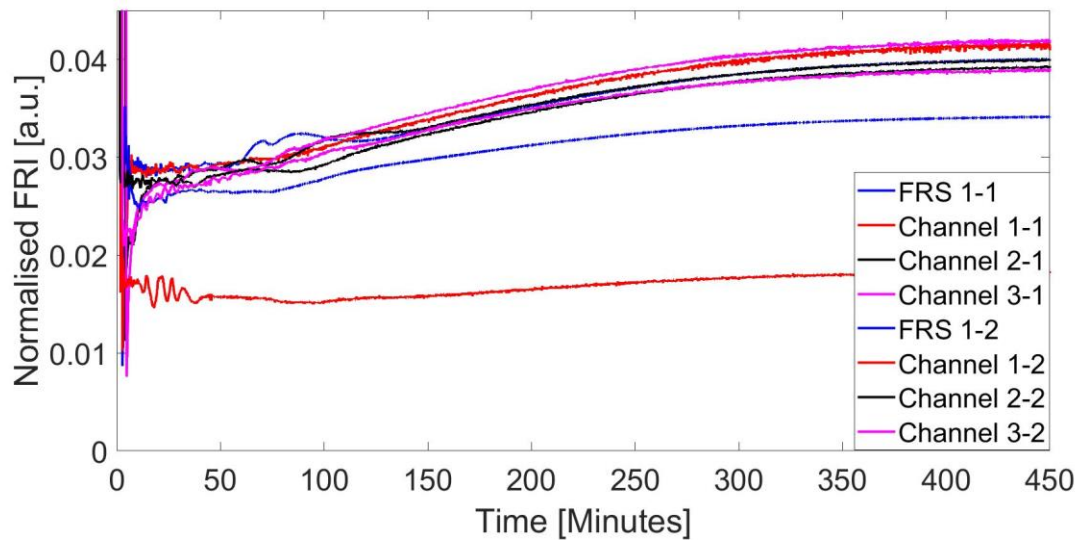
Figure 70 FRS traces for both 30 °C experiments.

Figure 70 illustrates both experiments at 30 °C. As can be seen from the normalised FRI, the signal dropped sharply after the two substrates with the fixed sensors and the applied adhesive were joined in the SLJ rig. The signal then proceeds to increase until it reaches its maximum. The initial noise, as reported in the cuvette experiments, was also observable. The initial signal drop during the heat ramp could not be observed, indicating the aforementioned lower heating rate of the glove box within the rig. One of the FRS (Channel 1-2) was considered substandard as it had a significantly reduced intensity from the start.
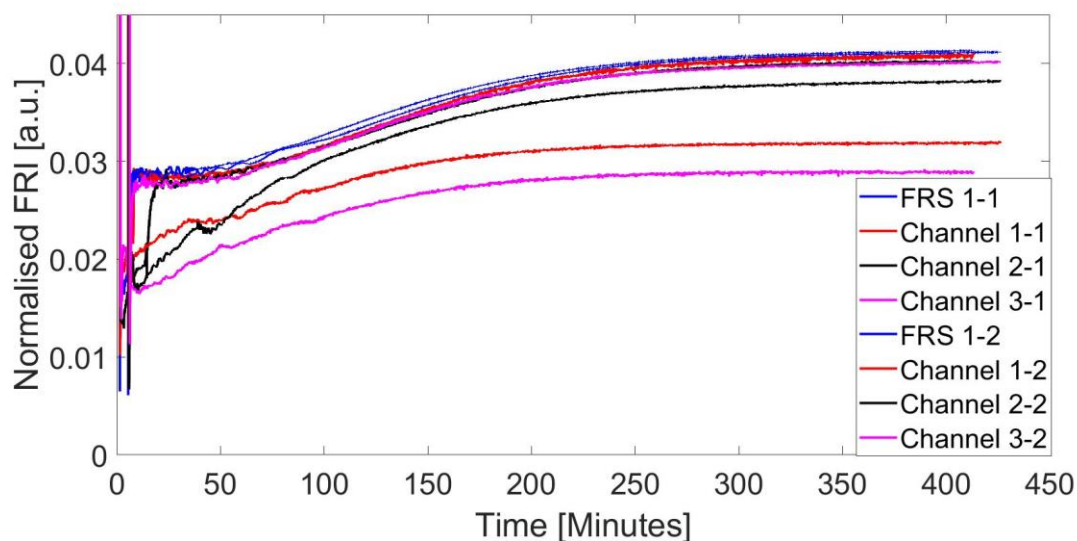
Figure 71 FRS traces for both 40 °C experiments.

4.4.3 Fresnel reflection-based sensors

The 40 °C experiments, as illustrated in Figure 71, also do not show any signal drops during the heating phase initially. As both parameters, namely temperature and cross-linking are of opposing nature at this setup, the missing signal drop is evidence for the lower heating rate as the initial signal for the FRS band without the substandard FRS (channel 1-2 and 3-1) appears to be constant for the first 50 minutes.
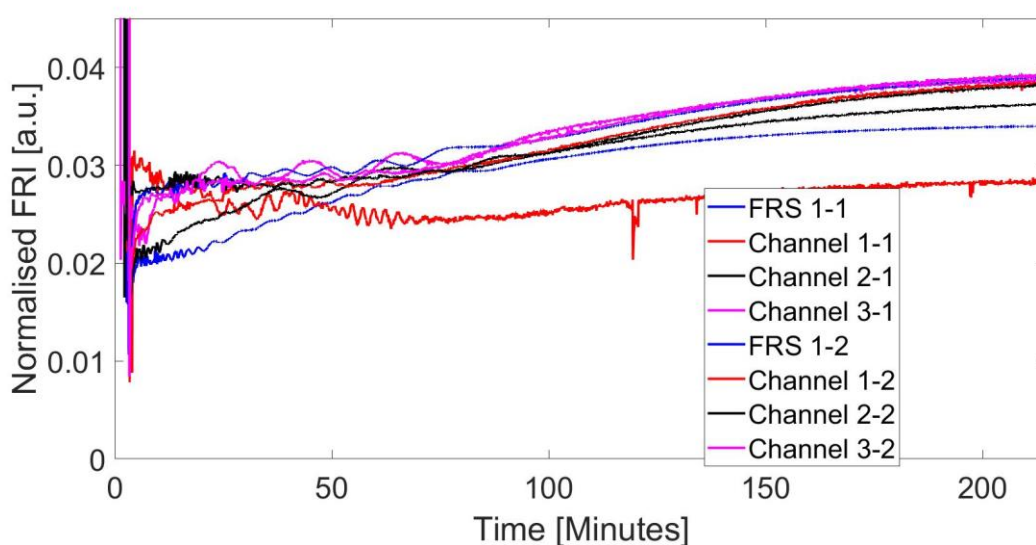
Figure 72 FRS traces for both 50 °C experiments.

The 50 °C experiments in Figure 72 appear to have higher noise levels in the initial phase of the cross-linking reaction. This might be indicative of the noise being correlated with higher temperatures.

4.4.4. Comparison of cuvette-based FRS and glove box FRS

The most distinctive difference between the two experimental setups was the signal trace scatter. Table 23 details the calculated scatter for the 30, 40, and 50 °C experiments.

4.4.4 Comparison of cuvette-based FRS and glove box FRS

Table 23 Numerical analysis of trace scatter between the cuvette and the glove box experiments.

Experiment	Avg FRI	FRS 1	FRS 2	FRS 3	FRS 4	Avg
30 °C-G1		00.679	03.127	01.247	04.487	
	0.040425					2.538
30 °C-G2		15.288	54.442	02.275	03.413	
30 °C-C	0.039913	01.093	01.180	02.626	02.538	1.859
40 °C-G1		02.464	01.405	00.197	28.730	
	0.040287					1.991
40 °C-G2		02.104	20.705	05.284	00.491	
40 °C-C	0.039652	00.137	00.279	01.591	01.734	0.935
50 °C-G1		15.466	29.337	09.720	03.826	
	0.039379					2.254
50 °C-G2		00.922	02.818	02.783	00.923	
50 °C-C	0.038669	01.365	01.462	02.273	02.176	1.819

The scatter was measured at the same time within an experimental trial and after the signal had plateaued. To calculate the average scatter, the substandard (scatter >5%) sensors were excluded, but their individual deviation from the average is included in the table. The reason why some of the FRS during the glove box experiments do deviate from the mean signal is unknown. Possible reasons might be a higher microvoid content of the polymer. For the cuvette experiments, the adhesive was syringed into the cuvette with a 21-gauge needle on top of the static mixer in order to be able to syringe the adhesive into the 1 mm path cuvette. For the glove box experiments, just the static mixer was used, which might have caused differences in the degree of mixing and microvoid and void content within the polymer. The FRS sensor core

4.4.4 Comparison of cuvette-based FRS and glove box FRS

was not in contact with the substrate surface as the FRS was fixed on the coating. The distance from the centre of the core to the substrate surface was, therefore, approximately 250 microns. A minor offset in maximum FRI was observed between the glove box and cuvette-based experiments, as illustrated in Figure 73.
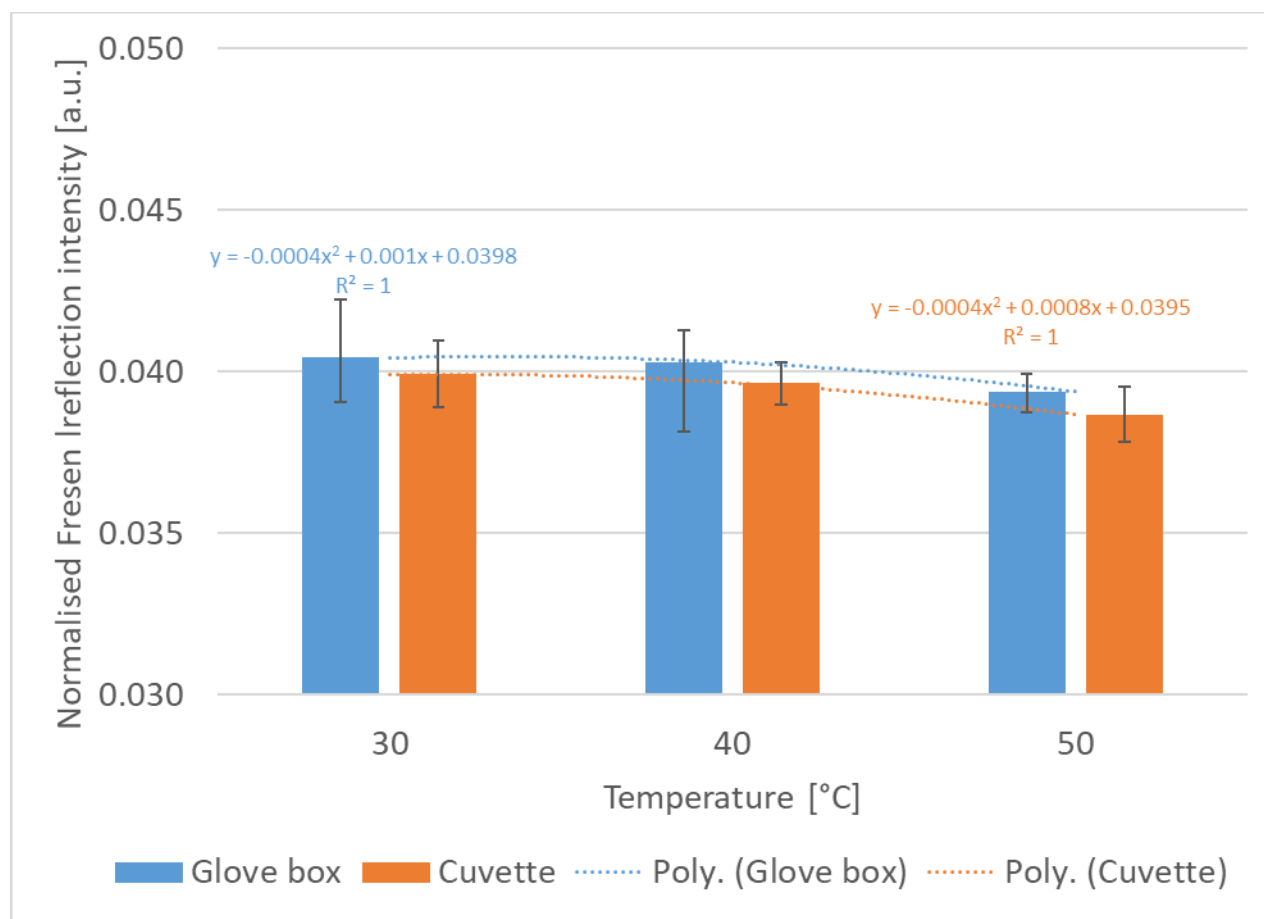
Figure 73 FRS maximum intensity decrease for the 30, 40, and 50 °C experiments.

As can be seen, the averaged maximum intensity is decreasing for increasing temperatures. This behaviour is due temperature influencing the refractive index. To determine the absolute maximum of Fresnel reflection intensity, the polymer would have to be cooled down to a set temperature, for example, 25 °C. As the experiments at higher temperatures do reach a higher degree of epoxy conversion, the FRI will be higher as well, when compared at the same temperature. The offset does behave in a similar manner for the three isothermal temperatures. The percentual deviation between cuvette-based experiments and glove box experiments is as

4.4.4 Comparison of cuvette-based FRS and glove box FRS

follows: This deviation is considered to be negligible. A possible reason for this offset are temperature management differences within both experimental setups. For better illustration, the 50 °C glove box FRS traces were plotted with a superimposed trace from the 50 °C cuvette experiment, as illustrated in Figure 74.
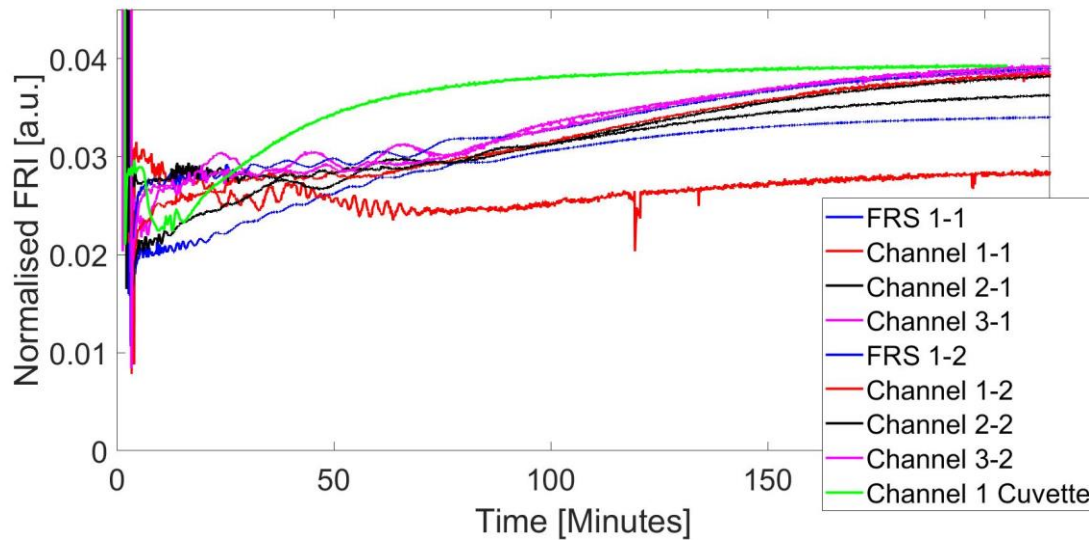
Figure 74 FRS traces with superimposed trace of the cuvette experiments at 50 °C.

The initial refractive index evolution behaves differently, due to different heating rates. The maximum refractive index reached by both experimental setups was seen to be highly similar for all FRS experiments. This is considered to be an appropriate predictor of cross-compatibility of FRS traces when monitoring cross-linking reactions in different environments.

4.4.5. Fibre Bragg grating sensors

The following subchapter details the results from the FBG measurements during the glove box experiments. A schematic of an FBG is illustrated in Figure 75, and can be linked to Equations 12-15.

4.4.5 Fibre Bragg grating sensors
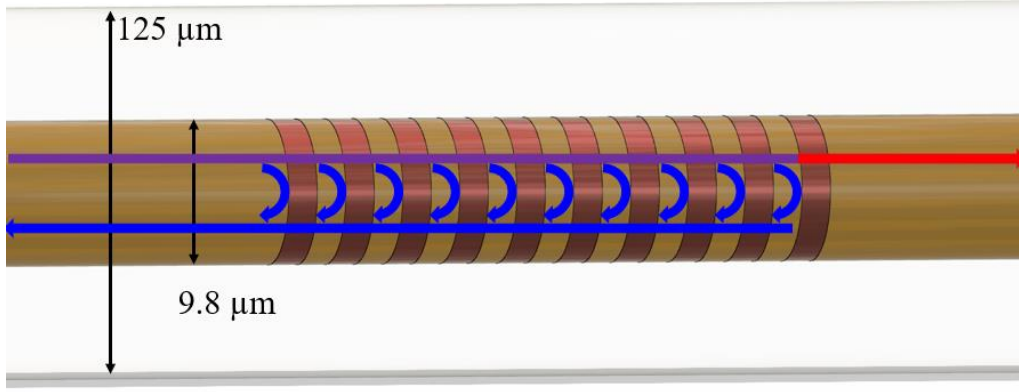
Figure 75 Schematic illustration of an FBG.

4.4.5.1. Fibre Bragg grating temperature sensors

The FBGs sealed in glass capillaries were decoupled from the strain caused by the polymer shrinkage during the cross-linking, and therefore used as temperature sensors, as illustrated in Figure 76.
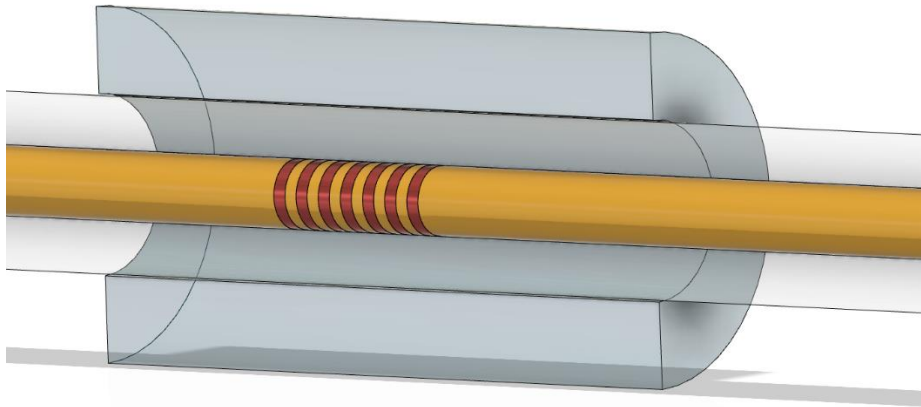
Figure 76 Schematic illustration of an FBG enclosed in a capillary.

As the FBGs were written on different central wavelengths, a normalisation was relevant to enable comparability. The normalisation was conducted using the following equation:

$$\Delta\lambda_{norm[\%]} = \frac{\Delta\lambda}{\lambda_0} \times 100 \qquad [34]$$

4.4.5.1 Fibre Bragg grating temperature sensors

, where $\Delta\lambda_{norm[\%]}$ represents the normalised wavelength shift in per cent, $\Delta\lambda$ is the absolute wavelength shift between two data points, and λ_0 is the central wavelength of the FBG at room temperature.

The normalised [%] wavelength shift for the three isothermal experiments are illustrated in Figure 77. The first 50 °C experiments were found to be substandard, as the FBG showed implausible values. Eventually, this FBG was damaged.
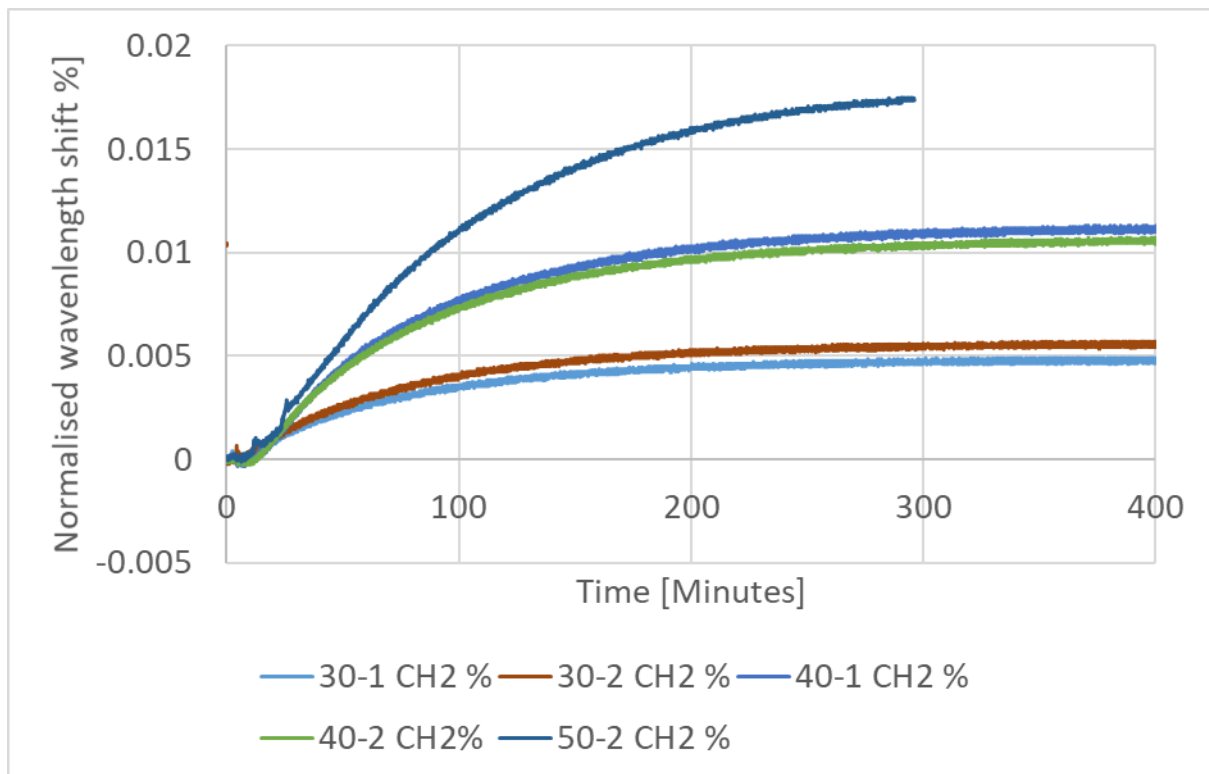
Figure 77 Normalised wavelength shifts for the temperature FBGs.

The three different isothermal target temperatures are clearly distinguishable from the normalised FBG data. A minor deviation between the 30 and 40 °C FBGs was observed, which was taken into consideration for the temperature conversion below.

The next step was to convert the normalised wavelength shift to temperature. The temperature reading of the glove box (HP21) was used to determine the starting and ending temperatures. To convert the absolute wavelength shift to temperature, a linear interpolation was used,

4.4.5.1 Fibre Bragg grating temperature sensors

assuming that the relationship between the absolute wavelength shift and temperature is of a linear nature. The conversion equation is illustrated below:

$$T = T_{min} + \Delta\lambda \times (T_{max} - T_{min}) \qquad [35]$$

where T is the conversion temperature, T_{min} is the starting temperature, T_{max} represents the target temperature, and $\Delta\lambda$ is the absolute wavelength shift.

The 40 °C temperature calibration for both FBGs and the normalised data is illustrated in Figure 78. The goodness of fit of the conversion was determined by determining the correlation coefficient and then R^2. The results are presented in Table 24.
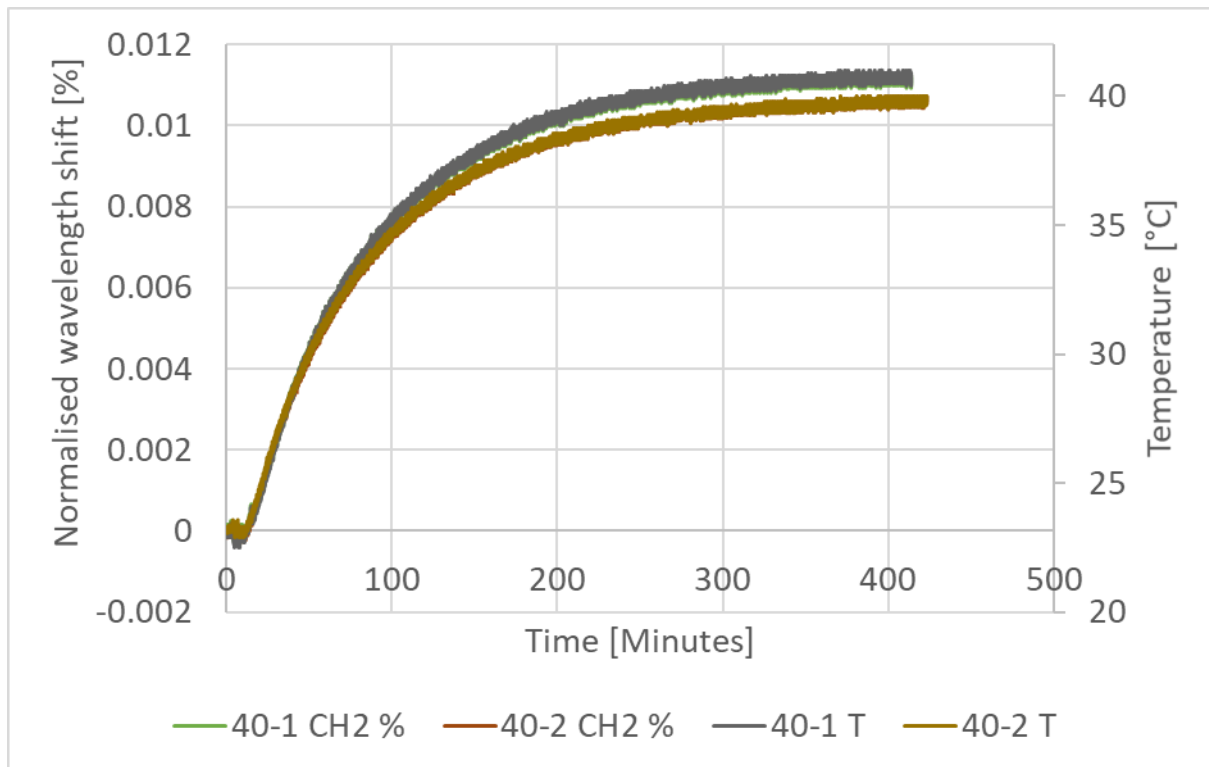
Figure 78 Temperature calibration for both 40 °C FBGs.

From this data, the temperature sensitivity coefficient could be determined for the temperature FBGs. Therefore, the conversion temperature was plotted against the absolute wavelength shift of each FBG. The slope of the linear fits represents the temperature sensitivity. The results are illustrated in Table 24 and Figure 79.

157

4.4.5.1 Fibre Bragg grating temperature sensors

Table 24 Determined isothermal temperatures and temperature sensitivities.

Experiment	R^2 of T-conversion	T-isothermal [°C]	K_T [pm°C^{-1}]
30-1	1	29.848±0.211	11.4
30-2	1	30.840±0.193	11.7
40-1	1	40.722±0.318	09.6
40-2	1	39.792±0.208	10.0
50-2	1	49.958±0.147	10.2

The resulting maximum temperature deviation within the adhesive joints after reaching isothermal conditions was determined to be 0.318 °C. The maximum deviation of the glove box (HP21) was calculated to be 0.72 °C. As both maximum deviations were found within the same experiment (40-1), it may be concluded that the temperature FBGs are sensitive to minute deviations within the environment. The lower deviation within the adhesive joint can be explained by the SLJ rig, and on a smaller scale, the cross-linking adhesive itself behaves as a thermal buffer for temperature deviations.

4.4.5.1 Fibre Bragg grating temperature sensors
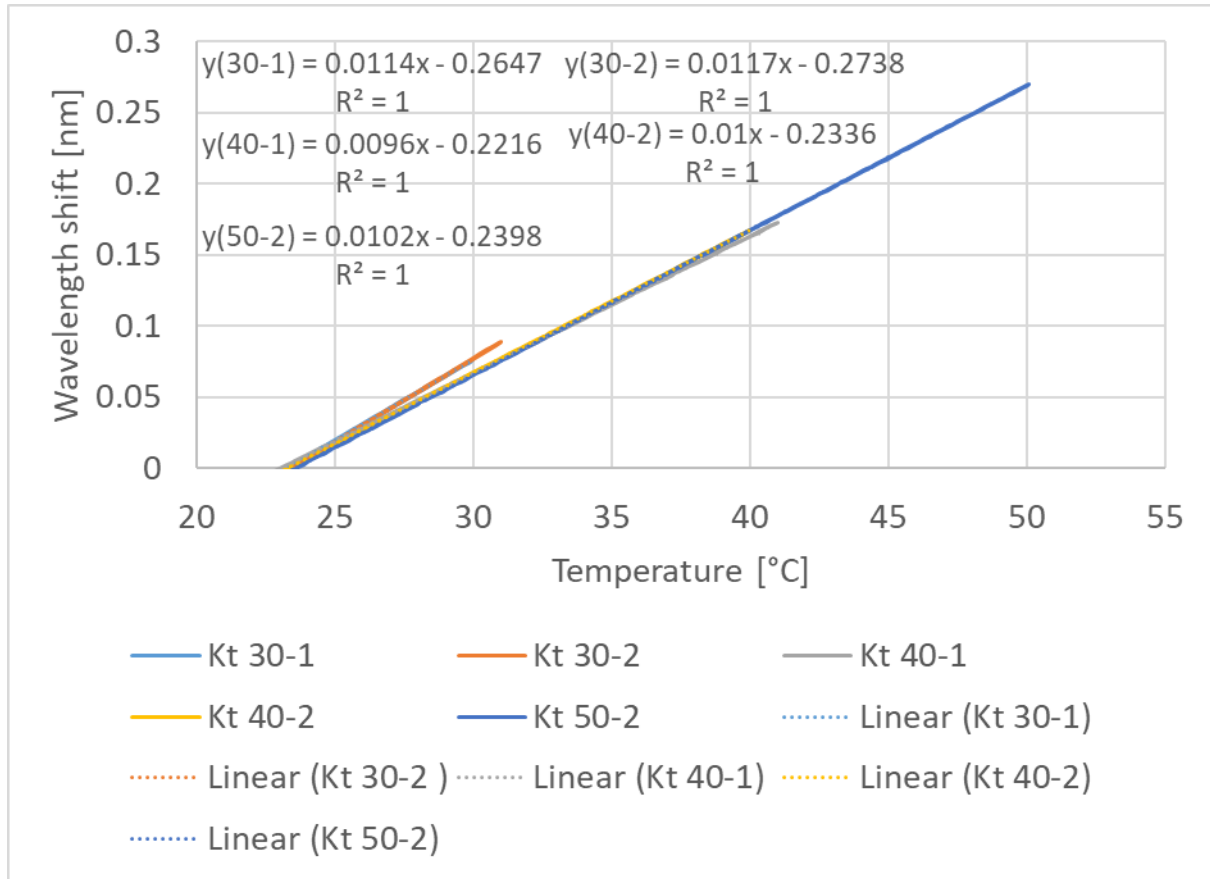
Figure 79 Determined temperature sensitivities for embedded FBGs.

The determined temperature sensitivities range from 9.6 to 11.7 pm°C^{-1}, which correlates with the literature (Mahakud et al., 2013, Wang et al., 2018). The two 30 °C experiments seem to have a slightly higher sensitivity, but overall, the sensitivity band is considered consistent. As the temperature FBGs represent the temperature within the adhesive joints, the thermal lag between the adhesive joints and the glove box temperature sensor could be determined. Therefore, the HP21 data and the FBG temperature data are illustrated in Figure 80.

4.4.5.1 Fibre Bragg grating temperature sensors
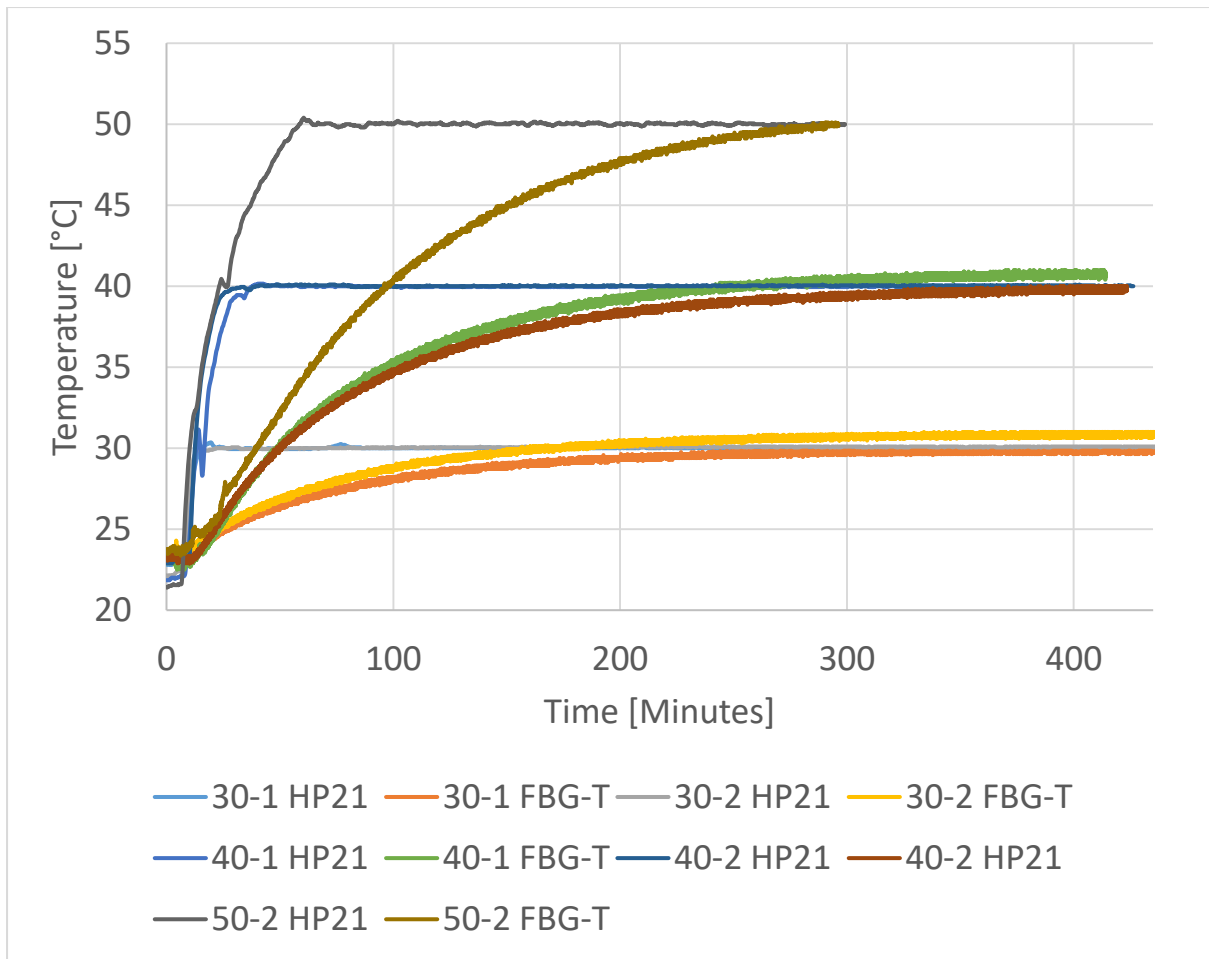
Figure 80 Illustration of the HP21 and FBGs reaching isothermal conditions.

The temperature within the glove box reaches the target temperature significantly faster than the temperature in the adhesive joints. As the joints are fixed within the SLJ manufacturing rig, the mild-steel rig heats at a significantly reduced rate compared to the air within the glove box, causing the observed difference in reaching the target temperatures. The determined time differences for reaching isothermal conditions (no signal increase) are presented in Table 25.

4.4.5.1 Fibre Bragg grating temperature sensors

Table 25 Numerical comparison of HP21 and FBGs reaching isothermal conditions.

Experiment	HP21 [min]	FBG [min]	Δ-t [min]
30 °C	17.0	310	293
40 °C	34.0	320	286
50 °C	58	285	226

The increase in time for the HP21 appears to be of a linear nature, which indicates a constant heat ramp. The measured temperature within the adhesive joints is not of a linear nature. While the 30 and 40 °C runs show a similar offset compared to the glove box data, the 50 °C experiment reaches the target temperature significantly faster. Possible reasons for this might be different room temperatures and possibly a different fan position. The heater did not have a locking mechanism, so it is possible that it was slightly misaligned and heated the SLJ rig in a more direct manner.

4.4.5.2.   Fibre Bragg grating temperature and strain sensors

The second applied FBG type was used to determine the adhesive shrinkage during the isothermal glove box experiments. These FBGs were not enclosed in a glass capillary and were, therefore, sensitive to temperature and strain, as shown in Figure 81.
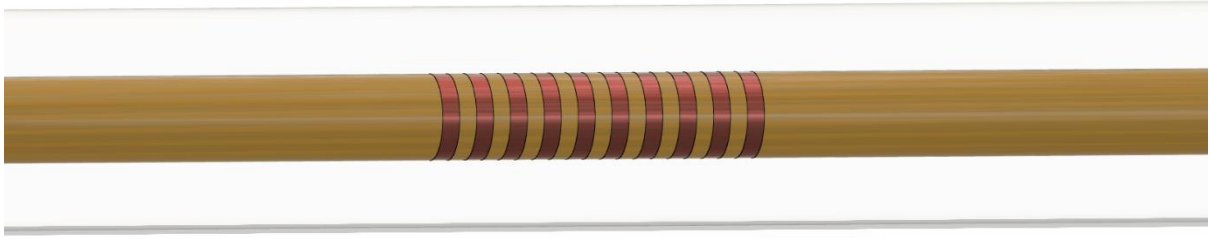
Figure 81 Schematic illustration on an FBG without capillary.

To illustrate the temperature and strain evolution during the experiments, Figure 82**Error!**

Reference source not found. presents one temperature and one temperature + strain FBG from

each isothermal cross-linking experiment.
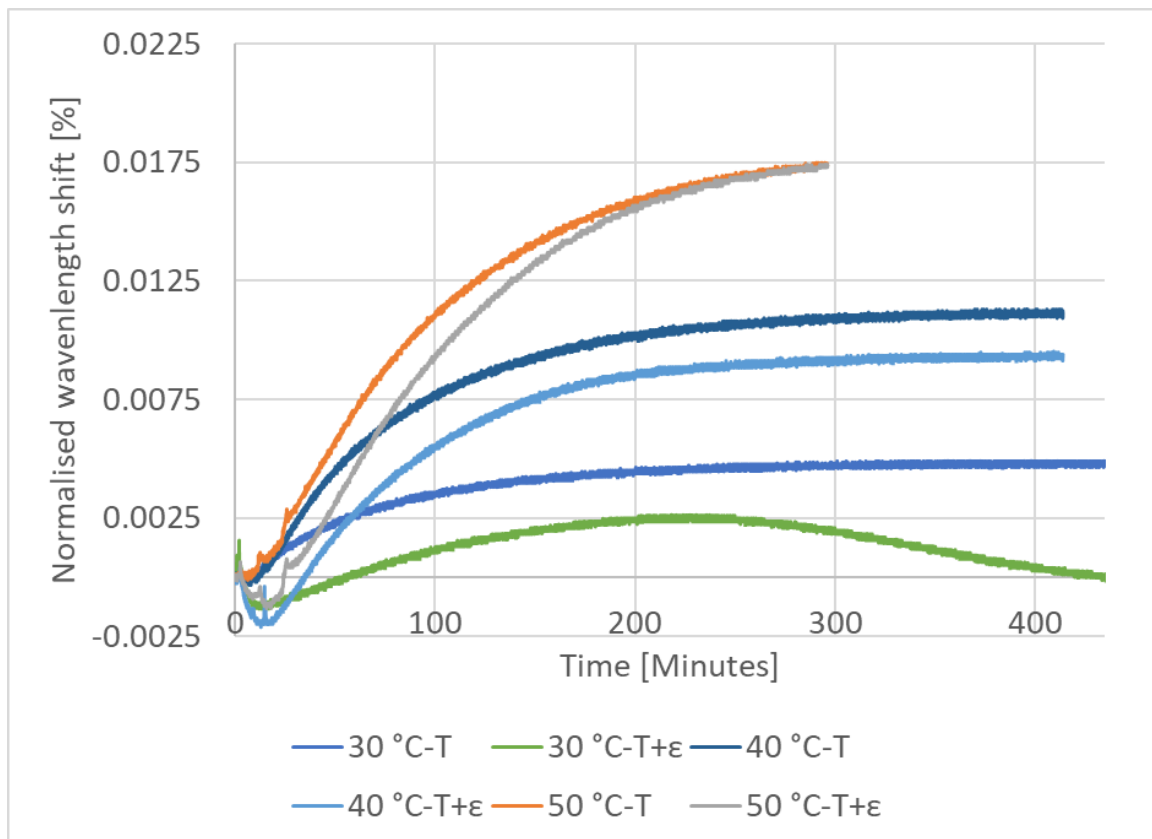
Figure 82 Strain and temperature data of the embedded FBGs during the 30, 40, and 50 °C experiments.

4.4.5.2 Fibre Bragg grating temperature and strain sensors

When examining both 30 °C FBGs, the wavelength shifts to the red until it reaches the target temperature and then remains constant. The temperature + strain sensor firstly blueshifts after the SLJ was set up and fixed into the rig. This initial decrease is due to the polymer already applying pressure on the fibre. After the initial decrease, it redshifts quasi-parallel to the temperature FBG, which correlates with the literature (Kim et al., 2013). The following blueshift indicates the evolving shrinkage pressure on the optical fibre becoming more prominent as the temperature is constant. This strain prominence decreases with increasing temperature. The reason for this is the relation between temperature sensitivity and strain sensitivity of the FBG. To determine the strain caused by the shrinkage of the adhesive, the temperature needed to be decoupled from the strain. The temperature and strain-dependent wavelength shifts can be described by the following equation:

$$\Delta\lambda_B = \lambda_B \times (k_T \times \Delta T + k_\varepsilon \times \varepsilon)$$ [36]

, where $\Delta\lambda_B$ is the total Bragg wavelength shift, λ_B is the initial Bragg wavelength or central wavelength, k_T and k_ε represent the temperature and strain sensitivity, ΔT stands for the temperature change, and ε is the strain.

As SLJ testing was not conducted with the embedded FBGs, k_ε could not be determined. As the FBG was written into a silica fibre, a typical reference value of $p_{11} = 0.0013$nm/$\mu\epsilon$ for the strain sensitivity was obtained from literature (Bertholds and Daendliker, 1994). ΔT and k_T could be obtained from the temperature FBGs. The resulting shrinkage-induced compressive strain data for the 30, 40 and 50 °C experiments are illustrated in Figure 83.

4.4.5.2 Fibre Bragg grating temperature and strain sensors
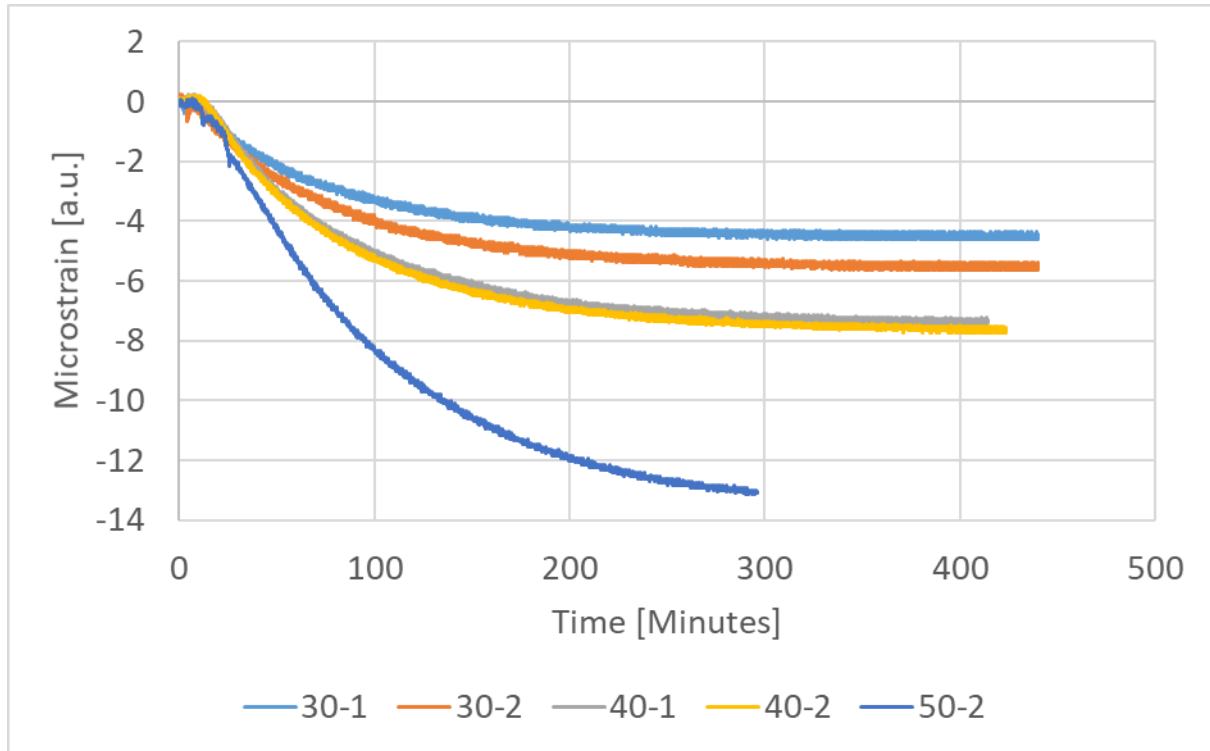
Figure 83 Shrinkage-induced compressive strain data for the 30, 40 and 50 °C experiments.

After the decoupling of strain and temperature, the temperature-dependent evolution of compressive strain can clearly be observed. As the shrinkage is directly correlated to the DoC, a higher isothermal temperature will result in a higher DoC and, therefore, a larger compressive strain. The two 30 °C experiments do show scatter, which might be caused by different factors, namely (i) the homogeneity of the mixed adhesive, (ii) a larger void within the adhesive surrounding or touching the FBG, (iii) minute bond-line thickness variations, and (iv) the FBG positioning on the overlap area. Figure 84 illustrates the averaged resulting strain for the different isothermal experiments.

4.4.5.2 Fibre Bragg grating temperature and strain sensors
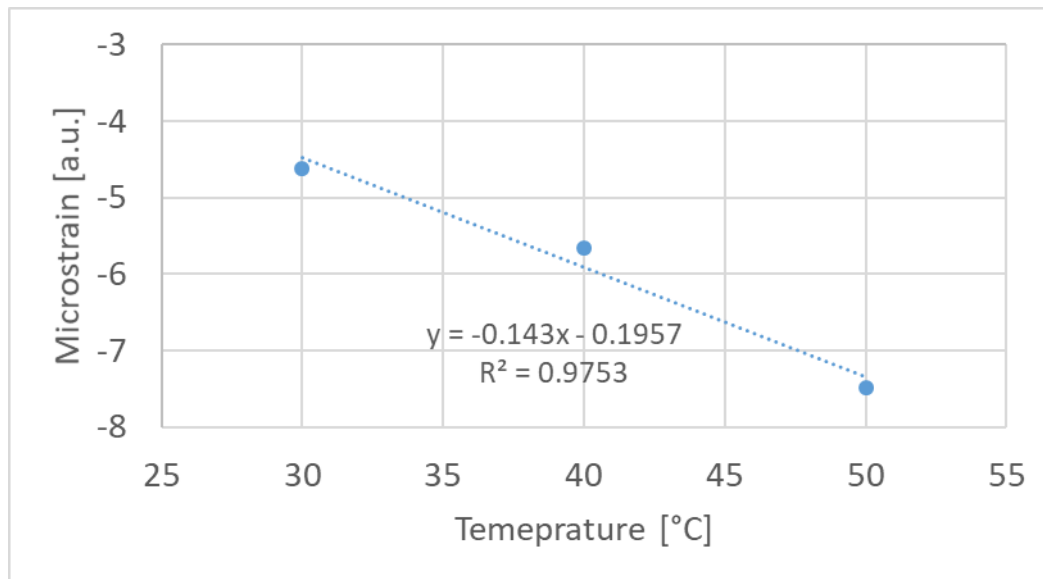
Figure 84 Strain response of FBGs.

When plotting the determined microstrain against the isothermal target temperature, a liner relationship could be observed. This might be used as a predictor of temperature-dependent shrinkage behaviour for this specific adhesive. It has to be noted that the strain sensitivity was not determined but assumed. A proper strain calibration might result in slightly different sensitivities and, therefore, affect the linear relationship between temperature and shrinkage. The shrinkage-induced strain values in the literature are mostly larger (165, 167), but it is worth noting that these values are primarily obtained from composite manufacturing experiments, where the matrix volume, and therefore the shrinkage, is significantly larger.

4.4.6.   Fabry-Perot cavity sensors for refractive index sensing

The following subchapter presents the results of refractive index measurements using extrinsic FP cavities and the associated custom-written code, which enables peak detection in conjunction with the SM130 interrogator. A schematic of an extrinsic FP sensor is illustrated

in Figure 85. The extrinsic FP sensors were manufactured similarly to the surface-mounted

FTIR sensors, but with a significantly shorter cavity length of approximately 41.7 microns.
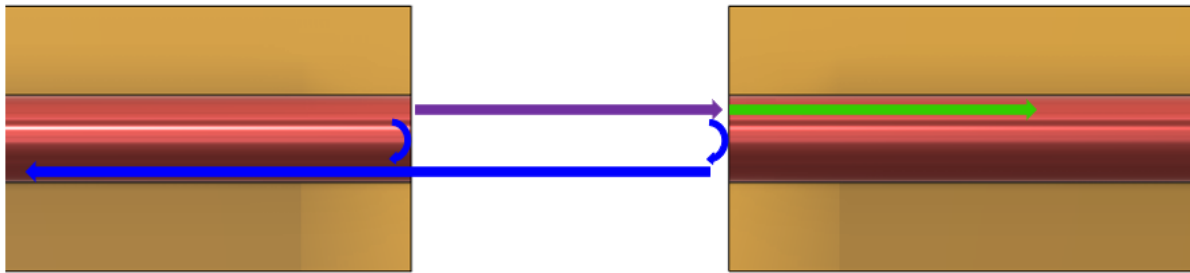
Figure 85 Schematic of the reflections within an FP

4.4.6.1. Development and validation of a peak-tracking routine to enable FP data analysis

The SM130 interrogator was designed to automate FBG interrogation but was not capable of

monitoring FP fringe movement via peak tracking. As it was possible to save the full FP spectra,

a set of programs was developed using MATLAB to enable peak tracking for the FP sensors.

The code was split into three segments, namely (i) data extraction and conversion into Excel,

(ii) Fourier curve fitting and determination of goodness of fit, and (iii) dy/dx peak tracking. A

schematic of the overall MATLAB routine is illustrated in Figure 86.
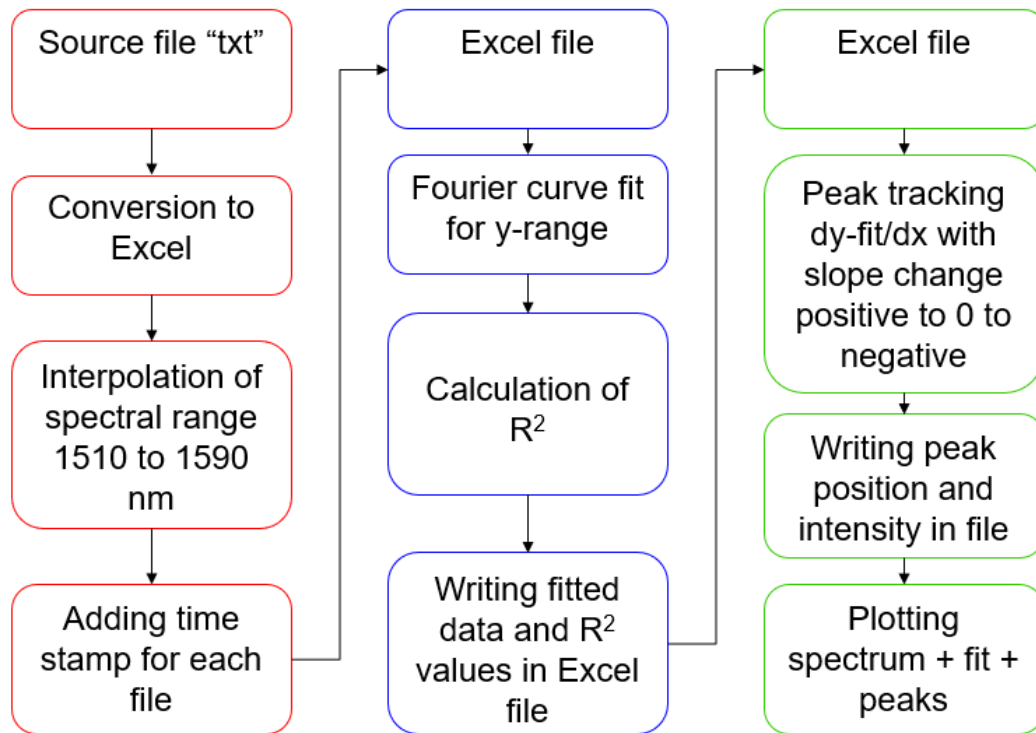
Figure 86 Flow diagram of MATLAB routine.

To validate the peak-tracking routine, an artificial FP signal was simulated with the same amount of x-data points (12874) as the spectra from the SM130 to approximate the exact resolution. Points of interest were noise levels and fringe spacing. Four different fringe spacings were used, namely 5, 10, 15, and 22.5. As the amount of x-data points was constant, increasing fringe spacing resulted in fewer fringes, representing a smaller cavity. Additionally, three noise levels were simulated, namely 0.01 (smooth), 0.1 (medium noise), and 0.25 (high noise). The peak positions were manually pre-determined from the source data, as this function had no noise. Figure 87 illustrates the different noise levels for the FSP-10 configuration.

4.4.6.1 Development and validation of a peak-tracking routine to enable FP data analysis
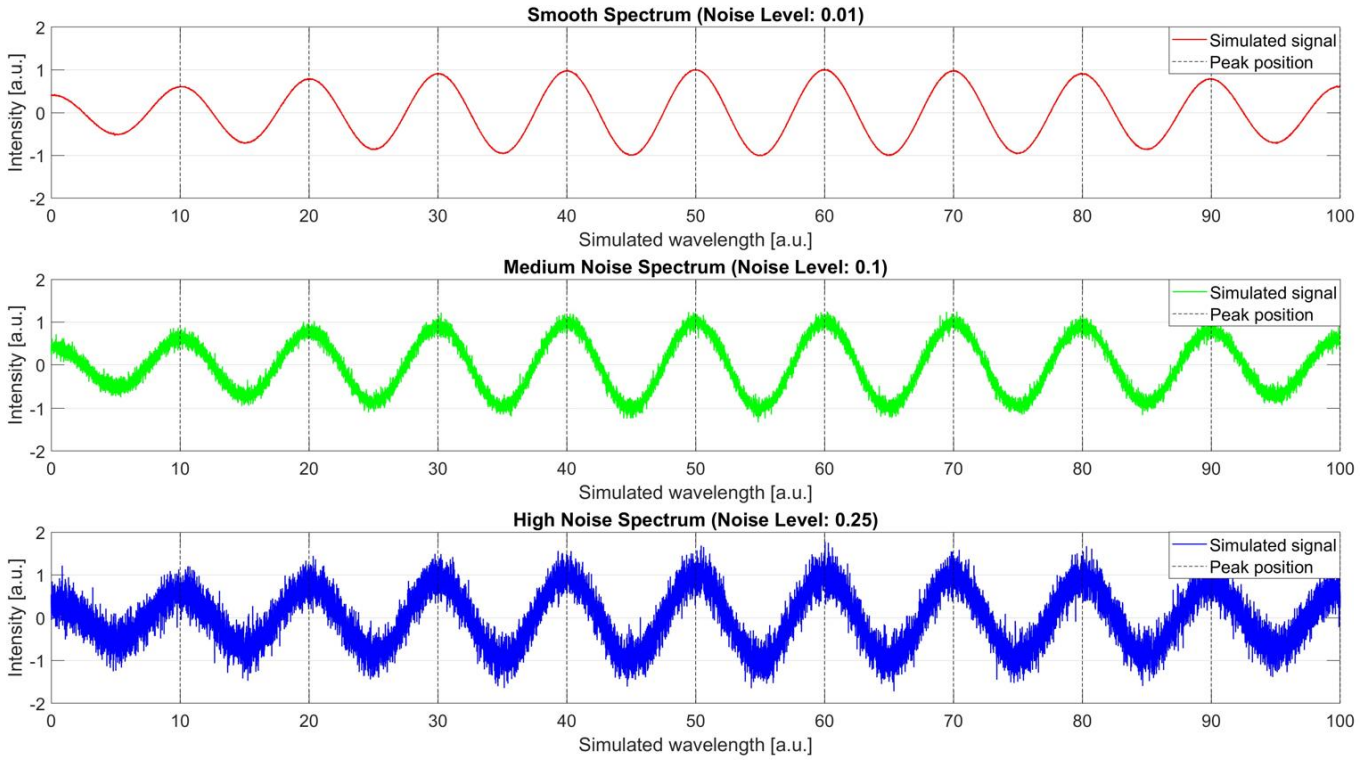
Figure 87 Simulated comparison of noise levels.

The determined peak positions were observed to shift slightly from the theoretical peaks. The observed shift was taken into consideration for the peak precision determination, as they were the actual source data for the peak tracking routine. The standard deviation of the observed peak drift was found to be 0.272%. As this shift was observed between theoretical values and manually determined source data (not-fitted), the "drifted" peaks were used as reference and not the theoretical values. To visualise the peak-tracking, Figure 88 illustrates the FSP15-M configuration.

4.4.6.1 Development and validation of a peak-tracking routine to enable FP data analysis
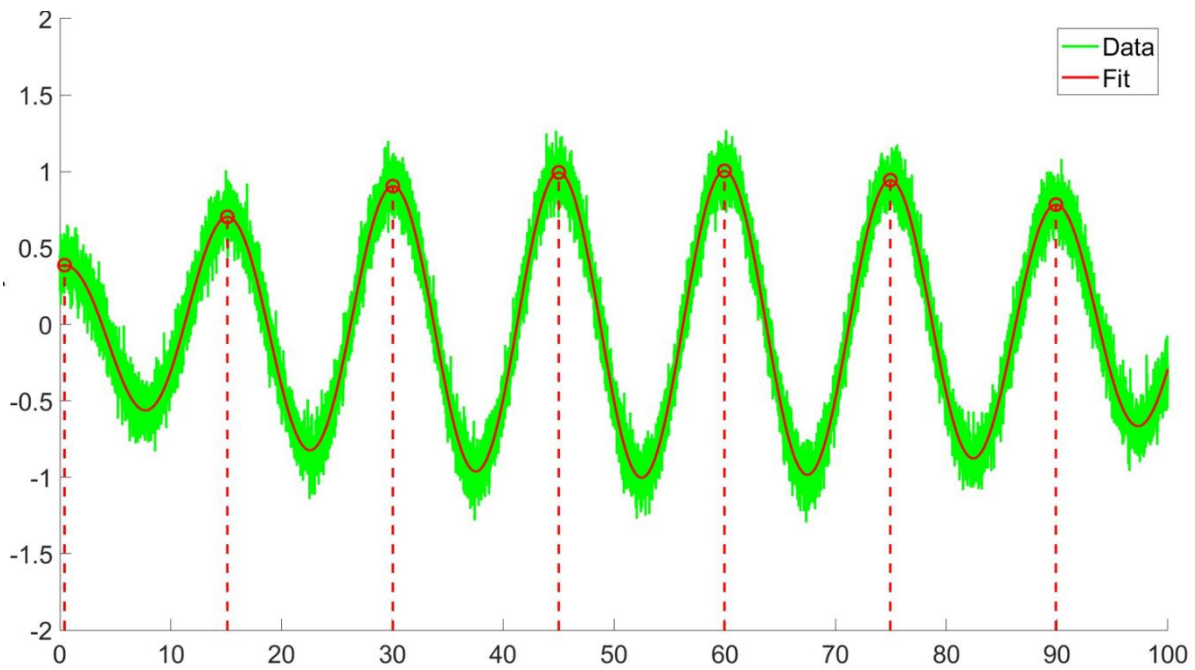
Figure 88 Visualisation of the raw spectra and peak tracking.

To evaluate the peak tracking at changing cavity length, the standard deviation of the smooth spectrum at different fringe spacings was determined. The results regarding the percentual standard deviation for all iterations are presented in Table 26. The standard deviation [%] for the FSPX-S is illustrated in Figure 89.

4.4.6.1 Development and validation of a peak-tracking routine to enable FP data analysis
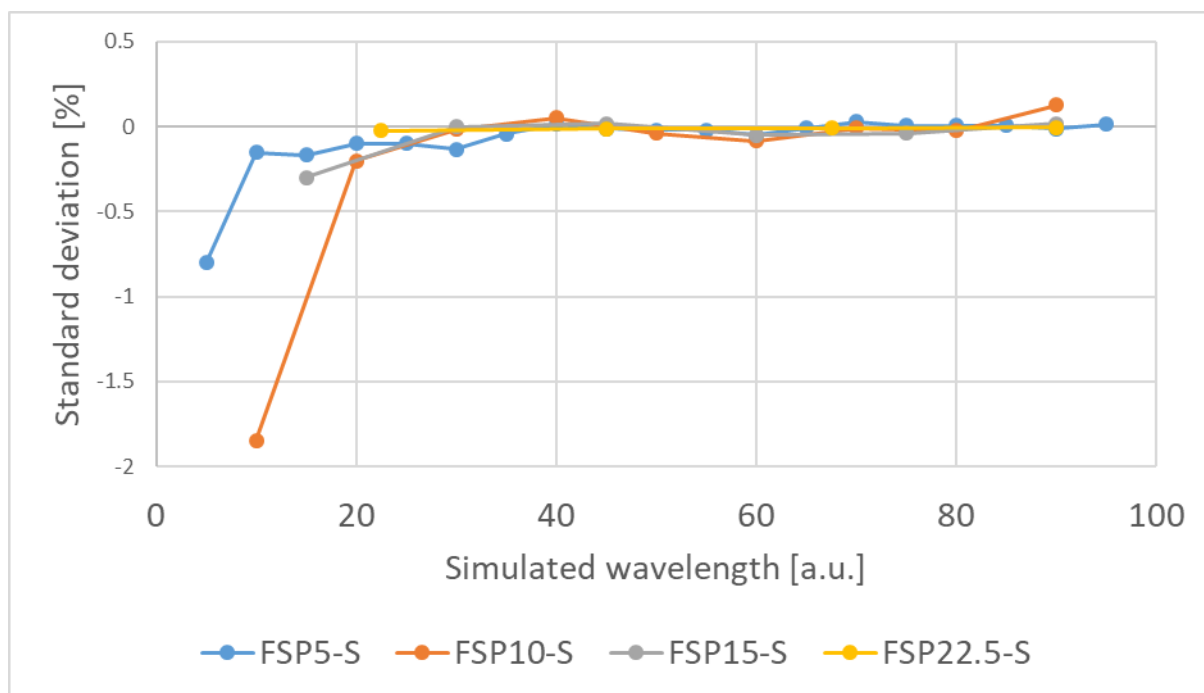
Figure 89 Standard deviation [%] distribution for the different configurations.

As the noise level was constant, the more significant standard deviation error is believed to be caused by the curve fit not being highly aligned with the simulated data.

Table 26 Determined standard deviation for the different configurations.

Configuration	Standard deviation Smooth noise [%]	Standard deviation Medium noise [%]	Standard deviation High noise [%]
FSP5	0.1846	0.1404	0.0981
FSP10	0.6139	0.6122	0.6455
FSP15	0.0319	0.1216	0.1911
FSP22.5	0.0074	0.0272	0.1245

The deviation generally was seen to be higher at the first peaks, especially for the FSP5 and FSP10 configurations. This indicates that the Fourier curve fit is not highly congruent for

4.4.6.1 Development and validation of a peak-tracking routine to enable FP data analysis

spectra with a large number of peaks (larger cavities). To assess the congruency of the Fourier fit with the respective data, the R^2 values were determined and are presented in Table 27.

Table 27 Determined R^2 values for the different configurations.

Configuration	R^2 smooth noise [%]	R^2 medium noise [%]	R^2 high noise [%]
FSP5	0.9724	0.9467	0.8326
FSP10	0.9791	0.9533	0.8401
FSP15	0.9997	0.9743	0.8547
FSP22.5	0.9997	0.9726	0.8490

A prominent difference in R^2 between FSP10 and FSP15 could be observed, indicating that the used 8th-degree Fourier fit is reaching its limits at larger FP cavities. To illustrate this difference, Figure 90 illustrates the FSP10-S and Figure 91 illustrates the FSP15-S plots from the curve fit routine.

4.4.6.1 Development and validation of a peak-tracking routine to enable FP data analysis
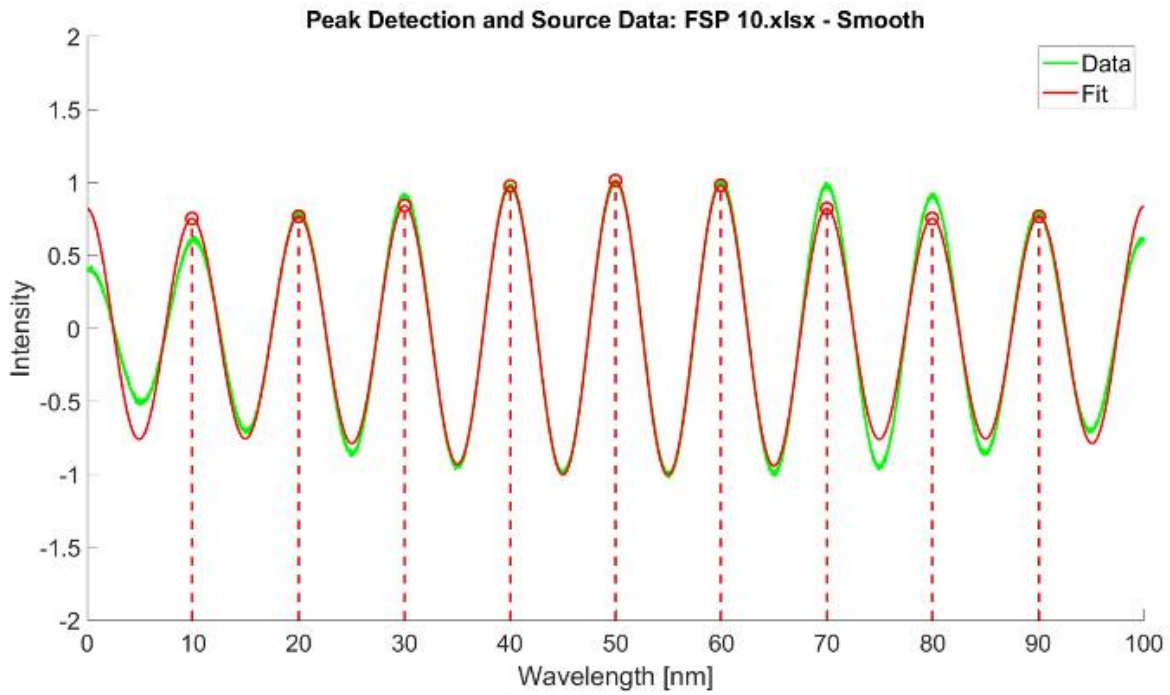
Figure 90 Peak tracking routine used on the FSP10-S simulated spectrum.
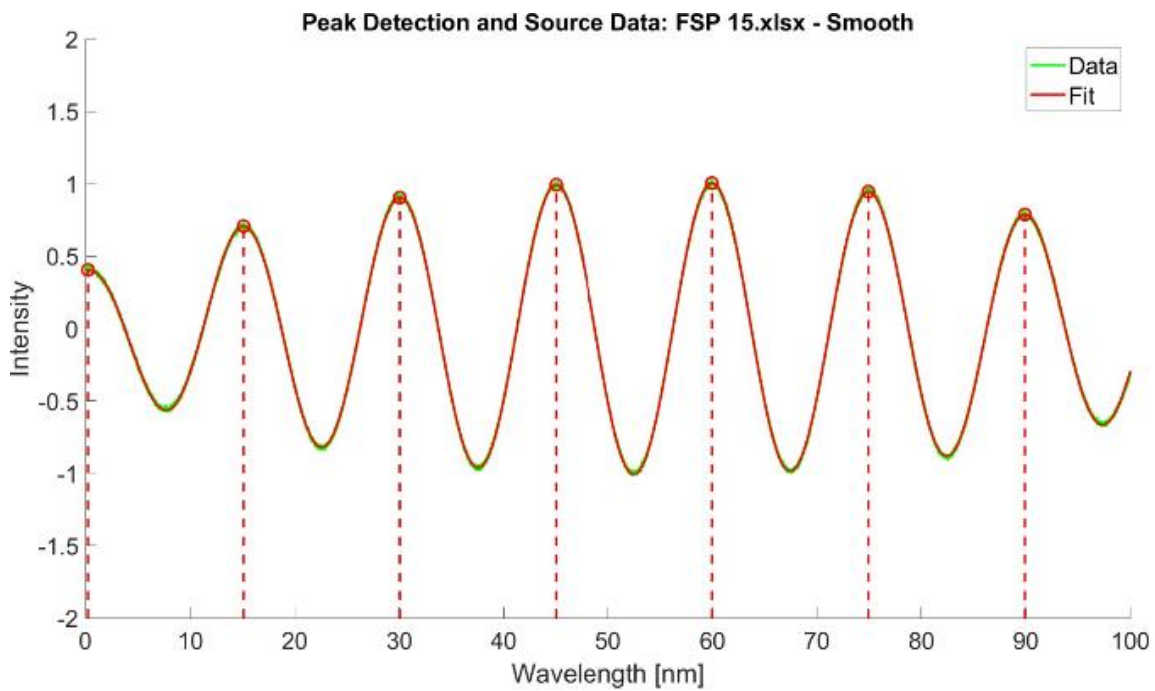
Figure 91 Peak tracking routine used on the FSP15-S simulated spectrum.

The non-congruency is observable for the FSP10-S dataset. The peak intensities are more affected than the peak positions. From this analysis, the peak-fitting routine demonstrates appropriate peak tracking. The main factor for precise peak tracking is the goodness of fit of

4.4.6.1 Development and validation of a peak-tracking routine to enable FP data analysis

the Fourier curve fit. The influence of noise was the second parameter assessed. As shown in Table 27, the R^2 values decrease with increasing noise. This is an expected behaviour as the noise deviates from the average signal. Therefore, the goodness of fit decreases. This decrease is not a predictor of reduced peak tracking precision, as the tracker determines the positions from the curve fit. The absolute deviation from the reference peaks was investigated for the FSP15 and FSP 22.5 configurations to determine the noise influence, as these were affected by the demonstrated curve-fitting errors. To illustrate the deviation, the data sets were combined, and for the overlapping peaks, the maximum value of both datasets was chosen. This resulted in a dataset with "Smooth noise", "Medium noise", and "High noise" as series, as illustrated in Figure 92.
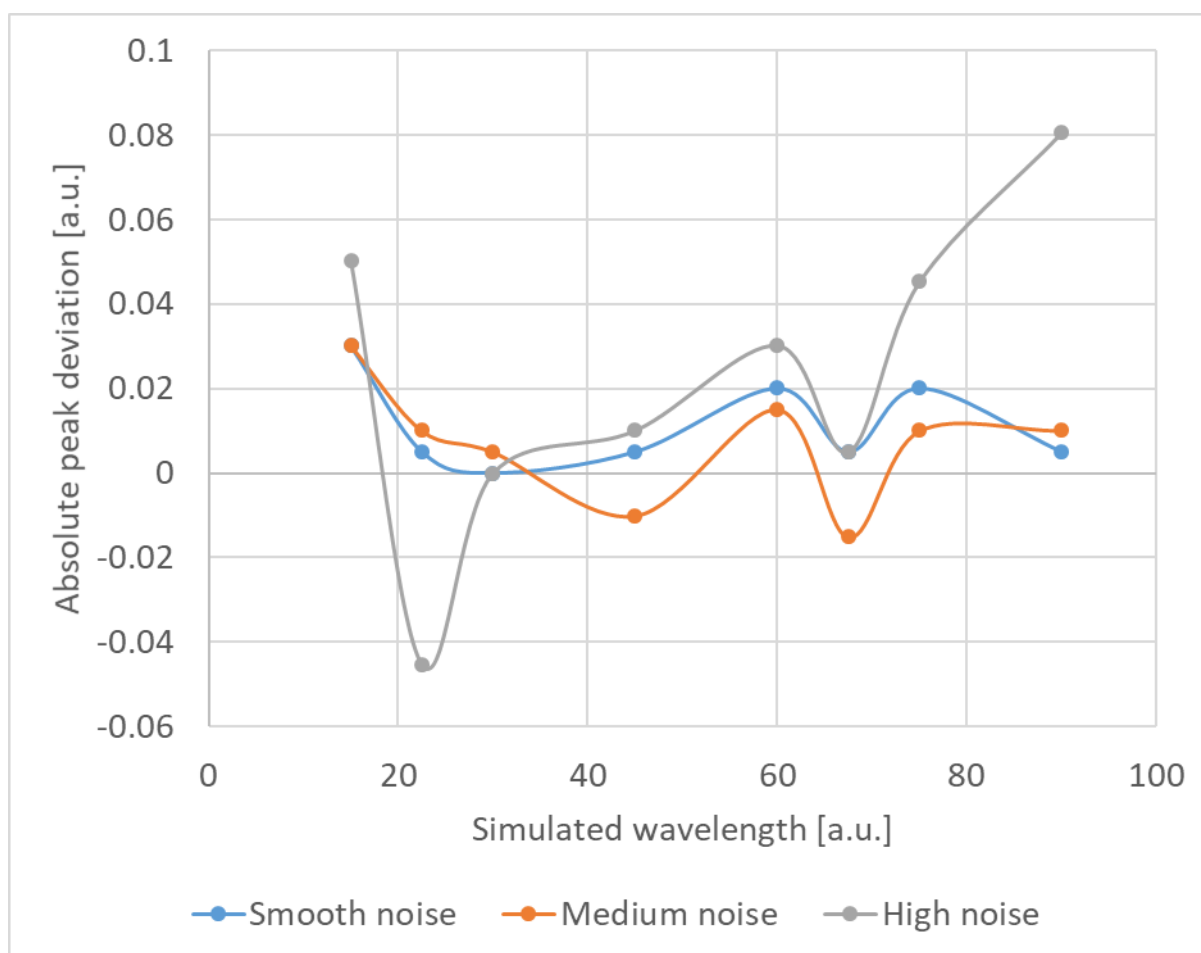
Figure 92 Determined peak deviation for the different noise levels.

4.4.6.1 Development and validation of a peak-tracking routine to enable FP data analysis

The overall peak deviation is largely similar for the noise levels, indicating that it may also be curve-fit correlated. The margin of deviation increases slightly with increasing noise levels. From this data, the Mean Absolute Error (MAE) could be determined for the three noise levels by using the following equation:

$$MAE = \frac{1}{N} \sum_{i=1}^{N} \left| \frac{x_{tracked} - x_{ref}}{x_{ref}} \right| \qquad [37]$$

, where N is the total number of peaks, $x_{tracked}$ is the peak position of the peak-tracking routine, and x_{ref} stands for the reference peak position. The results for FSP15 and FSP22.5 are illustrated in Figure 93. FSP10 and FSP5 were not included, as the error was influenced by the curve-fit itself and, therefore, the MAE calculation would be falsified.
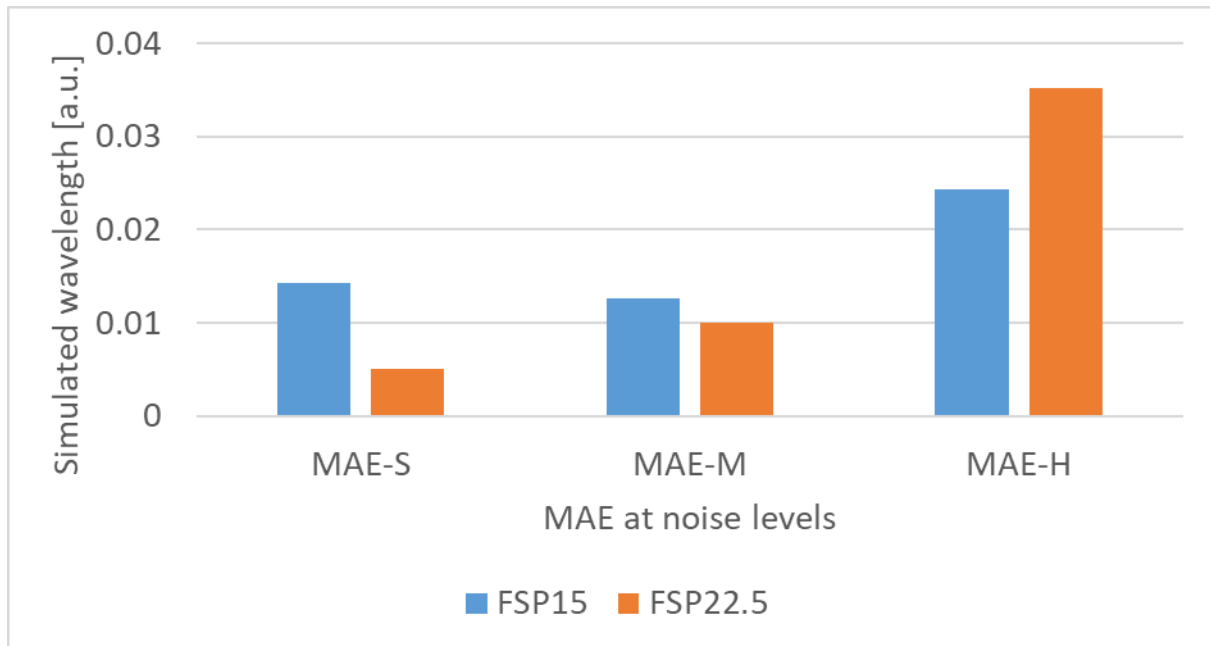
Figure 93 MAE influence at different noise levels.

In summary, the peak tracking routine was found appropriate, provided sufficient goodness of fit is a given. As the manufactured FP for refractive index sensing are small (~ 40 microns), the goodness of fit could not negatively affect the peak tracking results. Noise levels might affect the accuracy of the peak tracking, but from the previous MAE determinations, possible

4.4.6.1 Development and validation of a peak-tracking routine to enable FP data analysis

noise effects might be negligible. The accuracy of the fringe intensity was not investigated, as it was considered irrelevant for the refractive index determination. The intensities (y-position) seem to be highly congruent when observing the plotted data, under the condition that the curve fits are congruent.

4.4.6.2. Monitoring refractive index changes within adhesive joints

Intrinsic FPs

Capillary-enclosed intrinsic FP sensors were utilised to assess whether an FP can be embedded within the adhesive without being subjected to strain induced by polymerisation shrinkage. If successful, this approach would enable the integration of strain sensors that remain unaffected by mechanical deformation, thereby eliminating the need for decoupling mechanisms when used as strain gauges.

To evaluate this, interference peaks were tracked, and the free spectral range (FSR) was calculated between successive peaks, which were then averaged. The results are presented in Figure 94.

4.4.6.2 Monitoring refractive index changes within adhesive joints
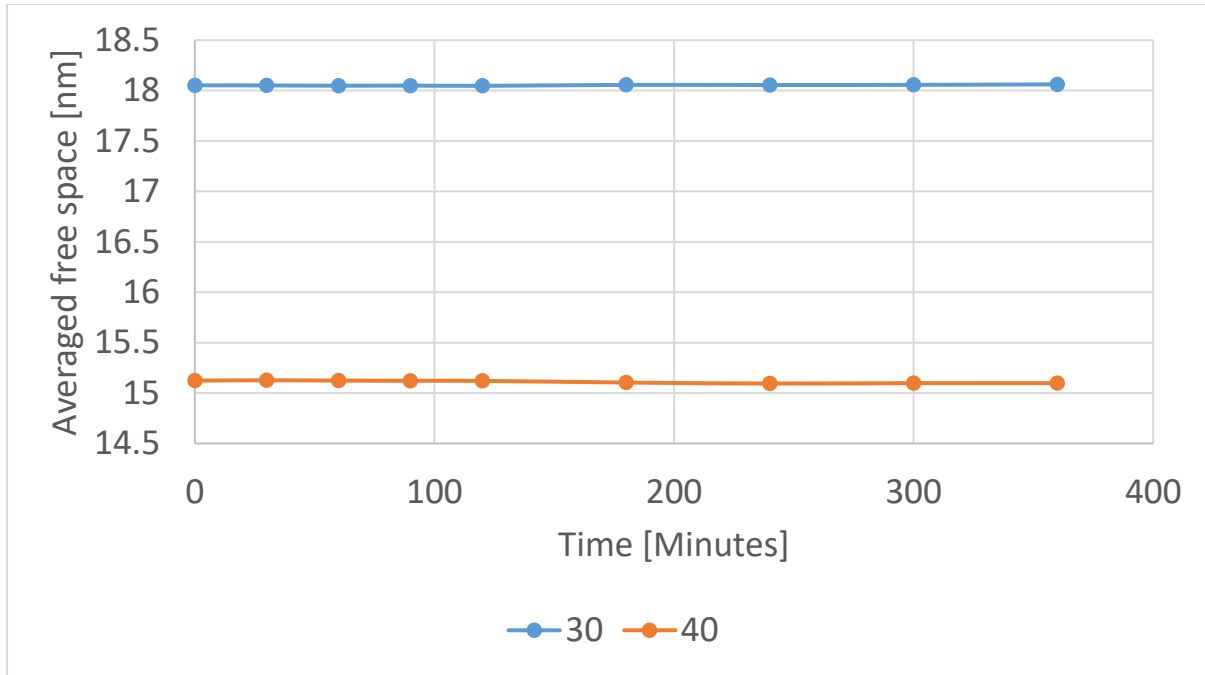
Figure 94 Free space determination for the capillary enclosed IFPs at 30 and 40 °C.

As evident from the data, no observable compression of the peak positions was detected, indicating that the averaged free spectral range remained constant throughout the polymerisation process.

The experiment conducted at 30 °C exhibited a peak position variation of ±0.015 nm, while the 40 °C experiment demonstrated a slightly higher scatter of ±0.032 nm. These findings suggest that the intrinsic FP sensor remained unaffected by the polymerisation process, confirming its potential for strain-independent sensing applications.

EFP RI sensing

The extrinsic Fabry-Perot interferometer (EFPI) sensors required careful optimisation of two critical parameters. Firstly, the cavity length could not be excessively large, as this would result in a significant reduction in peak intensity, rendering them untrackable. Conversely, the cavities could not be too small, as this would prevent the adhesive from fully infiltrating them. To ensure reliable interrogation of RI variations during polymerisation, the cavities were

4.4.6.2 Monitoring refractive index changes within adhesive joints

fabricated with an approximate length of 40 μm. The pre-immersion gap length of the cavities was determined using the following equation (Liu et al., 1998):

$$l = \frac{m\lambda_1\lambda_2}{2(\lambda_2-\lambda_1)} \qquad [38]$$

, where λ_1 and λ_2 are the consecutive resonance wavelengths of the Fabry-Perot cavity, and m is an integer mode number corresponding to the order of interference. Table 28 details the obtained gap length values for the FP sensors used in the isothermal cross-linking experiments.

Table 28 Calculated cavity lengths for the isothermal glove box experiments.

Experiment	Calculated gap length [Microns]
30 °C	46.71
40 °C	33.39
50 °C	45.00

Following the joining of the two substrates, the adhesive infiltrated the FP cavities, thereby altering the refractive index within the cavity. This modification resulted in a corresponding change in the interference fringe pattern. Figure 95 presents a comparison of the cavity structure before and after immersion in the adhesive.

4.4.6.2 Monitoring refractive index changes within adhesive joints
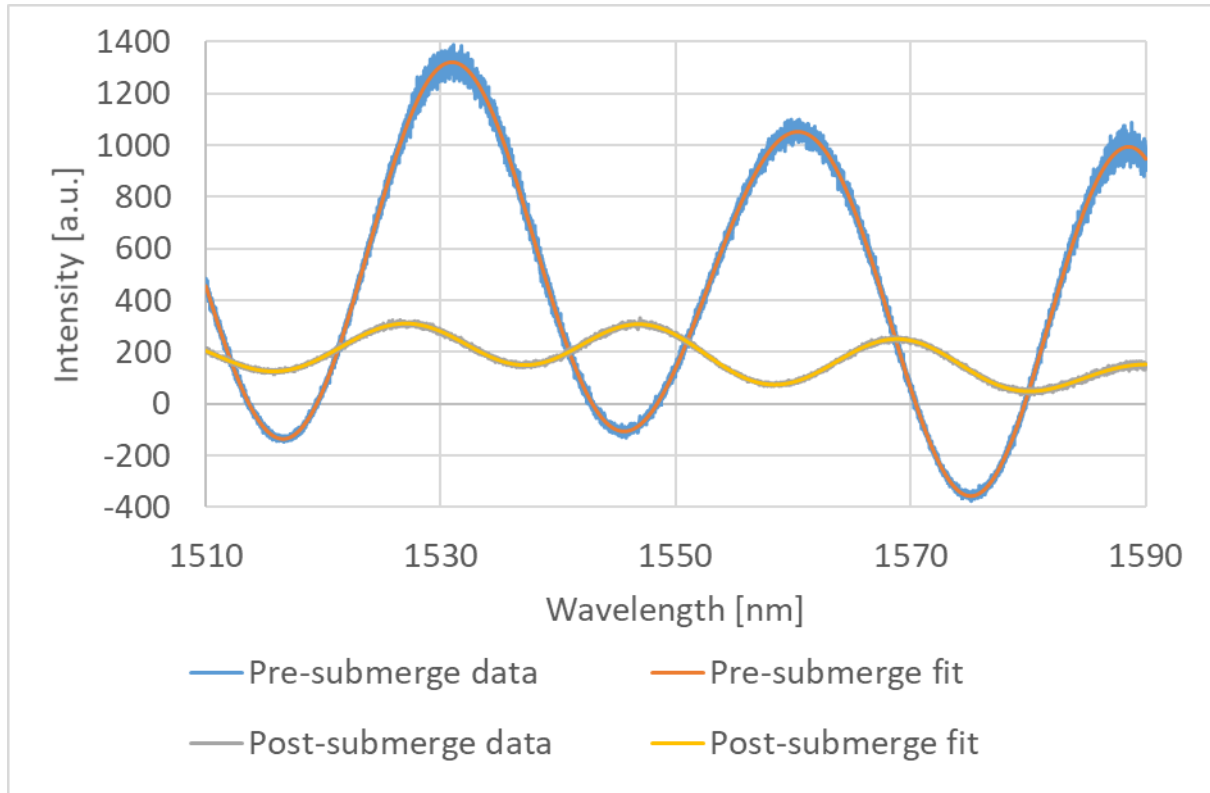
Figure 95 FP spectra pre- and post-submerge during the 50 °C experiment.

Two distinct phenomena were consistently observed during adhesive infiltration into the FP cavities. Firstly, a significant reduction in intensity occurred due to the higher refractive index of the polymer (~1.54) compared to air (~1.00 at room temperature). This change, along with variations in the polymer's optical properties, influenced both reflection and transmission at the interfaces. Secondly, an increase in the number of interference fringes was observed, which can be attributed to the alteration of the optical path length resulting from the higher refractive index of the adhesive. During polymerisation, progressive compression of the peak spacing was evident, as illustrated in Figure 96. As a qualitative approach, the averaged overall fringe spacing was determined and plotted against time.

4.4.6.2 Monitoring refractive index changes within adhesive joints
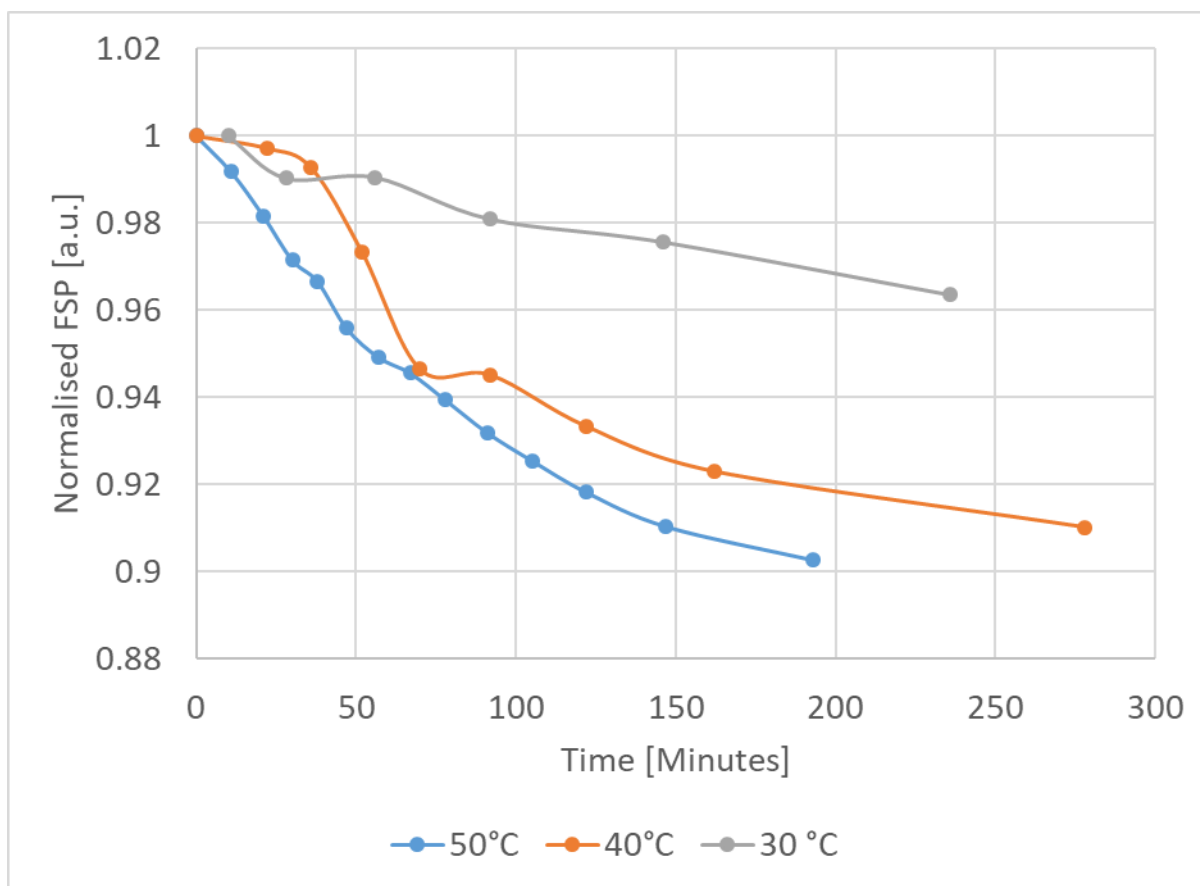
Figure 96 Free space compression during the cross-linking experiments at 30, 40, and 50 °C.
As evident from the results, the compression of interference fringes, indicative of refractive index evolution, is more pronounced at higher temperatures. This observation suggests that the RI increases more rapidly and to a greater extent at elevated temperatures.

The variability observed within the signal traces may be attributed to the fact that the adhesive remained in a liquid state during the early stages of polymerisation. Consequently, minor fluctuations in refractive index could arise from the diffusion of the two reactive components into one another, as discussed in the Fresnel analysis section (4.3). Due to the larger interrogation volume of the FP sensor compared to the smaller interrogation area of the FRS, the diffusion effects are expected to occur at a slower rate in the FP measurements.

4.4.6.2 Monitoring refractive index changes within adhesive joints

Two main approaches to determine the refractive index were found in literature, namely (i) the relative RI change where only the refractive index delta is determined, as expressed in the following equation (Xiao et al., 2005):

$$\Delta n = \frac{\Delta \lambda_m}{\lambda_{m0}} n_0 \qquad [39]$$

, where Δn is the relative change of refractive index, $\Delta \lambda_m$ denotes the shift in the initial wavelength $\Delta \lambda_{m0}$ corresponding to the m-th reflectance peak, while n_0 represents the initial refractive index of the cavity. Δn is the change in the refractive index, and $n_o + n$ is the new refractive index after the change.

The second approach is to determine the absolute refractive index by using the following equation: and (ii) the determination of the absolute refractive index, as stated in the following equation (Wei et al., 2008):

$$l \times n = \frac{1}{2} \left(\frac{\lambda_{v1} \lambda_{v2}}{\lambda_{v2} - \lambda_{v1}} \right) \qquad [40]$$

, where l is the cavity length, n is the absolute refractive index, and λ_{v1} and λ_{v2} are the centre wavelengths of two adjacent troughs within the FP spectrum. Literature notes that the absolute refractive index equation is less sensitive to changes (Qi et al., 2003). The absolute refractive index calculations did initially show implausible results; therefore, the determined cavity lengths were slightly adjusted to enable a starting refractive index of approximately 1.53. The results and the adjusted cavity lengths are presented in Table 29.

4.4.6.2 Monitoring refractive index changes within adhesive joints

Table 29 Comparison of absolute refractive index calculations.

Temperature	Adjusted l [Microns]	l deviation [Microns]	RI start	RI end	RI increase [%]
50	48.0	±03.0	1.5321	1.6881	10.2
40	34.5	±01.0	1.5321	1.6506	07.7
30	35.2	±11.5	1.5371	1.5913	03.5

The results appear to be plausible, as the increase in temperature corresponds with a higher refractive index, which aligns with expectations. However, the necessity for a significant cavity length adjustment in the 30 °C experiment raises some concerns, as such an adjustment was not required for the other temperature conditions. Despite this, the findings demonstrate that the refractive index within an adhesive joint can be determined with high precision.

To further validate these results, additional hyphenated experimental techniques are required to ensure reproducibility and accuracy. Moreover, the IFP sensors were found to be unaffected by the shrinkage associated with the polymerisation process, confirming their suitability for embedding strain sensors that remain independent of shrinkage effects in adhesive joints. It is anticipated that this principle may also be applicable to FBGs, offering further potential for strain sensing applications in bonded structures.

4.4.6.2 Monitoring refractive index changes within adhesive joints

5. Results and Discussion – Adhesive Bonding

This chapter reports the results of adhesive bonding investigations across aluminium–aluminium, composite–composite, and aluminium–composite SLJs. The work begins with the validation of focus variation microscopy for quantifying surface roughness and texture of grit-blasted substrates. The influence of manufacturing factors, including blasting pressure, surface treatments, dimensional tolerances, environmental conditions, and bond-line thickness, is then examined.

Mechanical performance is assessed through tensile testing, supported by analyses of surface chemistry, surface free energy, and interfacial features, including microvoid formation. The effects of additional treatments, including silane application and solvent cleaning, are also taken into consideration. Together, these studies establish the link between surface preparation, interfacial characteristics, and adhesive joint strength across different material combinations.

5.1. Validation of focus variation microscopy to assess surface roughness and texture of grit-blasted substrates

To evaluate the changes in roughness and texture induced by grit-blasting and their impact on the surface characteristics of a substrate using the Alicona G5 3D profilometry, it was necessary to investigate the effect of magnification. This is because the manufacturer specifies varying roughness sensitivities associated with different magnifications, as shown in Table 30.

Ra	Rz	Vertical resolution	Objective
5	30	≤ 2 µm	5x, 10x ,20x ,50x ,100x
1	6	≤ 400 nm	10x ,20x ,50x ,100x
0.5	3	≤ 200 nm	10x, 20x, 50x, 100x
0.1	0.6	≤ 40 nm	20x, 50x, 100x
0.05	0.3	≤ 20 nm	50x, 100x

The ISO 4288 (Standardization, 1998) method was applied to determine the relationship between Alicona magnification and the surface roughness profile using surface calibration blocks. Furthermore, area scans were performed after selecting the appropriate magnification and compared to the surface roughness values of the corresponding surface finish blocks. The Alicona method for evaluating surface roughness is depicted in Figure 97.

Measurement

Form removal

Adjustment of reference plane

Surface roughness

Calculation of parameters
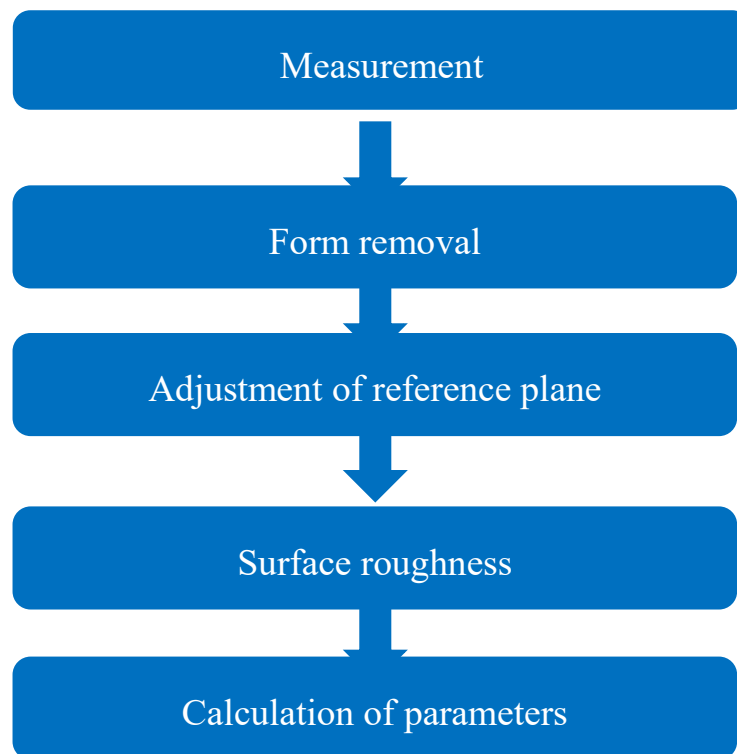
Figure 97 Alicona surface roughness evaluation steps (Alicona Imaging GmbH, 2013).

5.1 Validation of focus variation microscopy to assess surface roughness and texture of grit-blasted substrates

The following roughness parameters were employed to characterise the surface profile.

Ra: Arithmetic average of height distributions from the mean line (Alicona Imaging GmbH, 2013)

$$Ra = \frac{1}{l}\int_0^l z(x)dx \qquad [42]$$

Sa: Arithmetic mean surface height (Alicona Imaging GmbH, 2013)

$$Sa = \frac{1}{A}\int\int_0^A z(x,y)dxdy \qquad [43]$$

, where l is the evaluation length and A is the evaluation area.

To obtain valid results, the defined z-range is crucial. An inadequate z-range will lead to white spots or holes, as no focal point can be determined during the scan. Figure 98 shows the scan of a calibration block with an insufficient z-range.
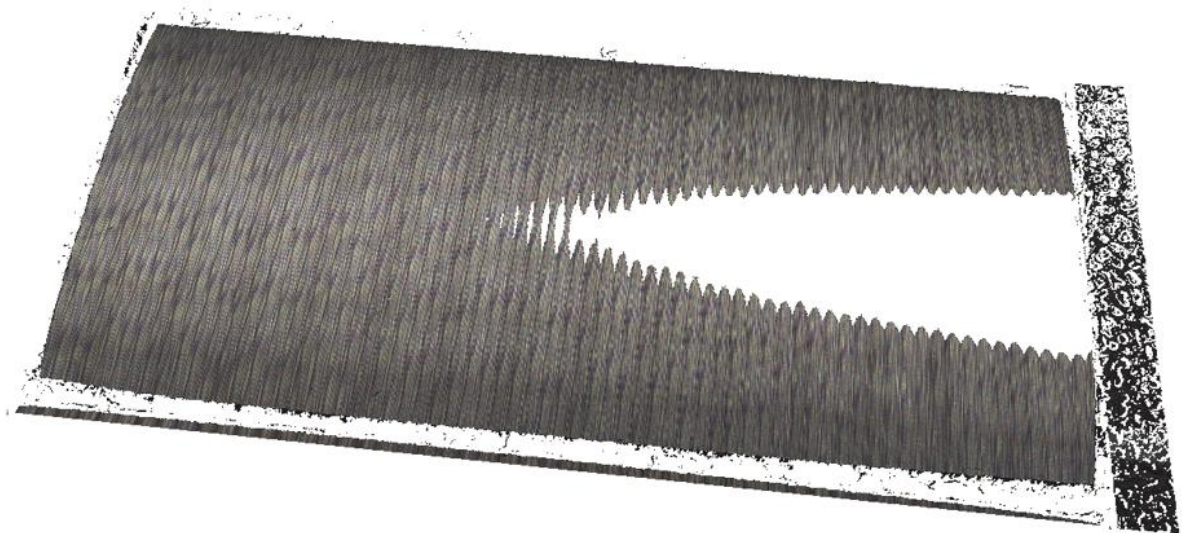
Figure 98 The surface roughness calibration block was measured at an insufficient z-range. The z-range was chosen too small for the curvature of the block; therefore, the white section on the right was out of range.

5.1 Validation of focus variation microscopy to assess surface roughness and texture of grit-blasted substrates

The starting point for evaluating roughness or texture is the determination of the mean width of profile elements (RSm), which represents the average width of consecutive profiles—in the case of the calibration blocks, this refers to the lay width. The Alicona system automatically calculates this value. The sampling and evaluation lengths must be selected appropriately, as shown in Table 31. As a general guideline, the larger the RSm, the longer the sampling length (lr) and evaluation length (ln) should be selected appropriately, as shown in Table 31. As a general guideline, the larger the RSm, the longer the sampling length (lr) and evaluation length (ln) should be.

Table 31 Roughness sampling and evaluation lengths in dependency to the RSm (Alicona Imaging GmbH, 2013).

RSM [mm]	Roughness sampling length lr [mm]	Roughness evaluation length ln [mm]
0.013 < RSm ≤ 0.04	**0.08**	**0.4**
0.04 < RSm ≤ 0.13	**0.25**	**1.25**
0.13 < RSm ≤ 0.4	**0.8**	**4**
0.4 < RSm ≤ 1.3	**2.5**	**12.5**
1.3 < RSm ≤ 4	**8**	**40**

Blocks with defined roughnesses were scanned and evaluated at different magnifications. Multiple line scans were performed using the minimal evaluation length and all specified magnifications to assess the impact of form correction on roughness values. Five random profiles were measured, each corresponding to the exact minimum sampling length (Table 31 of the recommended Lc filter. All samples included applied reference planes.

5.1 Validation of focus variation microscopy to assess surface roughness and texture of grit-blasted substrates
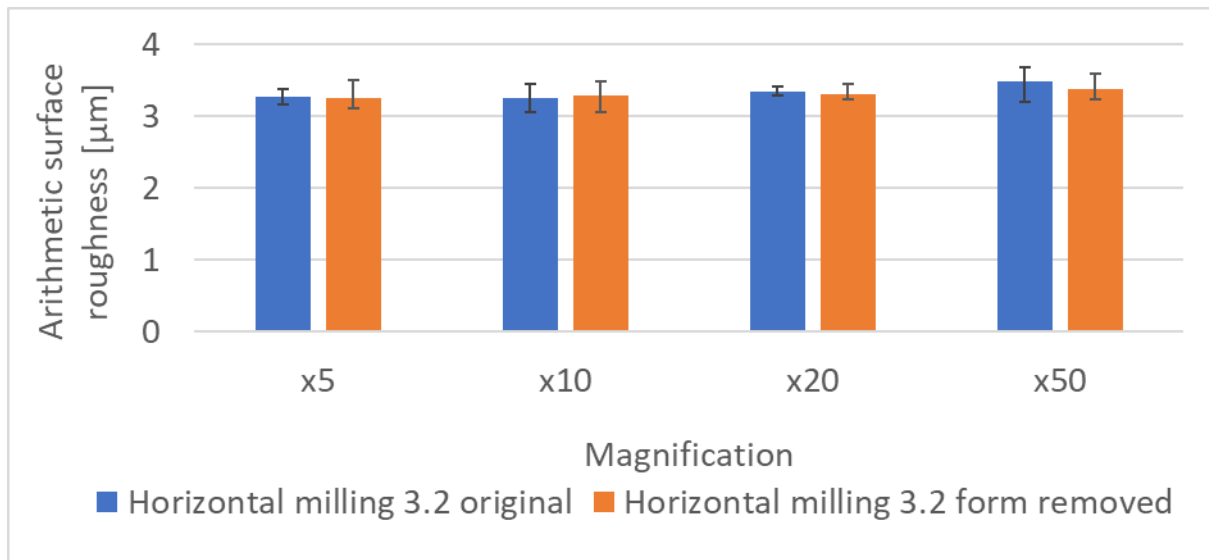
Figure 99 Investigation of the influence of form at different magnifications.

No significant changes in Ra were observed in the form-corrected measurements at their respective magnifications. No discernible trends were noted regarding the deviations. The impact of reference planes was also examined. Figure 100 depicts a grit-blasted sample without a reference plane, using a colour filter range of +15 μm to -15 μm. Figure 100 displays the same sample with the applied reference plane (whole dataset) and the identical colour filter range.

5.1 Validation of focus variation microscopy to assess surface roughness and texture of grit-blasted substrates
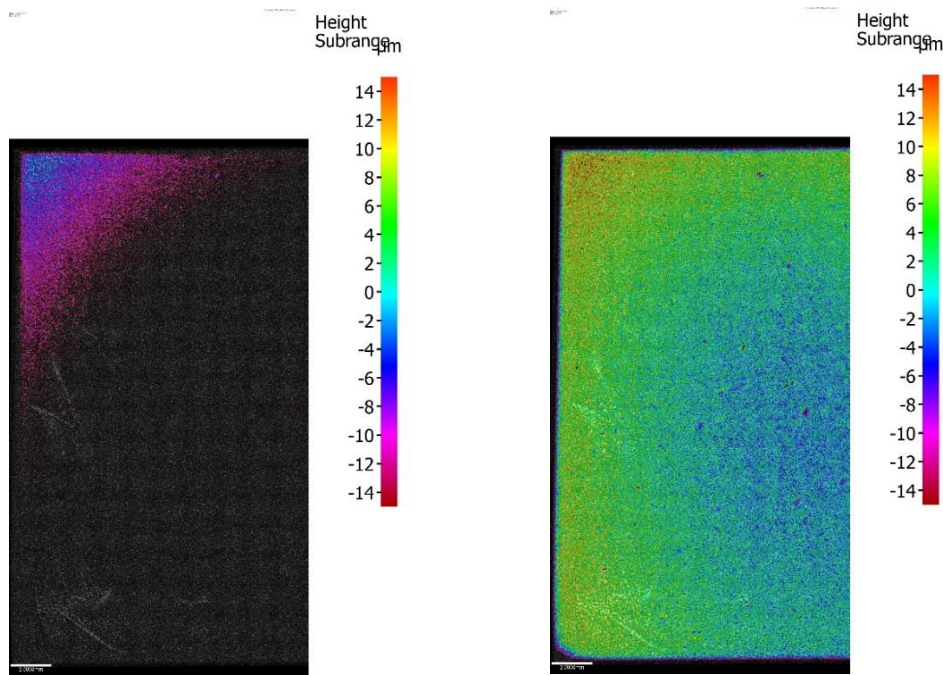
Figure 100 Investigation of applied reference planes. (a) illustrates the sample with a colour filter with no reference plane and (b) with a reference plane.

As shown in Figure 100 (a) the manually selected colour filter range is only applied to the upper left corner (-14 μm to 0 μm), meaning that the 0-point for the z-axis, without an applied reference plane, is approximately 15 μm above the actual 0-point. Figure 100 (b) shows the same specimen with the applied reference plane. Although the manual does not provide information about the original 0-point, it can be assumed that the Alicona system uses a calibrated 0-point to measure the absolute movement of the 3D stage (x, y) and the microscope (z). Figure 101 compares roughness scans (centre line horizontally with l = 12.5 mm) using different Lc filters (Lc 800 μm, Lc 2500 μm, and Lc 8000 μm) for five samples of the same area and grit-blasting parameters, specifically 60 seconds, a stand-off distance of 189 mm, and a 90° angle between the nozzle and the surface.

5.1 Validation of focus variation microscopy to assess surface roughness and texture of grit-blasted substrates
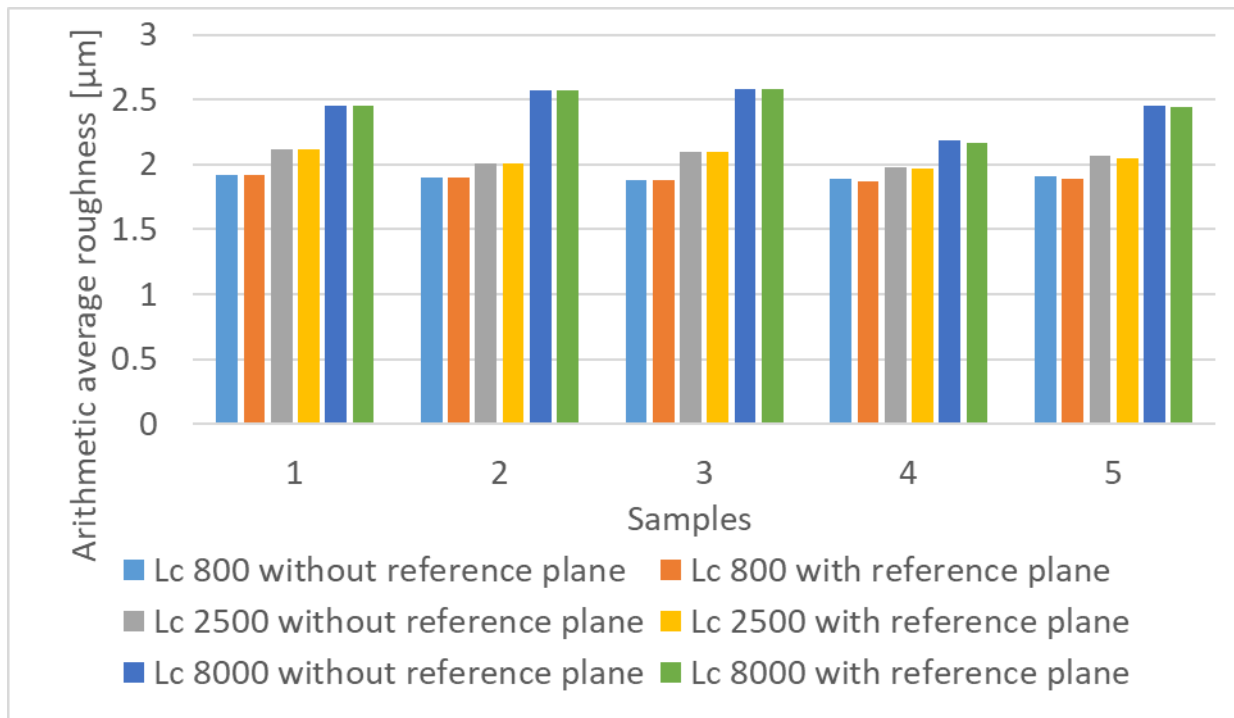
Figure 101 Influence of reference planes on the surface roughness.

As shown for samples 1 to 5 in, the Ra values for the three Lc filters used do not exhibit significant changes when comparing the "without reference plane" parameters to the "with reference plane" parameters. The minor Ra deviations observed across the samples may be attributed to the grit-blasting process. To investigate the effects of magnification on surface roughness, several calibration blocks were measured, including (i) 0.8 μm horizontal milling, (ii) 0.8 μm turning, (iii) 1.6 μm turning, and (iv) 3.2 μm horizontal milling. Each of the aforementioned samples was measured five times at random locations (full profile length = 21 mm). The results are presented in Figure 102.

5.1 Validation of focus variation microscopy to assess surface roughness and texture of grit-blasted substrates
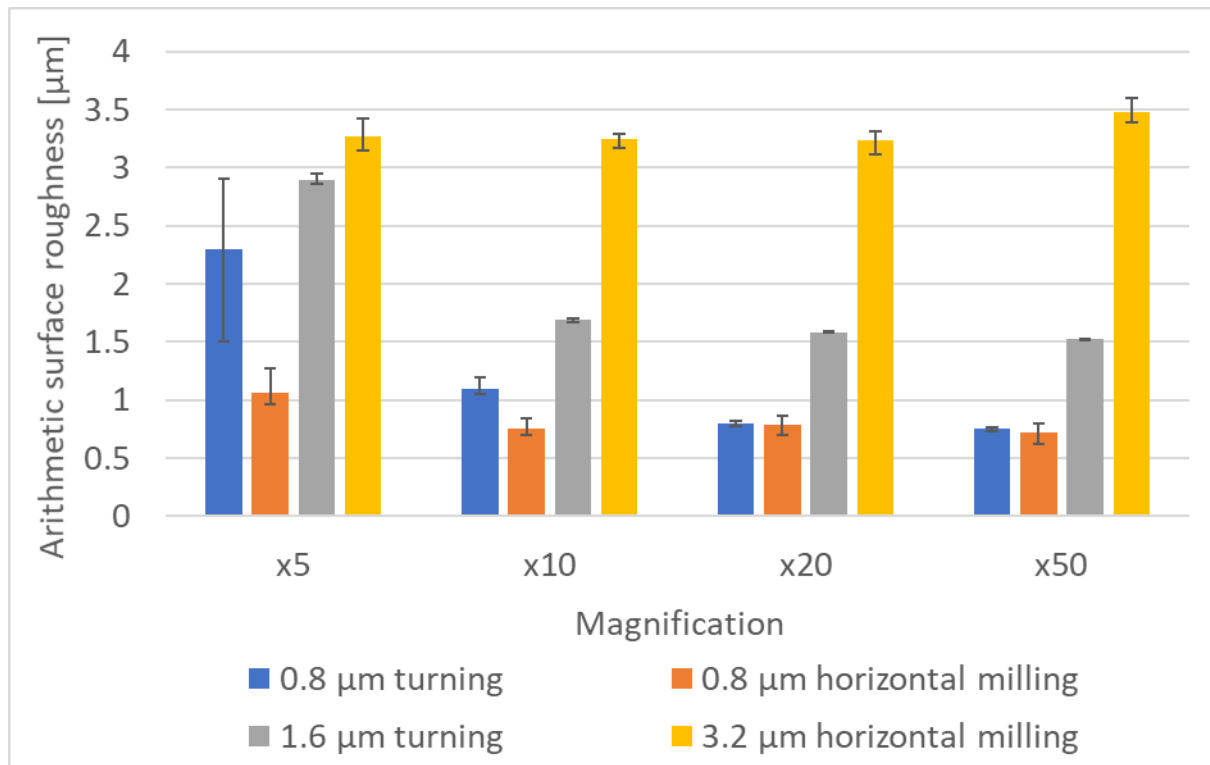
Figure 102 Magnification influence on surface roughness of different surface calibration blocks.

As anticipated, the Ra values decrease with increasing magnification from 5x to 10x. Beyond this point, no noticeable changes were observed that corresponded to the manufacturer-stated roughness sensitivity, as shown in Table 31. The 3.2 µm horizontal milling appears to be an exception, as it does not follow the expected trend and remains relatively constant. Additionally, a roughness evaluation was conducted on 2024 T3 aluminium before and after 60 seconds of grit-blasting at a stand-off distance of 189 mm and a 90° angle between the nozzle and the sample. Before grit-blasting, the sample was degreased in MEK for 5 minutes. The results are illustrated in Figure 103.

5.1 Validation of focus variation microscopy to assess surface roughness and texture of grit-blasted substrates
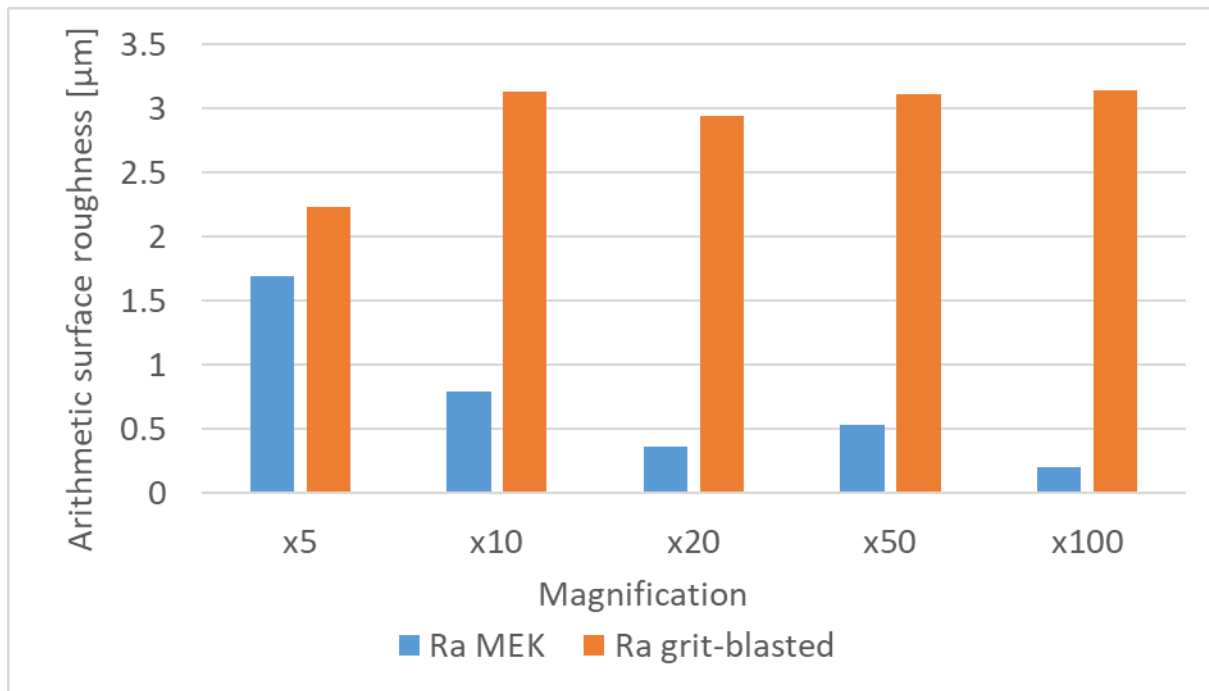
Figure 103 Magnification influence on de-greased and grit-blasted 2024 T3 aluminium

The de-greased and grit-blasted 2024 T3 aluminium samples had dimensions of $l = 12.7$ mm and $w = 25.4$ mm. The roughness measurements of the de-greased specimen follow a similar trend to the surface calibration blocks, with increasing magnification leading to a decrease in roughness. In contrast, the roughness of the grit-blasted area appears to increase to approximately 3 μm. A possible explanation for this is the small crevices created by the grit-blasting process. While the calibration blocks feature a smooth surface with lays, the grit-blasted surface contains numerous small crevices. These crevices may be of such a fine nature that higher magnifications reveal more of them, causing the roughness to increase as magnification rises.

Additionally, the roughness values were compared with area scans (texture). Typically, area scans are not directly comparable to roughness scans, as they may share the same profile length but only represent a single point along the area width. However, it was assumed that the periodically homogeneous surface finish blocks might exhibit similar characteristics to the

5.1 Validation of focus variation microscopy to assess surface roughness and texture of grit-blasted substrates

roughness profile, as profile changes could remain consistent over the width distribution. To investigate this hypothesis, area scans were performed on two different surface calibration blocks: (i) horizontal milling 3.2 μm, and (ii) vertical milling 3.2 μm. The magnification for both measurements was set at 10x. The area scans are shown in Figure 104 and Figure 105.
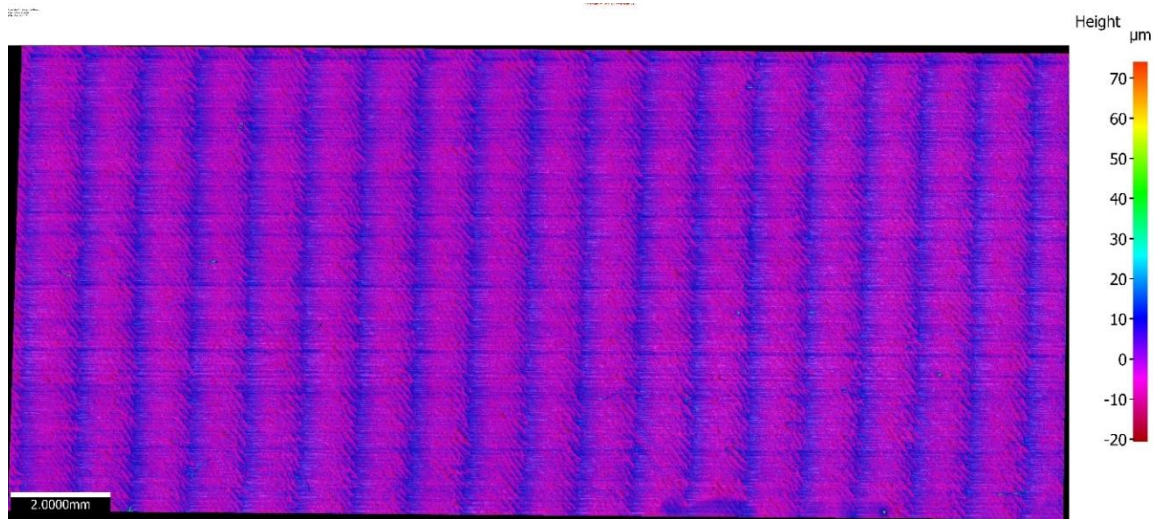
Figure 104 Surface area scan of the 3.2 μm horizontal milling block.

Figure 105 Surface area scan of the 3.2 μm vertical milling block.

As shown in Figure 106, the form correction behaves differently for the two calibration blocks. The manufacturing method and the resulting form might be a possible reason for this behaviour. If both blocks have different surface curvatures, this correction will affect the form-corrected

5.1 Validation of focus variation microscopy to assess surface roughness and texture of grit-blasted substrates

surface texture. Additionally, since the roughness of the calibration block is believed to have been measured using a stylus profilometer, minor deviations are not unusual, as the stylus method and focus variation microscopy are two different evaluation techniques and optical techniques have been shown to be slightly more sensitive to minor surface changes (Piska and Metelkova,   2014).
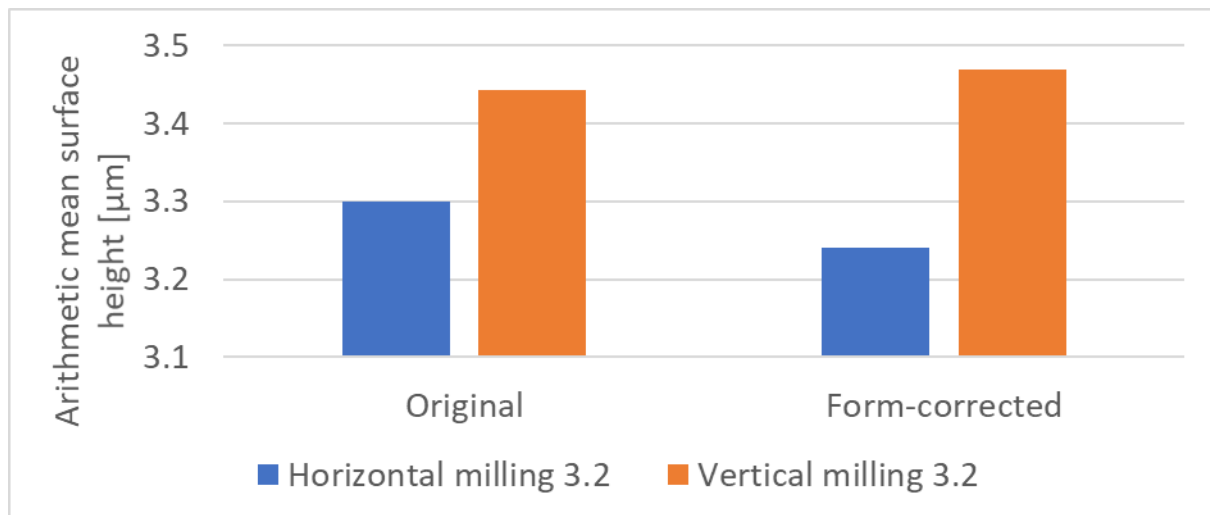
Figure 106 Comparison of original and form-corrected Sa values.

Within a certain margin of error, surface texture and roughness might be correlated, as they fall within the same range as the stated Ra values of the calibration blocks. For this study, all scans were performed using the same methodology, meaning that changes in texture or roughness within this system can be attributed to the influence of the grit-blasting process. The magnification for all subsequent experiments was set to 10x, which was deemed suitable for the expected roughness and textures (>1 Ra).

5.2. Manufacturing and testing single-lap joints with different surface treatments

Single-lap joints were selected to house the optical fibre sensors within the applied adhesive. These joints are relatively simple to manufacture and are commonly used in industry. However,

5.2 Manufacturing and testing single-lap joints with different surface treatments

they do experience bending during testing, which complicates the distinction between shear forces and bending forces in tensile testing.

5.2.1. Assessment of pressure constancy within the grit-blasting cabinet

Since the grit-blasting was performed manually, it was necessary to evaluate the operation of the cabinet and its influence on the blasting pressure. The system-inherent pressure loss over time was initially monitored after filling the compressor to 8.4 bar (0.1 bar above the target grit-blasting pressure).
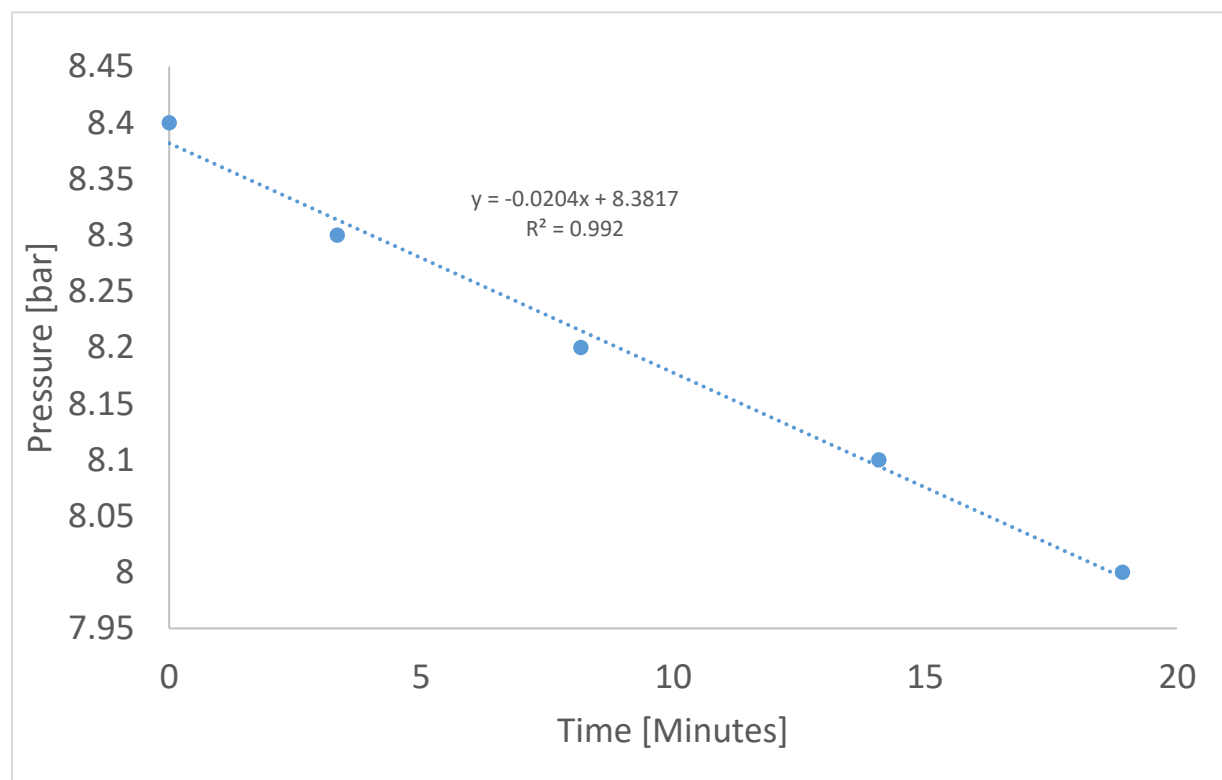
Figure 107 Investigation of pressure loss within the compressor-air-receiver assembly.

5.2.1 Assessment of pressure constancy within the grit-blasting cabinet

After filling the air receiver of the compressor, it took approximately 15 seconds to return to the grit-blast cabinet and begin the blasting procedure. This resulted in a calculated pressure drop of 0.0051 bar, which was considered negligible. The time required for the pressure to drop from 8.3 to 8.25 bar was calculated to be 2.45 minutes. Therefore, the operation of the grit-blasting cabinet was deemed to be well-controlled. Since the compressor supplied compressed air for the entire workshop, all other equipment connected to the compressor was switched off during the grit-blasting procedures. The pressures recorded for the different grit-blasting durations are shown in Figure 108.
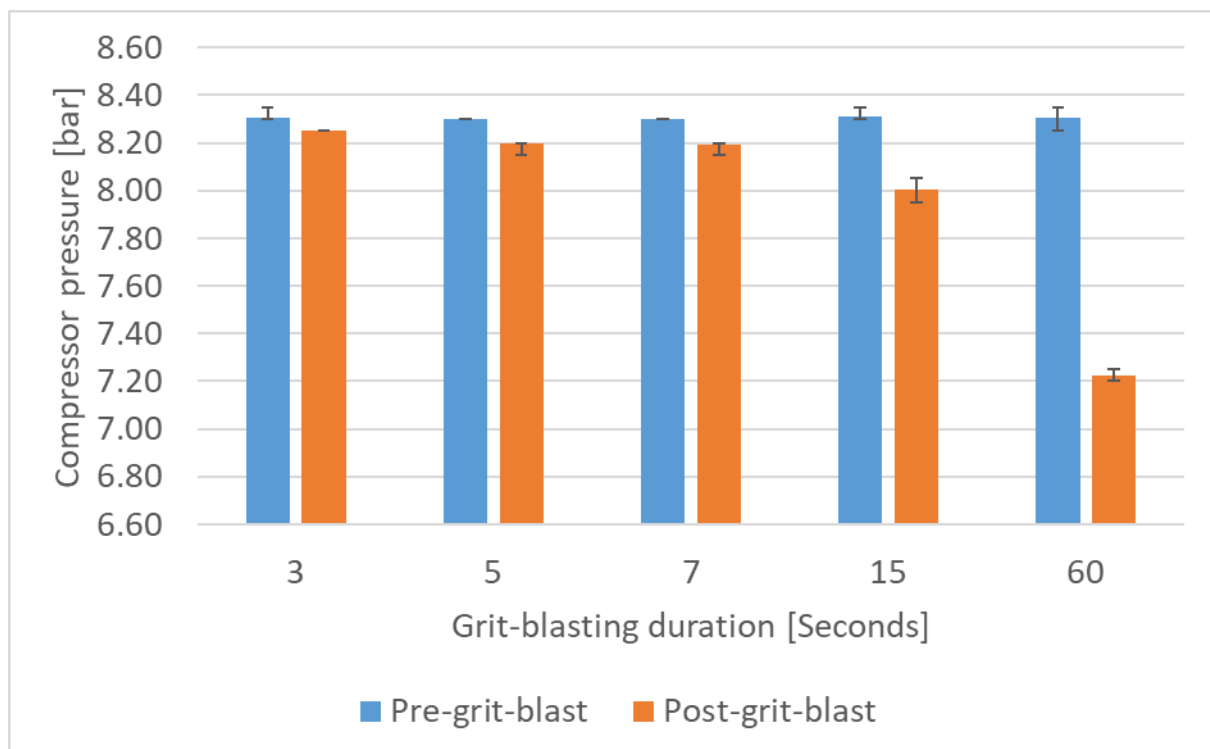
Figure 108 Measured pressure loss at different grit-blasting durations.

As anticipated, the pressure drop increases with the duration of grit-blasting. The minimum and maximum deviations observed across the grit-blasting trials are relatively small, with ± 0.05 bar being the maximum deviation. These variations may also stem from parallax error, as the pressure gauge was positioned at the top of the compressor. The grit-blasting treatments lasting 120 and 180 seconds were not performed in a single continuous trial but were split into

5.2.1 Assessment of pressure constancy within the grit-blasting cabinet

two and three cycles of 60 seconds, respectively. Between cycles, the compressor-air-receiver assembly was refilled to 8.3 bar to ensure the abrasive media retained sufficient kinetic energy, preventing any reduction in pressure that could affect the grit-blasting process.

5.2.2. Overview of applied surface treatments

The objective of the surface treatments for both the aluminium and CFRP substrates was similar: (i) to increase surface roughness/texture through grit-blasting, and (ii) to enhance bonding strength further by applying an aqueous silane solution at varying concentrations. For the grit-blasting process, the blasting time was adjusted to produce different textures. The grit-blasting setup that yielded the highest bond strength was selected for further treatment with the silane solutions. Table 32, Table 33, and Table 34 outline the surface treatments applied to aluminium-to-aluminium, CFRP-to-CFRP, and hybrid single-lap joints, while Table 35 provides details of the process steps involved in these surface treatments.

Table 32 Applied surface treatments for aluminium to aluminium single lap joints.

Surface treatments of aluminium-to-aluminium single-lap joints			
Batch / ID	Degrease	Grit-blast	Silane
1 / AL - MEK	MEK - submerge	None	None
2 / AL - GB60	MEK - submerge	60 seconds	None
3 / AL - GB120	MEK - submerge	2 x 60 seconds	None
4	Substandard batch, repeated in batch 5		
5 / AL - GB180	MEK - submerge	3 x 60 seconds	None
6 / AL - S1	MEK - submerge	1 x 60 seconds	1% silane

5.2.2 Overview of applied surface treatments

Batch	Degrease	Grit-blast	Silane
7 / AL - S2	MEK - submerge	1 x 60 seconds	2% silane
8 / AL - S3	MEK - submerge	1 x 60 seconds	3% silane
9 / AL - GB15	MEK - submerge	1 x 15 seconds	None

Table 33 Applied surface treatments for composite to composite single lap joints.

Surface treatments of composite-to-composite single-lap joints

Batch	Degrease	Grit-blast	Silane
10 / C - ACE	Acetone wipe	None	None
11 / C - GB5	Acetone wipe	1 x 5 seconds	None
12 / C – GB3	Acetone wipe	1 x 3 seconds	None
13	Substandard batch, repeated in batch 18		
14 / C - S1	Acetone wipe	1 x 5 seconds	1% silane
15 / C - S2	Acetone wipe	1 x 5 seconds	2% silane
16 / C - S3	Acetone wipe	1 x 5 seconds	3% silane
18 / C – GB7	Acetone wipe	1 x 7 seconds	None

Table 34 Applied surface treatments for aluminium to composite (hybrid) single lap joints.

Surface treatments of aluminium to composite single-lap joints

Batch	Degrease	Grit-blast	Silane
17 / H-S2 (alu)	MEK - submerge	1 x 60 seconds	2% silane

5.2.2 Overview of applied surface treatments

17 / H-S2 (CFRP)	Acetone wipe	1 x 5 seconds	None
19 / H-GB (alu)	MEK - submerge	1 x 60 seconds	None
19 / H-GB (CFRP)	Acetone wipe	1 x 5 seconds	None

Table 35 Manufacturing process details for applied surface treatments.

Surface treatment details		
Treatment	**Aluminium**	**Composite**
Degrease	5 minutes MEK-submerge; rinse with deionised water; oven dry for 1 hour at 115 °C	5 linear strokes with acetone-drenched tissue; rinse with deionised water; oven dry for 2 hours at 60°C
Grit-blast	90 °C nozzle angle at 189 mm SoD followed by aluminium degrease procedure	90 °C nozzle angle at 189 mm SoD followed by composite degrease procedure
Silane	5-minute submersion followed by 1-hour oven dry at 115 °C	5-minute submersion followed by 2-hour oven dry at 60 °C

5.2.3. Assessment of substrate geometrical tolerances

To determine ASTM-conforming dimensions, each substrate was ground and measured, as described in Section 3.8. Additionally, the thickness of the overlap area was assessed to allow for the determination of the bond-line thickness. Figure 109 illustrates the measurements taken on each substrate.

5.2.3 Assessment of substrate geometrical tolerances
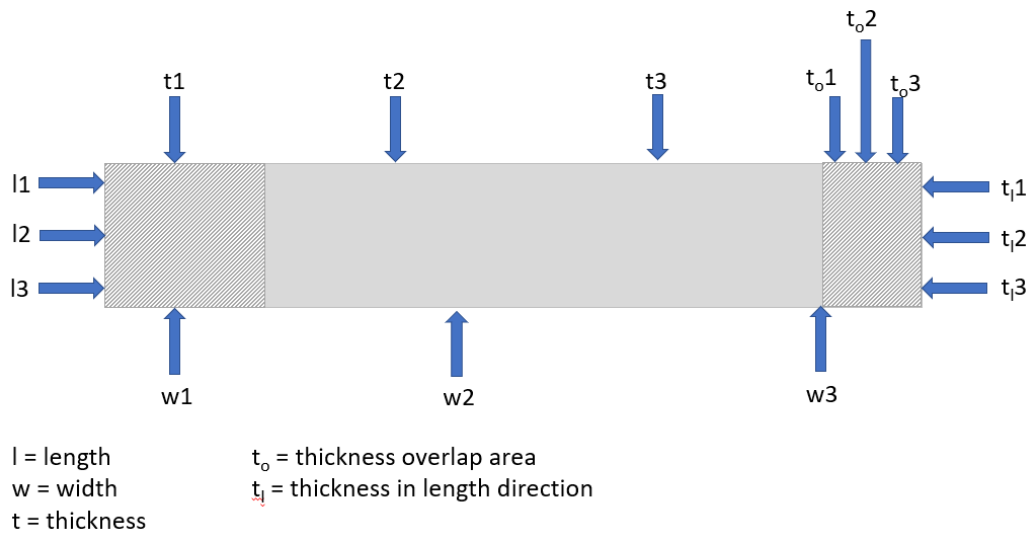
Figure 109 Schematic of measurement point to quantify substrate dimensions.

Throughout 19 batches manufactured, the dimensions were measured and recorded. The averaged results are presented in Table 36.

Table 36 Averaged substrate dimensions for the 19 manufactured single lap joint batches in [mm].

Batch	Length	Width	$t_{substrate}$	$t_{overlap}$
1	101.53±0.12	25.30±0.03	2.03±0.02	2.03±0.02
2	101.48±0.14	25.27±0.05	2.03±0.02	2.03±0.01
3	101.53±0.18	25.28±0.03	2.02±0.02	2.02±0.02
4	101.48±0.10	25.28±0.04	2.02±0.01	2.02±0.01
5	101.62±0.18	25.25±0.05	2.03±0.01	2.03±0.02
6	101.51±0.11	25.27±0.07	2.02±0.02	2.02±0.02
7	101.55±0.18	25.28±0.04	2.02±0.02	2.02±0.02
8	101.52±0.29	25.27±0.06	2.02±0.01	2.03±0.01

5.2.3 Assessment of substrate geometrical tolerances

9	101.48±0.23	25.31±0.06	2.03±0.01	2.03±0.01
10	101.67±0.12	25.27±0.09	2.00±0.03	2.03±0.06
11	101.65±0.15	25.29±0.07	2.00±0.08	2.03±0.03
12	101.68±0.06	25.32±0.05	2.02±0.01	2.03±0.01
13	101.48±0.18	25.32±0.07	2.03±0.03	2.03±0.02
14	101.46±0.18	25.23±0.12	2.03±0.03	2.02±0.02
15	101.49±0.08	25.28±0.13	2.01±0.03	2.01±0.02
16	101.55±0.05	25.30±0.09	2.02±0.01	2.03±0.02
17	101.48±0.18	25.30±0.07	2.02±0.02	2.02±0.02
18	101.65±0.12	25.31±0.10	2.02±0.03	2.03±0.03
19	101.40±0.10	25.28±0.11	2.03±0.01	2.03±0.01

As observed, there are slight variations in length and width. The length deviation might stem from the water jet cutting process and did not affect the overlap, as this was individually adjusted using the adjustment block of the manufacturing rig. The width was targeted to be ground to 25.30 mm, as the single lap joint rig holding pin width distance was manufactured to 25.40 mm. A substrate width of 25.30 mm was an appropriate compromise, as it allowed for a straightforward fit of the substrate between the pins without causing excessive tilt angles within the joints. The CFRP substrates were found to have a thickness highly similar to that of the aluminium substrates, as shown in the thickness evaluation. Throughout the 19 batches, no significant changes in thickness were observed, indicating a consistent thickness of approximately 2 mm for both the aluminium and CFRP substrates.

5.2.3 Assessment of substrate geometrical tolerances

5.2.4. Monitoring relative humidity and temperature during the SLJ manufacture

Temperature and humidity were monitored during the production of the SLJs to examine the potential effects of these factors on the bond strength of the joints. The recorded data from these measurements are presented in Figure 110 and Table 37.
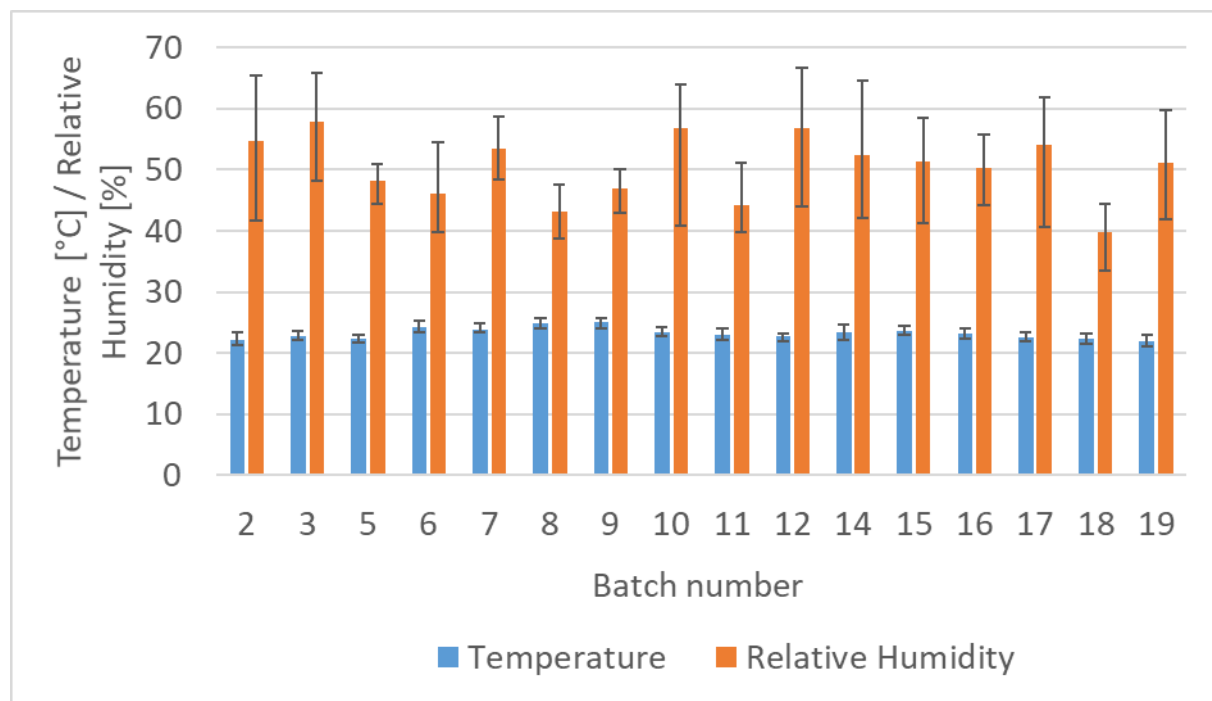
Figure 110 Monitored temperature and relative humidity during the manufacture of SLJ batches.

Batches 1, 4, and 13 have been excluded from the dataset. The data for batch 1 could not be saved due to a forced Windows update during logging, while batches 4 and 13 were excluded due to the substandard quality of the joints. As shown, the average temperatures fall within a range of±1.21 °C, with the influence of this temperature variation considered negligible. The relative humidity data is also included. Literature indicates that exposure to humidity significantly affects the thermal and mechanical properties of cold-curing epoxy adhesives. Water ingress leads to plasticisation, reducing Tg and stiffness, particularly at humidity levels

5.2.4 Monitoring relative humidity and temperature during the SLJ manufacture

above 75% RH. However, for lower humidity levels, such as 65% RH (the maximum observed in the manufactured SLJ), the effects should remain limited, especially as the maximum humidity was not seen over long periods. The study found that at moderate humidity, water uptake is minimal, and mechanical properties remain stable, with only slight reductions in Tg and stiffness due to absorbed moisture. Given that significant changes only occur beyond 75% RH, the measured humidity in my SLJ is unlikely to introduce major alterations in bond strength or long-term performance (Lettieri and Frigione, 2012).

Table 37 HP21 temperature and relative humidity data from the 19 SLJ manufacturing processes.

Batch	Average temperature [°C]	Deviation temperature [°C]	Average relative humidity [%]	Deviation relative humidity [%]
2	22.18	±01.22	54.65	±13.05
3	22.75	±00.90	57.78	±09.48
5	22.27	±00.73	48.30	±03.90
6	24.19	±01.21	46.17	±08.23
7	23.90	±01.00	53.53	±05.27
8	24.82	±00.93	43.16	±04.46
9	25.00	±00.85	47.01	±04.11
10	23.52	±00.77	56.82	±15.92
11	23.04	±01.01	44.24	±06.96
12	22.74	±00.74	56.85	±12.75

5.2.4 Monitoring relative humidity and temperature during the SLJ manufacture

14	23.49	±01.29	52.32	±12.28
15	23.70	±00.80	51.29	±09.99
16	23.18	±00.92	50.22	±05.92
17	22.51	±00.99	54.11	±13.51
18	22.30	±00.90	39.85	±06.35
19	22.02	±01.03	51.08	±09.08
Overall	23.23	±1.21	50.46	±10.61

5.2.5. Determination of bond-line thickness

Literature suggests a correlation between bond-line thickness and the shear strength of single-lap joints, with the trend being that thicker bond-lines decrease maximum bond-strength(Davies et al., 2009, Kostin et al., 2021). Consequently, the manufactured bond-lines needed to be controlled. The bond-line thickness for each joint was calculated using the following equation:

$$BLT = avg_{SLJ} - avg_{o1} - avg_{o2} \hspace{2cm} [44]$$

where BLT represents the calculated bond-line thickness, avg_{o1} and avg_{o2} refer to the averaged thicknesses of overlap areas 1 and 2, respectively, and avg_{SLJ} denotes the averaged overall thickness of the SLJ after bonding. The results are presented in Figure 111. Batches 4 and 13 are not included, as the bonding in these batches was deemed faulty.

5.2.5 Determination of bond-line thickness
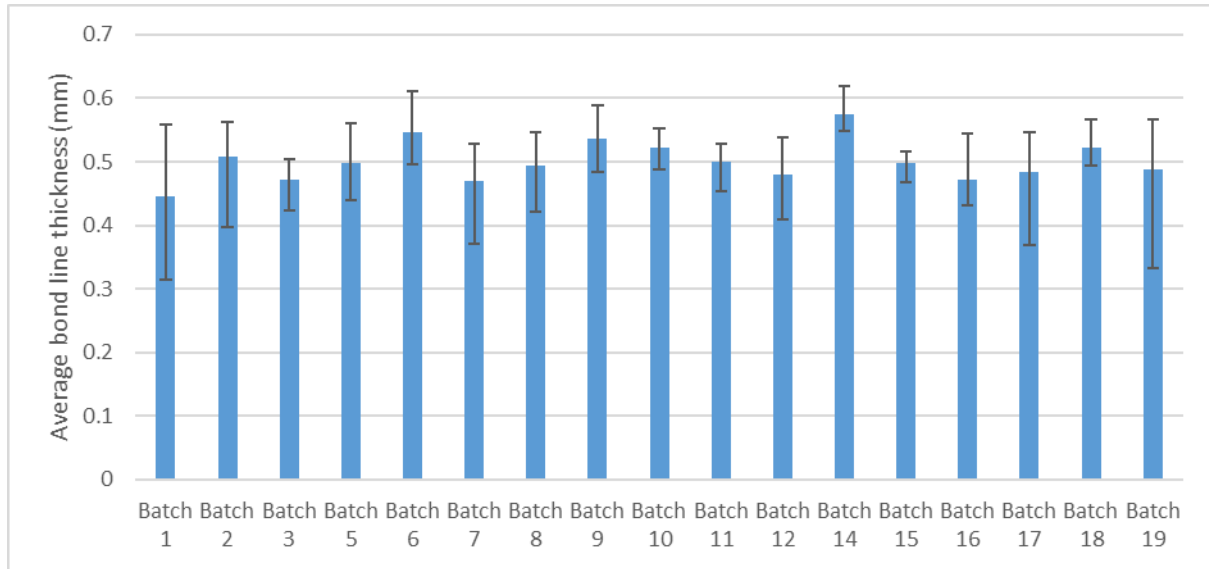
Figure 111 Averaged bond line thicknesses of the 19 manufactured SLJ batches.

The averaged BLT for all batches was found to be 0.5008 mm, with a maximum deviation of ±0.1557 mm. As bond-line control depends on the substrate thickness and spacer thickness, a standard error was defined as the maximum deviation of the substrate thickness and the deviation in spacer thickness. The error was calculated as the maximum substrate thickness deviation for each batch from the average thickness prior to bonding, with the measured deviation of the spacer thickness ±0.0072 mm also included. The overall error was determined to be ±0.0345 mm. Since the actual deviation exceeds the standard error, it suggests that the manufacturing process itself may contribute to the observed BLT deviations. Possible causes for this include (i) the uneven lowering of the top plate, (ii) particles on the substrate surface or manufacturing rig, and (iii) surface deviations of the manufacturing rig. The top plate was always lowered using a spirit level to ensure it was not tilted. Although the dowel pins were designed as fittings to limit tilting, batch 1, for example, was lowered too quickly, resulting in the highest deviation across all batches. The plates and substrates were thoroughly inspected and cleaned with a tissue (excluding the overlap areas) before the joints were set up; however, some particles may have remained. Unevenly manufactured plates could introduce a constant

5.2.5 Determination of bond-line thickness

error in certain SLJs across all batches, but no trend suggesting such an error was observed. The author believes that the primary factors affecting bond-line control are the lowering procedure and the presence of particles. To illustrate the extremes in bond-line thickness, the worst batch (1) and the best batch (15) are shown in Figure 112.
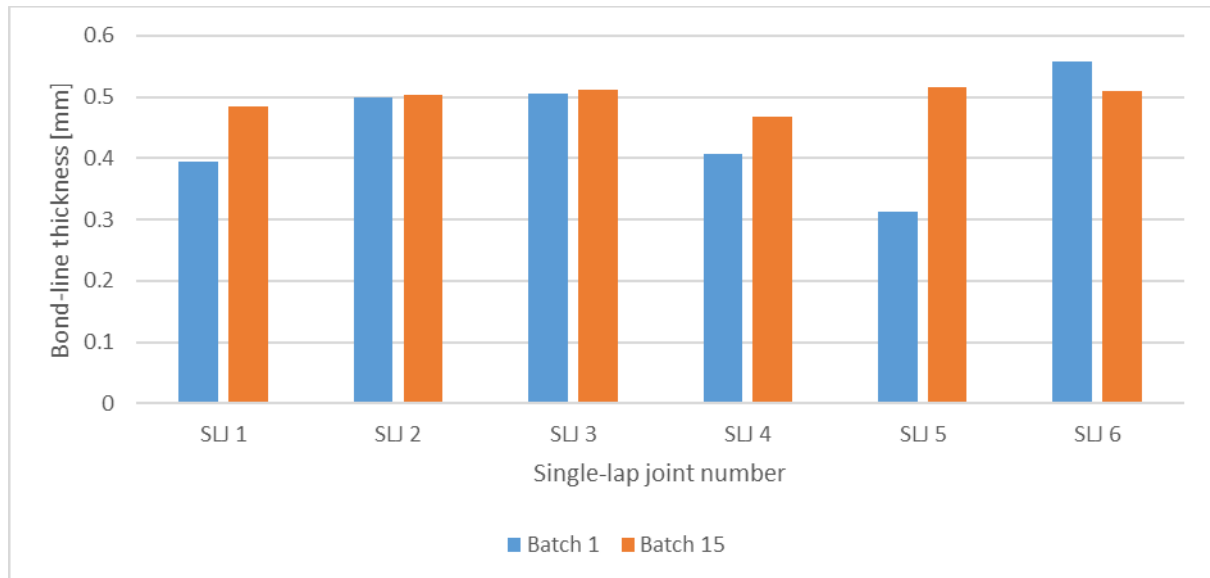
Figure 112 BLT comparison of batch 1 and batch 15.

5.2.6. Investigation of single-lap joint bond strength

To quantify the impact of grit-blasting and silane treatments on the bond strength of aluminium and CFRP joints, the batches were subjected to destructive testing. The test setup is outlined in Section 3.7.1. For an initial overview, the overall results related to the ultimate tensile strength (UTS) are presented in Figure 113. A detailed analysis and discussion of the various joint types are provided in the following sub-chapters.

5.2.6 Investigation of single-lap joint bond strength
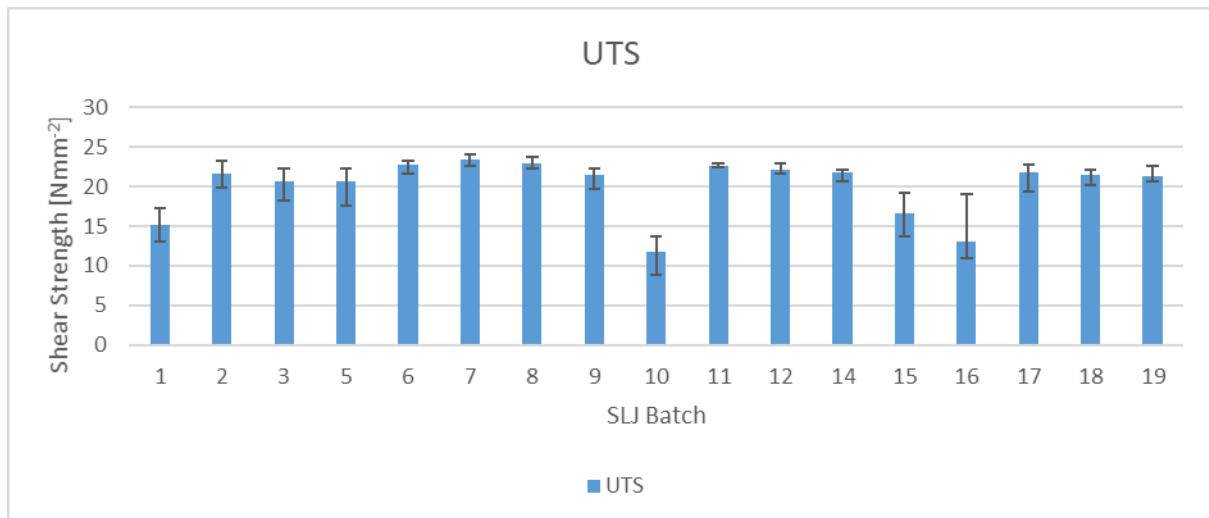
Figure 113 UTS results, including maximum deviation for the 19 manufactured SLJ batches. Batch 4 and 13 are excluded due to being substandard.

5.2.6.1.   Aluminium-to-aluminium bonding

The following sub-chapters elaborate on the aluminium to aluminium results regarding MEK degrease results, tensile testing, surface roughness/texture evaluation, silane treatments, and the determination of the free surface energy.

5.2.6.2.   Evaluation of the effect of methyl ethyl ketone (MEK) on the surface composition of aluminium

To investigate the effect of MEK on the surface composition of as-received 2024 T3 aluminium substrates, EDX was utilised, as described in 3.7.1.2. Three samples of $l = w = 25.4$ mm were scanned, with five scans each sample, before and after the MEK treatment to obtain data on removed surface contaminants. The averaged results are presented in Figure 114 and in Table 38.
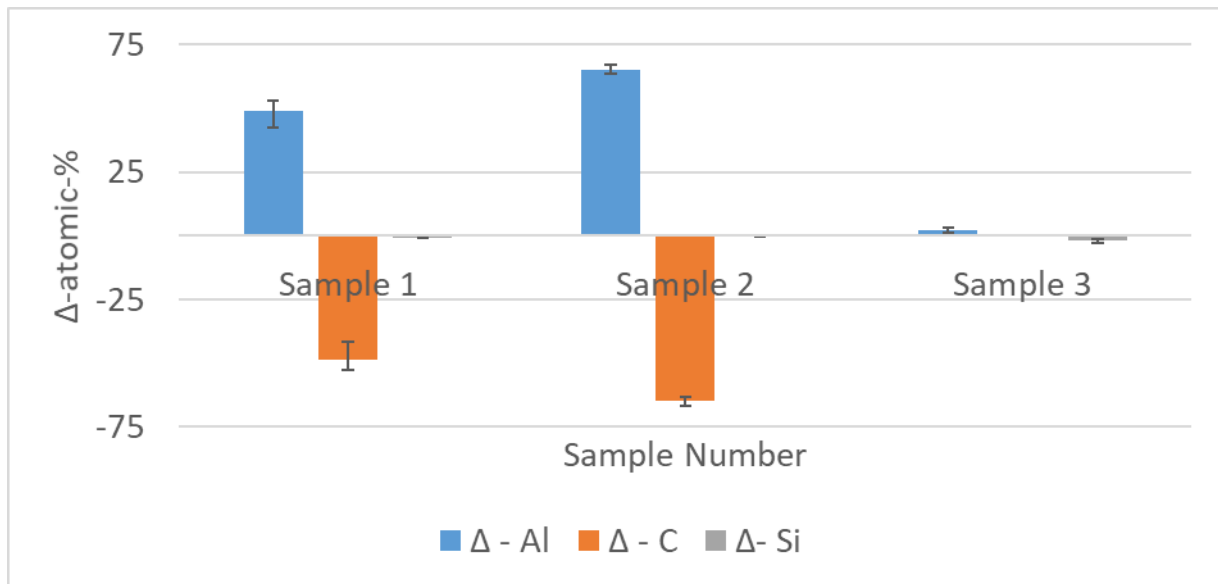
Figure 114 Chemical composition of 2024 T3 aluminium before and after MEK de-greasing.

The increase in aluminium in samples 1 and 2 directly correlates with the decrease in carbon. None of the 5 zones in sample 3 showed any carbon contamination. Here, the reduction of silicone directly correlates with the increase of aluminium. For all three samples, it may be assumed that the found silicone originates from abrasive garnet from the water jet cutting process used to cut the substrates out of the sheet metal.

Table 38 Chemical compositions of 2024 T3 aluminium before and after MEK de-greasing.

	Al – pre MEK	Al – post MEK	C – pre MEK	C – post MEK	Si – pre MEK	Si – post MEK
Sample 1	50.41	99.60	48.58	0.00	0.98	0.33
Sample 2	34.36	99.40	64.97	0.00	0.61	0.53
Sample 3	97.14	99.37	0.00	0.00	2.47	0.53

5.2.6.2 Evaluation of the effect of methyl ethyl ketone (MEK) on the surface composition of aluminium

As the carbon content is reduced to zero, an eventual re-coating with contaminants occurs during the specimen removal from the MEK. Regarding the silicone content, it may be assumed that MEK does not remove silicones in the same manner as carbon contaminants. Re-coating can be ruled out as silicones (~2.33 g/cm^3 at 25 °C) have a higher density than MEK (~0.805 g/cm^3 at 25 °C. Therefore, they would not float at the surface where the re-coating would take place. Figure 115 illustrates a sample area (sample 3, zone 2) pre- and post-MEK degreasing.
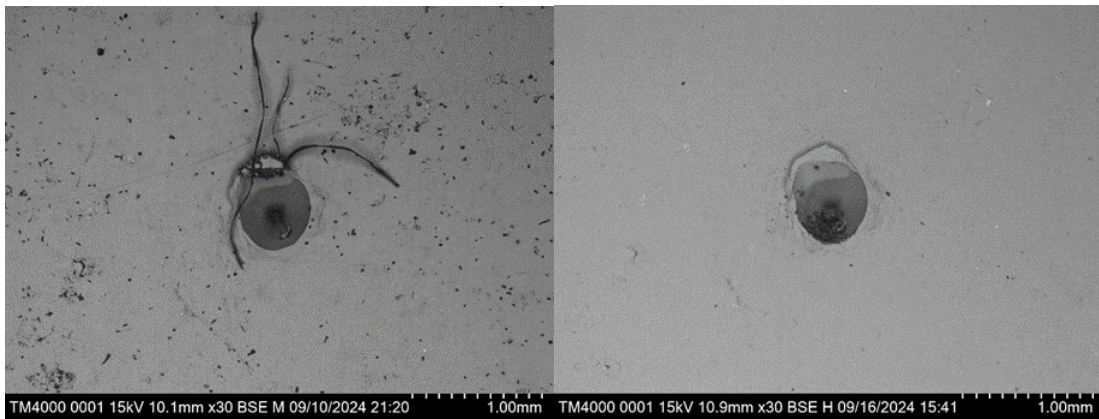
Figure 115 2024 T3 aluminium before (left) and after (right) MEK de-greasing.

The surface contaminants (black spots) are fully removed post-MEK treatment. The centre crater was created with a scriber in order to be able to adjust the SEM to the same region to create comparable results. In conclusion, the 5-minute MEK treatment for the aluminium substrates was considered an appropriate degreasing method as it did remove all of the carbon contaminants and reduced the content of silica. The average aluminium increase was found to be approximately 39%, which correlates with the literature regarding MEK treatment of 2024 aluminium (Sorrentino and Carrino, 2009, Carrino et al., 2005).

5.2.6.2 Evaluation of the effect of methyl ethyl ketone (MEK) on the surface composition of aluminium

5.2.6.3. Tensile testing results

In order to determine the UTS of the aluminium to aluminium SLJs, the tensile forces measured were converted into shear stress by the following equation:

$$\tau = \frac{F}{l \times w} \qquad\qquad [45]$$

Where τ represents the shear stress, F stands for the tensile force, l is the overlap length and w is the overlap width. The overlap area used for all calculations was the ASTM conform overlap of l = 12.7 mm and w = 25.4 mm, which results in an overlap area of 322.58 mm^2. The results of the worst batch (AL – MEK) and the best batch (AL – S2) are illustrated in Figure 116 and Figure 117.
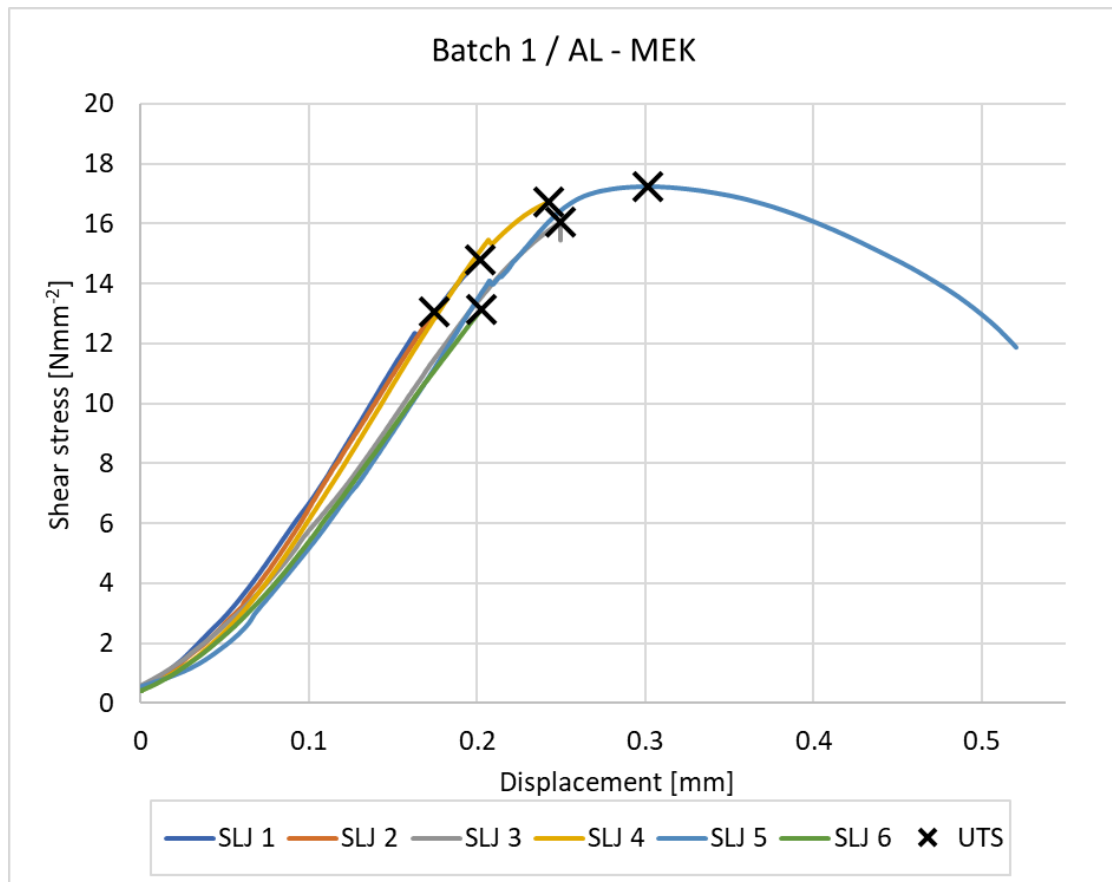
Figure 116 Tensile testing results for batch 1 / AL - MEK. The UTS is superimposed for each curve.

5.2.6.3 Tensile testing results

When comparing AL - MEK and AL - S2, an obvious difference apart from the difference in UTS is the elongation after reaching the UTS. The degreased batch immediately fails after reaching the UTS, except for SLJ 5. On the contrary, the grit-blasted and silane-treated batches are further elongated by 0.4 mm (averaged). This might be evidence for increased mechanical interlocking of the grit-blasted substrates compared to the non-grit-blasted batch. Literature confirms that the larger displacement is due to higher surface roughness (Dos Reis et al., 2017). Displacement increase of up to 50% was observed. The observed slope change during the tensile tests may be attributed to the increased bending during the tests. Bending cannot be avoided as it is a well-known phenomenon in single-lap joint testing.
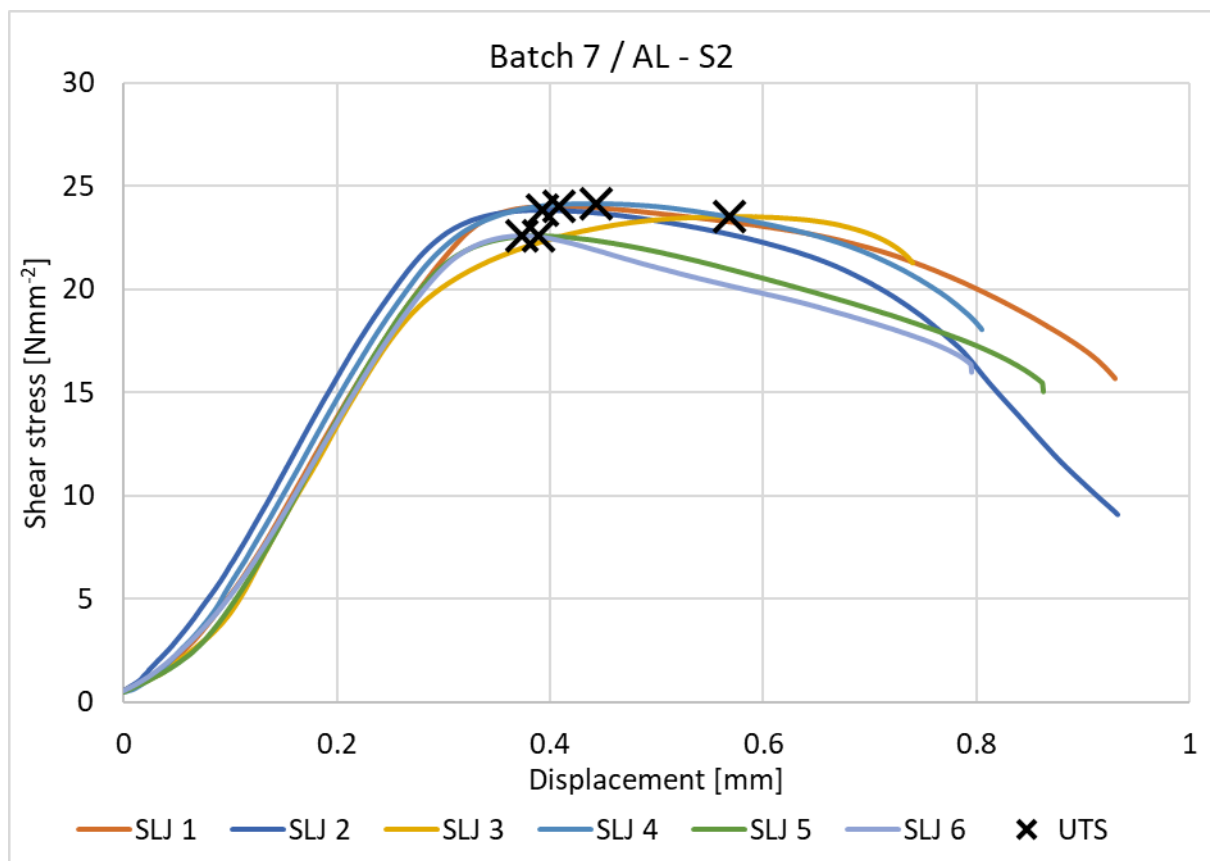
Figure 117 Tensile testing results for batch 7 / AL - S2. The UTS is superimposed for each curve.

The averaged UTS results and the deviation within the batches are listed up in Table 39.

5.2.6.3 Tensile testing results

Table 39 UTS and deviation for aluminium SLJ.

Batch ID	Average UTS [Nmm^{-2}]	Max deviation [Nmm^{-2}]
AL - MEK	15.17	±2.12
AL - GB 15	21.43	±1.72
AL - GB60	21.63	±1.72
AL - GB120	20.61	±2.31
AL - GB180	20.68	±3.04
AL - S1	22.71	±1.08
AL - S2	23.44	±0.88
AL - S3	22.85	±0.88

When observing the tensile testing results and their deviation, the silane treatments appear to have a homogenising effect as the deviation does significantly decrease. When comparing the solely grit-blasted batch AL – GB60 with the silane-treated batches, a decrease in maximum deviation of 0.84 Nmm^{-2} could be observed.

5.2.6.4. Effect of surface roughness and texture on the adhesive bond strength

While there is an increase in UTS when comparing not-grit-blasted batch with the grit-blasted ones, the different grit-blasting do not show a significant or linear change on the UTS. This behaviour has been confirmed in the literature (Fernando et al., 2013, Dos Reis et al., 2017). In order to investigate possible reasons that could explain the plateauing of bond strength at

5.2.6.4 Effect of surface roughness and texture on the adhesive bond strength

different blasting durations, the surface roughness was investigated as well as some fractured bonds post-tensile testing. The surface roughness and texture results are illustrated in Figure 118.
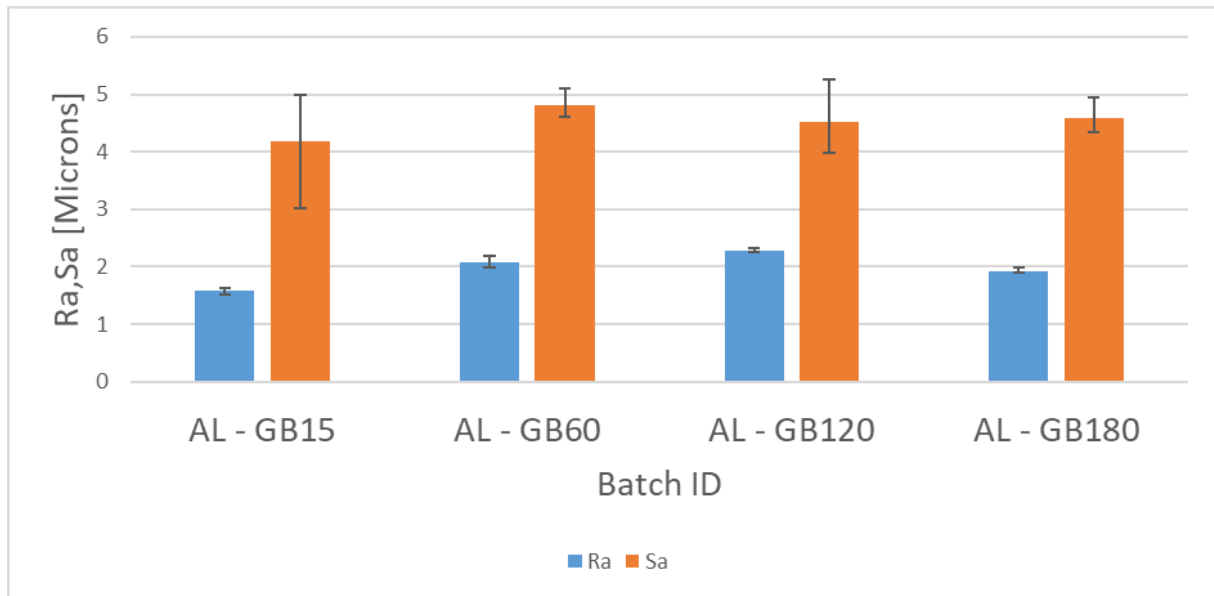
Figure 118 Determined Ra and S values for grit-blasted aluminium.

The roughness and texture do behave in a similar manner for the different grit-blasting durations. Both parameters do increase from AL – GB15 to AL – GB60 and then plateau. A possible reason for this would be the grit-blasting process creating a rougher surface from theoretically 0 seconds to 60 second. An aluminium substrate pre- and post- 60 seconds grit-blasting is illustrated in Figure 119.

5.2.6.4 Effect of surface roughness and texture on the adhesive bond strength
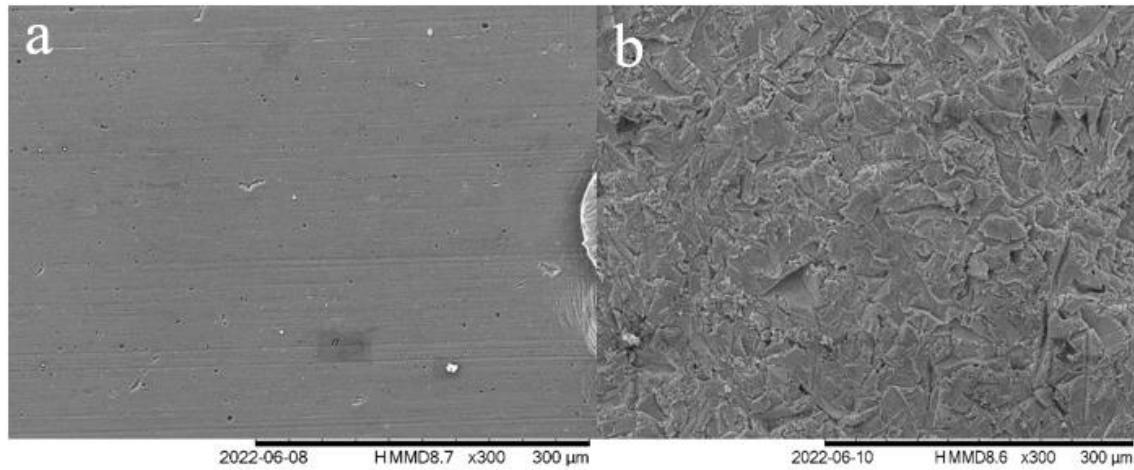
Figure 119 SEM micrograph of 2024 T3 aluminium pre-(a) and post (b) 60 second grit-blasting.

After that, material is still being abraded, but the abrasive media will also abrade the created peaks. Eventually, the abrasive process with its parameters of blasting angle, pressure, stand-off-distance, nozzle diameter, abrasive media, and substrate material, will create a certain "peak" roughness. Once this roughness is reached, the process only abrades more material but does not increase the roughness. Regarding the surface texture, Sz is defined as maximum peak to maximum valley distance in microns. When observing the Sz values for the grit-blasted batches, no increasing trend could be observed, which may be evidence for the previously mentioned hypothesis. The Sz values for the grit-blasted batches are presented in Figure 120.
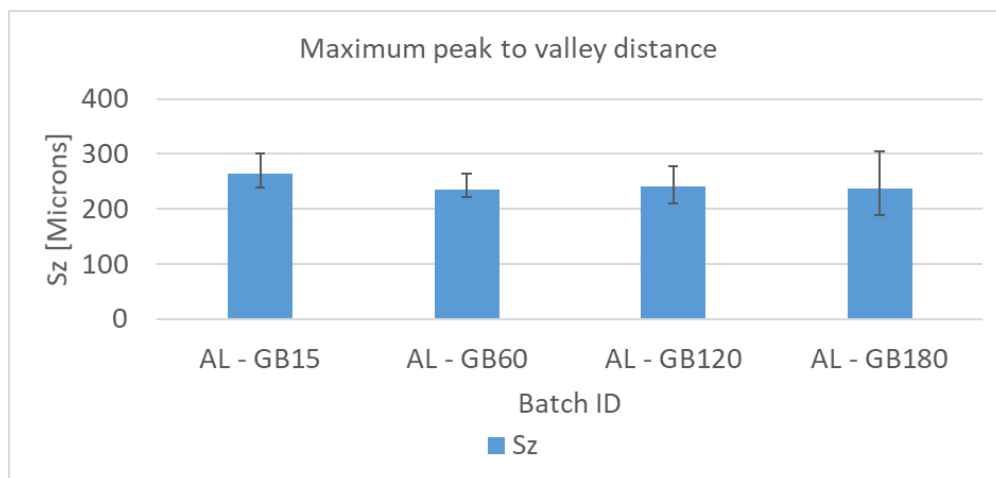
Figure 120 Maximum peak to valley (Sz) values determined for different grit-blast durations on 2024 T3 aluminium.

5.2.6.4 Effect of surface roughness and texture on the adhesive bond strength

As the maximum peak-to-valley distance does not vary between the batches in a significant manner, it can be assumed that the grit-blasting process does create peaks and valleys and also abrades the peaks simultaneously. This may explain the plateauing of surface roughness and,therefore, the plateauing of adhesive bond strength.

5.2.6.5. Investigation of the relationship between surface roughness and interfacial microvoids

During the investigation of the fracture surfaces, micro voids were found on named surfaces for the grit-blasted samples. For this work, the author differentiates between voids and microvoids by the diameter of the voids. As the static mixer does not guarantee mixing without air inclusions, voids were found on the fracture surface, that are assumed to be air inclusions from the mixing- and application process. Figure 121 illustrates present voids on a fracture surface. When examining the colour variations, it can be inferred that the lighter shade suggests the removal of the adhesive bond-line from the surface. This assumption is reasonable, given that peeling caused by bending was observed as the initiator of failure.
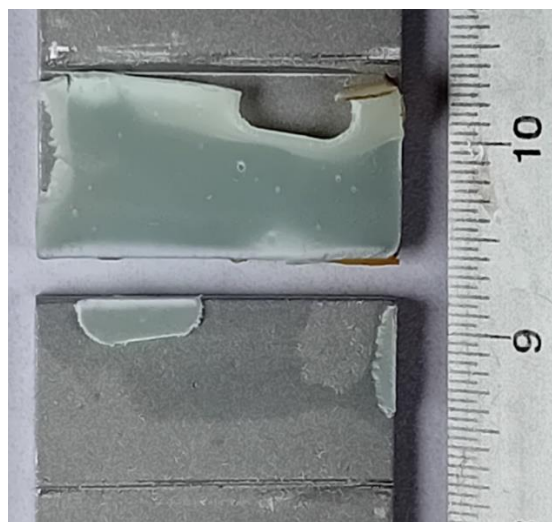
Figure 121 Fracture surface of grit-blasted 2024 T3 SLJ. Voids can be seen within the bond line.

Microvoids were only observed during microscopy and had diameters of approximately 20 to 40 microns. Figure 122 illustrates two fracture surfaces, one with no microvoids (AL – MEK) and one with found microvoids (AL – GB60).
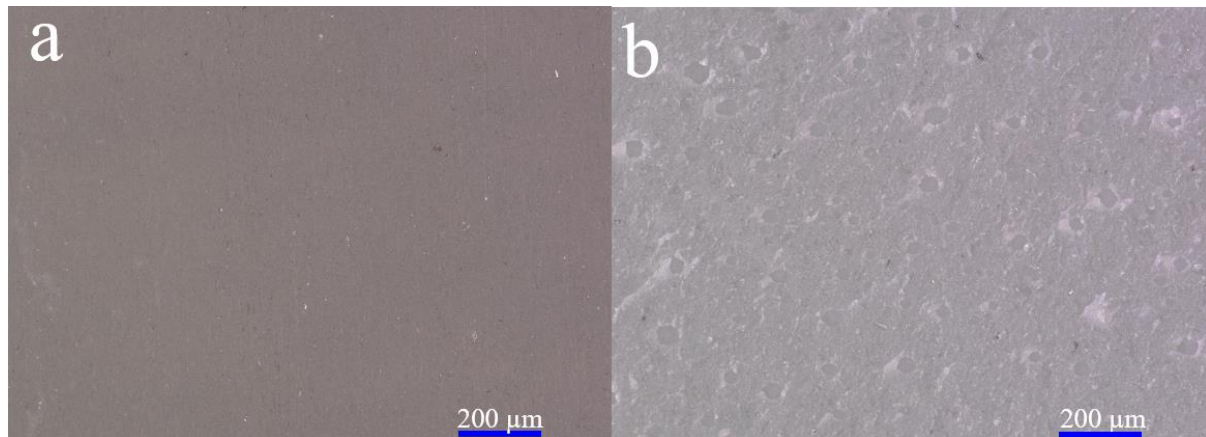
Figure 122 Fracture surfaces with (a) MEK treatment and (b) grit-blasted. The MEK treated surface shows no traces of microvoids.

ImageJ was used to enhance the contrast between the microvoids and the adhesive bond-line, as illustrated in Figure 123
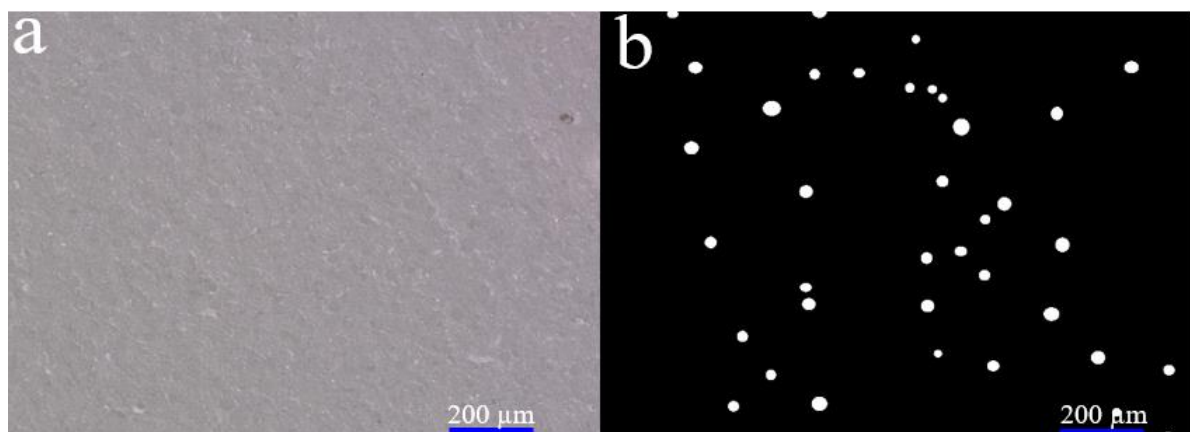
Figure 123 Fracture surface of grit-blasted SLJ with (a) original image and (b) contrast-enhanced.

5.2.6.5 Investigation of the relationship between surface roughness and interfacial microvoids

In order to quantify these microvoids, five images of the fracture surface of each grit-blasting duration have been taken using a Keyence digital microscope. The void fraction has been calculated using ImageJ. The results are presented in Figure 124.
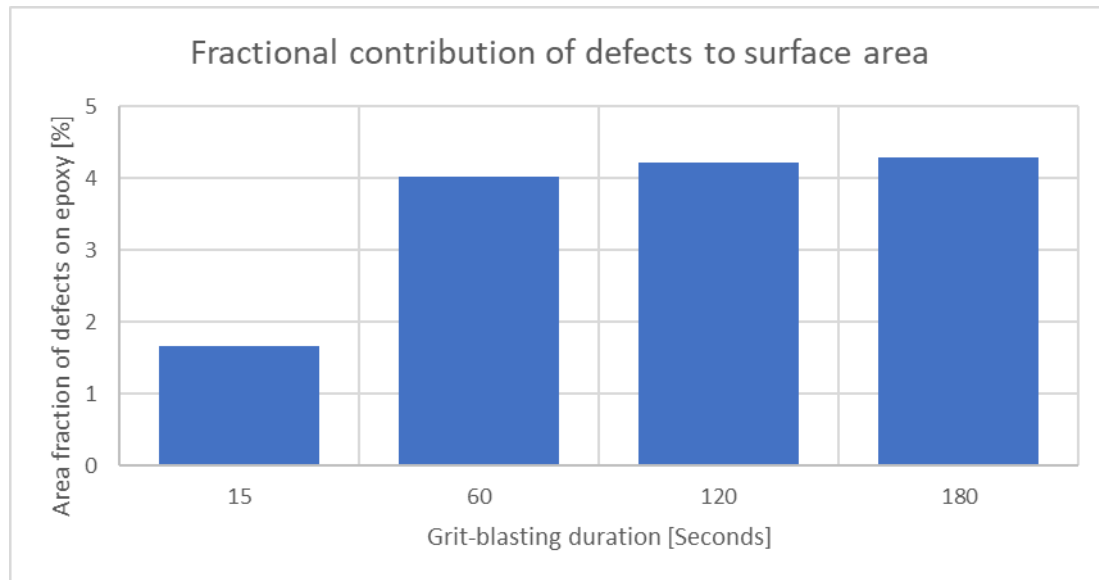
Figure 124 Determined microvoid fraction for different grit-blasting durations.

The microvoid fraction behaves in a similar manner to the roughness and texture concerning the grit-blasting duration. To what extent these microvoids affect the tensile testing results is unclear, as the tests indicate that the SLJs fail primarily due to peeling, which is caused by the induced bending of the joint during loading. For the AL – MEK batch that was not grit-blasted, no microvoids could be observed. To create a clearer view of the fracture surface, the Alicona G5 was used to scan the undeformed areas of the fracture. The results are illustrated in Figure 125, Figure 126, and Figure 127. To enable a better view on the microvoids, the scanned areas have been cut in two halfs (top and bottom). The AL – MEK, AL – GB15, and AL – GB60 bottom parts are illustrated below. The remaining grit-blasting durations and top parts can be found in Appendix B.

5.2.6.5 Investigation of the relationship between surface roughness and interfacial microvoids
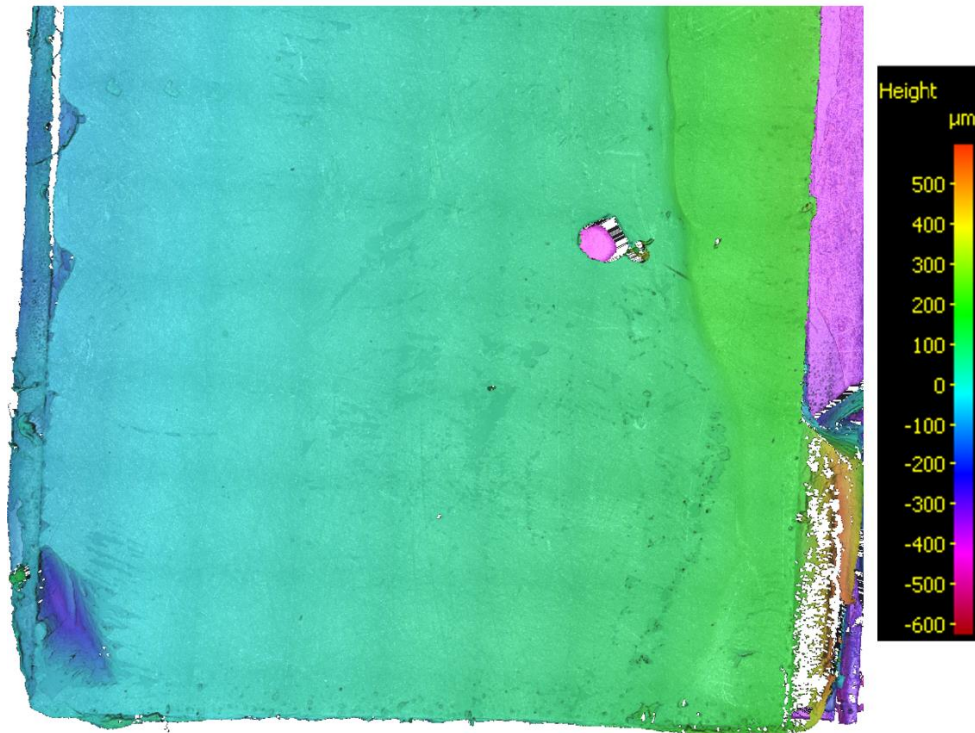
Figure 125 Bottom part of fracture surface of solely de-greased substrate.

The AL – MEK batch does not exhibit a significant number of microvoids on the fracture surface. Although some isolated microvoids may be present, there is no clear indication of a clustered formation. This suggests that the surface roughness characteristics of this batch did not promote extensive void formation,

5.2.6.5 Investigation of the relationship between surface roughness and interfacial microvoids
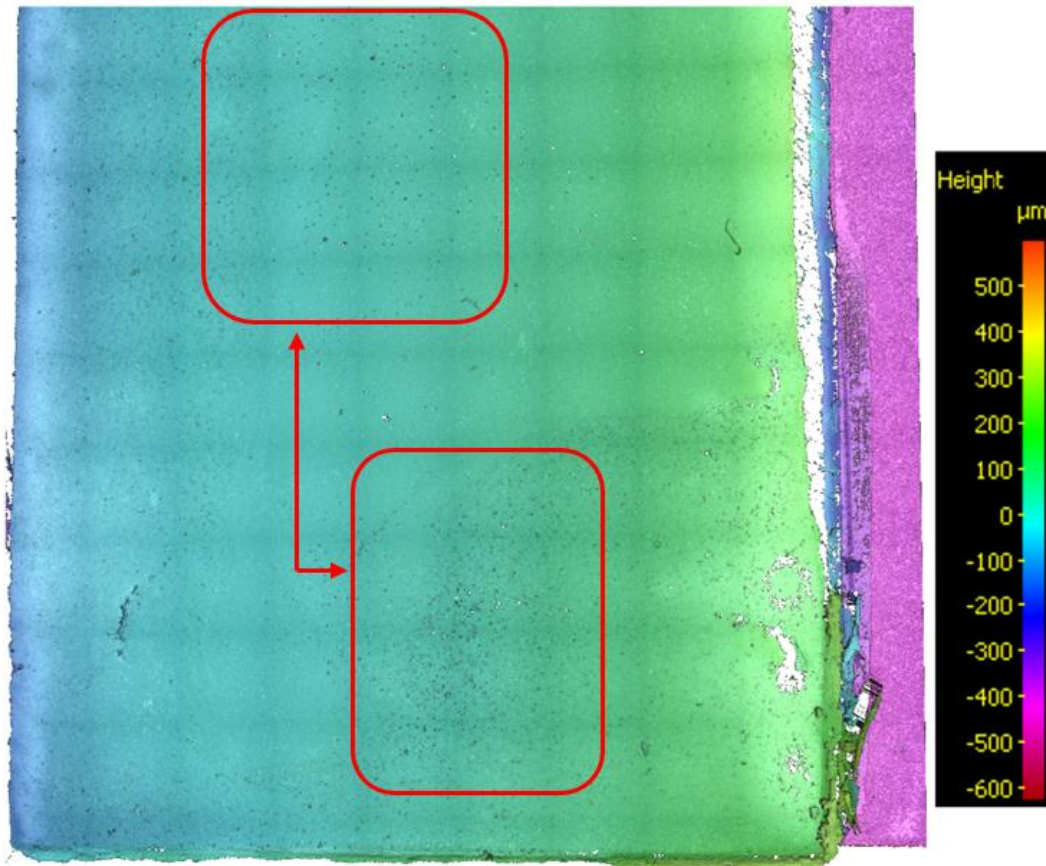
Figure 126 Bottom part of fracture surface of 15 seconds grit-blasted substrate. Microvoid clusters are indicated within the red frame

In the AL – GB15 batch, microvoids are clearly present, but their distribution is not homogeneous. Instead, they appear to be clustered in specific regions rather than evenly dispersed across the fracture surface. Notably, two distinct clusters can be identified near the centre, suggesting that the surface characteristics influenced the localised formation of these voids. This non-uniform distribution may indicate areas of increased stress concentration or variations in adhesive interaction with the substrate.

5.2.6.5 Investigation of the relationship between surface roughness and interfacial microvoids
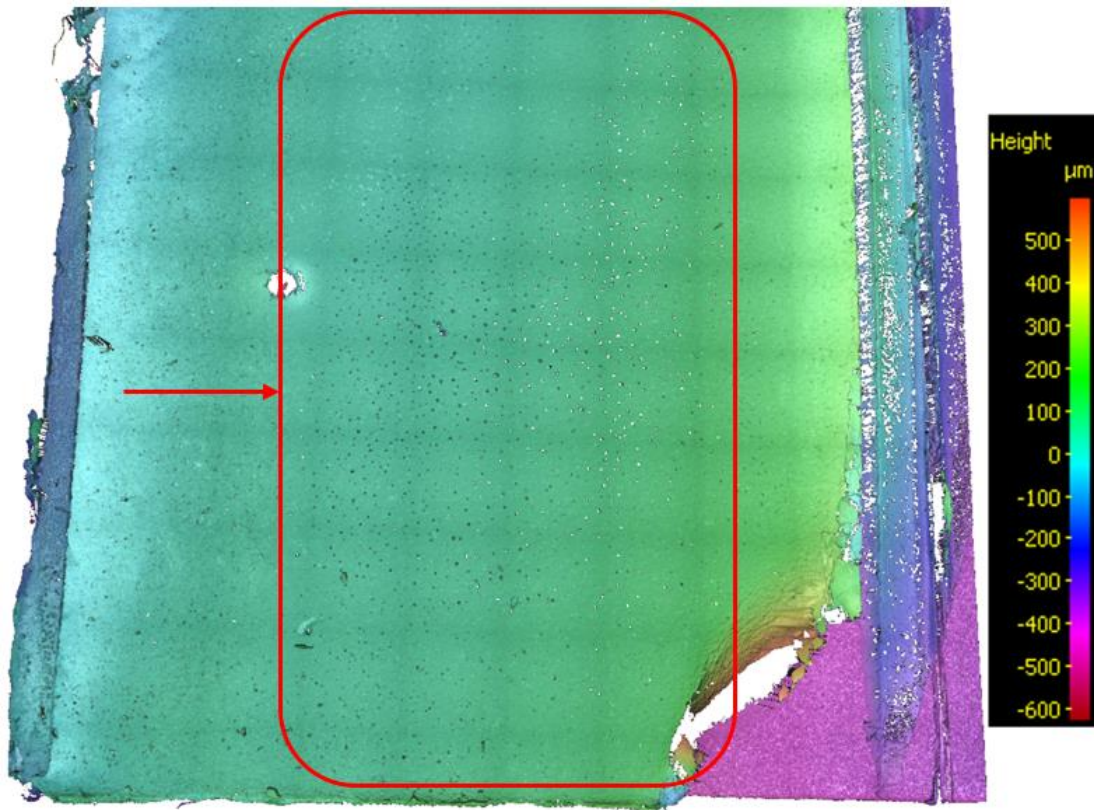
Figure 127 Lower region of the fracture surface of the 60-second grit-blasted substrate, with a microvoid cluster indicated within the red frame.

The AL – GB60 batch exhibits a substantial number of clustered microvoids across the surface. These voids appear notably larger than those observed in the AL – GB15 batch and are more densely packed. In contrast to the 15-second grit-blasted sample, a larger cluster of microvoids extends across the entire width of the lower region. Additionally, the increased void size and density suggest a more pronounced influence of the surface preparation process on the fracture characteristics. The large void located towards the centre-left of the surface is presumed to have originated from the static mixing process, potentially due to inconsistencies in adhesive mixing or application.

Previous research has shown that the mixing technique significantly influences microvoid formation in two-part epoxy adhesives, with static mixing resulting in fewer and smaller voids compared to manual mixing. Dispenser-mixed specimens typically exhibit void sizes in the

5.2.6.5 Investigation of the relationship between surface roughness and interfacial microvoids

range of 5–20 µm, whereas hand-mixed adhesives contain larger voids (20–100 µm), suggesting that air entrapment during mixing is a key factor (Katnam et al., 2011).

In this study, microvoids were analysed using a Alicona G5, revealing an increase in void content with surface roughness. This indicates that surface conditions may affect the efficiency of adhesive mixing at the interface, where rougher surfaces could impede proper adhesive flow and wetting, leading to localised air entrapment. These findings suggest that void formation is not solely governed by the bulk mixing method but also by the interaction between the adhesive and the substrate surface.

5.2.6.6. Assessment of the effect of silane treatment on the SLJs

The different silane solutions did result in slightly different bonding strengths. As the average UTS and the maximum deviations of the tensile testing results are of minor significance, a statistical relevance between the different silane concentrations could not be established. EDX was utilised to investigate the silicon content on substrates treated with the three different concentrations. The results are illustrated in Figure 128.
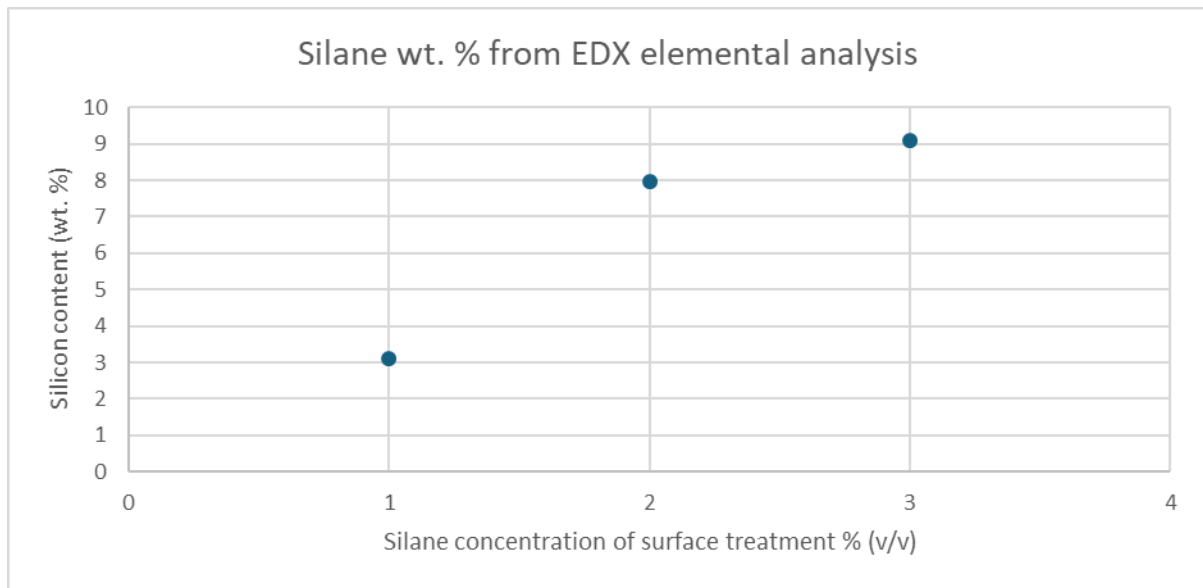
Figure 128 Silicon content on the treated surface, determined by EDX analysis, as a function of the silane concentration in the applied solution.

As the silicon content increases with the silane concentration in the aqueous solutions, it may be assumed that the higher silane concentrations result in a better silane coverage on a substrate area. As the tensile tests show no significant changes in bond strength with higher silicon contents, it may be assumed that the silicon content on a substrate surface does not linearly increase the bond strength. When observing SEM scans taken during the EDX analysis, it was observed that the silanes do no homogeneously cover the the substrate area, as illustrated in Figure 129.
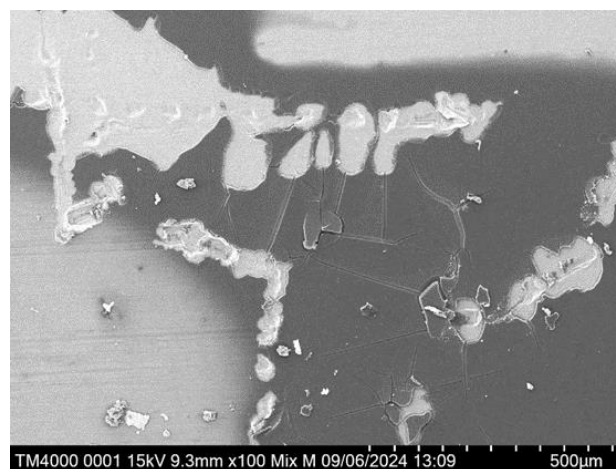
Figure 129 Silane deposition on aluminium substrate illustrates silane pooling.

5.2.6.6 Assessment of the effect of silane treatment on the SLJs

5.2.6.7. Surface free energy determination

Each test liquid was measured five times with five contact angle measurements for each surface treatment. The average contact angles were then used to calculate SFE using the extended Fowkes method. The results are illustrated in Table 40

Table 40 Free surface energy determination for aluminium substrates.

	Pre-MEK	Post-MEK	1% Silane	2% Silane	3% Silane
Water contact angle [°]	94.13	80.03	79.20	78.21	76.95
1 – bromonaphthalene contact angle [°]	17.46	15.71	10.40	12.28	17.15
Solid SFE dispersive component [mJm^{-2}]	43.26	43.64	44.58	44.29	43.33
Solid SFE polar component [mJm^{-2}]	03.88	17.10	17.57	18.75	20.51
Solid SFE [mJm^{-2}]	47.14	60.74	62.15	63.04	63.84

When plotting the SFE data against the used silane concentrations, a highly linear correlation could be observed, as illustrated in Figure 130. This may be evidence of a thicker silane deposition at higher concentrations.
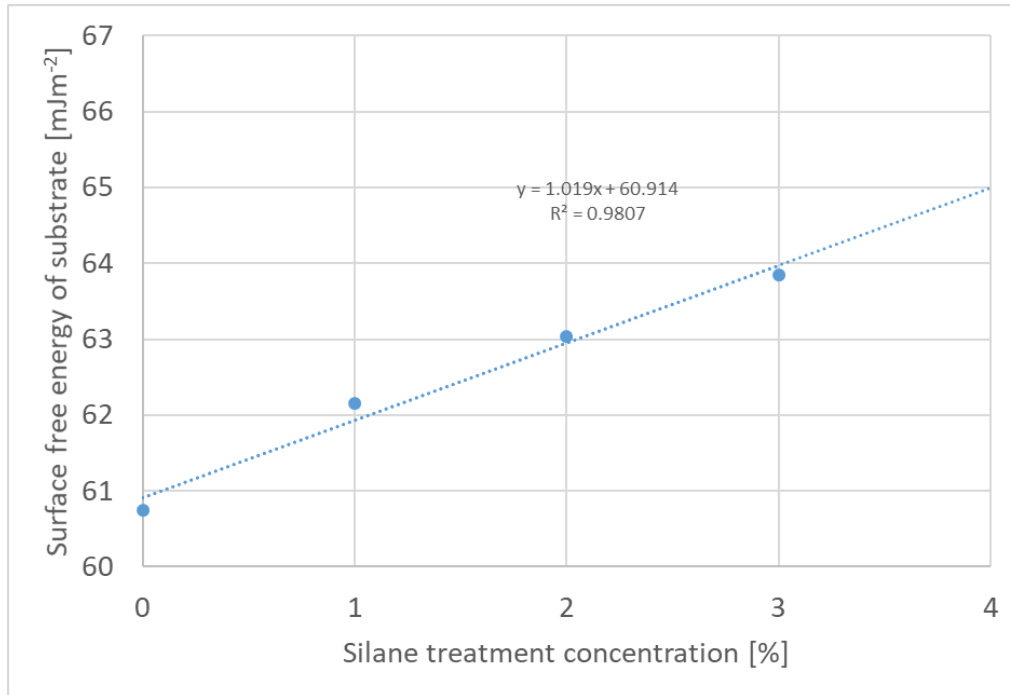
Figure 130 Surface energy vs silane concentration, including trend line.

An example of a contact angle measurement is illustrated in Figure 131.
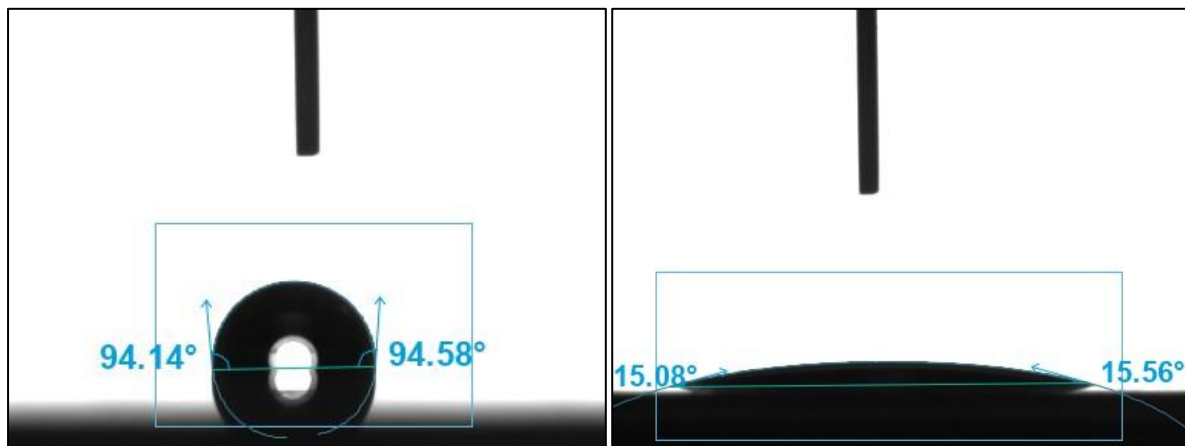
Figure 131 Contact angle measurements of aluminium substrates.

5.2.7. Composite-to-composite bonding

The composite-to-composite joints were evaluated in a similar manner to the aluminium-to-aluminium joints. As XPS was not available to analyse the CFRP surfaces, the assessment of

the acetone degrease influence, and the silane deposition on the CFRP surface could not be conducted.

5.2.7.1.   Tensile testing results

The worst (C – ACE) and the best (C – GB5) batch are illustrated in
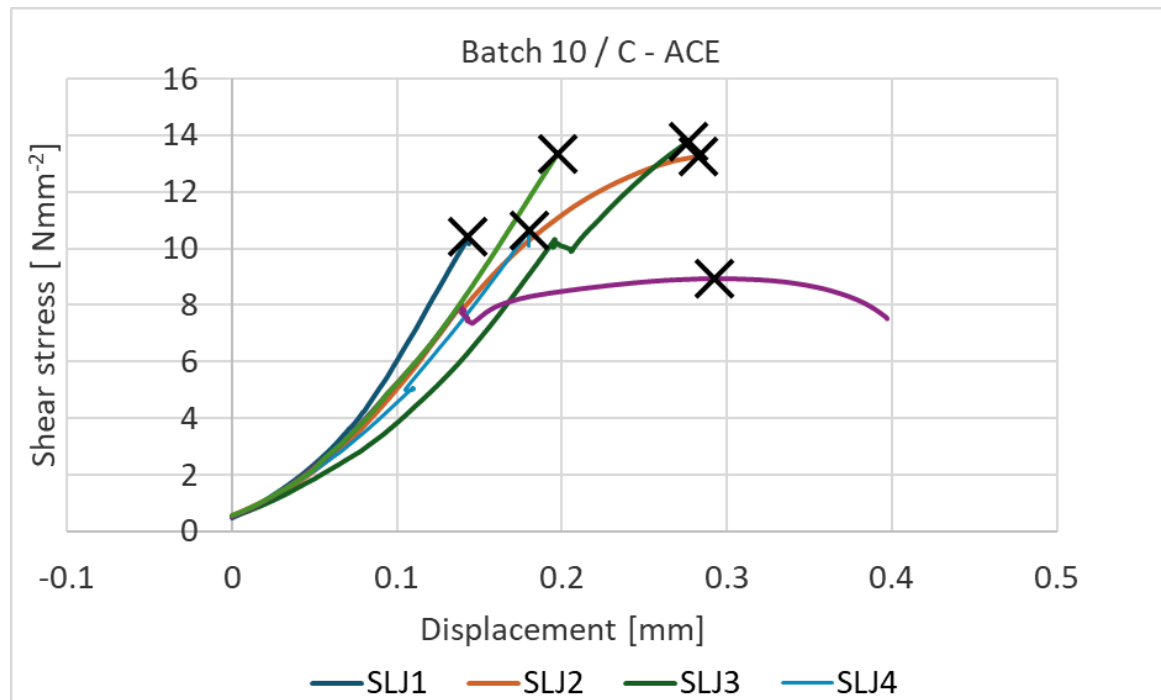
Figure 132 Tensile testing results for batch 10. and *Figure 133*. Like the aluminium-to-aluminium batches, the degreased CFRP batches fail almost immediately after reaching the UTS. Substrate delamination could not be observed for the C – ACE batch. Upon visual inspection after tensile testing, colour changes in the bond line indicate interfacial failure on both sides. This interfacial delamination could cause sharp stress drops within the stress-strain curves.

5.2.7.1 Tensile testing results
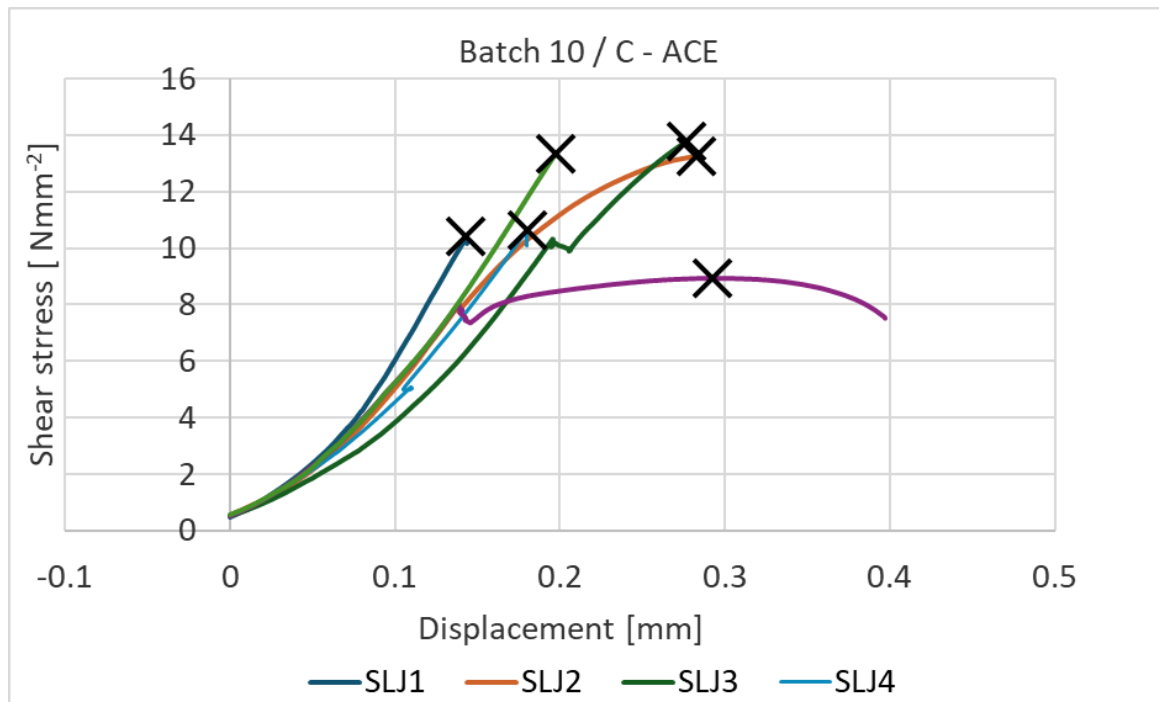
Figure 132 Tensile testing results for batch 10.

When comparing the C – GB5 batch to the C - ACE batch, the slopes of all SLJ until UTS are nearly congruent for the grit-blasted batch, which indicates a highly similar stress distribution until reaching UTS. The average elongation after UTS was found to be 0.38 mm. Stress drops during the test could not be observed. The maximum stress deviation was decreased by 2.51 Nmm^{-2}.

5.2.7.1 Tensile testing results
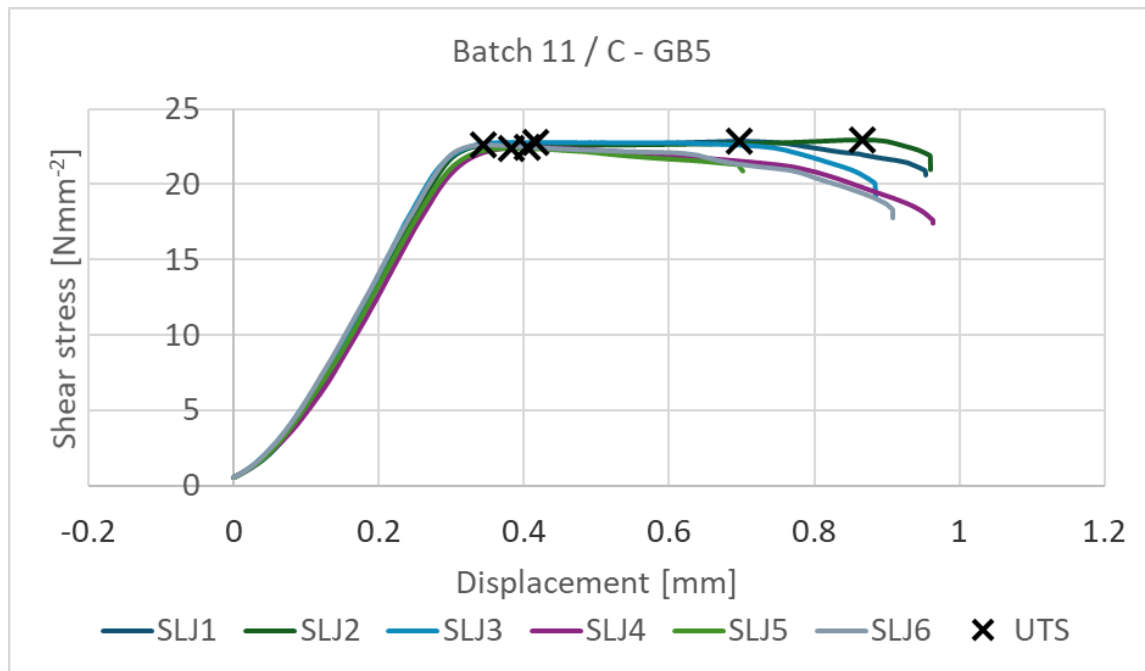
Figure 133 Tensile testing results of batch 11.

The numeric results for the composite to composite single-lap joints are presented in *Table 41*.

Table 41 Tensile testing results for composite SLJ.

Batch ID	Average UTS [Nmm^{-2}]	Max deviation [Nmm^{-2}]
C - ACE	11.72	±02.81
C - GB3	22.18	±00.72
C – GB5	22.68	±00.30
C – GB7	21.42	±01.21
C – S1	21.73	±01.01
C – S2	16.69	±03.00
C – S3	13.11	±06.01

For the CFRP single-lap joints, GB3 and GB5 were found to have the lowest maximum deviation among all batches. The 1% silane treatment performs slightly worse than the regular

5.2.7.1 Tensile testing results

GB5 treatment regarding bonding strength and significantly worse in maximum deviation. The 2% and 3% silane concentrations significantly decreased bonding strength and maximum deviation.

5.2.7.2. Effect of surface roughness and texture on the adhesive bond strength

Similar to the aluminium-to-aluminium batches, there is a significant increase in UTS when comparing the acetone-degreased batch with the grit-blasted ones. The different grit-blasting durations do not show a significant change in the UTS. A constant increase in RA and SA between the grit-blasting durations could be observed, meaning the substrates do get rougher at longer grit-blasting durations without significant increases in bond strength. Void fraction analysis could not be conducted on the CFRP samples due to time limitations. The surface roughness and texture results are illustrated in *Figure 134*.

5.2.7.2 Effect of surface roughness and texture on the adhesive bond strength
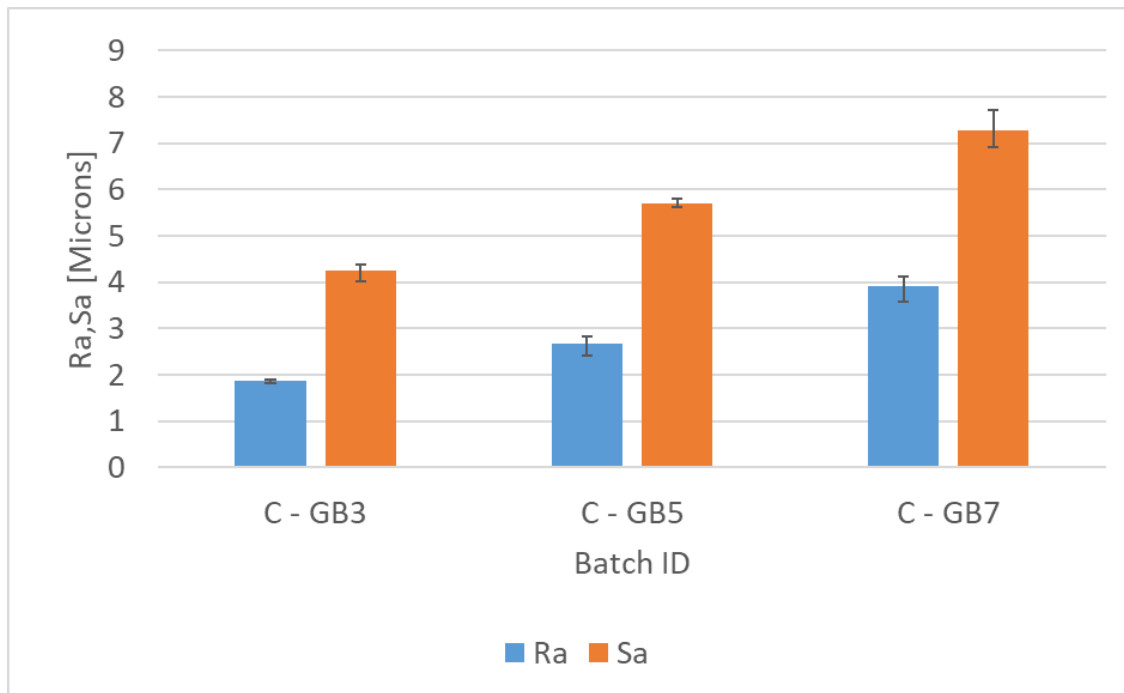
Figure 134 Surface roughness values of composite substrates.

The roughness and texture behave in a similar manner for the different grit-blasting durations. Both parameters do constantly increase with increasing grit-blasting duration. When comparing the composite to composite batches to the aluminium to aluminium batches, the increase in roughness happens much more rapid on the composite surface. As the grit-blasting setup was the same, it can be assumed that the polymeric matrix offers significantly less resistance to the blasted abrasive media. Another reason could be the nature of the composite. It may be assumed that the grit is able to abrade the matrix faster than the carbon fibres, which would additionally increase the roughness as the height distributions from the mean line could increase. Alicona scans were conducted to investigate this hypothesis for the three different composite grit-blast durations. The results are illustrated in *Figure 135*.

5.2.7.2 Effect of surface roughness and texture on the adhesive bond strength
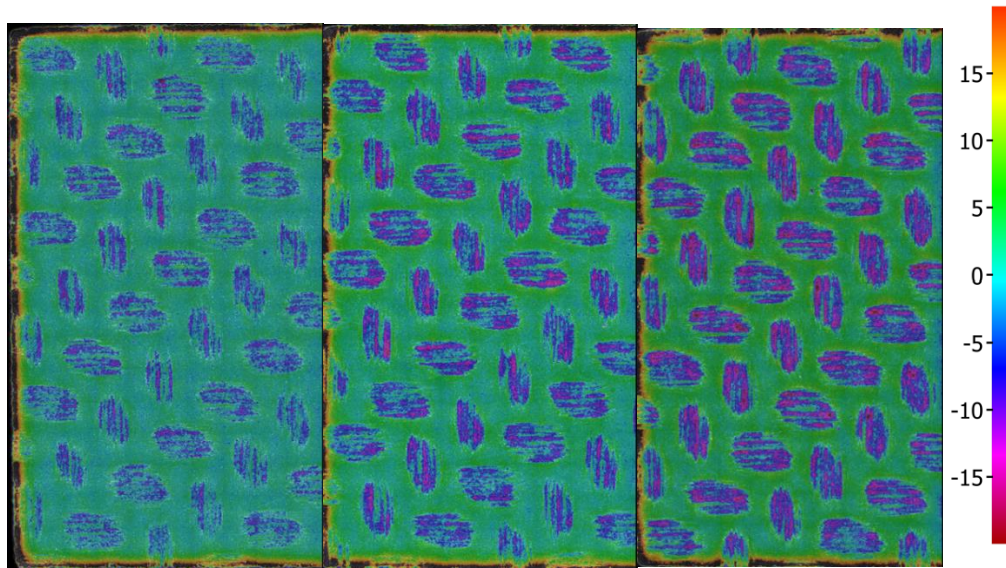
Figure 135 CFRP substrates at different grit-blasting durations analysed with the Alicona G5.

The increasing grit-blasting duration increasingly removes the matrix from the twill layer of the composite. The weft wand warp fibres are becoming more exposed with increasing blasting duration. Unidirectional fibre arrays could not be detected, which might indicate the first UD ply not being affected by the grit-blast procedure. As the amount of twill becomes more prominent with increasing blasting time, it might be concluded that the matrix is being removed faster than the reinforcement. This could also explain the rapid increase in Ra and Sa.

5.2.7.3. Assessment of the effect of silane treatment on the SLJs

A detailed view of the results of the silane-treated CFRP substrates and the c – GB5 batch as reference are illustrated in *Figure 136*.

5.2.7.3 Assessment of the effect of silane treatment on the SLJs
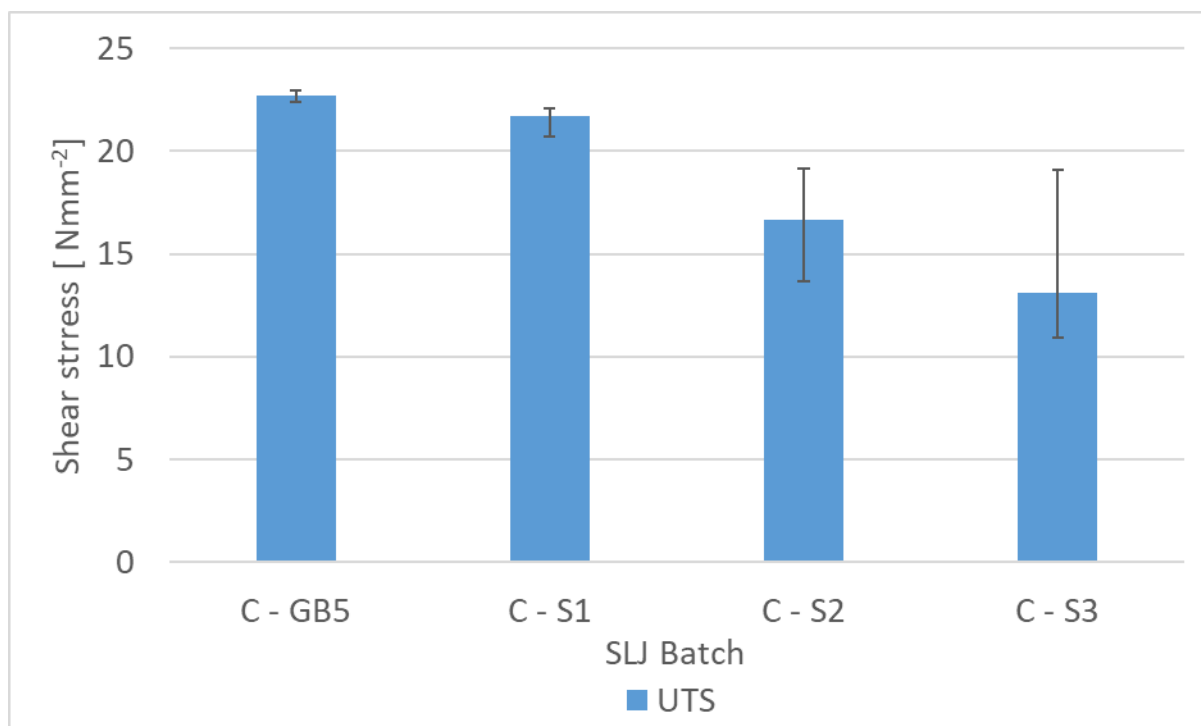
Figure 136 Shear stress results for composite joints.

A linear decrease of ultimate tensile strength was observed for the silane-treated C-GB5 batch. This might result from weaker intermolecular interactions between the substrate matrix material and the attached silane. Additionally, the deposited silane layer might result in a decrease in the mechanical interlocking of the adhesive. The C-S3 batch was seen to show the second lowest UTS with 13.25 $Nmm^{-2.}$

5.2.7.4. Surface free energy determination

As the exposed fibres resulted in an inhomogeneous surface, the surface-free energy for the grit-blasted samples could not be appropriately determined. The free surface energy increase from 63.60 to 66.01 mJm^{-2} post-degrease was found to be of a smaller magnitude compared to the aluminium batches.

5.2.7.4 Surface free energy determination

Table 42 SFE determination for composite substrates.

Parameter	Pre-ACE	Post-ACE
Water contact angle [°]	76.06	74.12
1 – bromonaphthalene contact angle [°]	24.91	23.34
Solid SFE dispersive component [mJm^{-2}]	41.20	41.69
Solid SFE polar component [mJm^{-2}]	22.40	24.32
Solid SFE [mJm^{-2}]	63.60	66.01

5.2.8.   Aluminium-to-composite bonding

The tensile testing results for both hybrid batches are presented in Table 43. The values for pre-bond surface properties of both hybrid batches are similar to the AL – BG60, AL – S2 and C – GB5 batches, and are therefore not detailed again.

Table 43 UTS results for the hybrid batches.

Batch ID	Average UTS [Nmm^{-2}]	Max deviation [Nmm^{-2}]
H – S2	21.85	± 02.50
H - GB	21.32	± 01.25

Both hybrid batches produced lower UTSs than the same-substrate SLJs with the respective surface modifications. Eventually, variations in the elastic deformation of the substrate materials led to an imbalanced stress distribution across the SLJs. Consequently, one interface was subjected to a greater localised load than the other, ultimately triggering early joint failure.
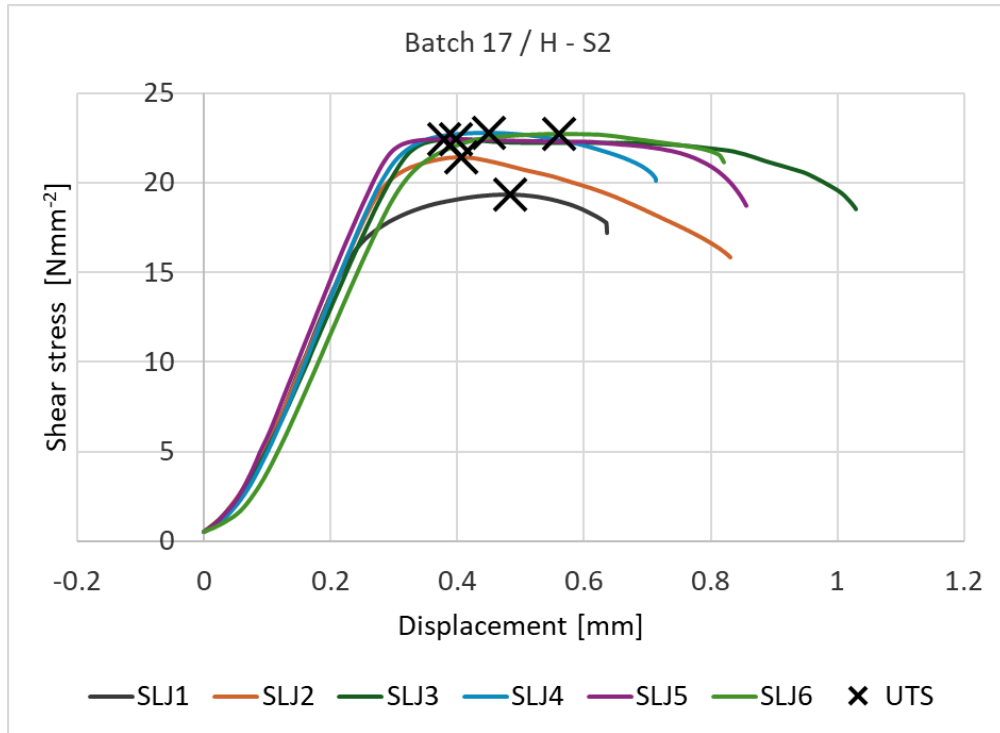
Figure 137 Tensile testing results of the silane-treated hybrid batch.

The H – S2 batch shows a highly congruent initial slope. No stress drops could be observed. The average elongation from UTS to failure for this batch was 0.37 mm. Stress drops during the test could not be observed.
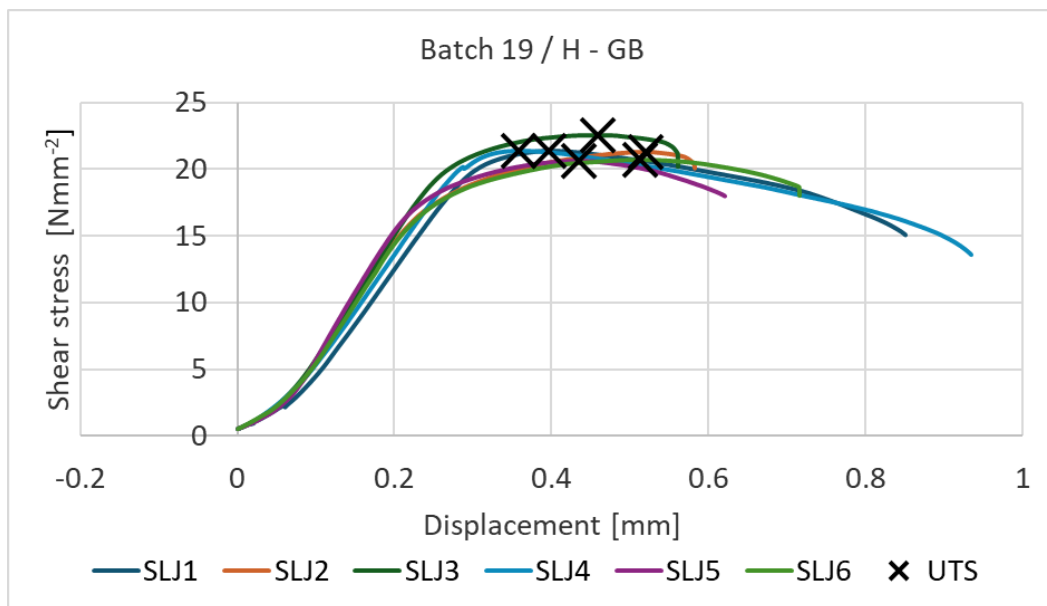
Figure 138 Tensile testing results of the grit-blasted hybrid batch.

5.2.8 Aluminium-to-composite bonding

The H – GB batch also does not show any stress drops throughout the testing. The UTS between the batches appeared not as clustered as for the H – S2 batch. The average elongation between UTS and failure was 0.26 mm. This is minutely less than the other hybrid batch, but as the UTS was not as densely arranged, the UTS shift might be a possible reason for the decreased elongation.

(Bora et al., 2020) investigated SLJ testing of CFRP and AA2024-T3 aluminium in a highly comparable setup with this work. EA 9396 was bonded using a 50 μm bond line, whereas EA 9466 was used in this study with a 0.5 mm bond line. Both studies employed grit-blasting for aluminium preparation, but Bora et al. additionally tested an epoxy-based silane treatment, finding 3 vol% to be optimal, leading to a UTS of 16.44 N/mm². In contrast, this study achieved 21.32 N/mm² for grit-blasted aluminium (Ra $\approx$ 2 μm), with a minor increase in UTS of 0.5 N/mm² when treated with 2% amine-based silane. The significantly higher bond strength here suggests that mechanical surface preparation plays a dominant role, while the influence of bond line thickness and overlap length requires further investigation (Bora et al., 2020). The raw data of the tensile testing data of the SLJ batches is illustrated in Appendix C.

5.2.8 Aluminium-to-composite bonding

6. Conclusion

Assessment of Fresnel reflection sensors

The investigation of FRS demonstrated that reliable and accurate calibration of multiple channels is feasible when key influencing factors are systematically addressed. The primary parameters requiring validation were the cleave angle, ambient temperature, refractive index of the analyte, and the stability of the light source.

The influence of the cleave angle was first examined through simulations and subsequently validated experimentally. By evaluating cleaves across several channel selector ports and normalising the data, appropriate conditions for consistent Fresnel reflection could be established. For the refractive index reference, the 60/ED refractometer was tested against certified refractive index oils across a broad range (1.4–1.7). The results confirmed a maximum deviation of only 0.00038 RI, in excellent agreement with manufacturer data and literature values, thus providing a highly accurate calibration standard.

The long-term stability of the FRS light source was further validated in a 25-hour experiment. While room temperature fluctuations could not be fully isolated, the recorded variations were minimal: the light source output deviated by only 0.535%, the FRS response by 1.186%, and the room temperature by 6.038%. These results indicated both a precise temperature controller within the light source and a negligible influence of environmental drift on the sensor output.

Finally, calibration of four FRS sensors using the refractometer confirmed the high accuracy of the approach. The experimental data closely followed the theoretical Fresnel reflection coefficient, with curve-fitting yielding R^2 values between 0.9994 and 0.9997. The small logged temperature deviations (±0.2 °C) further ensured that temperature effects could be neglected

within the measurement uncertainty. However, direct refractive index sensing remains limited, as the calibration inherently depends on the light source characteristics of the refractometer.

Overall, the studies confirmed that Fresnel reflection sensors, when properly calibrated, provide a robust and precise means of monitoring interfacial conditions. The combination of cleave optimisation, refractometer validation, and light source stability assessment ensures that FRS can be reliably integrated into adhesive joint monitoring applications.

Quantitative Comparison of FTIR and FRS Cure Kinetics

Temperature uniformity was first addressed by defining an optimal FRS immersion depth of 25 mm, which minimised gradients relative to the FTIR sensing zone, with maximum deviations limited to 0.27 °C. A notable observation was that the hardener exhibited threefold higher sensitivity to NIR light compared to the resin, suggesting potential photo-induced effects that could artificially accelerate curing and require further investigation.

Baseline FTIR measurements established the cure kinetics of Loctite EA9466 between 20–50 °C using the autocatalytic model. Embedding FRS sensors into the cuvettes enabled direct comparison of both methods under identical conditions. Despite the intensity-based nature of FRS, the measurements exhibited low scatter (2.6%) and demonstrated strong agreement with FTIR, once temperature effects were taken into account. By applying the Kamal model and Arrhenius analysis, highly consistent activation energies were obtained (FTIR: 75.29 kJ·mol^{-1}; FRS: 74.12 kJ·mol^{-1}), demonstrating that low-cost FRS can reliably capture polymer cure kinetics.

Further validation using parallel plate rheometry confirmed these findings. After correcting for a small thermal offset (1.76 °C), the characteristic transitions of all three techniques aligned: the rheometer crossover, the FRS noise cessation, and the FTIR secondary amine maximum.

6 Conclusion

The resulting activation energy from rheometry (63.10 kJ·mol⁻¹) was slightly lower than FTIR (69.98 kJ·mol⁻¹) and FRS (65.98 kJ·mol⁻¹), but still within reasonable agreement.

Overall, this study demonstrated that Fresnel reflection sensing can provide quantitative cure kinetics comparable to those obtained by FTIR and rheometry. FRS offer a cost-effective and integrable alternative for in-situ monitoring of adhesive curing.

In situ assessment of multiple parameters in adhesive joints

This study demonstrated the feasibility of simultaneously monitoring chemical, refractive index, strain, and temperature changes within single-lap joints (SLJs) using a multi-sensor approach under controlled glove box conditions. The glove box achieved high stability, with temperature and humidity deviations of only 0.72 °C and 1.03%, respectively, ensuring reliable experimental environments. Small offsets relative to the HP21 reference (0.2 °C, 4% RH) were identified and can be readily compensated.

Surface-mounted FTIR sensors successfully tracked cure kinetics at 30 °C and 40 °C, with degrees of cure deviating by only 4% and 1% from cuvette references despite higher scatter. Fresnel reflection sensors (FRS) showed similarly robust performance, with acceptable scatter increases at elevated temperatures (1.28–1.84%).

FBGs provided accurate thermal readings within SLJs (deviation ≤ 0.3 °C), with sensitivities (9.6–11.7 pm/°C) consistent with literature. The experiments revealed significant delays in achieving isothermal conditions within the joints (226–293 min), likely due to the manufacturing rig. Strain-sensitive FBGs captured shrinkage with high linearity ($R^2 = 0.9753$), confirming their suitability for polymerisation monitoring.

FP sensors required the development of a robust Fourier-based peak tracking routine. Simulations revealed that cavity size was the dominant factor influencing accuracy, leading to the selection of small cavities. Intrinsic FPs proved insensitive to shrinkage, with minimal drift

6 Conclusion

(≤ 0.032 nm), whereas extrinsic FPs with 33–46 µm cavities revealed a linear refractive index increase with curing temperature. Although absolute RI values require further validation, the trend highlights the potential of FPs for interfacial monitoring.

Collectively, these results establish a multisensor framework for in situ characterisation of adhesive joint curing. Each technique contributed complementary insights, and their combined deployment enables a comprehensive picture of the thermo-chemo-mechanical transformations during polymerisation.

Manufacturing, assessing and testing SLJs

The Alicona G5 focus variation microscope was successfully evaluated for assessing grit–blasting–induced surface roughness and texture changes. Smoother surfaces required higher magnification, as confirmed by degreased substrates, while grit-blasted surfaces were largely unaffected by magnification. Reference planes and form correction had minimal impact, and a magnification of ×10 was selected for all subsequent measurements to ensure standardised results.

The SLJ manufacturing process was carefully controlled. The grit-blasting cabinet exhibited a linear pressure loss ($R^2 = 0.992$), with negligible deviations in substrate geometry, room temperature (maximum 1.21°C), and relative humidity (maximum 65%). Bond-line thickness control revealed that observed deviations (max ±0.1557 mm) exceeded the calculated standard error (±0.0345 mm), suggesting minor contributions from manufacturing factors, such as uneven top-plate lowering or surface irregularities. MEK treatment effectively degreased aluminium substrates, removing carbon contaminants while minimally affecting silicone, and increased detectable aluminium by ~39 %, consistent with the literature.

For aluminium-to-aluminium SLJs, the best-performing treatment was AL-S2, with an average shear strength of 23.44±0.88 N/mm². Silanation slightly reduced deviation but did not

6 Conclusion

significantly improve strength. Extended grit-blasting and MEK-only degreasing resulted in reduced bond strength, whereas grit-blasting increased displacement at failure, indicating improved toughness.

For CFRP-to-CFRP SLJs, the highest shear strength (22.68 ± 0.30 N/mm²) was achieved with short (5 s) grit-blasting, whereas acetone-degreased specimens performed worst (11.72 ± 2.81 N/mm²). Increasing silane concentration correlated with reduced bond strength and higher deviations. Hybrid void-containing specimens exhibited similar UTS (~21.50 N/mm²), but grit-blasted specimens had smaller deviations than silanated ones.

Surface roughness analysis showed that for aluminium, short grit-blasting increased roughness, whereas longer durations decreased it, potentially explaining lower shear strength. For CFRP, roughness and texture increased more linearly with grit-blasting. Silanes increased the silicone content and surface free energy for aluminium ($R^2 = 0.9807$), but had less influence on CFRP. Microvoid analysis revealed that the void content increased with grit-blasting duration (1.7% at 15 s to 4% at 60 s) before plateauing, correlating with surface roughness trends and possibly affecting bond strength.

Overall, the study demonstrates that surface treatment, grit-blasting duration, and degreasing methods have a significant influence on SLJ performance, with optimal combinations varying depending on the substrate material. AL-S2 and short-duration grit-blasting were consistently the most effective treatments, achieving high shear strength, low deviation, and improved joint toughness.

6 Conclusion

7. Future work

Building on the findings of this research, several promising directions for future investigations have been identified. These aim to enhance the understanding of single lap joints (SLJs), improve surface preparation techniques, and expand the applications of optical fibre sensors (OFS) in adhesive bonding. A key area of focus is the role of microvoids in adhesive bonding. Quantifying their influence on bond strength and understanding their formation mechanisms are critical for improving joint performance. Future studies should explore strategies to reduce microvoid content, such as optimising adhesive application techniques and formulations. Additionally, further investigation into grit-blasting as a texturing method is warranted, particularly to identify parameters that minimise pore formation while maintaining surface roughness conducive to strong bonding. Reducing pore content is expected to yield higher bond strength and greater durability in SLJs. In the context of spectroscopy techniques, the integration of Fresnel Reflection Spectroscopy (FRS) with Fourier Transform Infrared (FTIR) reflectometry revealed interesting phenomena, such as the increased sensitivity of amines to the 1550 nm light source used in FRS. This raises the need for further research into potential self-falsification effects in spectroscopy measurements. Ensuring the reliability of these techniques is vital for their application in chemical monitoring during adhesive curing processes. FRS itself holds significant potential for further development. The sources of noise observed during FRS measurements should be systematically studied, with a focus on understanding the role of polymer diffusion during curing. Additionally, FRS could be explored as a sensor for assessing the degree of mixing in adhesive formulations. This capability would provide real-time feedback during preparation, ensuring consistency in adhesive properties and curing behaviour. The use of FP and FTIR fibre sensors within a glove box environment also presents exciting opportunities for future research. These sensors could be evaluated for their ability to detect and quantify moisture ingress in SLJs, providing valuable data on

environmental degradation over time. Moreover, FP sensors could be employed to monitor shrinkage in adhesives as strain gauges after SLJ manufacturing, offering insights into residual stresses and their implications for joint performance. Expanding the applications of optical fibre sensors to investigate chemical interactions at the adhesive-substrate interface represents another valuable avenue. For instance, OFS could be used to detect amine enrichment on metallic substrates, improving the understanding of surface treatment effects. Furthermore, a multi-sensor approach could be employed to map spatial variations within SLJs, enabling detailed analysis of localised differences in bond properties, curing dynamics, and environmental responses. These future directions provide a foundation for advancing adhesive bonding technologies and monitoring methods. By addressing these areas, a deeper understanding of SLJs can be achieved, leading to optimised manufacturing processes and enhanced performance across diverse applications.

Assessing surface roughness and texture

Firstly, the Alicona G5 focus variation microscope was evaluated for its suitability in assessing grit–blasting–induced surface roughness and texture changes. Surface roughness calibration blocks with defined roughness values were purchased and measured at different magnifications, both with and without reference planes applied. The influence of Lc-filters was also investigated.

According to the Alicona manual, smoother surfaces require higher magnification. This was confirmed by the results: degreased (smooth) surfaces exhibited an apparent increase in roughness with increasing magnification, while grit-blasted surfaces remained relatively constant. The use of reference planes was found to have little effect on the measurements. However, when colour filters were applied, the zero reference point lay outside the measurable range, rendering the filters ineffective.

7 Future work

Form correction was also tested and, as reported in the literature, was found to have only a minor effect on the results. This may be attributed to the relatively uniform geometry of the calibration blocks. Based on these findings, a magnification of ×10 was selected for subsequent experiments. Reference planes and form correction were also applied to standardise the measurements.

7 Future work

Bibliography

ACHILIAS, D. S., KARABELA, M. M., VARKOPOULOU, E. A. & SIDERIDOU, I. D. 2012. Cure kinetics study of two epoxy systems with fourier tranform infrared spectroscopy (FTIR) and differential scanning calorimetry (DSC). *Journal of Macromolecular Science, Part A,* 49**,** 630-638.

AGRAWAL, G. P. 2012. *Fiber-optic communication systems*, John Wiley & Sons.

ALICONA IMAGING GMBH 2013. IF-MeasureSuite.

AMADA, S. & HIROSE, T. 1998. Influence of grit blasting pre-treatment on the adhesion strength of plasma sprayed coatings: fractal analysis of roughness. *Surface and Coatings Technology,* 102**,** 132-137.

AMADA, S. & SATOH, A. 2000. Fractal analysis of surfaces roughened by grit blasting. *Journal of Adhesion Science and Technology,* 14**,** 27-41.

ARGON, A. S. 2013. The physics of deformation and fracture of polymers. *New York.: Cambridge.*

ASL, S. K. & SOHI, M. H. 2010. Effect of grit-blasting parameters on the surface roughness and adhesion strength of sprayed coating. *Surface and Interface Analysis,* 42**,** 551-554.

ASTM 2019. D907-15 Standard Terminology of Adhesives.

BALDAN, A. 2004a. Adhesively-bonded joints and repairs in metallic alloys, polymers and composite materials: Adhesives, adhesion theories and surface pretreatment. *Journal of materials science,* 39**,** 1-49.

BALDAN, A. 2004b. Adhesively-bonded joints in metallic alloys, polymers and composite materials: Mechanical and environmental durability performance. *Journal of Materials Science,* 39**,** 4729-4797.

BALDAN, A. 2012. Adhesion phenomena in bonded joints. *International Journal of Adhesion and Adhesives,* 38**,** 95-116.

BANEA, M. D., DE SOUSA, F. S. M., DA SILVA, L. F. M., CAMPILHO, R. & PEREIRA, A. M. D. 2011. Effects of Temperature and Loading Rate on the Mechanical Properties of a High Temperature Epoxy Adhesive. *Journal of Adhesion Science and Technology,* 25**,** 2461-2474.

BERTHOLDS, A. & DAENDLIKER, R. 1994. Determination of the individual strain-optic coefficients in single-mode optical fibers (from Journal of Lightwave Technology 1988). *SPIE MILESTONE SERIES MS,* 101**,** 63-63.

BIKERMAN, J. J. 2013. *The science of adhesive joints*, Elsevier.

BILLAUD, C., VANDEUREN, M., LEGRAS, R. & CARLIER, V. 2002. Quantitative analysis of epoxy resin cure reaction: A study by near-infrared spectroscopy. *Applied spectroscopy,* 56**,** 1413-1421.

BILLMEYER, F. 1984. *Textbook of polymer science*, John Wiley & Sons.

BLUDAU, W. 2013. *Lichtwellenleiter in Sensorik und optischer Nachrichtentechnik*, Springer-Verlag.

BOERIO, F., ROBY, B., DILLINGHAM, R., BOSSI, R. & CRANE, R. 2006. Effect of grit-blasting on the surface energy of graphite/epoxy composites. *The Journal of Adhesion,* 82**,** 19-37.

BORA, M. Ö., ÇOBAN, O., AKMAN, E., OZTOPRAK, B. G. & KUTLUK, T. 2020. Comparison of novel surface treatments of Al 2024 alloy for al/cfrp adhesive bonded joints. *International Journal of Adhesion and Adhesives,* 103**,** 102721.

BORSELLINO, C., DI BELLA, G. & RUISI, V. F. 2009. Adhesive joining of aluminium AA6082: The effects of resin and surface treatment. *International Journal of Adhesion and Adhesives,* 29**,** 36-44.

BOUTAR, Y., NAÏMI, S., MEZLINI, S. & ALI, M. B. S. 2016. Effect of surface treatment on the shear strength of aluminium adhesive single-lap joints for automotive applications. *International Journal of Adhesion and Adhesives,* 67**,** 38-43.

BRUEL, C., QUEFFEULOU, S., DARLOW, T., VIRGILIO, N., TAVARES, J. R. & PATIENCE, G. S. 2019. Experimental methods in chemical engineering: Contact angles. *The canadian journal of chemical engineering,* 97**,** 832-842.

BUCH, X. & SHANAHAN, M. E. R. 2000. Thermal and thermo-oxidative ageing of an epoxy adhesive. *Polymer Degradation and Stability,* 68**,** 403-411.

BUCK, J. A. 2004. *Fundamentals of optical fibers*, John Wiley & Sons.

CARRINO, L., NAPOLITANO, G. & SORRENTINO, L. 2005. Correlation of wettability and superficial cleaning of 2024 aluminium alloy with air cold plasma treatment time. *International Journal of Advanced Manufacturing Technology,* 26**,** 1026-1031.

CHANDER, K. P., VASHISTA, M., SABIRUDDIN, K., PAUL, S. & BANDYOPADHYAY, P. 2009. Effects of grit blasting on surface properties of steel substrates. *Materials & Design,* 30**,** 2895-2902.

CHANG, T. D., CARR, S. H. & BRITTAIN, J. O. 1982. Studies of epoxy resin systems: Part B: Effect of crosslinking on the physical properties of an epoxy resin. *Polymer Engineering and Science,* 22**,** 1213-1220.

CHEN, J. & HUANG, X. 2010. Fresnel-reflection-based fiber sensor for on-line measurement of ambient temperature. *Optics Communications,* 283**,** 1674-1677.

CHIN, J. W. & WIGHTMAN, J. P. 1996. Surface characterization and adhesive bonding of toughened bismaleimide composites. *Composites Part A: Applied Science and Manufacturing,* 27**,** 419-428.

CHOLAKE, S. T., MADA, M. R., RAMAN, R. K. S., BAI, Y., ZHAO, X. L., RIZKALLA, S. & BANDYOPADHYAY, S. 2014. Quantitative Analysis of Curing Mechanisms of Epoxy Resin by Mid- and Near-Fourier Transform Infra Red Spectroscopy. *Defence Science Journal,* 64**,** 314-321.

CIOBOTARU, I.-A., MAIOR, I., VAIREANU, D.-I., COJOCARU, A., CAPRARESCU, S. & CIOBOTARU, I.-E. 2016. The determination of the optimum hydrolysis time for silane films deposition. *Applied Surface Science,* 371**,** 275-280.

COGNARD, P. 2006. *Handbook of adhesives and sealants: general knowledge, application of adhesives, new curing techniques*, Elsevier.

COMYN, J. 1992. Contact angles and adhesive bonding. *International Journal of Adhesion and Adhesives,* 12**,** 145-149.

CORNING, I. 2002. Corning Single-Mode Optical Fiber.

CORNING, I. 2010. Corning® SMF-28e+® Photonic Optical Fiber.

CROSBY, P. A., POWELL, G. R., FERNANDO, G. F., FRANCE, C. M., SPOONCER, R. C. & WATERS, D. N. 1996. In situ cure monitoring of epoxy resins using optical fibre sensors. *Smart Materials & Structures,* 5**,** 415-428.

CROSBY, P. A., POWELL, G. R., FERNANDO, G. F., WATERS, D. N., FRANCE, C. M. & SPOONCER, R. C. 1997. A comparative study of optical fibre cure monitoring methods. Conference on Smart Sensing, Processing, and Instrumentation - Smart Structures and Materials 1997, Mar 03-05 1997 San Diego, Ca. 141-153.

CUEVAS-SUÁREZ, C. E., RAMOS, T. S., RODRIGUES, S. B., COLLARES, F. M., ZANCHI, C. H., LUND, R. G., DA SILVA, A. F. & PIVA, E. 2019. Impact of shelf-life simulation on bonding performance of universal adhesive systems. *Dental Materials,* 35**,** E204-E219.

DAVIES, P., SOHIER, L., COGNARD, J.-Y., BOURMAUD, A., CHOQUEUSE, D., RINNERT, E. & CRÉAC'HCADEC, R. 2009. Influence of adhesive bond line

thickness on joint strength. *International journal of adhesion and adhesives,* 29**,** 724-736.

DEFLORIAN, F., ROSSI, S. & FEDRIZZI, L. 2006. Silane pre-treatments on copper and aluminium. *Electrochimica Acta,* 51**,** 6097-6103.

DEGAMBER, B. & FERNANDO, G. F. 2006. Fibre optic dilato-spectroscopic sensor: Simultaneous thermal, spectral, and physical analyses of materials. *Smart Materials & Structures,* 15**,** 1054-1062.

DEL REAL, J., CANO DE SANTAYANA, M., ABENOJAR, J., PANTOJA, M. & MARTINEZ, M. 2008. Influence of silanisation parameters with γ-methacryloxypropyltrimethoxysilane on durability of aluminium/acrylic adhesive joints. *Journal of adhesion science and technology,* 22**,** 1461-1475.

DEPARIS, O., MEGRET, P., DECRETON, M. C. & BLONDEL, M. Temperature sensitivity of microbending losses in radiation-resistant optical fibers. Photonics for Space Environments V, 1997. SPIE, 2-8.

DOS REIS, M., BANEA, M., BUDHE, S. & DE BARROS, S. 2017. Effect of adherend surface preparation on the mechanical properties of aluminium bonded joints. *Annals of the" Dunarea de Jos"University of Galati. Fascicle II. Mathematics, Physics, Theoretical Mechanics.*

DOYLE, C., MARTIN, A., LIU, T., WU, M., HAYES, S., CROSBY, P. A., POWELL, G. R., BROOKS, D. & FERNANDO, G. F. 1998. In-situ process and condition monitoring of advanced fibre-reinforced composite materials using optical fibre sensors. *Smart Materials & Structures,* 7**,** 145-158.

DUBEY, P. K. & SHUKLA, V. 2014. Dispersion in optical fiber communication. *International Journal of Science and Research (IJSR),* 3**,** 236-239.

DUEMICHEN, E., JAVDANITEHRAN, M., ERDMANN, M., TRAPPE, V., STURM, H., BRAUN, U. & ZIEGMANN, G. 2015. Analyzing the network formation and curing kinetics of epoxy resins by in situ near-infrared measurements with variable heating rates. *Thermochimica Acta,* 616**,** 49-60.

EBNESAJJAD, S. 2010. *Handbook of adhesives and surface preparation: technology, applications and manufacturing*, William Andrew.

ENCINAS, N., OAKLEY, B., BELCHER, M., BLOHOWIAK, K., DILLINGHAM, R., ABENOJAR, J. & MARTÍNEZ, M. 2014. [Surface modification of aircraft used composites for adhesive bonding]. *INTERNATIONAL JOURNAL OF ADHESION AND ADHESIVES,* 50**,** 157-163.

ENGELBRECHT, R. 2015. *Nichtlineare Faseroptik: Grundlagen und Anwendungsbeispiele*, Springer-Verlag.

FERNANDO, D., TENG, J.-G., YU, T. & ZHAO, X.-L. 2013. Preparation and characterization of steel surfaces for adhesive bonding. *Journal of Composites for Construction,* 17**,** 04013012.

FERNANDO, G. F. & DEGAMBER, B. 2006. Process monitoring of fibre reinforced composites using optical fibre sensors. *International Materials Reviews,* 51**,** 65-106.

FIBERCORE, H. 2020. Dual Band Bend Insensitive Fiber.

FIORE, V., ORLANDO, V., SANFILIPPO, C., BADAGLIACCO, D. & VALENZA, A. 2020. Effect of silane coupling treatment on the adhesion between polyamide and epoxy based composites reinforced with carbon fibers. *Fibers,* 8**,** 48.

FLEMING, J. & WOOD, D. 1983. Refractive index dispersion and related properties in fluorine doped silica. *Applied Optics,* 22**,** 3102-3104.

GARCIA, F. G., SOARES, B. G., PITA, V. J., SÁNCHEZ, R. & RIEUMONT, J. 2007. Mechanical properties of epoxy networks based on DGEBA and aliphatic amines. *Journal of Applied Polymer Science,* 106**,** 2047-2055.

GARDNER, D. J. 2017. Theories and mechanisms of adhesion. *Handbook of Adhesive Technology.* CRC Press.

GARSCHKE, C., PARLEVLIET, P., WEIMER, C. & FOX, B. 2013. Cure kinetics and viscosity modelling of a high-performance epoxy resin film. *Polymer Testing,* 32**,** 150-157.

GAZO HANNA, E., YOUNES, K., AMINE, S. & ROUFAYEL, R. 2023. Exploring gel-point identification in epoxy resin using rheology and unsupervised learning. *Gels,* 9**,** 828.

GHARA, T., PAUL, S. & BANDYOPADHYAY, P. 2021. Effect of grit blasting parameters on surface and near-surface properties of different metal alloys. *Journal of Thermal Spray Technology,* 30**,** 251-269.

GRANGEAT, R., GIRARD, M., LUPI, C., LEDUC, D. & JACQUEMIN, F. 2020. Measurement of the local water content of an epoxy adhesive by fiber optic sensor based on Fresnel reflection. *Mechanical Systems and Signal Processing,* 141**,** 106439.

GROBNIC, D., SMELSER, C., MIHAILOV, S. & WALKER, R. Long-term thermal stability tests at 1000 °C of silica fiber Bragg grating made with ultrafast laser radiation. 17TH International Conference on Optical Fibre Sensors, Pts 1 and 2, 2005-01-01 2005. 106-109.

GÜNTHER + SCHRAMM 2015. Technisches Datenblatt AlCuMg2 / AW - 2024.

HARAN, F. M., REW, J. K. & FOOTE, P. D. 1998. A strain-isolated fibre Bragg grating sensor for temperature compensation of fibre Bragg grating strain sensors. *Measurement Science and Technology,* 9**,** 1163.

HARRIS, A. & BEEVERS, A. 1999. The effects of grit-blasting on surface properties for adhesion. *International journal of adhesion and adhesives,* 19**,** 445-452.

HARRIS, D. 2011. *Design and development of a hyphenated technique for monitoring the cure of epoxy-amine resin systems.* University of Birmingham.

HAYES, B. S. & SEFERIS, J. C. 2000. Effects of in situ esterification on the performance of carboxyl functionalized rubber-modified epoxy film adhesives. *Journal of applied polymer science,* 76**,** 728-734.

HILL, K. O., FUJII, Y., JOHNSON, D. C. & KAWASAKI, B. S. 1978. Photosensitivity in optical fiber waveguides: Application to reflection filter fabrication. *Applied physics letters,* 32**,** 647-649.

HILL, K. O. & MELTZ, G. 1997. Fiber Bragg grating technology fundamentals and overview. *Journal of lightwave technology,* 15**,** 1263-1276.

HITCHCOCK, S., CARROLL, N. & NICHOLAS, M. 1981. Some effects of substrate roughness on wettability. *Journal of Materials Science,* 16**,** 714-732.

HOLC, K., MARONA, L., CZERNECKI, R., BOCKOWSKI, M., SUSKI, T., NAJDA, S. & PERLIN, P. 2010. Temperature dependence of superluminescence in InGaN-based superluminescent light emitting diode structures. *Journal of Applied Physics,* 108.

HOLST, M., SCHANZLIN, K., WENZEL, M., XU, J. J., LELLINGER, D. & ALIG, I. 2005. Time-resolved method for the measurement of volume changes during polymerization. *Journal of Polymer Science Part B-Polymer Physics,* 43**,** 2314-2325.

HORENSTEIN, M. N. 2009. Electrostatics and nanoparticles: What's the same, what's different? *Journal of electrostatics,* 67**,** 384-393.

HUANG, C., SUN, X., YUAN, H., SONG, C., MENG, Y. & LI, X. 2020. Study on the reactivity and kinetics of primary and secondary amines during epoxy curing by NIR spectroscopy combined with multivariate analysis. *Vibrational Spectroscopy,* 106**,** 102993.

HÜBNER, M., DUMSTORFF, G., MOGADDAM, M. K., PLAGEMANN, P. & LANG, W. 2018. Online monitoring of the curing of adhesives with a miniaturised interdigital

sensor using impedance spectroscopy. *Journal of Adhesion Science and Technology,* 32**,** 772-786.

JOJIBABU, P., JAGANNATHAM, M., HARIDOSS, P., RAM, G. D. J., DESHPANDE, A. P. & BAKSHI, S. R. 2016. Effect of different carbon nano-fillers on rheological properties and lap shear strength of epoxy adhesive joints. *Composites Part a-Applied Science and Manufacturing,* 82**,** 53-64.

KARKANAS, P. I. & PARTRIDGE, I. K. 2000. Cure modeling and monitoring of epoxy/amine resin systems. I. Cure kinetics modeling. *Journal of applied polymer science,* 77**,** 1419-1431.

KATNAM, K. B., STEVENSON, J. P. J., STANLEY, W. F., BUGGY, M. & YOUNG, T. M. 2011. Tensile strength of two-part epoxy paste adhesives: Influence of mixing technique and micro-void formation. *International Journal of Adhesion and Adhesives,* 31**,** 666-673.

KHADKA, S., HOFFMAN, J. & KUMOSA, M. 2020. FBG monitoring of curing in single fiber polymer composites. *Composites Science and Technology,* 198**,** 108308.

KHAN, A. A., MOHAMED, B. A., MIRZA, E. H., SYED, J., DIVAKAR, D. D. & VALLITTU, P. K. 2019. Surface wettability and nano roughness at different grit blasting operational pressures and their effects on resin cement to zirconia adhesion. *Dental Materials Journal,* 38**,** 388-395.

KIM, H.-S., YOO, S.-H. & CHANG, S.-H. 2013. In situ monitoring of the strain evolution and curing reaction of composite laminates to reduce the thermal residual stress using FBG sensor and dielectrometry. *Composites Part B: Engineering,* 44**,** 446-452.

KIM, H., JUNG, D.-H., JUNG, I., CIFUENTES, J., RHEE, K. & HUI, D. 2012. Enhancement of mechanical properties of aluminium/epoxy composites with silane functionalization of aluminium powder. *Composites Part B: Engineering,* 43**,** 1743-1748.

KIM, J., MOON, T. J. & HOWELL, J. R. 2002. Cure kinetic model, heat of reaction, and glass transition temperature of AS4/3501-6 graphite-epoxy prepregs. *Journal of Composite Materials,* 36**,** 2479-2498.

KIM, J. G., CHOI, I. & SEO, I. S. 2011. Flame and silane treatments for improving the adhesive bonding characteristics of aramid/epoxy composites. *Composite Structures,* 93**,** 2696-2705.

KIM, W.-S., YUN, I.-H., LEE, J.-J. & JUNG, H.-T. 2010. Evaluation of mechanical interlock effect on adhesion strength of polymer–metal interfaces using micro-patterned surface topography. *International Journal of Adhesion and Adhesives,* 30**,** 408-417.

KING, D. G. 2018a. *FIBRE-OPTIC SENSOR DEVELOPMENT FOR PROCESS MONITORING OF EPOXY RESINS.* PhD, University of Birmingham.

KING, D. G. 2018b. *Fibre-optic sensor development for process monitoring of epoxy resins.* University of Birmingham.

KINLOCH, A. J. 2012. *Adhesion and adhesives: science and technology*, Springer Science & Business Media.

KIRALFY, M. 2024. *An Investigation into the Effects of Specified Surface Treatments for Composite-to-Metal and Metal-to-Metal Adhesive Single-Lap Joints.* MSc, University of Birmingham.

KOSTIN, V., NASONOV, F. & ZININ, A. Influence of adhesive bond line thickness on joint strength of composite aircraft structures. Journal of Physics: Conference Series, 2021. IOP Publishing, 012070.

KWOK, D. Y. & NEUMANN, A. W. 1999. Contact angle measurement and contact angle interpretation. *Advances in colloid and interface science,* 81**,** 167-249.

LACHENAL, G., PIERRE, A. & POISSON, N. 1996. FT-NIR spectroscopy: Trends and application to the kinetic study of epoxy/triamine system (comparison with DSC and SEC results). *Micron,* 27**,** 329-334.

LEE, W., LOOS, A. & SPRINGER, G. 1982. Heat of Reaction, Degree of Cure, and Viscosity of Hercules 3501-6 Resin. *Journal of Composite Materials,* 16**,** 510-520.

LETTIERI, M. & FRIGIONE, M. 2012. Effects of humid environment on thermal and mechanical properties of a cold-curing structural epoxy adhesive. *Construction and Building Materials,* 30**,** 753-760.

LI, P., FU, C., ZHONG, H., DU, B., GUO, K., MENG, Y., DU, C., HE, J., WANG, L. & WANG, Y. 2022. A Nondestructive Measurement Method of Optical Fiber Young's Modulus Based on OFDR. *Sensors,* 22.

LIN, W., LI, X., DONG, W., ZHAO, Y., LI, M. & WANG, Y. 2021. Ultrahigh bonding strength and excellent corrosion resistance of Al-TPU hybrid induced by microstructures and silane layer. *Journal of Materials Processing Technology,* 296**,** 117180.

LIU, T., WU, M., RAO, Y., JACKSON, D. A. & FERNANDO, G. F. 1998. A multiplexed optical fibre-based extrinsic Fabry-Perot sensor system for in-situ strain monitoring in composites. *Smart materials and structures,* 7**,** 550.

LIU, Y.-L., WEI, W.-L., HSU, K.-Y. & HO, W.-H. 2004. Thermal stability of epoxy-silica hybrid materials by thermogravimetric analysis. *Thermochimica Acta,* 412**,** 139-147.

LOCTITE 2006. Technical Data Sheet Hysol 9466.

LUYCKX, G. 2009. *Multi-axial strain monitoring of fibre reinforced thermosetting plastics using embedded highly birefringent optical fibre Bragg sensors.* Ghent University.

MACHAVARAM, V. R., WANG, L. W., PANDITA, S. D., HELLMANN, S., BOGONEZ, F. N. & FERNANDO, G. F. 2014. Multi-Point Monitoring of Cross-Linking Reactions. *Journal of Applied Polymer Science,* 131.

MAFI, R., MIRABEDINI, S., ATTAR, M. & MORADIAN, S. 2005. Cure characterization of epoxy and polyester clear powder coatings using Differential Scanning Calorimetry (DSC) and Dynamic Mechanical Thermal Analysis (DMTA). *Progress in Organic Coatings,* 54**,** 164-169.

MAHAKUD, R., KUMAR, J., PRAKASH, O. & DIXIT, S. 2013. Study of the nonuniform behavior of temperature sensitivity in bare and embedded fiber Bragg gratings: experimental results and analysis. *Applied Optics,* 52**,** 7570-7579.

MARCATILI, E. A. J. 1977. Modal Dispersion in Optical Fibers With Arbitrary Numerical Aperture and Profile Dispersion. *Bell System Technical Journal,* 56**,** 49-63.

MATHEW, J., SCHNELLER, O., POLYZOS, D., HAVERMANN, D., CARTER, R. M., MACPHERSON, W. N., HAND, D. P. & MAIER, R. R. 2015. In-fiber Fabry–Perot cavity sensor for high-temperature applications. *Journal of Lightwave Technology,* 33**,** 2419-2425.

MAXWELL, I. D. & PETHRICK, R. A. 1983. Low-Temperature Rearrangement of Amine Cured Epoxy-Resins. *Polymer Degradation and Stability,* 5**,** 275-301.

MAZZOLA, L., BEMPORAD, E. & CARASSITI, F. 2012. An easy way to measure surface free energy by drop shape analysis. *Measurement,* 45**,** 317-324.

MEIJER, H. E. & GOVAERT, L. E. 2005. Mechanical performance of polymer systems: The relation between structure and properties. *Progress in polymer science,* 30**,** 915-938.

MELLALI, M., GRIMAUD, A., LEGER, A., FAUCHAIS, P. & LU, J. 1997. Alumina grit blasting parameters for surface preparation in the plasma spraying operation. *Journal of Thermal spray technology,* 6**,** 217-227.

MIJOVIC, J. & ANDJELIC, S. 1995. A study of reaction kinetics by near-infrared spectroscopy. 1. Comprehensive analysis of a model epoxy/amine system. *Macromolecules,* 28**,** 2787-2796.

MIJOVIC, J., ANDJELIC, S. & KENNY, J. M. 1996. In situ real-time monitoring of epoxy/amine kinetics by remote near infrared spectroscopy. *Polymers for Advanced Technologies,* 7**,** 1-16.

MISHRA, V., LOHAR, M. & AMPHAWAN, A. 2016. Improvement in temperature sensitivity of FBG by coating of different materials. *Optik,* 127**,** 825-828.

MOLITOR, P., BARRON, V. & YOUNG, T. 2001. Surface treatment of titanium for adhesive bonding to polymer composites: a review. *International Journal of Adhesion and Adhesives,* 21**,** 129-136.

MONDEN, A. 2016. Adhäsion zwischen epoxidharzbasiertem CFK und oberflächenmodifiziertem Stahl: grenzschichtversagen von Hybridlaminaten unter Mode I, Mode II und Mixed-Mode Belastung.

MONTANINI, R. & D'ACQUISTO, L. 2007. Simultaneous measurement of temperature and strain in glass fiber/epoxy composites by embedded fiber optic sensors: I. Cure monitoring. *Smart Materials and Structures,* 16**,** 1718.

MORGAN, R., KONG, F. & WALKUP, C. 1984. Structure-property relations of polyethertriamine-cured bisphenoI-Adiglycidyl ether epoxies. *Polymer,* 25**,** 375-386.

MORSCH, S., WAND, C. R., GIBBON, S., IRWIN, M., SIPERSTEIN, F. & LYON, S. 2023. The effect of cross-linker structure on interfacial interactions, polymer dynamics and network composition in an epoxy-amine resin. *Applied Surface Science,* 609**,** 155380.

MURAYAMA, H., KAGEYAMA, K., UZAWA, K., OHARA, K. & IGAWA, H. 2012. Strain monitoring of a single-lap joint with embedded fiber-optic distributed sensors. *Structural Health Monitoring,* 11**,** 325-344.

NAIR, A. K., MACHAVARAM, V. R., MAHENDRAN, R. S., PANDITA, S. D., PAGET, C., BARROW, C. & FERNANDO, G. F. 2015. Process monitoring of fibre reinforced composites using a multi-measurand fibre-optic sensor. *Sensors and Actuators B-Chemical,* 212**,** 93-106.

NOESKE, M., DEGENHARDT, J., STRUDTHOFF, S. & LOMMATZSCH, U. 2004. Plasma jet treatment of five polymers at atmospheric pressure: surface modifications and the relevance for adhesion. *International journal of adhesion and adhesives,* 24**,** 171-177.

OELHAFEN, J., MAYR, T., DORNER, F., MOUTZOURIS, K., ROTHS, J. & DRECHSLER, K. 2017. Fiber optic measurement system for fresnel reflection sensing: calibration, uncertainty, and exemplary application in temperature-modulated isothermal polymer curing. *Journal of Lightwave Technology,* 36**,** 939-945.

OSBORNE, B. G. 2006. Near-infrared spectroscopy in food analysis. *Encyclopedia of analytical chemistry: applications, theory and instrumentation*.

PALENCIA, M. 2017. Surface free energy of solids by contact angle measurements. *J. Sci. Technol. Appl,* 2**,** 84-93.

PALMESE, G. R. & MCCULLOUGH, R. L. 1992. EFFECT OF EPOXY AMINE STOICHIOMETRY ON CURED RESIN MATERIAL PROPERTIES. *Journal of Applied Polymer Science,* 46**,** 1863-1873.

PANDITA, S. D., WANG, L. W., MAHENDRAN, R. S., MACHAVARAM, V. R., IRFAN, M. S., HARRIS, D. & FERNANDO, G. F. 2012. Simultaneous DSC-FTIR spectroscopy: Comparison of cross-linking kinetics of an epoxy/amine resin system. *Thermochimica Acta,* 543**,** 9-17.

PARK, S., WEI, J., HU, Y., ENCK, R., LUCIANI, V., KONOPLEV, O., WILSON, S. & HEIM, P. J. 100 mW high-power depolarized-superluminescent diode at 1550nm wavelength. Light-Emitting Diodes: Research, Manufacturing, and Applications X, 2006. SPIE, 96-103.

PARK, S. Y., CHOI, W. J., CHOI, H. S., KWON, H. & KIM, S. H. 2010. Recent trends in surface treatment technologies for airframe adhesive bonding processing: a review (1995–2008). *The Journal of Adhesion,* 86**,** 192-221.

PATIL, P. N., RATH, S. K., SHARMA, S. K., SUDARSHAN, K., MAHESHWARI, P., PATRI, M., PRAVEEN, S., KHANDELWAL, P. & PUJARI, P. K. 2013. Free volumes and structural relaxations in diglycidyl ether of bisphenol-A based epoxy-polyether amine networks. *Soft Matter,* 9**,** 3589-3599.

PAZABUIN, S., LOPEZQUINTELA, A., VARELA, M., PAZOSPELLIN, M. & PRENDES, P. 1997. Method for determination of the ratio of rate constants, secondary to primary amine, in epoxy-amine systems. *Polymer,* 38**,** 3117-3120.

PEARSON, C., PIZZI, A. & MITTAL, K. 2003. Handbook of Adhesive Technology, Revised and Expanded. Marcel Dekker, Inc., United States of America.

PISKA, M. & METELKOVA, J. 2014. On the comparison of contact and non-contact evaluations of a machined surface. *MM Sci. J,* 2**,** 476-480.

POWELL, G. R., CROSBY, P. A., FERNANDO, G. F., FRANCE, C. M., SPOONCER, R. C. & WATERS, D. N. 1996. Optical fibre evanescent wave cure monitoring of epoxy resins. Conference on Smart Sensing, Processing, and Instrumentation - Smart Structures and Materials 1996, Feb 26-28 1996 San Diego, Ca. 80-92.

PRAKASH, V. A. & JAISINGH, S. J. 2018. Mechanical strength behaviour of silane treated E-glass fibre/Al 6061 & SS-304 wire mesh reinforced epoxy resin hybrid composite. *Silicon,* 10**,** 2279-2286.

PUSTKOVA, P., HUTCHINSON, J. M., ROMÁN, F. & MONTSERRAT, S. 2009. Homopolymerization effects in polymer layered silicate nanocomposites based upon epoxy resin: Implications for exfoliation. *Journal of Applied Polymer Science,* 114**,** 1040-1047.

QI, B., PICKRELL, G. R., XU, J., ZHANG, P., DUAN, Y., PENG, W., HUANG, Z., HUO, W., XIAO, H. & MAY, R. G. 2003. Novel data processing techniques for dispersive white light interferometer. *Optical engineering,* 42**,** 3165-3171.

RASCHE, M. 2012. *Handbuch Klebtechnik*, Carl Hanser Verlag GmbH Co KG.

RIDER, A. & ARNOTT, D. 2000. Boiling water and silane pre-treatment of aluminium alloys for durable adhesive bonding. *International journal of adhesion and adhesives,* 20**,** 209-220.

RIDER, A., BRACK, N., ANDRES, S. & PIGRAM, P. 2004. The influence of hydroxyl group concentration on epoxy–aluminium bond durability. *Journal of adhesion science and technology,* 18**,** 1123-1152.

RUDAWSKA, A., WAHAB, M. A. & MÜLLER, M. 2022. Strength of epoxy-bonded aluminium alloy joints after sandblasting. *Advances in Science and Technology. Research Journal,* 16.

SAFARI, A., FARAHANI, M. & GHABEZI, P. 2022. Experimental study on the influences of different surface treatment processes and adhesive type on the aluminum adhesive-bonded joint strength. *MECHANICS BASED DESIGN OF STRUCTURES AND MACHINES,* 50**,** 2400-2413.

SALDANHA, D. F. S., CANTO, C., DA SILVA, L. F. M., CARBAS, R. J. C., CHAVES, F. J. P., NOMURA, K. & UEDA, T. 2013. Mechanical characterization of a high elongation and high toughness epoxy adhesive. *International Journal of Adhesion and Adhesives,* 47**,** 91-98.

SENIOR, J. M. & JAMRO, M. Y. 2009. *Optical fiber communications: principles and practice*, Pearson Education.

SIMON, S. L. & GILLHAM, J. K. 1992. Reaction kinetics and TTT cure diagrams for off-stoichiometric ratios of a high-Tg epoxy/amine system. *Journal of Applied Polymer Science,* 46**,** 1245-1270.

SKALSKÝ, M., HNIDKA, J. & HAVRÁNEK, Z. 2022. Improvement of the Temperature Stability of the Erbium-Doped Superfluorescent Fiber Source by Tuning the Reflectivity of the Fiber End. *Journal of Lightwave Technology,* 41**,** 1843-1850.

SONG, J.-W. & FAN, L.-W. 2021. Temperature dependence of the contact angle of water: A review of research progress, theoretical understanding, and implications for boiling heat transfer. *Advances in colloid and interface science,* 288**,** 102339.

SORRENTINO, L. & CARRINO, L. 2009. 2024 aluminium alloy wettability and superficial cleaning improvement by air cold plasma treatment. *Journal of Materials Processing Technology,* 209**,** 1400-1409.

SPAGGIARI, A. & DRAGONI, E. 2013. Effect of mechanical surface treatment on the static strength of adhesive lap joints. *The Journal of Adhesion,* 89**,** 677-696.

STANDARDIZATION, I. O. F. 1998. BS EN ISO 4288:1998-Geometric Product Specification (GPS) — Surface texture — Profile method: Rules and procedures for the assessment of surface texture.

STJOHN, N. A. & GEORGE, G. A. 1992. Cure kinetics and mechanisms of a tetraglycidyl-4, 4′-diaminodiphenylmethane/diaminodiphenylsulphone epoxy resin using near ir spectroscopy. *Polymer,* 33**,** 2679-2688.

STUTZ, H., MERTES, J. & NEUBECKER, K. 1993. Kinetics of thermoset cure and polymerization in the glass transition region. *Journal of Polymer Science Part a-Polymer Chemistry,* 31**,** 1879-1886.

SU, C. & WOO, E. 1995. Cure kinetics and morphology of amine-cured tetraglycidyl-4,4′-diaminodiphenylmethane epoxy blends with poly(ether imide). *Polymer,* 36**,** 2883-2894.

TACK, J. L. & FORD, D. M. 2008. Thermodynamic and mechanical properties of epoxy resin DGEBF crosslinked with DETDA by molecular dynamics. *Journal of Molecular Graphics and Modelling,* 26**,** 1269-1275.

TAMAI, Y. & ARATANI, K. 1972. Experimental study of the relation between contact angle and surface roughness. *The Journal of Physical Chemistry,* 76**,** 3267-3271.

TANAKA, Y. 2018. Synthesis and characteristics of epoxides. *Epoxy resins.* Routledge.

TANAKA, Y., STANFORD, J. L. & STEPTO, R. 2012. Interpretation of Gel Points of an Epoxy-Amine System Including Ring Formation and Unequal Reactivity: Measurements of Gel Points and Analyses on Ring Structures. *Macromolecules,* 45**,** 7197-7205.

TEMIN, S. C. 1990. Pressure-sensitive adhesives for tapes and labels. *Handbook of Adhesives.* Springer.

THOMSEN, F. 2008. Practical Contact Angle Measurement (5). *Custom–made models: from contact angle to surface free energy. KRUSS Technical Note TN315e***,** 1-6.

THORLABS 2024. SpecSheet FG105LCA Multimode Fiber.

TORRES, B., PAYÁ-ZAFORTEZA, I., CALDERÓN, P. A. & ADAM, J. M. 2011. Analysis of the strain transfer in a new FBG sensor for structural health monitoring. *Engineering Structures,* 33**,** 539-548.

VACHER, S., MOLIMARD, J., GAGNAIRE, H. & VAUTRIN, A. 2004. A Fresnel's reflection optical fiber sensor for thermoset polymer cure monitoring. *Polymers and polymer composites,* 12**,** 269-276.

VENGHAUS, H. 2006. *Wavelength filters in fibre optics*, springer.

VENGHAUS, H. & GROTE, N. 2017. *Fibre optic communication: key devices*, Springer.

WANDEL, M. E. 2006. *Attenuation in silica-based optical fibres.* PhD, Technical University of Denmark.

WANG, L. W. & FERNANDO, G. F. 2014. Cure Monitoring of Epoxy Resin by Simultaneous DSC/FTIR. *Chemical, Material and Metallurgical Engineering Iii, Pts 1-3,* 881-883, 905-+.

WANG, X., SUN, X., HU, Y., ZENG, L., LIU, Q. & DUAN, J. A. 2022. Highly-sensitive fiber Bragg grating temperature sensors with metallic coatings. *Optik,* 262, 169337.

WANG, Y., HUANG, Q., ZHU, W. & YANG, M. 2018. Simultaneous measurement of temperature and relative humidity based on FBG and FP interferometer. *IEEE Photonics Technology Letters,* 30, 833-836.

WEI, T., HAN, Y., LI, Y., TSAI, H.-L. & XIAO, H. 2008. Temperature-insensitive miniaturized fiber inline Fabry-Perot interferometer for highly sensitive refractive index measurement. *Optics Express,* 16, 5764-5769.

WEISS, H. 1995. Adhesion of advanced overlay coatings: mechanisms and quantitative assessment. *Surface and Coatings Technology,* 71, 201-207.

WINGFIELD, J. 1993. Treatment of composite surfaces for adhesive bonding. *International journal of adhesion and adhesives,* 13, 151-156.

WU, C. S., LIU, Y. L., CHIU, Y. C. & CHIU, Y. S. 2002. Thermal stability of epoxy resins containing flame retardant components: an evaluation with thermogravimetric analysis. *Polymer degradation and stability,* 78, 41-48.

WU, M., TONG, X., WANG, H., HUA, L. & CHEN, Y. 2020. Effect of ultrasonic vibration on adhesive bonding of CFRP/Al alloy joints grafted with silane coupling agent. *Polymers,* 12, 947.

XIAN, G. & KARBHARI, V. M. 2007. DMTA based investigation of hygrothermal ageing of an epoxy system used in rehabilitation. *Journal of applied polymer science,* 104, 1084-1094.

XIAO, G., ADNET, A., ZHANG, Z., SUN, F. & GROVER, C. 2005. Monitoring changes in the refractive index of gases by means of a fiber optic Fabry-Perot interferometer sensor. *SENSORS AND ACTUATORS A-PHYSICAL,* 118, 177-182.

YAMAGUCHI, K., KAWAGUCHI, D., MIYATA, N., MIYAZAKI, T., AOKI, H., YAMAMOTO, S. & TANAKA, K. 2022. Kinetics of the interfacial curing reaction for an epoxy–amine mixture. *Physical Chemistry Chemical Physics,* 24, 21578-21582.

YAMASAKI, H. & MORITA, S. 2014. Identification of the epoxy curing mechanism under isothermal conditions by thermal analysis and infrared spectroscopy. *Journal of Molecular Structure,* 1069, 164-170.

YANG, Y., PLOVIE, B., CHIESURA, G., VERVUST, T., DAELEMANS, L., MOGOSANU, D. E., WUYTENS, P., DE CLERCK, K. & VANFLETEREN, J. 2021. Fully Integrated Flexible Dielectric Monitoring Sensor System for Real-Time <i>In Situ</i> Prediction of the Degree of Cure and Glass Transition Temperature of an Epoxy Resin. *Ieee Transactions on Instrumentation and Measurement,* 70.

YU, H., MHAISALKAR, S. G. & WONG, E. H. 2005. Observations of gelation and vitrification of a thermosetting resin during the evolution of polymerization shrinkage. *Macromolecular rapid communications,* 26, 1483-1487.

Appendix A

PRODUCT DATASHEET

Product group:	CARBON FIBER SHEETS		
Type	High Strength		
Description	The High Strength sheets are laminated using industrial T700 fibres and are produced in the Netherlands. The combination of uni-directional and twill fabrics ensure a high strength performance of this product. The strength of the sheet is evenly distributed 50-50 in both longitudinal and transverse direction. The surface is silk gloss with a 3K twill fabric. The carbon material is chemically resistant, does not rust, is dimensionally stable and virtually insensitive to shrinkage or expansion.		
Important	The panels with a thickness of 10mm and 12mm are not kept in stock but are produced after an order is placed (+- 10 production days).		
Manufacturing process	Laminated from Pre-Preg High Strength carbon fibers and epoxy resin.		
Application	Lightweight frames for machine building and product handling systems, lightweight structures, medical equipment, model building, drones and more. Using Araldite 2031 epoxy glue, inserts, tubes and other items can be attached.		
More info	https://www.carbonwebshop.com/carbon-fiber-sheets/high-strength		

OUR VALUES

Produced in house @Refitech B.V.
Delivery from stock | Client specific orders on request
Prototyping and series production
Contact for further details: info@carbonwebshop.nl

Industrial services:
- Engineering, FEM analyses
- Cutting
- CNC Milling
- Waterjetting
- (Glue) Assemblies
- Quick delivery from stock

Document nr.	PDSCF Panels
Issue Date	15/12/2017
Revision	4
Revision date	9/03/2023

Refitech COMPOSITE SOLUTIONS

Symbol	Description	Unit
A	Width	mm
B	Length	mm
C	Wall Thickness	mm

Chemical Properties

Fibers	High Strength Carbon Fiber Tow 3K
Resin	Standard grade Epoxy Resin
Core material	App. 50% UD-0° fibers placed in length direction of the sheet
	App. 50% UD-90° fibers placed 90° on width direction of the sheet
Skin material	Pre-Preg Twill weaved fibers
Fiber Volume content	Product Specific

Physical properties

Glass Transition Temperature	80°C (temperature resistance)
Surface fabric	Carbon Fiber Twill weave
Surface finish	Semi Gloss / Satin, Non Painted
Visual grade on surface	Non Painted Surface Industrial Grade
	Small pinholes may occur, this is due to the production process

Mechanical properties

Approximate properties for reference only
Properties are theoretically approached with laminate analysis software. Values are an indication of the real mechanical properties.
Used software was validated with tensile testing following European standards: NEN-EN-ISO S27-4:2022

Product Reference	Product Description	Width		Length		Wall		Surface			Weight	Density	Fiber Volume Content	Young's Modulus X	Young's Modulus Y	Shear Modulus	Poisson's ratio	Poisson's ratio
		A		B		C		Skin Side 1	Side 2	Finish	W	ρ	FV	E_xx	E_yy	G_xy	v_xy	v_yx
											gram	kg/m^3	%	Gpa	Gpa	Gpa	(-)	(-)
HIGH STRENGTH CARBON FIBER SHEETS																		
CPL 1062 062 HS	Carbon High Strength Panel 1mm 620x620	620	+/- 0,3	620	+/- 0,3	1,0	+/- 0,2	Twill	Twill	Semi Gloss	475	1.600	69	56,40	59,60	3,44	0,0300	0,0317
CPL 1062 122 HS	Carbon High Strength Panel 1mm 1220x620	1.220	+/- 0,4	620	+/- 0,3	1,0	+/- 0,2	Twill	Twill	Semi Gloss	950	1.600	69	56,40	59,60	3,44	0,0300	0,0317
CPL 1562 062 HS	Carbon High Strength Panel 1,5mm 620x620	620	+/- 0,3	620	+/- 0,3	1,5	+/- 0,2	Twill	Twill	Semi Gloss	725	1.600	69	61,59	62,42	4,04	0,0347	0,0352
CPL 1562 122 HS	Carbon High Strength Panel 1,5mm 1220x620	1.220	+/- 0,4	620	+/- 0,3	1,5	+/- 0,2	Twill	Twill	Semi Gloss	1450	1.600	69	61,59	62,42	4,04	0,0347	0,0352
CPL 2062 062 HS	Carbon High Strength Panel 2mm 620x620	620	+/- 0,3	620	+/- 0,3	2,0	+/- 0,3	Twill	Twill	Semi Gloss	950	1.600	69	70,69	53,76	4,07	0,0407	0,0309
CPL 2062 122 HS	Carbon High Strength Panel 2mm 1220x620	1.220	+/- 0,4	620	+/- 0,3	2,0	+/- 0,3	Twill	Twill	Semi Gloss	1900	1.600	69	70,69	53,76	4,07	0,0407	0,0309
CPL 3062 062 HS	Carbon High Strength Panel 3mm 620x620	620	+/- 0,3	620	+/- 0,3	3,0	+/- 0,3	Twill	Twill	Semi Gloss	1425	1.600	69	76,21	52,23	3,75	0,0439	0,0303
CPL 3062 122 HS	Carbon High Strength Panel 3mm 1220x620	1.220	+/- 0,4	620	+/- 0,3	3,0	+/- 0,3	Twill	Twill	Semi Gloss	2850	1.600	69	76,21	52,23	3,75	0,0439	0,0303
CPL 4062 062 HS	Carbon High Strength Panel 4mm 620x620	620	+/- 0,3	620	+/- 0,3	4,0	+/- 0,35	Twill	Twill	Semi Gloss	1925	1.600	69	85,65	49,77	4,78	0,0488	0,0284
CPL 4062 122 HS	Carbon High Strength Panel 4mm 1220x620	1.220	+/- 0,4	620	+/- 0,3	4,0	+/- 0,35	Twill	Twill	Semi Gloss	3850	1.600	69	85,65	49,77	4,78	0,0488	0,0284
CPL 5062 062 HS	Carbon High Strength Panel 5mm 620x620	620	+/- 0,3	620	+/- 0,3	5,0	+/- 0,4	Twill	Twill	Semi Gloss	2400	1.600	69	71,10	62,28	4,28	0,0365	0,0319
CPL 5062 122 HS	Carbon High Strength Panel 5mm 1220x620	1.220	+/- 0,4	620	+/- 0,3	5,0	+/- 0,4	Twill	Twill	Semi Gloss	4800	1.600	69	71,10	62,28	4,28	0,0365	0,0319
CPL 6062 062 HS	Carbon High Strength Panel 6mm 620x620	620	+/- 0,3	620	+/- 0,3	6,0	+/- 0,4	Twill	Twill	Semi Gloss	2900	1.600	69	67,69	67,96	4,28	0,0337	0,0338
CPL 6062 122 HS	Carbon High Strength Panel 6mm 1220x620	1.220	+/- 0,4	620	+/- 0,3	6,0	+/- 0,4	Twill	Twill	Semi Gloss	5800	1.600	69	67,69	67,96	4,28	0,0337	0,0338
CPL 8062 062 HS	Carbon High Strength Panel 8mm 620x620	620	+/- 0,3	620	+/- 0,3	8,0	+/- 0,4	Twill	Twill	Semi Gloss	3800	1.600	69	62,61	72,98	3,76	0,0334	0,0390
CPL 8062 122 HS	Carbon High Strength Panel 8mm 1220x620	1.220	+/- 0,4	620	+/- 0,3	8,0	+/- 0,4	Twill	Twill	Semi Gloss	7600	1.600	69	62,61	72,98	3,76	0,0334	0,0390

Approximate properties for reference only
Properties are theoretically approached with laminate analysis software. Values are an indication of the real mechanical properties.
Used software was validated with tensile testing following European standards: NEN-EN-ISO S27-4:2022

Product Reference	Product Description	Width		Length		Wall		Surface			Weight	Density	Fiber Volume Content	Young's Modulus X	Young's Modulus Y	Shear Modulus	Poisson's ratio	Poisson's ratio
		A		B		C		Skin Side 1	Side 2	Finish	W	ρ	FV	E_xx	E_yy	G_xy	v_xy	v_yx
											gram	kg/m^3	%	Gpa	Gpa	Gpa	(-)	(-)
CPL 10062 062 HS	Carbon High Strength Panel 10mm 620x620	620	+/- 0,3	620	+/- 0,3	10,0	+/- 0,5	Twill	Twill	Semi Gloss	4725	1.600	69	76,68	60,20	3,78	0,0411	0,0323
CPL 10062 122 HS	Carbon High Strength Panel 10mm 1220x620	1.220	+/- 0,4	620	+/- 0,3	10,0	+/- 0,5	Twill	Twill	Semi Gloss	9450	1.600	69	76,68	60,20	3,78	0,0411	0,0323
CPL 12062 062 HS	Carbon High Strength Panel 12mm 620x620	620	+/- 0,3	620	+/- 0,3	12,0	+/- 0,5	Twill	Twill	Semi Gloss	5750	1.600	69	78,33	58,22	3,78	0,0424	0,0315
CPL 12062 122 HS	Carbon High Strength Panel 12mm 1220x620	1.220	+/- 0,4	620	+/- 0,3	12,0	+/- 0,5	Twill	Twill	Semi Gloss	11500	1.600	69	78,33	58,22	3,78	0,0424	0,0315

Disclaimer:

The mentioned tensile properties are values that are expected if the laminates would be tested. The values are theoretical, and are not reduced. The designer should take into account the appropriate loading factors, material reduction factors, environmental influences, etc. that are required for each design.

Thinwalled and slender structures are subject to buckling in some loadcases. The mentioned values are tensile properties, and do not contain any buckling checks. Refitech can not take responsibility that products will meet the specification and will take no responsibility for any damages, directly or indirectly, related to the use of these products.

If you want to use our parts for specific situations where mechanical properties are to be proofed or validated we strongly advise to functional test the products in the environment you are intend to use it. We have engineering expertise to support you with dedicated FEM analyses. If needed please contact us for further details at: info@carbonwebshop.nl

TYPICAL PERFORMANCE OF CURED MATERIAL
Adhesive Properties

Cured for 5 days @ 22 °C
  Lap Shear Strength, ISO 4587:

Steel (grit blasted)	N/mm²	37.0
	(psi)	(5,365)
Aluminum (abraded)	N/mm²	26.0
	(psi)	(3,770)
Aluminum (anodised)	N/mm²	17.9
	(psi)	(2,595)
Galvanized Steel (Hot Dipped)	N/mm²	8.5
	(psi)	(1,230)
Stainless steel	N/mm²	23.0
	(psi)	(3,335)
Polycarbonate	N/mm²	5.3
	(psi)	(765)
Nylon	N/mm²	1.6
	(psi)	(230)
Wood (Fir)	N/mm²	11.3
	(psi)	(1,635)
GRP	N/mm²	5.0
	(psi)	(725)
ABS	N/mm²	4.7
	(psi)	(680)

180° Peel Strength, ISO 8510-2:

Steel (grit blasted)	N/mm	8.0
	(lb/in)	(45.5)

Tensile Strength, ISO 6922:

Steel pin (grit blasted) to Soda glass	N/mm²	43.2
	(psi)	(6,260)

Impact Strength, ISO 9653, J/m² :
  Steel (grit blasted)   5.8

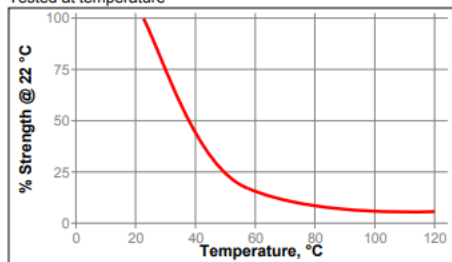## TYPICAL ENVIRONMENTAL RESISTANCE
Cured for 5 days @ 22 °C
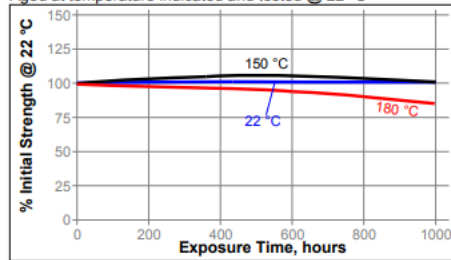 Lap Shear Strength, ISO 4587:
    Steel (grit blasted)

Hot Strength
Tested at temperature

Heat Aging
Aged at temperature indicated and tested @ 22 °C

Chemical/Solvent Resistance
Aged under conditions indicated and tested @ 22 °C.

		% of initial strength	
Environment	°C	500 h	1000 h
Motor oil (10W30)	87	135	145
Unleaded gasoline	22	95	125
Water/glycol 50/50	87	75	75
Salt fog	22	---	80
98% RH	40	85	90
Condensing Humidity	49	---	90
Water	22	---	90
Acetone	22	75	90
Isopropanol	22	90	100

		% of initial strength	
Environment	°C	500 h	1000 h
98% RH	40	90	90

GENERAL INFORMATION
For safe handling information on this product, consult the Safety Data Sheet (SDS).

This product is not recommended for use in pure oxygen and/or oxygen rich systems and should not be selected as a sealant for chlorine or other strong oxidizing materials.

Where aqueous washing systems are used to clean the surfaces before bonding, it is important to check for compatibility of the washing solution with the adhesive. In some cases these aqueous washes can affect the cure and performance of the adhesive.

Directions for use:
1. For best performance part surfaces should be clean and free of grease.
2. For high strength structural bonds, remove surface contaminants such as paint, oxide films, oils, dust, mold release agents and all other surface contaminants.
3. **Dual Cartridges:** To use simply insert the cartridge into the application gun and start the plunger into the cylinders using light pressure on the trigger. Next, remove the cartridge cap and expel a small amount of adhesive to be sure both sides are flowing evenly and freely. If automatic mixing of resin and hardener is desired, attach the mixing nozzle to the end of the cartridge and begin dispensing

Henkel Americas
+860.571.5100

Henkel Europe
+49.89.320800.1800

Henkel Asia Pacific
+86.21.2891.8859

For the most direct access to local sales and technical support visit: www.henkel.com/industrial

the adhesive. For hand mixing, expel the desired amount of the adhesive and mix thoroughly. Mix for approximately 15 seconds after uniform color is obtained.

Bulk Containers: Mix thoroughly by weight or volume in the proportions specified in Product Description section. Mix vigorously, approximately 15 seconds after uniform color is obtained.

4. Do not mix quantities greater than 4 kg as excessive heat build-up can occur. Mixing smaller quantities will minimise the heat build-up.

5. Apply the adhesive as quickly as possible after mixing to one surface to be joined. For maximum bond strength apply adhesive evenly to both surfaces. Parts should be assembled immediately after mixed adhesive has been applied.

6. Keep assembled parts from moving during cure. The bond should be allowed to cure 24 hours before subjecting to any service loads.

7. Excess uncured adhesive can be wiped away with organic solvent (e.g. Acetone).

8. After use and before adhesive hardens mixing and dispensing equipment should be cleaned with hot soapy water.

Not for product specifications

The technical data contained herein are intended as reference only. Please contact your local quality department for assistance and recommendations on specifications for this product.

Storage

Store product in the unopened container in a dry location. Storage information may be indicated on the product container labeling.

Optimal Storage: 8 °C to 21 °C. Storage below 8 °C or greater than 28 °C can adversely affect product properties. Material removed from containers may be contaminated during use. Do not return product to the original container. Henkel Corporation cannot assume responsibility for product which has been contaminated or stored under conditions other than those previously indicated. If additional information is required, please contact your local Technical Service Center or Customer Service Representative.

Conversions

(°C x 1.8) + 32 = °F
kV/mm x 25.4 = V/mil
mm / 25.4 = inches
µm / 25.4 = mil
N x 0.225 = lb
N/mm x 5.71 = lb/in
N/mm² x 145 = psi
MPa x 145 = psi
N·m x 8.851 = lb·in
N·m x 0.738 = lb·ft
N·mm x 0.142 = oz·in
mPa·s = cP

Note:

The information provided in this Technical Data Sheet (TDS) including the recommendations for use and application of the product are based on our knowledge and experience of the product as at the date of this TDS. The product can have a variety of different applications as well as differing application and working conditions in your environment that are beyond our control. Henkel is, therefore, not liable for the suitability of our product for the production processes and conditions in respect of which you use them, as well as the intended applications and results. We strongly recommend that you carry out your own prior trials to confirm such suitability of our product.

Any liability in respect of the information in the Technical Data Sheet or any other written or oral recommendation(s) regarding the concerned product is excluded, except if otherwise explicitly agreed and except in relation to death or personal injury caused by our negligence and any liability under any applicable mandatory product liability law.

In case products are delivered by Henkel Belgium NV, Henkel Electronic Materials NV, Henkel Nederland BV, Henkel Technologies France SAS and Henkel France SA please additionally note the following:

In case Henkel would be nevertheless held liable, on whatever legal ground, Henkel's liability will in no event exceed the amount of the concerned delivery.

In case products are delivered by Henkel Colombiana, S.A.S. the following disclaimer is applicable:

The information provided in this Technical Data Sheet (TDS) including the recommendations for use and application of the product are based on our knowledge and experience of the product as at the date of this TDS. Henkel is, therefore, not liable for the suitability of our product for the production processes and conditions in respect of which you use them, as well as the intended applications and results. We strongly recommend that you carry out your own prior trials to confirm such suitability of our product.

Any liability in respect of the information in the Technical Data Sheet or any other written or oral recommendation(s) regarding the concerned product is excluded, except if otherwise explicitly agreed and except in relation to death or personal injury caused by our negligence and any liability under any applicable mandatory product liability law.

In case products are delivered by Henkel Corporation, Resin Technology Group, Inc., or Henkel Canada Corporation, the following disclaimer is applicable:

The data contained herein are furnished for information only and are believed to be reliable. We cannot assume responsibility for the results obtained by others over whose methods we have no control. It is the user's responsibility to determine suitability for the user's purpose of any production methods mentioned herein and to adopt such precautions as may be advisable for the protection of property and of persons against any hazards that may be involved in the handling and use thereof. In light of the foregoing, **Henkel Corporation specifically disclaims all warranties expressed or implied, including warranties of merchantability or fitness for a particular purpose, arising from sale or use of Henkel Corporation's products. Henkel Corporation specifically disclaims any liability for consequential or incidental damages of any kind, including lost profits.** The discussion herein of various processes or compositions is not to be interpreted as representation that they are free from domination of patents owned by others or as a license under any Henkel Corporation patents that may cover such processes or compositions. We recommend that each prospective user test his proposed application before repetitive use, using this data as a guide. This product may be covered by one or more United States or foreign patents or patent applications.

Trademark usage

Except as otherwise noted, all trademarks in this document are trademarks of Henkel Corporation in the U.S. and elsewhere. ® denotes a trademark registered in the U.S. Patent and Trademark Office.

Reference 1.2

Henkel Americas
+860.571.5100

Henkel Europe
+49.89.320800.1800

Henkel Asia Pacific
+86.21.2891.8859

For the most direct access to local sales and technical support visit: www.henkel.com/industrial

LOCTITE® EA 9466™

September 2014

PRODUCT DESCRIPTION

LOCTITE® EA 9466™ provides the following product characteristics:

Technology	Epoxy
Chemical Type	Epoxy
Appearance (Resin)	White opaque paste
Appearance (Hardener)	White translucent liquid
Appearance (Mixture)	Off-white opaque paste
Components	Two component - requires mixing
Viscosity	Medium
Mix Ratio, by volume - Resin : Hardener	2 : 1
Mix Ratio, by weight - Resin : Hardener	100 : 50
Cure	Room temperature cure after mixing
Application	Bonding

LOCTITE® EA 9466™ is a toughened, industrial grade epoxy adhesive with extended work life. Once mixed, the two component epoxy cures at room temperature to form a tough, off-white bondline which provides high peel resistance and high shear strengths. The fully cured epoxy is resistant to a wide range of chemicals and solvents, and acts as an excellent electrical insulator. LOCTITE® EA 9466™ provides excellent bond strengths to a wide variety of plastics and metals. Typical applications include general purpose industrial applications requiring extended work life for adjusting parts during assembly .

TYPICAL PROPERTIES OF UNCURED MATERIAL

Resin:
Specific Gravity @ 25 °C	1.0
Flash Point - See SDS	
Viscosity, Brookfield - RVT, 25 °C, mPa·s (cP):	
Spindle 6, speed 20 rpm,	15,000 to 50,000

Hardener:
Specific Gravity @ 25 °C	1.0
Flash Point - See SDS	
Viscosity, Brookfield - RVT, 25 °C, mPa·s (cP):	
Spindle 5, speed 50 rpm,	25,000 to 60,000

Mixed:
Working life, minutes	60

TYPICAL CURING PERFORMANCE

Fixture Time

Fixture time is defined as the time to develop a shear strength of 0.1 N/mm² .

Fixture Time, ISO 4587, minutes:
Steel (grit blasted)	180

Cure Speed vs. Time, Temperature

The rate of cure will depend on the ambient temperature, elevated temperatures may be used to accelerate the cure. The graph below shows shear strength developed with time at various temperatures on grit blasted steel lap shears and tested according to ISO 4587.
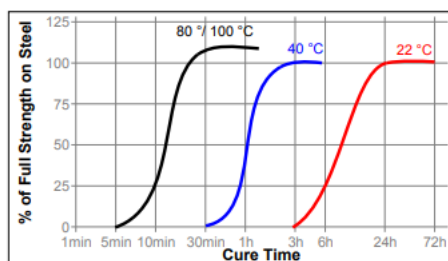
TYPICAL PROPERTIES OF CURED MATERIAL

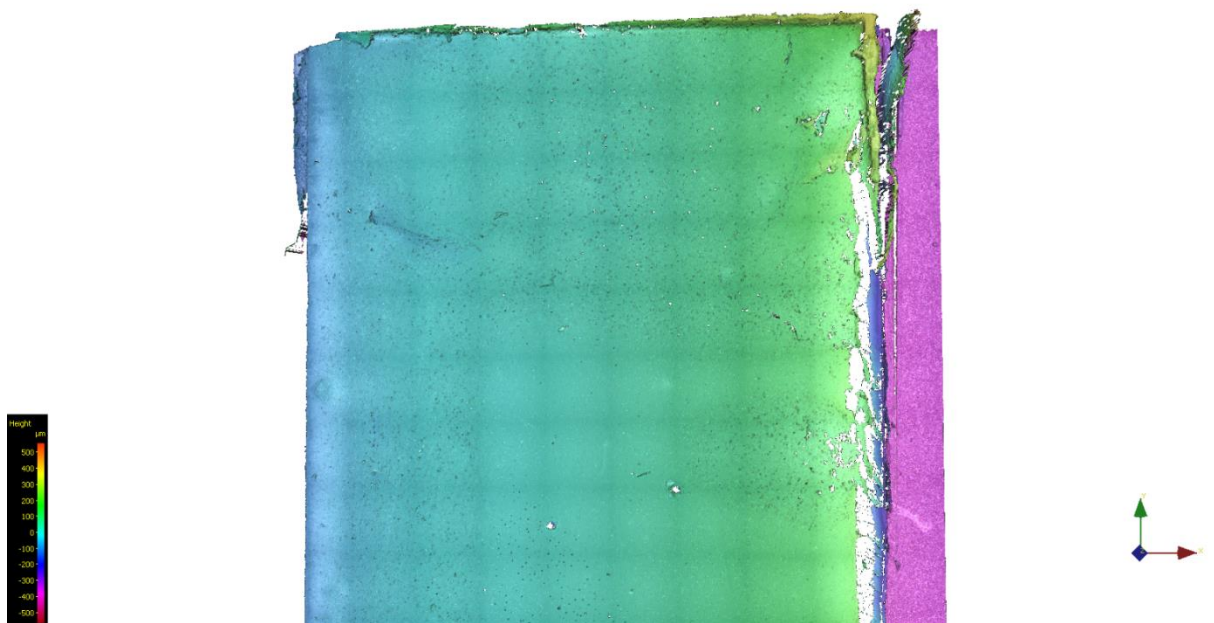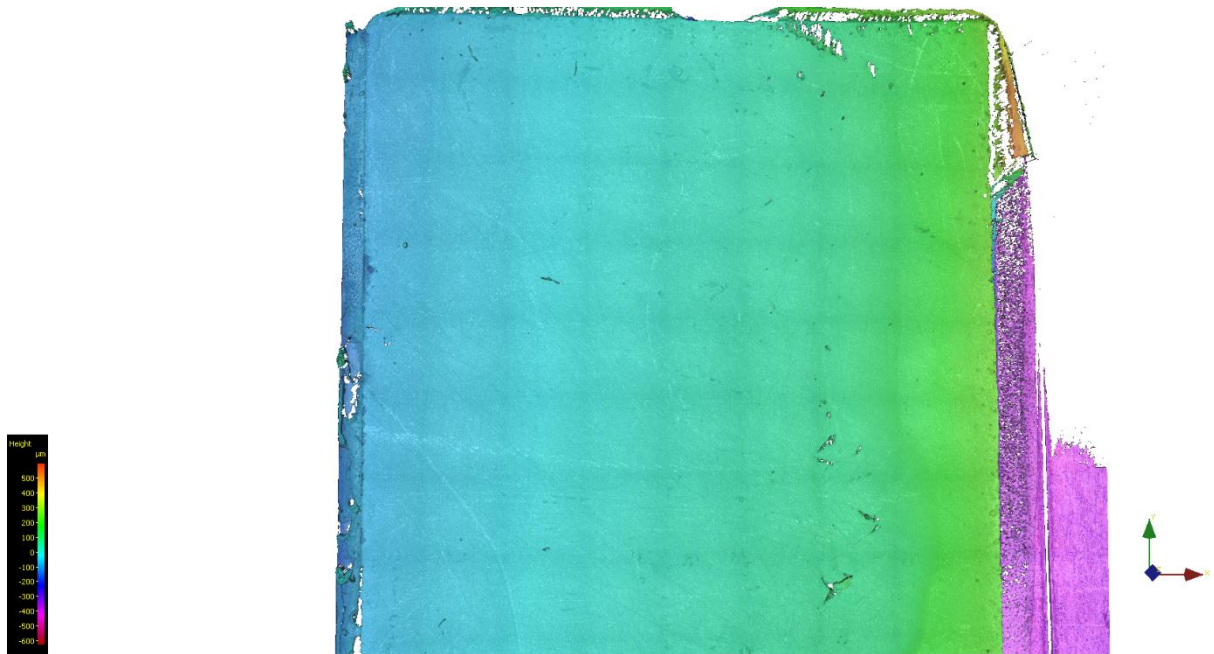Cured for 7 days @ 22 °C, 1.2 mm thick film

Physical Properties:
Glass Transition Temperature, ASTM E 1640, °C		62
Shore Hardness, ISO 868, Durometer D		60
Elongation, ISO 527-3, %		3
Tensile StrengthASTM D 882	N/mm²	32
	(psi)	(4,640)
Tensile Modulus, ISO 527-3	N/mm²	1,718
	(psi)	(249,110)

Electrical Properties:
Dielectric Breakdown Strength, IEC 60243-1, kV/mm	30

Appendix B

Appendix C

Batch 2 — Stress [Nmm⁻²] vs Displacement [mm]: SLJ 1, SLJ 2, SLJ 3, SLJ 4, SLJ 5, SLJ 6

Batch 3 — Stress [Nmm⁻²] vs Displacement [mm]: SLJ 1, SLJ 2, SLJ 3, SLJ 4, SLJ 5, SLJ 6

Batch 5

SLJ 1 · SLJ 2 · SLJ 3 · SLJ 4 · SLJ 5 · SLJ 6

Batch 6

SLJ 1 · SLJ 2 · SLJ 3 · SLJ 4 · SLJ 5 · SLJ 6

Batch 8

Batch 9

Batch 12

Batch 14

Batch 18